AAA Workshop Series Vol. 11
Asociación Argentina de Astronomía

II Workshop on

Chemical Abundances in Gaseous Nebulae

Open problems in Nebular Astrophysics

São José dos Campos, Brazil, 11-14 March 2019

Proceedings

Edited by
Mónica V. Cardaci, Guillermo F. Hägele & Enrique Pérez-Montero

Michael Dopita, a leading researcher in this field and originally invited as lecturer sadly passed away last year. This workshop proceedings book is dedicated to his memory.

ASOCIACIÓN ARGENTINA DE ASTRONOMÍA
WORKSHOP SERIES

Vol. 11

CHEMICAL ABUNDANCES IN GASEOUS NEBULAE

OPEN PROBLEMS IN NEBULAR ASTROPHYSICS

Proceedings of the Workshop to celebrate the
50th anniversary of the Peimbert & Costero (1969) work.
Universidade do Vale do Paraíba, São José dos Campos, Brasil
March 11-14, 2019

In memory of Michael Dopita

Edited by

Mónica V. Cardaci
Instituto de Astrofísica de La Plata, CONICET-UNLP, Argentina

Guillermo F. Hägele
Instituto de Astrofísica de La Plata, CONICET-UNLP, Argentina

Enrique Pérez-Montero
Instituto de Astrofísica de Andalucía, Granada, Spain

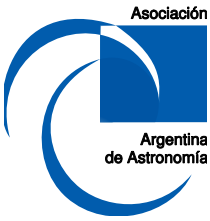

Published by:
ASOCIACIÓN ARGENTINA DE ASTRONOMÍA

ISBN: 978-987-24948-6-5

Credits:
Cover picture: NGC 1569 taken with the Hubble Space Telescope.
Credit: NASA, ESA, Hubble Heritage (STScI/AURA).
https://apod.nasa.gov/apod/ap081229.html
Cover design: Mónica V. Cardaci
Logo design: Lilia C. Rodrigues & UNIVAP Marketing Department
Conference photo: Luiz Madureira
LaTeX editor: Mónica V. Cardaci
using LaTeX's 'confproc' package, version 0.8

Only electronic format — August 2019

Cardaci, Mónica V..
Chemical Abundances in Gaseous Nebulae : open problems in nebular astrophysics / Mónica V. Cardaci ; Guillermo F. Hägele ; Enrique Pérez-Montero. - 1a ed . - La Plata : Asociación Argentina de Astronomía, 2019.
Libro digital, PDF - (Asociación Argentina de Astronomía Workshop Series ; 11)
Archivo Digital: online
ISBN 978-987-24948-6-5
1. Astrofísica. 2. Astronomía. I. Guillermo F. Hägele, II. Pérez-Montero, Enrique III. Título
CDD 523.01

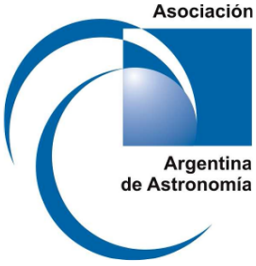

ASOCIACIÓN ARGENTINA DE ASTRONOMÍA

Fundada en 1958

Personería Jurídica (Legajo 21.459 - Matr. 1.421), Pcia. de Buenos Aires

Comisión Directiva

(2014 – 2017)

PRESIDENTE:	Leonardo J. Pellizza
VICEPRESIDENTE:	Susana E. Pedrosa
SECRETARIO:	Rodrigo F. Díaz
TESORERA:	Daniel D. Carpintero
VOCAL 1RO:	Andrea V. Ahumada
VOCAL 2DO:	Andrea P. Buccino
VOCAL SUP. 1RO:	Georgina Coldwell
VOCAL SUP. 2DO:	Hebe Cremades

Comisión Revisora de Cuentas

TITULARES:	Sofía A. Cora
	Gerardo Juan M. Luna
	Luis R. Vega

Comité Nacional de Astronomía

SECRETARIA:	Cristina Mandrini
MIEMBROS:	Lydia Cidale
	Hebe Cremades
	Federico González
	Hernán Muriel

1st Workshop on

Chemical Abundances in Gaseous Nebulae (CAGN2019)

São José dos Campos, Brasil, March 11-14, 2019

Scientific Organizing Committee

Oli Dors (UNIVAP/Brazil) *chair*
Guillermo Hägele (IALP/Argentina)
Mónica Cardaci (IALP/Argentina)
César Esteban (IAC/Spain)
Ângela Krabbe (UNIVAP)
Evan Skillman (UMN/USA)
Jorge García Rojas (IAC/ES)
Enrique Pérez-Montero (IAA/Spain)
Leonid Pilyugin (MAO/Ukraine)

Local Organizing Committee

Oli Dors (UNIVAP)
Ângela Krabbe (UNIVAP)
Mónica Cardaci (IALP/Argentina)
Guillermo Hägele (IALP/Argentina)
Thays Bentes (UNIVAP/BR)
Irapuan Rodrigues (UNIVAP/BR)
Alexandre Oliveira (UNIVAP/BR)
Adriano Monteiro (UNIVAP/BR)
Alberto Alves (UNIVAP/BR)

Editorial Committee

Mónica V. Cardaci
Guillermo F. Hägele
Enrique Pérez-Montero

Foreword

The determination of the abundance of heavy elements (e.g. O, N, S, Ar) in gaseous nebulae is fundamental to understand the formation and the chemical evolution of galaxies and of the Universe. Despite recent surveys (e.g. Califa, Sloan Digital Sky Survey) have provided advances in the knowledge of gaseous nebulae and their host galaxies, important aspects in the study of these objects remain ill-defined. In particular, the abundance discrepancy problem in HII regions and planetary nebulae, generally interpreted as being caused by the presence of temperature fluctuation, calling into question the nebular abundance scale of the Milk Way and extragalactic objects. In order to address this problem this workshop brought together a group of scientists and students to stimulate extensive discussions about crucial questions related to the study of the chemical abundances in gaseous nebulae.

During this workshop we celebrated the 50th anniversary of the seminal paper Peimbert & Costero (1969, BOTT, 5, 3), one of the first works to present the formalism to calculate the abundance of heavy elements, electron temperature fluctuation and Ionization Correction Factors in gaseous nebulae.

The present volume contains the set of contributions presented at the workshop.

Oli Dors, Mónica V. Cardaci and Guillermo F. Hägele
São José dos Campos, Brazil, March 2019

Words of the editors

The editors wish to thank Oli Dors for make possible this successful workshop. They also want to thank the hospitality of the Universidade do Vale do Paraíba and the hospitality of its *Instituto de Pesquisa e Desenvolvimento - IP&D -*.

M. Cardaci, G. Hägele and E. Pérez-Montero
Editors.

CONTENTS

Posters

Honor and Invited Talks

Chemical Abundances in Gaseous Nebulae:
Open problems in Nebular astrophysics
AAA Workshop Series 11, 2019
M. Cardaci, G. Hägele & E. Pérez-Montero, eds.

Honour Talk

50 YEARS OF TEMPERATURE INHOMOGENEITIES IN GASEOUS NEBULAE

Manuel Peimbert

Instituto de Astronomía, Universidad Nacional Autónoma de México, Apdo. Postal 70-264 Ciudad Universitaria, México

Abstract. A review of some of the papers that discuss the relevance of the temperature structure present in HII regions and planetary nebulae is presented. Particular attention is given to the determination of the chemical abundances of these objects.

Key words: ISM: abundances — galaxies: ISM — primordial nucleosynthesis — HII regions — Magellanic Clouds

1. Introduction

Some of the following ideas are the result of my collaboration with: Silvia Torres-Peimbert, Antonio Peimbert, Valentina Luridiana, Rafael Costero, Julieta Fierro, Miriam Peña, Leticia Carigi, Gloria Delgado-Inglada, César Esteban, Jorge García-Rojas, María Teresa Ruiz, Charles Robert O'Dell, and Gary Ferland.
The determination of the chemical abundances of HII regions and Planetary Nebulae is paramount for the study of the evolution of the stars, the galaxies and the universe as a whole. The determination of the chemical abundances strongly depends on the temperature structure of the gaseous nebulae.
This review is based on two papers the first one (Peimbert, 1967) discusses the differences in the electron temperatures derived from different methods, and the second one (Peimbert & Costero, 1969) applies the formulation of the first paper to derive the chemical composition of gaseous nebulae.
A recent review on the determination of the physical conditions and chemical abundances of gaseous nebulae has been presented by Peimbert et al. (2017).

2. Temperature determinations

The average temperature of a gaseous nebula is given by

$$T_0(X^{i+}) = \frac{\int T_e n_e n(X^{i+}) dV}{\int n_e n(X^{i+}) dV}. \quad (1)$$

The mean square temperature fluctuation is given by

$$t^2(X^{i+}) = \frac{\int \left[T_e - T_0(X^{i+})\right]^2 n_e n(X^{i+}) dV}{T_0(X^{i+})^2 \int n_e n(X^{i+}) dV}. \quad (2)$$

The temperature derived from the [OIII] lines is given by

$$T_{4363/5007} = T_0 \left[1 + \frac{t^2}{2}\left(\frac{91300}{T_0} - 2.68\right)\right]. \quad (3)$$

The temperature given from the ratio of the Balmer continuum to Hβ is given by

$$T_{Bac} = T_0 \left(1 - 1.67 t^2\right). \quad (4)$$

3. Presence of temperature Inhomogeneities

For the best observed objects it is found that the forbidden line temperatures are higher than the Balmer temperatures, the differences are higher than those predicted by the theoretical photoionization models. From photoionization models the t^2 values predicted by `CLOUDY` for PNe and HII regions are in the 0.000 to 0.015 range with a typical value of about 0.004 (Ferland et al., 2013, 2017).
Peimbert et al. (2012) from 37 galactic and extragalactic HII regions found $0.019 < t^2 < 0.120$ with an average value of 0.044.
Toribio San Cipriano et al. (2017) from 5 HII regions in the LMC found $0.028 < t^2 < 0.069$ with an average value of 0.038, and from 4 HII regions in the SMC found that $0.075 < t^2 < 0.107$ with an average value of 0.089.
The abundances relative to hydrogen derived from recombination lines of oxygen and carbon are almost unaffected by temperature variations.
The abundances derived from collisionally excited lines, under the assumption of constant temperature, typically underestimate the abundances relative to hydrogen by a factor of 2 to 3 (C, O, Ne), the so called abundance discrepancy factor, ADF. By adopting t^2 values different from 0.00 it is possible to reconcile the abundances derived from forbidden lines with those derived from permitted lines.

4. Planetary Nebulae

There are two families of PNe, the chemically homogeneous ones and the chemically inhomogeneous ones.
For well observed chemically homogeneous PNe, Classical PNe, it has been found that the t^2 values derived from $T(Balmer)$ and T([O III]) are similar to those derived from a) T(He I) and T([O III]), b) T(C II) and T([O III]), and c) T(O II) and T([O III]). In addition Classical PNe have ionized masses in the 0.05 to 0.40 M_{sun} range (e.g., Mallik & Peimbert, 1988).
From a study of 20 well observed Classical PNe, Peimbert et al. (2014) found the following properties: a) they do not have inclusions of high density and low temperature. b) they have t^2 values in the 0.024 to 0.128 range with a typical t^2 value of 0.064, and c) they have ADF values in the 1.4 to 10.0 range with a

typical value of 2.3. For NGC 5307 and NGC 5315 the radial velocities and the FWHM of the OII and [OIII] emission lines are the same, indicating that they originate in the same volume elements.
PNe with inhomogeneous chemical composition have the following properties: a) they do have gaseous inclusions of high density and low temperature in the gaseous envelope, possibly the result of mass loss during close binary evolution, b) their O/H values decrease from the center outward, c) they present large temperature inhomogeneities that cannot be analyzed with the t^2 formalism in a one phase model, and d) their ADF values are in the 10 to 100 range.
Peimbert et al. (1995) found that the ratio of C^{++} derived from recombination lines to that from forbidden lines amounts to about three for about 40 PNe.
Galactic chemical evolution models (Carigi et al., 1995; Matteucci, 2006) indicate that about half of the carbon in the Galaxy has been produced by intermediate mass stars. This result is consistent with the carbon abundances derived from recombination lines, but not with the carbon abundances derived from collisionally excited lines assuming constant temperature that are typically two to three times smaller than those derived from recombination ones.

5. HII Regions

5.1. The O/H ratio in the solar vicinity

The brightest, closest, and most studied HII region is the Orion Nebula. Under the assumption of constant temperature and based on the [OII] and [OIII] line intensities the $12 + \log(O/H)$ value derived by different groups amounts to 8.50 ± 0.02 (Peimbert & Torres-Peimbert, 1977; Osterbrock et al., 1992; Peimbert et al., 1993; Esteban et al., 1998; Deharveng et al., 2000; Esteban et al., 2004). Alternatively Esteban et al. (2004) based on the OII recombination lines obtain $12 + \log(O/H) = 8.72 \pm 0.03$. The difference between both results is real and is called the abundance discrepancy factor, ADF. We consider that the proper O/H abundances are those obtained from the O and H recombination lines since their ratio is almost independent of the temperature, consequently we consider that the ADF is due to spatial temperature variations that affect the O/H determinations based on O forbidden lines.
In many papers the abundances derived from forbidden lines (those of [OIII]) are called the direct method abundances, DM, while those derived from recombination lines (like those of OII and CII) are called the temperature independent method abundances, TIM.
It is important to compare the HII region abundances with the stellar abundances, since the stellar determinations are based on different methods and can help us to decide if the DM or the TIM method is the proper one to determine the O/H abundances.
To compare the HII region abundances with stellar abundances we have to take into account two considerations: a) we have to add to the gaseous abundances the fraction of O atoms trapped up in dust, and b) the age of the stars, because the O/H abundance increases with time in the interstellar medium.
Espíritu et al. (2017) found that the fraction of oxygen atoms embedded in dust in the Orion nebula amounts to 0.126 dex $\pm$0.024 dex in agreement with the value

of 0.12 dex derived by Mesa-Delgado et al. (2009) and Peimbert & Peimbert (2010). Therefore the gaseous value derived from recombination lines plus the dust O abundance amounts to $12 + \log(O/H) = 8.85 \pm 0.05$. This result is in excellent agreement with the six most O-rich thin disk F and G dwarfs of the solar vicinity studied by Bensby & Feltzing (2006) that show an average value of $12 + \log(O/H) = 8.85$. Nieva & Simón-Díaz (2011) have determined the O/H ratio for 13 B stars of the Ori OB1 association and obtain a $12 + \log(O/H) = 8.77 \pm 0.03$.

A third comparison between stars and the Orion nebula can be made by using the solar O/H value. The Sun has an age of 4.6 billion years and might have migrated from the place where it was born. Carigi et al. (2019) have made two chemical evolution models to fit the galactic HII region abundances in our galaxy derived with the TIM and DM. The TIM model, that fits the HII region abundances for the present time, agrees with the B stars and Cepheids abundances, while the model based on the DM abundance determinations that fits the HII region abundances predicts O/H values about 0.25 dex smaller. Similarly, the O/H value predicted by the TIM model for an age of 4.6 yrs agrees with the solar abundance derived by Asplund et al. (2009), where the probable migration of the Sun due to its age was taken into account. Alternatively the model based on the DM abundances of HII regions predicts values about 0.25 dex smaller than the solar abundances. See also Figures 7 and 9 of Carigi et al. (2019).

5.2. M33 and NGC 300

Toribio San Cipriano et al. (2016) from observations of HII regions across the disks of NGC 300 and M33 found higher O/H ratios from recombination lines, RL, than from collisionally excited lines, CEL. For NGC 300 the RL gave abundances 0.35 dex higher than the CEL, similarly for M33 the RL gave abundances 0.26 dex higher than the CEL (see their Figure 5).

6. Primordial Helium

From the determination of the primordial helium abundance, Y_p, it has been found that temperature variations affect the determination. Peimbert et al. (2007) find that for a given object the higher the t^2 value the lower the Y_p that is determined. Part of the differences between the Y_p value derived by Izotov et al. (2014) and the values derived by Peimbert et al. (2016) and Valerdi et al. (2019) are due to the t^2 values adopted. The primordial helium abundance also provides strong restrictions on the number of neutrino families and the neutron mean life.

7. Posible causes for temperature variations

7.1. Deposition of mechanical energy

Peimbert et al. (1991) suggest that the high t^2 values observed in PNe and HII regions might be due to the presence of shock waves. Many giant extragalactic HII regions, for example NGC 5471 (Skillman, 1985), and I Zw 18 (Skillman &

Kennicutt, 1993), present evidence of large velocity winds probably produced by Wolf-Rayet stars and supernovae.
González-Delgado et al. (1994) propose that stellar winds from WR stars play an important role explaining the high t^2 values derived from the giant extragalactic HII region NGC 2363.
Peimbert et al. (1995) find that $T(C^{++})$, the temperature derived from the [CIII] $I(1906 + 1909)$/CII $I(4267)$, ratio is in general considerably smaller than the $T(O^{++})$ temperature derived from the $I(5007)/I(4363)$ ratio. They also find that the objects with the highest $T(O^{++}) - T(C^{++})$ values are those that show large velocities and complex velocity fields, and consequently suggest that the deposition of mechanical energy by the stellar winds of the PNe is the main responsible for the temperature differences.

7.2. Chemical inhomogeneities

Tsamis et al. (2003); Tsamis & Péquignot (2005); Stasińska et al. (2007) suggested the presence of metal rich droplets produced by supernova ejecta as predicted by the scenario of Tenorio-Tagle (1996). These droplets do not get fully mixed with the interstellar medium until they become photoionized in HII regions and they could be responsible for the ADF problem. Moreover, these droplets, if present, had to be denser and cooler than the surrounding material in H II regions.
Peimbert & Peimbert (2013) based on high quality observations of multiplet V1 of OII of 8 galactic OII regions and one extragalactic HII region find that the signature of oxygen-rich droplets of high density and low temperature is absent, ruling out the possibility of chemical inhomogeneities in these HII regions.
González-Delgado et al. (1994) consider that some giant extragalactic HII regions, like NGC 2363, include WR stars and SNe remnants that will produce chemical inhomogeneities.
Corradi et al. (2015); García-Rojas (2016); García-Rojas et al. (2016b,a); Jones et al. (2016); McNabb et al. (2016); Wesson et al. (2017) and references therein have found a group of PNe that show ADF values in the 10 to 80 range. This group include Haro 2-33, (Hen 2-283), Fg 1, NGC 6778, NGC 6339, Pe 1-9, MPA 1759, M1-42, Hf 2-2, Abell 30, Abell 46 and Abell 63. These PNe correspond to binary stars that after a first ejection of gas produce a second one with a very small mass but with a very high overabundance of O/H relative to the first ejecta. The ADF in these objects is strongly centrally peaked. They propose that these ADF values should be explained in the framework of close binary evolution and discuss the possibility that these systems could have gone through a common envelope phase.

7.3. Other causes of temperature inhomogeneities

Peimbert et al. (2017) discuss other possible sources of temperature inhomogeneities in gaseous nebulae that have been presented in the literature: a) shadowed regions, b) spatially distributed ionization sources, c) density inhomogeneities, d) time dependent ionization, e) cosmic rays, f) overestimation of the intensity of weak lines, and g) magnetic reconnection.

8. Further Considerations

Most HII regions and PNe show temperature variations larger than predicted by chemically homogeneous photoionization models.
A small fraction of PNe show chemical inhomogeneities that can produce large temperature variations.
High quality observations are needed to show if a nebula is chemically homogeneous or not.
It is also possible to derive t^2 from a set of highly accurate intensity measurements of HeI emission lines.

9. Conclusions

To study the evolution of the stars, the galaxies and the Universe it is necessary to have accurate abundances of HII regions and planetary nebulae.
For chemically homogeneous nebulae the proper abundances are given by the carbon, oxygen and hydrogen recombination lines.
The ADF values for chemically homogeneous nebulae are due to temperature variations that can be represented by t^2. The abundances derived from collisionally excited lines, under the assumption of constant temperature typically underestimate the abundances relative to hydrogen by a factor of 0.25 to 0.35 dex.
The primordial helium abundance depends weakly on the adopted t^2 value, the higher the t^2 value the lower the Y_p value. This dependence is important for the study of the number of neutrino families and the neutron mean life.

Acknowledgments. I am grateful to Oli Dors and our Brazilian friends for organizing an excellent meeting.

References

Asplund M., Grevesse N., Sauval A. J., Scott P., 2009, *ARA&A*, **47**, 481
Bensby T., Feltzing S., 2006, *MNRAS*, **367**, 1181
Carigi L., Colin P., Peimbert M., Sarmiento A., 1995, *ApJ*, **445**, 98
Carigi L., Peimbert M., Peimbert A., 2019, *ApJ*, **873**, 107
Corradi R. L. M., García-Rojas J., Jones D., Rodríguez-Gil P., 2015, *ApJ*, **803**, 99
Deharveng L., Peña M., Caplan J., Costero R., 2000, *MNRAS*, **311**, 329
Espíritu J. N., Peimbert A., Delgado-Inglada G., Ruiz M. T., 2017, *RevMexAA*, **53**, 95
Esteban C., Peimbert M., García-Rojas J., Ruiz M. T., Peimbert A., Rodríguez M., 2004, *MNRAS*, **355**, 229
Esteban C., Peimbert M., Torres-Peimbert S., Escalante V., 1998, *MNRAS*, **295**, 401
Ferland G. J., Chatzikos M., Guzmán F., Lykins M. L., van Hoof P. A. M., Williams R. J. R., Abel N. P., Badnell N. R., Keenan F. P., Porter R. L., Stancil P. C., 2017, *RevMexAA*, **53**, 385

Ferland G. J., Porter R. L., van Hoof P. A. M., Williams R. J. R., Abel N. P., Lykins M. L., Shaw G., Henney W. J., Stancil P. C., 2013, *RMxAA*, **49**, 137
García-Rojas J., 2016, *arXiv: 1612.02568*
García-Rojas J., Corradi R. L. M., Monteiro H., Jones D., Rodríguez-Gil P., Cabrera-Lavers A., 2016a, *ApJL*, **824**, L27
García-Rojas J., Peña M., Flores-Durán S., Hernández-Martínez L., 2016b, *A&A*, **586**, A59
González-Delgado R. M., Pérez E., Tenorio-Tagle G., Vilchez J. M., Terlevich E., Terlevich R., Telles E., Rodriguez-Espinosa J. M., Mas-Hesse M., Garcia-Vargas M. L., Diaz A. I., Cepa J., Castaneda H., 1994, *ApJ*, **437**, 239
Izotov Y. I., Thuan T. X., Guseva N. G., 2014, *MNRAS*, **445**, 778
Jones D., Wesson R., García-Rojas J., Corradi R. L. M., Boffin H. M. J., 2016, *MNRAS*, **455**, 3263
Mallik D. C. V., Peimbert M., 1988, *RevMexAA*, **16**, 111
Matteucci F., 2006, S. Kubono, W. Aoki, T. Kajino, T. Motobayashi, and K. Nomoto (eds.), *Origin of Matter and Evolution of Galaxies*, Vol. 847 of *American Institute of Physics Conference Series*, pp 79–86
McNabb I. A., Fang X., Liu X.-W., 2016, *MNRAS*, **461**, 2818
Mesa-Delgado A., Esteban C., García-Rojas J., Luridiana V., Bautista M., Rodríguez M., López-Martín L., Peimbert M., 2009, *MNRAS*, **395**, 855
Nieva M.-F., Simón-Díaz S., 2011, *A&A*, **532**, A2
Osterbrock D. E., Tran H. D., Veilleux S., 1992, *ApJ*, **389**, 305
Peimbert A., Peña-Guerrero M. A., Peimbert M., 2012, *ApJ*, **753**, 39
Peimbert A., Peimbert M., 2010, *ApJ*, **724**, 791
Peimbert A., Peimbert M., 2013, *ApJ*, **778**, 89
Peimbert A., Peimbert M., Delgado-Inglada G., García-Rojas J., Peña M., 2014, *RevMexAA*, **50**, 329
Peimbert A., Peimbert M., Luridiana V., 2016, *RevMexAA*, **52**, 419
Peimbert M., 1967, *ApJ*, **150**, 825
Peimbert M., Costero R., 1969, *Boletin de los Observatorios Tonantzintla y Tacubaya*, **5**, 3
Peimbert M., Luridiana V., Peimbert A., 2007, *ApJ*, **666**, 636
Peimbert M., Peimbert A., Delgado-Inglada G., 2017, *PASP*, **129(8)**, 082001
Peimbert M., Sarmiento A., Fierro J., 1991, *PASP*, **103**, 815
Peimbert M., Storey P. J., Torres-Peimbert S., 1993, *ApJ*, **414**, 626
Peimbert M., Torres-Peimbert S., 1977, *MNRAS*, **179**, 217
Peimbert M., Torres-Peimbert S., Luridiana V., 1995, *RevMexAA*, **31**, 131
Skillman E. D., 1985, *ApJ*, **290**, 449
Skillman E. D., Kennicutt Jr. R. C., 1993, *ApJ*, **411**, 655
Stasińska G., Tenorio-Tagle G., Rodríguez M., Henney W. J., 2007, *A&A*, **471**, 193
Tenorio-Tagle G., 1996, *AJ*, **111**, 1641
Toribio San Cipriano L., Domínguez-Guzmán G., Esteban C., García-Rojas J., Mesa-Delgado A., Bresolin F., Rodríguez M., Simón-Díaz S., 2017, *MNRAS*, **467**, 3759
Toribio San Cipriano L., García-Rojas J., Esteban C., Bresolin F., Peimbert M., 2016, *MNRAS*, **458**, 1866
Tsamis Y. G., Barlow M. J., Liu X.-W., Danziger I. J., Storey P. J., 2003,

MNRAS, **338**, 687
Tsamis Y. G., Péquignot D., 2005, *MNRAS*, **364**, 687
Valerdi M., Peimbert A., Peimbert M., Sixtos A., 2019, *arXiv: 1904.01594*
Wesson R., Jones D., García-Rojas J., Corradi R. L. M., Boffin H. M. J., 2017, X. Liu, L. Stanghellini, and A. Karakas (eds.), *Planetary Nebulae: Multi-Wavelength Probes of Stellar and Galactic Evolution*, Vol. 323 of *IAU Symposium*, pp 70–73

Chemical Abundances in Gaseous Nebulae:
Open problems in Nebular astrophysics
AAA Workshop Series 11, 2019
M. Cardaci, G. Hägele & E. Pérez-Montero, eds.

Honour talk

Multiplicity of the Orion Trapezium stars

R. Costero[1]

[1]*Instituto de Astronomia, UNAM, A.P. 70-264, 04510 Ciudad de México, México*

Abstract.
Somewhat outside the topic of this conference, some preliminary results on the ongoing spectroscopic study of the six brightest Orion Trapezium stars is presented here. The main purpose of this work is to better understand the multiplicity and stability of each of these subsystems and the dynamical future of the group. So far the most interesting results reached are: 1) The orbit of the secondary star of the eclipsing Component A (V1016 Ori) is highly inclined with respect to the equatorial plane of its primary star. 2) The also eclipsing binary BM Ori (Trapezium Component B) does have a tertiary member with period about 3.5 years, as proposed by Vitrichenko & Klochkova (2004), and is the same as the companion recently found by the Gravity Collaboration et al. (2018). 3) Component D is indeed a spectroscopic and interferometric double star with a relatively high-mass companion ($q = M_2/M_1 = 0.5$) and period $52.90 \pm 0.05\,d$. 4) Component F, is a CP star (B 7.5 p Si); its radial velocity, $23.2 \pm 4.2\,km\,s^{-1}$, is smaller than that of all other Trapezium members and, possibly, the evolutionary stage of the star is more advanced than that of members with similar mass. Consequently, Component F is probably not physically related to the Trapezium. Several evidences point to the extreme youth of this stellar group; its further study, most likely, will shed light on the formation processes of massive stars.

Key words: binaries: spectroscopic — stars: early-type — stars: pre-main-sequence — stars: chemically peculiar — stars: individual: θ^1 Ori

1. Introduction

It has been a long time since I last participated in research on Gaseous Nebulae, so I apologize for my momentarily switching the subject matter of this meeting down to stellar affairs.
In the last years I have been working on the spectral analysis of the Orion Trapezium stars, based on Échelle spectra ($R \simeq 15000$) obtained with the 2.1-m telescope at the Observatorio Astronómico Nacional in San Pedro Mártir, Baja California. Many colleagues have contributed to obtain the spectra, reduce the data and calculate orbital and eclipsing parameters, among which Juan Echevarría, Yilen Gómez-Maqueo, Lester Fox and Alan Watson stand out. The aim of

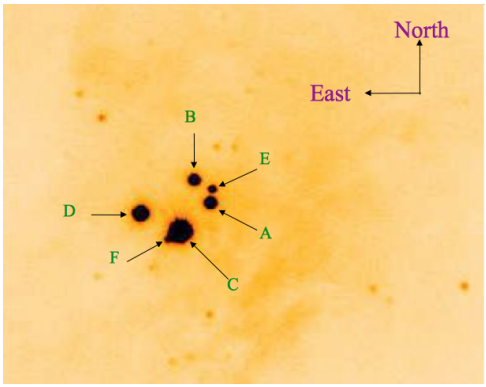

Figure 1. The Orion Trapezium in a two-second exposure image obtained with the $1.0\,m$ telescope at the Observatorio Astronómico Nacional in Tonantzintla, Puebla, using a Johnson V filter. The primary mirror was covered except for two equal circular openings $20\,cm$ in diameter. Components A and D are separated by about $21''$. Notice that Component A was near minimum light during primary eclipse.

this work is to clarify some observational parameters of this famous and complex stellar group.

The Orion Trapezium (θ^1 Ori = ADS 4186) is the center of the massive star forming region closest to the Sun and the main ionization source of the Orion Nebula. It consists of six bright stars (their V magnitudes spanning from 5.1 to 10.3) that fit inside a circle $22''$ in diameter (see Figure 1) and are immersed in the brightest part of the nebula. These circumstances have undoubtedly contributed to the fact that there are many important observational properties associated with this notorious stellar system that are either uncertain or remained unknown until recently. Indeed, the Trapezium stars are difficult targets for small telescopes because of their mutual proximity, whereas they are too bright for most stellar surveys undertaken with bigger telescopes. In particular, the radial velocity of most of its components is poorly known. This is understandable since, in addition to the already mentioned problems, nearly all of these stars are at least spectroscopic binaries. In fact, as we will show here, all but one of the six Trapezium stars are double-lined spectroscopic binaries, three of which are also known eclipsing binaries. It is important to obtain reliable velocity curves of these binaries, because the precise knowledge of their orbital parameters will allow a better calibration of the physical properties of high-mass young stars, in addition to understand their formation process and the evolution of massive multiple systems. For instance, to illustrate the latter point, Allen et al. (2017) find that realistic N-body simulations of the Orion Trapezium predict that the system will probably become dynamically unstable in a very short time ($< 30\,000\,y$) unless the mass of the components (as presently known) is substantially increased.

A few months before this meeting, a very high-resolution interferometric study of the Orion Trapezium Cluster was published (Gravity Collaboration et al., 2018), where some of the spectroscopic binaries observed were spatially resolved and the

existence of suspected companions were confirmed. These results highlight the importance of securing precise orbital parameters, derived from radial velocity curves, for the double and multiple members of this very young, compact and interesting stellar system.
Here, a short review of what is known about the multiplicity and the orbital elements of the Orion Trapezium members is presented. In addition, some relevant (though preliminary) results of our ongoing research are given, including a brief discussion about the membership to this very young system of Component F, apparently the only single star in this very young and compact stellar group.

2. Component A

θ^1 Ori A=HD 37020=V1016 Ori is at least a triple stellar system, with one B 0.5 Main Sequence (MS) star and two intermediate-mass, pre-MS companions. Considering that the Orion Nebula Cluster (ONC) has been well studied for stellar variability since the XIX Century, it is surprising that the eclipsing (Lohsen, 1975) and spectroscopic (Lohsen, 1976; Bossi et al., 1989) binary nature of this $V = 6.73$ mag star was discovered not long ago, rising speculations on a possible recent perturbation or capture in this system. In addition, θ^1 Ori A is a strong and variable radio (GMR 12 in Garay et al., 1987) and X-ray (*COUP* 745) source. At its maximum, this object becomes the brightest radio source in de ONC. It is important to note that the radio source **is not** the spectroscopic binary, as originally believed, but the third component in this system (Petr-Gotzens & Massi, 2008, and references therein).
The light curve of V1016 Ori during primary eclipse has been rather well established by Bondar' et al. (2000) and by Lloyd & Stickland (1999). It is about one magnitude deep, only slightly color dependent in the $UBVI$ photometric range, and approximately 21 hours long. Though wide, its bottom is not flat and corresponds to a partial eclipse produced by a relatively opaque object passing in front of a similar-sized but much brighter star. The secondary eclipse has never been observed and is expected to be very shallow (just a few hundredths of magnitud in V). The period of the eclipsing binary, $P = 65.433\,d$, obtained by both the above mentioned groups from the timing of primary minima, is frequently adopted when calculating the spectroscopic orbital parameters, as is the case of those determined by Vitrichenko et al. (1998) and by Stickland & Lloyd (2000) using nearly equal archival data and a few additional measurements of their own. Not surprisingly, both groups reach nearly equal orbital parameters: $e = 0.65(3)$ $K_1 = 33(2)\,km\,s^{-1}$, $\gamma = 28(1)\,km\,s^{-1}$, $\omega = 180°(4)$ (numbers in parenthesis are representative of the error in the last digit, as given by those authors).
The physical properties of the secondary star of the eclipsing binary have eluded convincing identification, though the initial (and correct) educated guess by Lohsen (1975), based on the eclipse light curve, has almost always been confirmed: it is a pre-MS star. Vitrichenko & Plachinda (2001), in a very high signal-to noise ratio (S/N) spectrum obtained during the descending branch of a primary eclipse, clearly detected low-excitation lines that they interpret to arise from the secondary and tertiary stars, the former with $T_{eff} \approx 8000\,K$ and the latter with $T_{eff} \approx 3500\,K$. Indeed, the average heliocentric radial velocity of the 13 lines attributed to the secondary (eclipsing) component is $128.8 \pm 5.5\,km\,s^{-1}$

and that of that of the 7 lines associated to the tertiary star is $33.4 \pm 11.6\, km\, s^{-1}$ (errors are the standard deviation from the mean). From the former radial velocity and the orbital elements obtained by Vitrichenko et al. (1998), the first reliable value of $q = M_2/M_1 = 0.19 \pm 0.01$ was obtained by Vitrichenko & Plachinda (2001). The radial velocity of the tertiary is, within errors, similar to the systemic velocity of the eclipsing binary. Although these results are very important, the spectral range these authors analyzed (5300-5365 Å) is small and the fit of the combined synthetic spectra with that of θ^1 Ori A is rather poor; however, their work is indicative of the excellent possibilities that high-dispersion spectroscopy may bring to the study of this stellar system.

Our early attempts (2004-2006) to improve the results for θ^1 Ori A obtained by Vitrichenko & Plachinda (2001) were fruitful. In the high S/N spectra obtained inside and around three primary eclipses (at minimum light in two of them), we realized that the spectrum arising from the secondary star was detected, even outside eclipse, when doing a cross-correlation with them and that of an early G-type standard star, and that the width of the spectral lines from the primary star was definitively smaller when inside eclipse as compared with their width well outside eclipse. This change in line width during primary eclipse is due to the Rossiter-McLaughlin (RM) effect (Rossiter, 1924; McLaughlin, 1924), that consists of an anomaly in the observed radial velocity of the occulted component, normally (when the the ecuatorial and orbital planes are coplanar) first rising above the orbital radial velocity, back to normal at mid-eclipse, and then below the expected radial velocity until the eclipse ends. However, in θ^1 Ori A, during the 21-hour long primary eclipse, the radial velocity of the primary star is always noticeably bellow the predicted orbital value, except perhaps in the first few hours. This abnormality is due to the highly inclined orbit of the secondary star with respect to the projected ecuatorial plane of the primary star (large orbital obliquity). Consequently, during the (partial) eclipse, the secondary occults mostly one side of the rotating primary, in this case the hemisphere receding from us.

The observed velocity curve inside and around primary eclipse, displaying the RM effect in θ^1 Ori A, is shown in Figure 2. In this figure, the horizontal axis is the photometric phase calculated using $P = 65.4330\, d$ and $HJD_\circ = 2\,453\,744.7585$. The latter date is that of the observed minimum light in the primary eclipse of 2006 Jan 6, calculated here from the photometric data obtained by Raul Michel Murillo and kindly made available to us. Note in this figure that the minimum radial velocity during the eclipse does not occur at phase zero (minimum light), but slightly later, and that there is a small anomalous rise in the velocity curve in the very inicial part of ingress. These features are indicative that the spin-orbit inclination is close to, but smaller than 90°.

Other orbital parameters we derive for θ^1 Ori A (still subject to revision), using the above mentioned photometric period, are: $e = 67 \pm 0.01$, $\omega = 180° \pm 2°$ and $q = M_2/M_1 = 0.20 \pm 0.1\, M_\odot$. They are in excellent agreement with those by Vitrichenko et al. (1998) and by Stickland & Lloyd (2000). From the mass ratio and assuming the mass of the primary to be $M_1 = 15\, M_\odot$ (that of a B 0.5 V star), the mass of the pre-MS secondary star is derived to be $M_2 = 3.0\, M_\odot$.

Preliminary analysis of the Échelle spectra obtained in 2004 and 2006, during and around three primary eclipses of θ^1 Ori A, was performed by Valle Lira (2011)

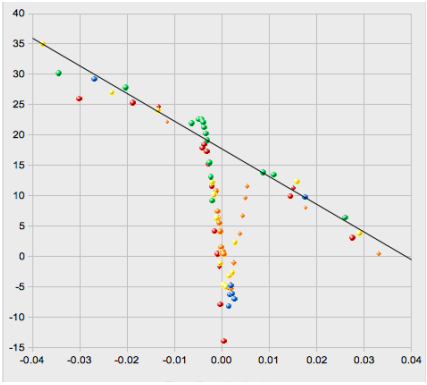

Figure 2. Velocity curve of θ^1 Ori A obtained during and around seven primary eclipses, showing the abnormal Rossiter-McLaughlin effect. The horizontal axis is the photometric phase (see text for details). Colors and shapes of data points correspond to different observing seasons.

for his BA thesis. All together, the spectra covered the complete ingress of the eclipse and well passed the minimum light. Adopting the projected rotational velocity, $v\,sin\,i = 55\,km\,s^{-1}$, obtained by Simón-Díaz et al. (2006) of the primary component, and by means of a very simple numerical simulations (no limb darkening in the primary component; opaque, non emitting secondary) Valle Lira (2011) reproduced the observed RM effect by adjusting the ratio of the stellar radii ($r = R_2/R_1$) and the spin-orbit (obliquity) angle, l. In every simulation, the impact parameter (the minimum projected distance between the two stars, in units of the primary star radius R_1, was fixed in order to fulfill one magnitude depth of the eclipse. The best fit found with this simple model occurs around $l = 70° \pm 10°$ and $r = 0.8 \pm 0.1$.

Such high orbital obliquity (spin-orbit angle) is totally abnormal in (eclipsing) binary stars. The only exception I know of is that of DI Her (Albrecht et al., 2009, 2011), where the equatorial plane of both members of the binary are strongly tilted with respect to their orbital plane; though no definitive explanation has been given to such misalignment, it could be the consequence of a relatively recent and strong orbital perturbation in a triple system, an extreme case of the Lidov-Kozai mechanism (Lidov, 1962; Kozai, 1962), or due to the capture of the secondary star by the primary. In any case, a third component in the system is required, either in a very eccentric orbit or ejected from the system as a consequence of the dynamical perturbation. Indeed, in θ^1 Ori A there is a third component (see below). Valle Lira (2011) also derived the effective temperature of the secondary star to be $T_{eff} = 5850 \pm 250\,K$, much lower than any of the other previous estimates. This was done by measuring nine close pair line ratios sensitive to temperature, in two very high S/N spectra of the secondary star (obtained during minimum light in two eclipses), and comparing each of the same pair ratios in synthetic spectra created in the 5000-9000K temperature range, with log g = 3.5 and solar abundances.

The third (hierarchical) companion in θ^1 Ori A, located about 0.2″north of the binary, was discovered by Petr et al. (1998) using holographic speckle interferometry in the H and K bands. In these bands, this star is about 1.4 magnitudes weaker than the out-of-eclipse, combined brightness of the binary components. As mentioned above, it is the highly variable (by at least a factor of 30) radio source that is frequently misidentified with the eclipsing binary; the physical process responsible for the radio emission and its large fluctuations has not been well established (for details, see Petr-Gotzens & Massi, 2008). The possibility that this third component is an interloper was ruled out very recently, when the Gravity Collaboration et al. (2018) proved that this interferometric companion is gravitationally bound to the eclipsing binary. When in cross-correlation of some of our high S/N spectra taken inside the primary eclipse, with a G5V standard, there is a hint of a late-type star at about the heliocentric systemic radial velocity of the eclipsing binary. This and other (currently preliminary) results await further analysis.

3. Component B

The weakest of the four stars that originally gave its name to the Orion Trapezium, θ^1 Ori B=HD 37021=BM Ori, is at least a sextuple stellar system, so itself constitutes a subtrapezium or mini-cluster. Its brightest member is, as in the case of Component A, a hierarchical triple star also consisting of an eclipsing and spectroscopic binary (BM Ori, in a nearly circular orbit with period $P = 6.4705\,d$) and a tertiary component, whose existence was recently, but inadvertently, confirmed beyond doubt by Gravity Collaboration et al. (2018). The reminding three components of the sextet are a resolved binary (separated from each other by about 0.12″ and at nearly 0.97″ from BM Ori), and a much fainter star located 0.6″ northwest from the main component. More information about these companions may be found in Gravity Collaboration et al. (2018) and references therein. The precarious dynamical stability of this subtrapezium has been studied by Allen et al. (2015). In what follows, only the close and massive triple system will be analyzed.

The eclipsing binary, BM Ori, is a very peculiar Algol-type system: 1) The light curve of the primary eclipse seams to be a total one, with a wide flat bottom (though with small fluctuations) but, during this part of the eclipse, the spectrum of the star is almost equal to that outside eclipse; 2) the secondary eclipse is very shallow, only reasonably well observed in the R and I filters; 3) some time between 1990 and 2010, the duration of the flat bottom of the primary eclipse changed from about 8 hours to less than 4 hours (Windemuth et al., 2013). Several models have been proposed to explain the first two peculiarities, including the presence of opaque circumsecondary material, a strongly oblate Pre-Main-Sequence secondary, and a compact third star in the system (see Popper & Plavec, 1976; Vasileiskii & Vitrichenko, 2000, and references therein). The change in the duration of the eclipse was interpreted by Windemuth et al. (2013) as probably due to the very young secondary star actively accreting its circumstellar disk.

The main star in Component B is a fast rotator ($v\,sin\,i = 240\,km\,s^{-1}$ according to Abt et al., 2002) so it is a challenging spectroscopic target. On the visi-

ble range and at low dispersion, only neutral Hydrogen and Helium lines from the primary component are detectable, all of them contaminated by their nebular counterparts to a greater or lesser degree. The only exception is the MgII λ4481 Å line, that has a strongly variable, non-Gaussian profile. Consequently, it is not surprising that its spectrum has been assigned diverse classifications, from B0 to B4, and that some radial velocity data points and certain parameters of the binary orbit, derived from the primary component spectral lines, differ strongly between authors and epochs. The spectrum of the secondary star of this binary was first weakly detected by Popper & Plavec (1976) in high dispersion photographic spectra, mainly during minimum light, as well as in the D, NaI doublet near quadrature. From the latter lines, these authors obtained orbital parameters for the secondary star and, from a group of HeI lines in the photographic range, those of the primary component. These authors conclude that the secondary must be a late A or early F Pre-MS star with mass ratio $q = M_2/M_1 = 0.31$, where M_1 and M_2 are the masses of the primary and secondary stars, respectively.

It took some time for observers to realize that large (up to $30\,km\,s^{-1}$) discrepancies in some radial velocity data, obtained at different epochs, were not only due to instrumental and measurement errors. Vitrichenko & Klochkova (2004) first proposed that a third star was needed in order to explain the discordant orbital parameters and radial velocity outliers. They conclude that the center of mass of the eclipsing binary moves around the center of mass of the putative triple system in a very eccentric orbit (e=0.92) with $P = 1302\,d$ and $K_{1,2} = 20\,km\,s^{-1}$. The problem with this proposed orbit is that, at periastron (assuming both orbits are coplanar), the tertiary star lays inside the orbit of the eclipsing binary, as shown by Vitrichenko et al. (2006), who, additionally, cross-correlated a single high S/N spectrum of θ^1 Ori B with that of synthetic spectra calculated in the 5100-5500 Å interval; in doing so, the latter mentioned authors clearly detect the secondary star with a $T_{eff} = 7000\,K$ synthetic spectrum, and claim to have detected the tertiary (with a much lower correlation height) with a $T_{eff} = 4000\,K$ template. Using their previously published orbital parameters (Vitrichenko & Klochkova, 2004) and the spectroscopic mass ($M_1 = 6.3 \pm 0.3\,M_\odot$) for the primary star, they estimate of the masses of the two *satellite stars* to be $M_2 = 2.5 \pm 0.1\,M_\odot$ and $M_3 = 1.8 \pm 0.2$ where subscript 2 and 3 refer to the eclipsing companion and the tertiary star, respectively.

The work by Vitrichenko et al. (2006) show that high resolution and S/N spectra of θ^1 Ori B, when cross-correlated with that of an early F-type narrow line star or with a $T_{eff} \approx 7000\,K$ synthetic spectrum, may yield precise radial velocities of the secondary component and, hence, accurate orbital parameters of the eclipsing binary, possibly with better precision than those obtained from the rapidly rotating primary star. In fact, the orbital eccentricity of the binary has been assumed to be zero in recent parameter determinations, even though in the first published orbital parameters, those by Struve & Titus (1944) and Doremus (1970), it was calculated to be 0.14 and 0.095, respectively. According to Vitrichenko & Klochkova (2004), the systemic velocity of the eclipsing binary, $\gamma_{1,2}$, is expected to vary with a period of about $1302\,d = 3.56\,y$ due to the putative tertiary star; consequently, the orbital parameters of the close binary (derived from the secondary star) should be obtained from data secured during a single cicle or, at most, during very few consecutive orbital cicles. We did that in Jan-

uary 2010, when we acquired (at least) one high S/N spectrum of the star every night during nine consecutive nights. Setting $P = 6.470524\,d$ (the photometric period of BM Ori revised by Vitrichenko, 2008), we derive the following orbital parameters of the secondary star: $e = 0.05$, $K_2 = 170\,km\,s^{-1}$, $\omega = 82°$ and $\gamma_{1,2} = 5.9\,km\,s^{-1}$. Notice the very low value of the systemic velocity, as compared to $24 \pm 3\,km\,s^{-1}$ obtained in previous publications for this binary. This result alone is in agreement with Vitrichenko & Klochkova (2004) proposal of a considerably massive tertiary.

This result encouraged us to pursue further observations, ideally covering one cycle in each run, by exchanging observing time with other programs. With these data we derive $\gamma_{1,2}$ at different epochs from the velocity curve of the secondary star and by fixing all the other orbital parameters to those calculated in the January 2010 observing run (by far the best sampled one). In Figure 3 the preliminary results of this work are shown; they correspond to the first nearly five years of observations (from 2010 Jan to 2014 Dec, spanning 1795 days). In this figure, the five available data points are folded with the 1302 d period proposed by Vitrichenko & Klochkova (2004); the vertical axis is the systemic velocity of the eclipsing binary system $\gamma_{1,2}$, obtained from the secondary star as described above. Care should be taken when interpreting this result since we are adjusting four orbital parameters of the triple system ($e, \omega, K_{1,2}$ and γ) with only five data points and, of course, there are other possible solutions, specially if the period is set free. What is clearly seen is that the systemic velocity of the eclipsing binary, $\gamma_{1,2}$, is indeed variable, with a semi-amplitude of about $20\,km\,s^{-1}$, in excellent agreement with Vitrichenko & Klochkova (2004), but with a much smaller eccentricity ($e \approx 0.3$ in the solution shown in Figure 3), surely a more stable configuration than that proposed by those authors. It is important to point out taht the stellar object detected by the Gravity Collaboration et al. (2018) around the eclipsing binary in θ^1 Ori B is the same tertiary star Vitrichenko & Klochkova (2004) postulate, and that its gravitational effects on the close binary are those shown here in Figure 3) ; at least, the one-year orbital segment obtained through the interferometric observations by the Gravity Collaboration et al. (2018) is fully consistent with the 1302-day period.

4. Components C and D

Nothing can be added here to what is mentioned by the Gravity Collaboration et al. (2018) about Component C. Summarizing, the brightest star in this subsystem, the intermediate O-type star that is the main source of ionizing photons in the Orion Nebula, is an oblique magnetic rotator, a rare characteristic that has been interpreted as evidence of a collision process in the formation of the star (Zinnecker & Yorke, 2007). In addition, it is an interferometric binary, with a relatively massive companion (also detected in high S/N spectra), in an eccentric orbit ($e = 0.69$) with period of 11.3 years. Additionally, it is suspected to be a spectroscopic binary, with a one solar mass secondary star in a 61.5.day period. The systemic radial velocity is, understandably, poorly known; probably its best estimate comes from the spectroscopic orbital parameters of the 11.3-year binary obtained by Balega et al. (2015), derived from a few usable primary and secondary lines, from which $\gamma(C_{1,2}) = 29.4 \pm 0.6\,km\,s^{-1}$ was obtained.

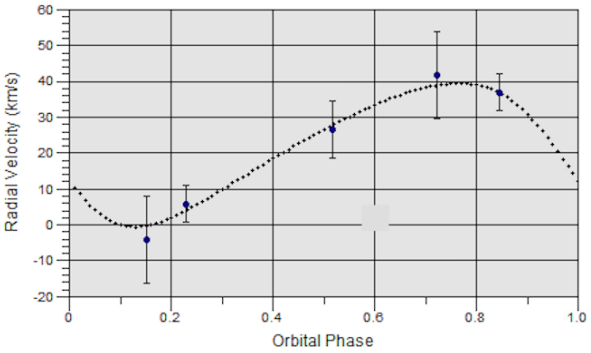

Figure 3. Velocity curve of the center of mass of the eclipsing binary in θ^1 Ori B (BM Ori) folded by the orbital period, $P = 1302\,d$, proposed by Vitrichenko & Klochkova (2004) for the tertiary star. Error bars are estimates, mostly due to zero-point shifts yet to be determined.

Component D (θ^1 Ori D = HD 37023), a $V = 6.7\,mag$, spaectral type B 0.5 V and $T_{eff} = 32\,000\,K$ according to Simón-Díaz et al. (2006), has been suspected to be a spectroscopic binary ever since its first spectral series was observed. However, efforts to find a period for it had been scarce, to put it mildly. Vitrichenko (2002a) gathered published radial velocities and measured available IUE spectra for this star; he derived two possible solutions for the orbit with periods $20.27d$ and $40.53d$. In some of our high dispersion and S/N spectra we clearly noticed that certain lines, namely the SiIII triplet around $\lambda\,4560$ and CII $\lambda\,4267$, appear double when the weaker component is significantly blue-shifted. These lines reach their maximum intensity at around $T_{eff} = 20\,000\,K$ (about type B 2 in the MS), so it is reasonable to estimate that the secondary star is about two magnitudes weaker than the primary.

Considering θ^1 Ori D as a double-lined spectroscopic binary, we have measured radial velocities of this star in several high quality spectra obtained, randomly and whenever posible, during the last 14 years. From these we derive $P = 52.90 \pm 0.05\,d$ and, from the primary component lines, the orbital parameters $e = 0.42$, $K_1 = 36\,km\,s^{-1}$, $\omega = 9.8°$ and $\gamma = 38\,km\,s^{-1}$. All these parameters are being updated and revised, specially the systemic velocity, that is surprisingly large when compared with the radial velocities of other Trapezium members. From those spectra in which the secondary star lines could be deblended from those of the primary, an average mass ratio $q = M_1/M_2 = 0.47 \pm 0.05$ has been derived, which is consistent with that expected for a binary made up of a B0 V primary and a B2 V secondary.

The period and the eccentricity we obtain for θ^1 Ori D are equal, within errors, to those derived by the Gravity Collaboration et al. (2018), $P = 53.0 \pm 0.7\,d$ and $e = 0.43 \pm 0.7$, an amazing and wonderful result of modern interferometry for a spectroscopic binary at $400pc$ from the Sun! A very weak additional visual companion, at $1.4''$ from the bright binary, has not been proved to be physically related to the binary (for details see Gravity Collaboration et al., 2018).

5. Components E and F

Components E and F are about 3.5 and 5.0 magnitudes weaker than, and located less than 5″ to, their closer Trapezium members (Component A and Component C, respectively; see Figure 1). This explains why their basic observational parameters were (and some, still are) poorly known.

θ^1 Ori E was discovered to be a a double-lined spectroscopic binary by Costero et al. (2006). Its nearly identical members are pre-MS stars with approximate spectral type G2IV; they are in circular orbit with $P = 9.8952\,d$ and $K_1 = K_2 = 84.4\,km\,s^{-1}$ (Costero et al., 2008). This binary is a variable radio (e.g. see Felli et al., 1993) and X-ray source source (*COUP* 732); it also varies by several tenths of magnitud in the visual range (Wolf, 1994) and by hundredths of magnitud in the $3,5\,\mu$ and $4.5\,\mu$ bands (Morales-Calderón et al., 2012). However, the scarcity of published absolute photometry data on this star is amazing, except for its K-magnitude for which five measures are found in the literature, averaging about $6.8\,mag$. In a *Spitzer* survey dedicated to the search and characterization of variability of the ONC stars, Morales-Calderón et al. (2012) found that Component E is a grazing eclipsing binary and derived the mass of its members to be $M_1 = M_2 = 2.80\,M_\odot$ with 2% accuracy. Together with its measured high- precision proper motion (Dzib et al., 2017) and parallax (Menten et al., 2007; Kounkel et al., 2017), these results make of θ^1 Ori E the highest mass pre-MS star with well known physical parameters.

Component F has received very little attention and practically nothing was known about it. Herbig (1950), in the last sentence of his early paper on the spectroscopy of variable stars in the ONC, just before the acknowledgements and after discussing the spectral type of Component E, writes: "*Star F can be classified, with considerably more confidence as of type B 8*". This short entry was noticed and registered by Parenago (1954) in his catalogue of stars in the ONC, perpetuating the only spectral classification I know of, published for this star. We have obtained Échelle spectra of θ^1 Ori F in six nights spanning six years, in order to verify this classification and, of course, to find out its radial velocity and possible multiplicity. To our surprise, the metallic spectral lines in this star are very narrow and numerous. The spectral type we estimate from them is in excellent agreement with that given by Herbig (1950), though in our spectra we register obvious peculiarities, like abnormally strong SiII, SiIII and PII lines, indicating overabundance of these elements and the chemically peculiar (CP) character of the star (also called Ap stars). The HeI lines, expected to be quite strong at $13\,000\,K$ (the temperature we estimate for it) are undetected, probably because they are both weak and filled-in by their nebular counterparts. Hence, we classify θ^1 Ori F as a CP B 7.5 p Si star.

The mean heliocentric radial velocity we obtain for θ^1 Ori F from our six spectra is $23.2 \pm 4.2\,km\,s^{-1}$; the error is the standard deviation from the mean. The internal error in our spectra is expected to be about $2\,km\,s^{-1}$, so this result is not conclusive upon the star being a spectroscopic binary or not. Hence, together with the non detection of a companion to this star by the Gravity Collaboration et al. (2018), there is no convincing evidence of multiplicity in Component F. Any way, this radial velocity is smaller than that of the three brighter Trapezium members (in particular, those of Components C and D). It is interesting to note that the spectroscopic mass of this B 7.5 star should be about $3.7M_\odot$ if it is in the

Main Sequence, slightly larger than that of the identical members of Component E ($2.8 M_\odot$) and of the secondaries of components A ($3.0 M_\odot$) and B ($2.5\,M_\odot$), all of them definitively pre-MS stars. So, if Component F is coeval with the other Trapezium members, it must be at or near the turn-on of the zero-age MS of the Trapezium Cluster. Alternatively, Component F is not a member af the Orion Trapezium, but an evolved star located by chance in front of theTrapezium, as proposed by Olivares et al. (2013).

6. Conclusions

In agreement with the short-term dynamical instability that Allen et al. (2017) found in θ^1 Ori, the Orion Trapezium (θ^1 Ori) stellar system, we have shown here that there is clear evidence of extreme youth of the components of this nearby Trapezium:
1) The large orbital obliquity (spin-orbit angle) we find in the eclipsing binary of Component A (part of a hierarchical triple system) is almost unique among binary stars and probably the consequence of tidal, secular friction with the tertiary member.
2) The change of the eclipse duration in the close binary, also hierarchical triple Component B (itself part of a six-member unstable mini-cluster, Allen et al., 2017), is probably the result of a sudden change in the circumstellar disk around the very young secondary star (Windemuth et al., 2013), possibly induced by the tertiary, for which we obtain a plausible, medium-eccentricity orbit.
3) The oblique magnetic rotator nature of the hottest and most massive member of Component C, that possibly originated in a collision during its formation (Zinnecker & Yorke, 2007), a process that could still be in progress through gravitational interactions between the massive interferometric companion and the relatively close, $1 M_\odot$ spectroscopic companion proposed by Vitrichenko (2002b) and Lehmann et al. (2010);
4) Component E —a variable radio, infrared, optical and X-ray source— is the highest-mass ($2.80 M_\odot$) pre-MS binary known, with most of the physical characteristics of its (practically identical) components determined with high precision.
Modern observational techniques will enable the precise dynamical study of the Orion Trapezium system that is probably in flagrant disintegration. They will also be important to better understand the physical characteristics that are still uncertain in several of its members, and to follow the evolution of those observables that are clearly varying. In doing so, I am sure, our knowledge of massive star formation will be greatly benefited.

Acknowledgments. I am deeply grateful to the meeting organizers for this affectionate celebration, and for their including me in it. I am particularly grateful to Oli Dors for obtaining the generous support that made possible my participation. Finally, I sincerely thank Yilen Gómez Maqueo Chew for her valuable suggestions that substantially improved this paper.

References

Abt H. A., Levato H., Grosso M., 2002, *ApJ*, **573**, 359

Albrecht S., Reffert S., Snellen I. A. G., Winn J. N., 2009, *Nature*, **461**, 373
Albrecht S., Winn J. N., Carter J. A., Snellen I. A. G., de Mooij E. J. W., 2011, *ApJ*, **726**, 68
Allen C., Costero R., Hernández M., 2015, *AJ*, **150(6)**, 167
Allen C., Costero R., Ruelas-Mayorga A., Sánchez L. J., 2017, *MNRAS*, **466(4)**, 4937
Balega Y. Y., Chentsov E. L., Rzaev A. K., Weigelt G., 2015, Y. Y. Balega, I. I. Romanyuk, and D. O. Kudryavtsev (eds.), *Physics and Evolution of Magnetic and Related Stars*, Vol. 494 of *Astronomical Society of the Pacific Conference Series*, p. 57
Bondar' N. I., Vitrichenko É. A., Zakirov M. M., 2000, *Astronomy Letters*, **26**, 452
Bossi M., Gaspani A., Scardia M., Tadini M., 1989, *A&A*, **222**, 117
Costero R., Allen C., Echevarría J., Georgiev L., Poveda A., Richer M. G., 2008, *Revista Mexicana de Astronomia y Astrofisica Conference Series*, Vol. 34, pp 102–105
Doremus C., 1970, *PASP*, **82(487)**, 745
Dzib S. A., Loinard L., Rodríguez L. F., Gómez L., Forbrich J., Menten K. M., Kounkel M. A., Mioduszewski A. J., Hartmann L., Tobin J. J., Rivera J. L., 2017, *ApJ*, **834**, 139
Felli M., Taylor G. B., Catarzi M., Churchwell E., Kurtz S., 1993, *A&AS*, **101**, 127
Garay G., Moran J. M., Reid M. J., 1987, *ApJ*, **314**, 535
Gravity Collaboration, Karl M., Pfuhl O., Eisenhauer F., Genzel R., Grellmann R., Habibi M., Abuter R., Accardo M., Amorim A., Anugu N., Ávila G., Benisty M., Berger J.-P., Blind N., Bonnet H., Bourget P., Brandner W., Brast R., Buron A., Caratti O Garatti A., Chapron F., Clénet Y., Collin C., Coudé Du Foresto V., de Wit W.-J., de Zeeuw T., Deen C., Delplancke-Ströbele F., Dembet R., Derie F., Dexter J., Duvert G., Ebert M., Eckart A., Esselborn M., Fédou P., Finger G., Garcia P., Garcia Dabo C. E., Garcia Lopez R., Gao F., Gendron É., Gillessen S., Gonté F., Gordo P., Grözinger U., Guajardo P., Guieu S., Haguenauer P., Hans O., Haubois X., Haug M., Haußmann F., Henning T., Hippler S., Horrobin M., Huber A., Hubert Z., Hubin N., Jakob G., Jochum L., Jocou L., Kaufer A., Kellner S., Kendrew S., Kern L., Kervella P., Kiekebusch M., Klein R., Köhler R., Kolb J., Kulas M., Lacour S., Lapeyrère V., Lazareff B., Le Bouquin J.-B., Léna P., Lenzen R., Lévêque S., Lin C.-C., Lippa M., Magnard Y., Mehrgan L., Mérand A., Moulin T., Müller E., Müller F., Neumann U., Oberti S., Ott T., Pallanca L., Panduro J., Pasquini L., Paumard T., Percheron I., Perraut K., Perrin G., Pflüger A., Duc T. P., Plewa P. M., Popovic D., Rabien S., Ramírez A., Ramos J., Rau C., Riquelme M., Rodríguez-Coira G., Rohloff R.-R., Rosales A., Rousset G., Sanchez-Bermudez J., Scheithauer S., Schöller M., Schuhler N., Spyromilio J., Straub O., Straubmeier C., Sturm E., Suarez M., Tristram K. R. W., Ventura N., Vincent F., Waisberg I., Wank I., Widmann F., Wieprecht E., Wiest M., Wiezorrek E., Wittkowski M., Woillez J., Wolff B., Yazici S., Ziegler D., Zins G., 2018, *A&A*, **620**, A116
Herbig G. H., 1950, *ApJ*, **111**, 15
Kounkel M., Hartmann L., Loinard L., Ortiz-León G. N., Mioduszewski A. J.,

Rodríguez L. F., Dzib S. A., Torres R. M., Pech G., Galli P. A. B., Rivera J. L., Boden A. F., Evans II N. J., Briceño C., Tobin J. J., 2017, *ApJ*, **834**, 142
Kozai Y., 1962, *AJ*, **67**, 591
Lehmann H., Vitrichenko E., Bychkov V., Bychkova L., Klochkova V., 2010, *A&A*, **514**, A34
Lidov M. L., 1962, *Planetary and Space Science*, **9**, 719
Lloyd C., Stickland D. J., 1999, *Information Bulletin on Variable Stars*, 4809
Lohsen E., 1975, *Information Bulletin on Variable Stars*, **988**, 1
Lohsen E., 1976, *Information Bulletin on Variable Stars*, **1211**, 1
McLaughlin D. B., 1924, *ApJ*, 60
Menten K. M., Reid M. J., Forbrich J., Brunthaler A., 2007, *A&A*, **474**, 515
Morales-Calderón M., Stauffer J. R., Stassun K. G., Vrba F. J., Prato L., Hillenbrand L. A., Terebey S., Covey K. R., Rebull L. M., Terndrup D. M., 2012, *ApJ*, **753(2)**, 149
Olivares J., Sánchez L. J., Ruelas-Mayorga A., Allen C., Costero R., Poveda A., 2013, *AJ*, **146**, 106
Parenago P. P., 1954, *Trudy Gosudarstvennogo Astronomicheskogo Instituta*, **25**, 3
Petr M. G., Coudé du Foresto V., Beckwith S. V. W., Richichi A., McCaughrean M. J., 1998, *ApJ*, **500(2)**, 825
Petr-Gotzens M. G., Massi M., 2008, S. Hubrig, M. Petr-Gotzens, and A. Tokovinin (eds.), *Multiple Stars Across the H-R Diagram*, p. 281
Popper D. M., Plavec M., 1976, *ApJ*, **205**, 462
Rossiter R. A., 1924, *ApJ*, 60
Simón-Díaz S., Herrero A., Esteban C., Najarro F., 2006, *A&A*, **448**, 351
Stickland D. J., Lloyd C., 2000, *The Observatory*, **120**, 141
Struve O., Titus J., 1944, *ApJ*, **99**, 84
Valle Lira J., 2011, *Bachelor thesis*, Facultad de Ciencias, UNAM
Vasileiskii A. S., Vitrichenko E. A., 2000, *Astronomy Letters*, **26**, 529
Vitrichenko É. A., 2002a, *Astronomy Letters*, **28**, 843
Vitrichenko É. A., 2002b, *Astronomy Letters*, **28**, 324
Vitrichenko É. A., 2008, *Astrophysics*, **51**, 424
Vitrichenko E. A., Klochkova V. G., 2004, *Astrophysics*, **47**, 169
Vitrichenko E. A., Klochkova V. G., Plachinda S. I., 1998, *Astronomy Letters*, **24**, 352
Vitrichenko É. A., Klochkova V. G., Tsymbal V. V., 2006, *Astrophysics*, **49**, 96
Vitrichenko E. I., Plachinda S. I., 2001, *Astronomy Letters*, **27**, 581
Windemuth D., Herbst W., Tingle E., Fuechsl R., Kilgard R., Pinette M., Templeton M., Henden A., 2013, *ApJ*, **768(1)**, 67
Wolf G. W., 1994, *Experimental Astronomy*, **5(1-2)**, 61
Zinnecker H., Yorke H. W., 2007, *ARA&A*, **45**, 481

Chemical Abundances in Gaseous Nebulae:
Open problems in Nebular astrophysics
AAA Workshop Series 11, 2019
M. Cardaci, G. Hägele & E. Pérez-Montero, eds.

Invited Review

Chemical abundance determinations of Lyman-α emitter objects at redshift $z > 5$: the CR7 case

O. L. Dors[1]

[1] *Universidade do Vale do Paraíba, Brazil*

Abstract. In this paper we discuss the chemical abundance determinations in the Lyman-α emitter (LAE) CR7 (clump C), one object at redshift z=6.604. We used a grid of photoionization models built with the Cloudy code in order to classify the clump C of CR7 in Active Galactic Nuclei or in Star-forming galaxies and for estimating the abundance of the elements O, N and C in relation to the hydrogen one. We found that, possibly, CR7 clump C hosts an AGN with metallicity in order of 0.5 the solar one. The helium luminosity and the metallicity of CR7 are in consonance with AGNs type 2 located at a wide range of redshift. Moreover, this object seems to have lower and higher C/O and N/O abundance ratios, respectively, than those in local H II regions. The N/O abundance ratio derived for CR7 is in agreement with values derived for local AGNs Seyfert 2.

Key words: galaxies: active – galaxies: abundances – galaxies: evolution – galaxies: nuclei – galaxies: formation– galaxies: ISM – galaxies: Seyfert

1. Introduction

The study of Lyman-α emitter objects (hereafter LAEs) at high redshift ($z > 5$) is fundamental in the understanding of the reionization epoch of the Universe and in the study of formation and chemical evolution of galaxies.
Thanks to the advancement of large ground-based telescopes (e.g. SUBARU; Very Large Telescope-VLT) together with the large amount of data produced by the Hubble Space Telescope (HST), several observational works have revealed the existence of the primeval galaxies, commonly referred to as LAEs (e.g. see Dors et al., 2018, and references therein).
Emission-line intensities and their ratios can be used to investigate the nature of the gas emission of LAEs, i.e., to classify these objects as a Star Forming region (SF) or an Active Galactic Nucleus (AGN) as well as to estimate their chemical abundances. Regarding the classification, there is no consensus on the nature of LAEs. A good example is for CR7, the most studied LAE and the one with the best observational data available in the literature. For example, Sobral et al. (2015), using the X-SHOOTER and SINFONI instruments mounted on the VLT, DEIMOS on the Keck telescope, the near-IR COSMOS/UltraVISTA survey, and the WFPC3 on board the HST found the the clumps A, B and C of CR7 are, possibly, ionized by population III stars, i.e. these objects are star-

forming galaxies. However, Agarwal et al. (2017), by comparing the observed H_{160}-[3.6] and [3.6]-[4.5] IR colors of CR7 obtained by Bowler et al. (2017) with photoionization model predictions, derived that the clump A potentially hosts an evolved direct collapse black hole (DCBH), while components B and C are consistent with metal enriched star forming regions.
Concerning the LAE metallicity, there is also several disagreements in the literature. For example, it is expected that objects located at very high redshifts ($z > 5$) present very low metallicity [$(Z/Z_{\odot}) \lesssim 0.1$] or, at least, present lower metallicity than their conterparts at local universe. However, as pointed out for Dors et al. (2018), this is not the case for the majority of the LAEs at $z > 6$, including CR7.
With the above in mind, in this paper we compared observational spectroscopic data of the clump C of CR7, taken from the literature, with results of photoionization models generated by considering distinct types of ionizing sources. Our main goals are:

1. Classifying CR7 in an AGN or star-forming galaxy.

2. Determining the physical parameters that can best describe CR7 (e.g. metallicity, number of ionizing photons).

This paper is organized as follows. In Section 2, we present the methodology used throughout the paper. In Section 3, the resulting classification and physical parameters that can help describe the nature of CR7 are presented. Finally our discussion and conclusions are presented in Sect, 4 and 5, respectively.

2. Methodology

2.1. Observational data

We compiled UV emission-line fluxes ($1000 < \lambda < 2000$) for a sample of LAEs located at redshift $z > 5$. Our selection criteria was as follows:

1. each selected object must be at $z > 5$,

2. the flux of the Lyα λ1216 emission-line was measured,

3. the flux of He II λ1640 was measured or at least an upper limit was estimated

4. the flux of at least one metal emission line of N V λ1239, C IV λ1550, O III]λ1666 or C III]λ1909 was measured and, at least, one upper or lower limit of the flux of one metal emission-line was estimated.

Applying these selection criteria five objects were selected, namely RXC J2248.7-4431-ID3, CR7 (clump C), HSC J233408+004403, COSY, and A1703-zd6. In this paper, we presented an analysis only for CR7 clump C, a LAE with redshift $z = 6.604$. CR7 is one of the most luminous LAEs and was discovered by Sobral et al. (2015) using the data obtained with the Subaru Telescope by Matthee et al. (2015). Follow-up observations of CR7 using the F110W (YJ) and F160W (H)

wide filters of the WFPC3 instrument on board the HST by Sobral et al. (2015), revealed that CR7 is composed of three components, namely A, B and C. Most recently, Sobral et al. (2019) presented new Hubble/WFC3 grism observations and a re-analysis of the VLT data of CR7, making it possible to obtain line fluxes of the components A, B and C. In their analysis, Sobral et al. (2019) measured the line N IV]λ1483.4Å, λ1486.6Å in clump A (not considered in our analysis) and N Vλ1240Å in clump C.
To represent a control sample, we compiled observational UV narrow emission line intensities (FWHM $\lesssim$ 1000 km/s) of a sample of confirmed star-forming regions (SFs) and AGNs from the literature (see Dors et al. 2018 for a detailed description of this sample).

2.2. Photoionization models

We used the Cloudy code version 17.00 (Ferland et al., 2013) to build a grid of photoionization models in order to compare the predicted UV emission-line intensities with those measured for the CR7 spectra.
The models were built assuming a simple approach, i.e. a static spherical geometry with a central ionizing source, constant electron density along the radius and with different values of metallicity and of number of ionizing photons emitted per second by the ionizing source. The values of metallicities were assumed to be $(Z/Z_{\odot})$=0.01, 0.5, 1.0 and 2.0, the electron density was assumed equal to $N_{\rm e} = 500\,{\rm cm}^{-3}$ while the number of ionizing photons was considered to be $50 \leq \log Q({\rm H}) \leq 55$.
We built models with distinct Spectral Energy Distribution (SED) to represent AGNs and SFs. One model grid considering the SED being composed of two continuum components, where one represents the Big Blue Bump peaking at 1 Ryd, and the other is characterized by a power law with different values of the spectral index α_{ox} describing the continuum between 2 keV and 2500Å. In the models, we consider the α_{ox} values -0.8, -1.4 and -2.0. Another grid of AGN models were built to be multi-temperature black body spectra, which simulate the radiation being emitted from a black hole accreting gas (DCBH). We consider four distinct parameters for this system: black hole with masses of $10^6\,M_{\odot}$ and $10^7\,M_{\odot}$ accreting at 50% and 100% of the Eddington rate (see Dors et al. 2018). Regarding the star-forming models, SEDs of Population II stars taken from STARBURST99 code (Leitherer et al., 1999) and representating a stellar cluster instantaneously formed with a mass of $10^6\,M_{\odot}$, with lower and upper stellar mass limit of 0.1 and 100 $M_{\odot}$ and with 10^4 yr, 2.5 Myr, and 6.0 Myr were assumed. The reader is referred to Dors et al. (2018) for a complete description of the photoionization models.

3. Results

3.1. CR7 classification

In Figure 1, left panel, the diagram log(C III]/He II) versus log(N V/He II) containing the line ratio intensities predicted by the photoionization models is shown. We defined one demarcation between the regions occupied by SF and AGN models. Also in Fig. 1, middle panel, the observational data of the control sample

are plotted, where a demarcation separating SFs and AGNs is defined. Finally, in Fig. 1, rigth panel, the CR7 clump C line ratios and the theoretical and observational demarcations are compared. We can see that CR7 clump C is clearly classified as an AGN.

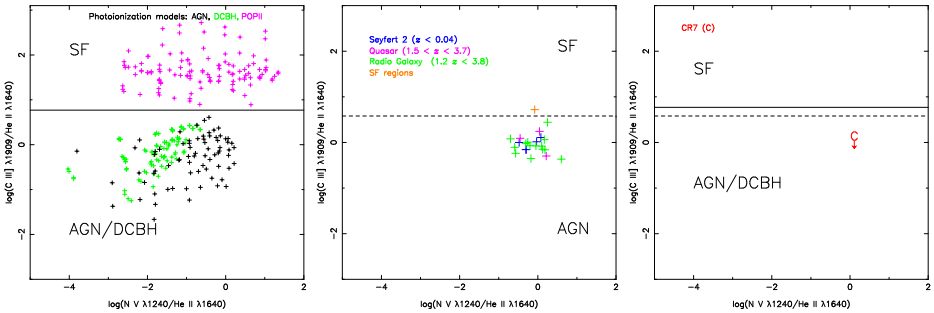

Figure 1. Diagnostic diagrams considering log(C III]/He II) versus log(N V/He II). Left panel: Line ratio intensities predicted by the photoionization models. The line separates SF-like objects zone from that of AGN/DCBH-like objects. Symbols with different colours represent distinct object types as indicated. Middle panel: Same than left panel but for emission-line ratios of the control sample as indicated. Right panel: Diagnostic considering the emission line ratios of CR7 (clump C) and the demarcation lines defined in the left and middle panels.

3.2. CR7 abundances

Once the spectral classification of CR7 Clump C is adopted, i.e. AGN, it is possible to derive some parameters describing this object by building detailed photoionization models. The methodology adopted is similar to that considered by Dors et al. (2017), who built detailed photoionization models to reproduce optical emission lines of Seyfert 2s in order to derive their chemical abundances. A detailed description of the fitting model is found in Dors et al. (2018). We reproduced the CR7 clump C observed line ratios log(Lα/He II)=0.41 $\pm$ 0.21, log(C III]/He II)<0.00, log(N V/He II)=0.11 $\pm$ 0.24, log(C IV]/He II)<0.15, and log(O III]/He II)<0.09 with one photoionization model with the parameters: $\log U = -2.0 \pm 0.50$, $(Z/Z_{\odot}) = 0.46 \pm 0.30$, $\log(C/O) < -1.20$ and $\log(N/O) = -0.50 \pm 0.40$. These parameters have a large uncertainty due to the small number and to the low signal/noise of the observational line ratios. It was not possible to reproduce Lα/He II, in the sense that the best model predicted 1.20 for the logarithm of this line ratio and the observed value is about 0.40. This can be an indication of escape of ionizing source in this object.

4. Discussion

Recents advancement of large ground-based telescopes has made possible to observe the primeval galaxies located in the reionization era ($z > 6$). These objects are the progenitors of the galaxies at low redshift and, probaly, are responsable by the reionization of the Universe. Nowadays, we are starting to observe these

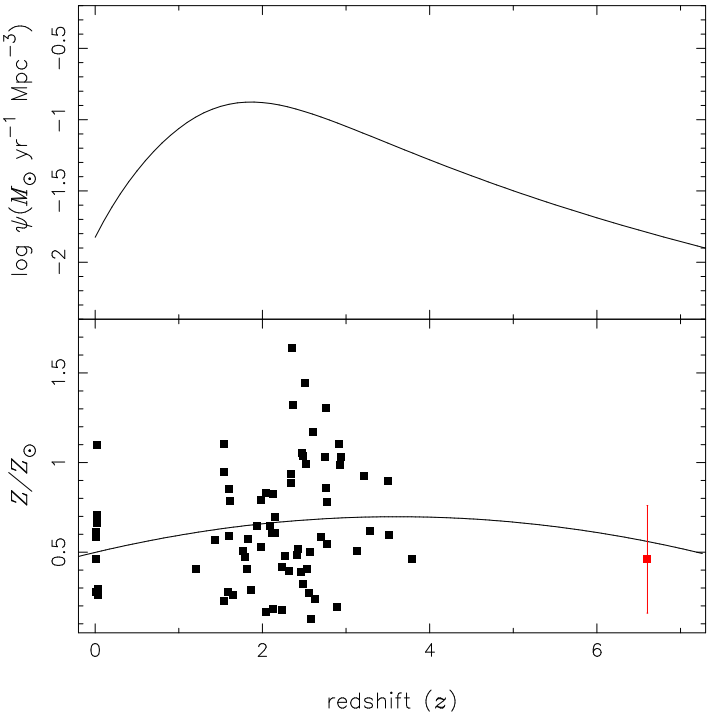

Figure 2. Botton panel: Metallicity (in unit of solar metallicity) versus the redshift. Black points represent estimations of AGNs type 2 (control sample) by Dors et al. (2014) while red point represents metalicity estimation for the LAE CR7 (clump C). Upper panel: Cosmic star formation rate versus the redshift calculated by using ultraviolet and infrared observational data of star formation regions compiled by Madau & Dickinson (2014).

objects and the available data, in the most part, have low signal/noise as well as small number of line ratios have been measured. Despite these limitations, efforts have been done in the sense of uncovering the nature of these galaxies. In the CR7 case, this object is the most studied galaxy at $z > 6$ and we found indications of that it hosts an AGN with moderate metallicity. With the goal to compare the derived metallicity of CR7 (clump C) with the ones of other galaxies, in Fig. 2, metallicity estimations for AGNs type 2 at a wide range of redshifts obtained by Dors et al. (2014) are compared to the value obtained for CR7. We can see that the CR7 presents metallicity similar to those of objects situated in all redshift range, or better, CR7 is not the poorest metal objects. One explanation for that is that CR7 had a quick chemical evolution, with stars forming with high rate at $z > 7$. We also used the Z estimations to obtain a fiting between the metallicity and the redshift given by:

$$(Z/Z_\odot) = (-0.015 \pm 0.014 \times z^2) + (0.110 \pm 0.075 \times z) + (0.49 \pm 0.10). \quad (1)$$

Obviously, due to the lack of estimations in some redshift ranges noted this expression is largely uncertain. Also in Fig. 2, upper panel, the cosmic star

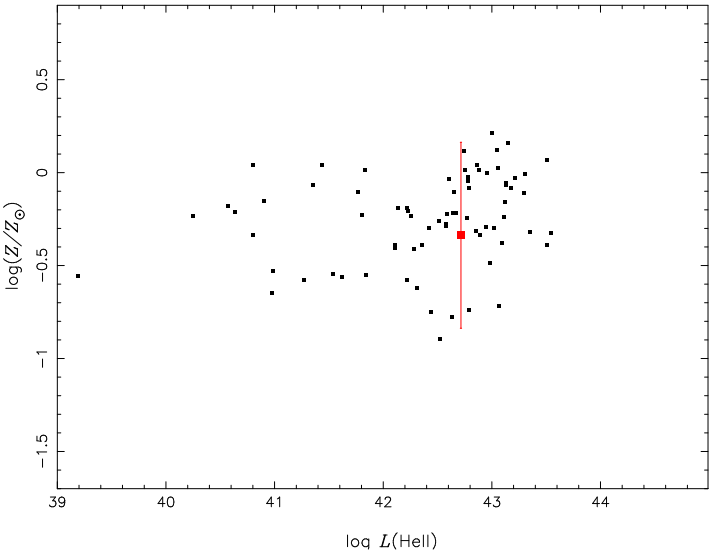

Figure 3. Logarithm of the metallicity in relation to the solar one versus the logarithm of the He II luminosity. Black points represent AGNs type 2 analysed by Dors et al. (2014) and the red point represent CR7 clump C.

formation rate calculated by using ultraviolet and infrared observational data of star formation rate (SFR) compiled by Madau & Dickinson (2014) is shown. We can note that both $(Z/Z_{\odot})$-z and SFR-z relations, shown in Fig. 2, seem to have the same behaviour, with the maximum metallicity and SFR values around the redshit 2-3.

Now, in Fig. 3, we compare the logarithm of the metallicity in relation to the solar one versus the logarithm of the He II luminosity for the AGNs type 2 sample analysed by Dors et al. (2014) with the values for CR7. One can see that CR7 is located in the same area occupied by the AGNs.

Finally, in Fig. 4, we compare the log(C/O), log(N/O) versus 12+log(O/H) estimations for CR7 (clump 7) with those for local H II regions and Seyfert 2 and for one galaxy at $z \approx 2.3$. Despite the large uncertainties in the CR7 estimations, we can see that CR7 has C/O abundance ratio lower than those derived for H II regions and N/O in consonance with Seyfert 2. Obviously, better CR7 data are need to improve this comparison.

5. Conclusion

We compared the available observational ultraviolet emission line intensities of the LAE CR7 with predictions from photoionization models. Based on one diagnostic diagram, we concluded that the clump C of CR7 probably hosts an AGN with moderate metallicity, similar to the metallicity of other AGNs at lower redshift. This indicates that CR7 had a quick chemical evolution at redshift $z > 7$. Our estimations indicate that CR7 has C/O abundance ratio lower than those derived for H II regions and N/O in consonance with Seyfert 2.

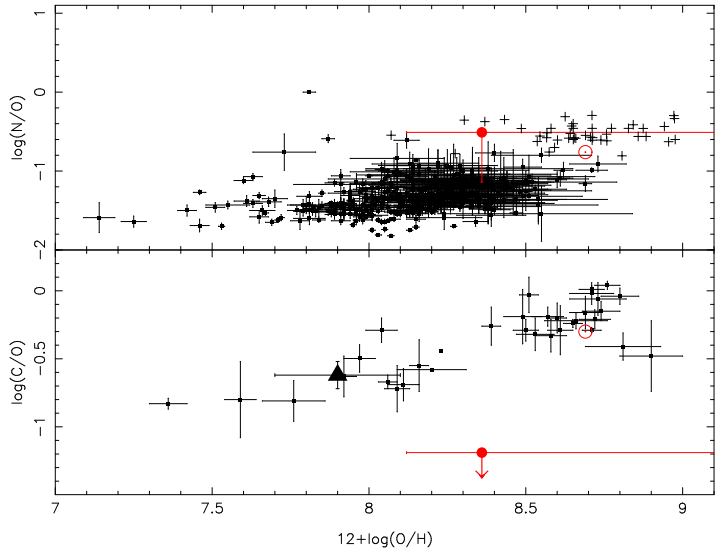

Figure 4. Bottom panel: log(C/O) versus 12+log(O/H). Black points represent estimations from optical-emission lines of star-forming regions taken from the literature (see Dors et al. 2018 for the references. Triangle represents the estimation for the galaxy Q2343-BX418 ($z \approx 2.3$) by Erb et al. (2010). Red points represents estimations for CR7 (clump C). Top panel: log(N/O) versus 12+log(O/H). Black symbols are as in bottom panel. Crosses are estimations for local Seyfert 2 AGNs by Dors et al. (2017).

Acknowledgments. On behalf of the participants of the "II CHEMICAL ABUNDANCES IN GASEOUS NEBULAE: OPEN PROBLEMS IN NEBULAR ASTROPHYSICS" I thank Manuel Peimbert & Rafael Costero for the effort of a life devoted to the study of gaseous nebulae. This work has been supported by FAPESP and CNPq.

References

Agarwal B., Johnson J. L., Khochfar S., Pellegrini E., Rydberg C.-E., Klessen R. S., Oesch P., 2017, *MNRAS*, **469**, 231

Bowler R. A. A., McLure R. J., Dunlop J. S., McLeod D. J., Stanway E. R., Eldridge J. J., Jarvis M. J., 2017, *MNRAS*, **469**, 448

Dors O. L., Agarwal B., Hägele G. F., Cardaci M. V., Rydberg C.-E., Riffel R. A., Oliveira A. S., Krabbe A. C., 2018, *MNRAS*, **479**, 2294

Dors O. L., Cardaci M. V., Hägele G. F., Krabbe Â. C., 2014, *MNRAS*, **443**, 1291

Dors Jr. O. L., Arellano-Córdova K. Z., Cardaci M. V., Hägele G. F., 2017, *MNRAS*, **468**, L113

Erb D. K., Pettini M., Shapley A. E., Steidel C. C., Law D. R., Reddy N. A., 2010, *ApJ*, **719**, 1168

Ferland G. J., Porter R. L., van Hoof P. A. M., Williams R. J. R., Abel N. P., Lykins M. L., Shaw G., Henney W. J., Stancil P. C., 2013, *RevMexAA*, **49**, 137

Leitherer C., Schaerer D., Goldader J. D., Delgado R. M. G., Robert C., Kune D. F., de Mello D. F., Devost D., Heckman T. M., 1999, *ApJS*, **123**, 3

Madau P., Dickinson M., 2014, *ARA&A*, **52**, 415

Matthee J., Sobral D., Santos S., Röttgering H., Darvish B., Mobasher B., 2015, *MNRAS*, **451**, 400

Sobral D., Matthee J., Brammer G., Ferrara A., Alegre L., Röttgering H., Schaerer D., Mobasher B., Darvish B., 2019, *MNRAS*, **482**, 2422

Sobral D., Matthee J., Darvish B., Schaerer D., Mobasher B., Röttgering H. J. A., Santos S., Hemmati S., 2015, *ApJ*, **808**, 139

Chemical Abundances in Gaseous Nebulae:
Open problems in Nebular astrophysics
AAA Workshop Series 11, 2019
M. Cardaci, G. Hägele & E. Pérez-Montero, eds.

Invited Review

Latest advances in the abundance discrepancy problem in photoionized nebulae

J. García-Rojas[1,2], R. Wesson[3], H. M. J. Boffin[4], D. Jones[1,2], R. L. M. Corradi[1,5], C. Esteban[1,2] and P. Rodríguez-Gil[1,2]

[1]*Inst. de Astrofísica de Canarias, E-38200, La Laguna, Tenerife, Spain*
[2]*Dept. de Astrofísica, Univ. de La Laguna, E-38206, La Laguna, Tenerife, Spain*
[3]*Department of Physics and Astronomy, University College London, Gower St, London WC1E 6BT, UK*
[4]*European Southern Observatory, Karl-Schwarzschild-Str. 2, D-85738 Garching bei München, Germany*
[5]*Gran Telescopio Canarias S.A., c/ Cuesta de San José s/n, Breña Baja, E-38712 Santa Cruz de Tenerife, Spain*

Abstract. In this paper, we will focus on the advances made in the last few years regarding the abundance discrepancy problem in ionized nebulae. We will show the importance of collecting deep, high-quality data of H II regions and planetary nebulae taken with the most advanced instruments attached to the largest ground-based telescopes. We will also present a sketch of some new scenarios proposed to explain the abundance discrepancy.

Key words: galaxies: abundances — galaxies: ISM — techniques: imaging spectroscopy

1. Introduction

In photoionized nebulae −both H II regions and planetary nebulae (PNe)− optical recombination lines (ORLs) provide abundance values that are systematically larger than those obtained using collisionally excited lines (CELs). This is the well-known *abundance discrepancy* (AD) problem of nebular astrophysics, which has remained unresolved for more than seventy five years (Wyse, 1942). This issue has obvious implications for the measurement of the chemical content of near and faraway galaxies, most often derived using CELs from their ionized interstellar medium. This abundance discrepancy is usually parametrized by the *Abundance Discprency Factor* (ADF) which is defined as the ratio of ORL and CEL abundances (Liu et al., 2000).
Several scenarios have been proposed to explain this behavior. In the following we summarize some of the possible interpretations suggested to explain the abundance discrepancy:

- Peimbert (1967) was the first to propose the presence of temperature variations in the gas in order to explain the discrepancy between T_e([O III]) and

T_e(H I) derived from the Balmer jump. Subsequently, Peimbert & Costero (1969) proposed an scheme to correct the abundances computed from CELs for the presence of temperature inhomogeneities. Torres-Peimbert et al. (1980) first suggested that the discrepancy between ORLs and CELs abundances could be explained if spatial temperature variations over the observed volume are considered. Possible causes to explain the presence of such temperature fluctuations in photoionized nebulae can be: mechanical energy injection by collisions (Peimbert, 1995) or by conduction fronts (Maciejewski et al., 1996); high-density condensations (Viegas & Clegg, 1994); ionizing source variability (Binette et al., 2003; Bautista & Ahmed, 2018); dust distribution inhomogeneities (Peimbert et al., 1993; Stasińska & Szczerba, 2001); the presence of shadowed regions (Huggins & Frank, 2006); cosmic rays ionization of neutral clumps (Giammanco & Beckman, 2005; Zhang et al., 2007) or the presence of dense X-ray irradiated regions (Ercolano, 2009).

- The existence of chemical inhomogeneities in the gas was first proposed by Torres-Peimbert et al. (1990) as a plausible mechanism to explain the abundance discrepancy. Later, Liu et al. (2000) proposed that metal-rich (i. e. H-poor) inclusions could solve the abundance discrepancy problem; in this scenario, metal recombination lines are emitted in the metal-rich inclusions, where cooling has been enhanced, while CELs are emitted in the "normal" metallicity (H-rich) zones. Several authors have constructed two-phase photoionization models that sucessfully reproduce simultaneously ORLs and CELs emissions in H II regions (Tsamis & Péquignot, 2005) and PNe (Yuan et al., 2011). However, the origin of such metal-rich inclusions has not been well established yet (see Henney & Stasińska, 2010; Stasińska et al., 2007, for a different scenarios proposed to explain the origin of such inclusions in PNe and H II regions).

- Nicholls et al. (2012) proposed that a non Maxwell-Boltzmann κ energy distribution of free electrons could explain the abundance discrepancies owing to the presence of a long tail of supra-thermal electrons that contribute to an increase in the intensity of the CELs at a given value of the kinetic temperature. However, there is little theoretical (Mendoza & Bautista, 2014; Ferland et al., 2016; Draine & Kreisch, 2018) or observational (Zhang et al., 2016) support for this scenario in photoionized nebulae. In particular, Ferland et al. (2016) have shown that the distance over which heating rates change are much longer than the distances over which supra-thermal electrons can travel, and that the timescale to thermalize these electrons is much shorter than the heating or cooling timescales. These estimates imply that supra-thermal electrons will have disappeared into the Maxwellian velocity distribution long before they affect the collisionally excited forbidden and RLs and therefore, the electron velocity distribution will be closely thermal and the κ formalism can be ruled out for these objects. Moreover, Draine & Kreisch (2018) demonstrated analytically the departures from Maxwellian distribution have negligible effects on line ratios. These authors show that the electron energy distribution relaxes rapidly to a steady-state distribution that is very close to a Maxwellian.

- Uncertainties in atomic data have also been traditionally claimed as a possible explanation for the abundance discrepancy problem. Rodríguez & García-Rojas (2010) found that the observed temperature structure of Galactic H II regions was easily reproduced with simple photoionization models with metallicities close to the ones implied by O CELs, and suggested that uncertainties in the ORLs recombination coeffcients could address this problem. Storey et al. (2017) computed a new set of recombination coefficients for O^{2+} accounting for departures of the local thermodynamic equilibrium, and extending the computations to low electron temperatures, T_e, where dielectronic recombination (DR) could be an important process. However, the new recombination coefficients applied to the available observations do not signifficantly change the obtained O^{2+} abundances from ORLs. On the other hand, Garnett & Dinerstein (2001) explored the possibility that high-temperature DR in a central hot bubble of the PN NGC 6720 could enhance the ORLs strengths in the central parts of the nebula, finding that the increase of recombination rates due to DR at $T_e \approx 10^5$ K was not enough to overcome the increase in collisionally excited emission. However, these authors conclude that a better understanding of the effects of DR on recombination line strengths in general is urgently needed. Finally, we want to stress that Escalante et al. (2012) have shown that additional excitation processes of the ORLs, such as fluorescence excitation by starlight can solve the abundance discrepancy problem in low-ionized, low-ADF PNe such as IC 418. However, this mechanism cannot explain the strong intensities of ORLs from f or g states, such as the widely observed C II λ4267 line.

2. The abundance discrepancy in H II regions

Since the pioneering work by Wyse (1942), the abundance discrepancy problem has been studied in several Galactic (see e. g. García-Rojas & Esteban, 2007) and extragalactic (see e. g. Esteban et al., 2014; Toribio San Cipriano et al., 2016) H II regions. A compilation of ADF measurements made in both H II regions and PNe can be found on Roger Wesson's webpage[1]. In general, ADFs computed for H II regions are in the range between 1.3 and 3, with an average value around 2 that is representative for most of the objects. Although the ADF in H II regions can therefore be considered approximately constant, Toribio San Cipriano et al. (2017) reported –for the first time– an apparent dependence of both ADF(O^{2+}) and ADF(C^{2+}) with metallicity (see their Figures 4 and 5), in the sense that the ADF seems to be higher as metallicity becomes lower. A similar result has also been reported by Esteban et al. (2018), who found a correlation between the ADF with T_e (see their Figure 4). Another test to explore the AD problem is to compare abundances derived from CELs and ORLs in H II regions with those determined in young B and A-type supergiant stars of their vicinity. Results obtained by Bresolin et al. (2016) and Toribio San Cipriano et al. (2017) indicate that the ORL-based nebular metallicities agree with the stellar ones better than

[1] https://www.nebulousresearch.org/adfs/

those from CELs in the high-metallicity regime, but that this situation reverses at low-metallicity values. Extending the baseline of the O/H ratios of H II regions or emission-line galaxies with precisely derived ADF to lower metallicities would shed light on the dependence of the ADF with metallicity.
On the other hand, Guseva et al. (2006, 2007) explored the behavior of T_e derived from [O III] CELs and from H I Balmer and Paschen jump, in a sample of low-metallicity H II regions and emission-line galaxies finding no statistically significant differences. This result would rule out the presence of temperature fluctuations in such objects, and suggests that the ADF, if present, should be small. These results appear to go in the opposite direction to those obtained from the direct measurement of the ADF, and reinforce the need for better quality data to disentangle this puzzle.
Although the origin of the ADF in H II regions is still unknown, it seems clear that several actors are contributing to it. Mesa-Delgado et al. (2008) used long-slit spectroscopy to cover several morphological structures in the Orion nebula, such as Herbig-Haro (HH) objects and protoplanetary disks (proplyds), finding prominent spikes of T_e([N II]) and n_e. They also found a significant enhancement of the ADF at the locations of the most conspicuous HH objects. Núñez-Díaz et al. (2012), using integral field spectroscopy, discovered a narrow arc of high T_e([N II]) at the head of the bow-shock of HH 204 in the Orion nebula. These arcs have been predicted by models of photoionized HH jets of Raga & Reipurth (2004), which are produced by shock heating at the leading working surface of the flow, just preceding the high-density compressed zone. Mesa-Delgado et al. (2009), using high-spectral resolution spectra at the head of HH 202-S, and were able to separate the spectrum of the high-velocity flow from the ambient ionized gas. These authors found large density differences between both components, as well as evidences of dust destruction and abundance anomalies in the gas flow component (i. e. CEL abundances were 0.2 dex lower than in the ambient gas, while ORL abundances remained unchanged), indicating that these gas flows play a role in the AD problem.
Additionally,Tsamis et al. (2011) and Mesa-Delgado et al. (2012), using integral field spectroscopy of fields in the Orion nebula containing proplyds, found that collisional de-excitation has a crucial influence on the line fluxes in the proplyds, owing to the high electron densities ($n_e \sim 10^5 - 10^6$ cm^{-3}) in these objects. They also found that the use of suitable density diagnostics and a proper background substraction returned an ADF(O^{2+})$\approx$ 1 for the intrinsic spectra of the proplyds, and therefore concluded that the presence of high-density ionized gas can severely affect the abundances determined from CELs.

3. The abundance discrepancy in planetary nebulae

In the last years there has been multiple studies on the AD problem in PNe. A compilation of the results obtained for PNe has been made by Roger Wesson on his webpage (see Section 2). ADFs in PNe show a behavior that is remarkably different to that of H II regions in the sense that, although the bulk of PNe shows an ADF distribution with values that are usually between 1.5 and 3, this distribution has a significant tail extending to much larger values. García-Rojas & Esteban (2007) proposed that, at least for the most extreme ADF PNe, the

origin of the abundance discrepancy should be different to that of the "normal" ADF PNe and H II regions.

Focusing on the physical conditions derived using different diagnostics, Zhang et al. (2004) derived T_e and n_e using the nebular hydrogen recombination spectrum, as well as T_e obtained from the ratio of the fine-structure far-IR [O III] 52, 88 μm to the nebular [O III] 4959 Å line, and compared the results with those obtained with the traditional nebular-to-auroral [O III] 4959/4363 ratio, finding that temperature and density fluctuations are generally present within PNe. They also found that T_e derived from the far-IR to optical diagnostic was generally higher than that derived from the optical [O III] lines, which was attributed to the existence of dense clumps in the PNe. This discrepancy in T_e was found to be anti-correlated with n_e, suggesting that it is related to nebular evolution.

Several authors have found evidence of the existence of two components with different physical conditions coexisting in PNe. Storey & Sochi (2014) studied the continuum emission spectrum of PN Hf 2-2 and found that the model which best fit the observations was one comprising two components with very different temperatures. Zhang et al. (2005) found that T_e derived from He I lines in PNe were lower than those derived from the H I Balmer decrement, which is at odds with what is expected from the temperature fluctuations scenario, but consistent with a two-abundance model. Storey et al. (2017) derived new recombination coefficients for O II ORLs, using an intermediate coupling treatment that fully accounts for the dependence of the distribution of the population among the ground levels of O^{2+} on n_e and T_e, and extending the computations down to low T_e to account for important effects owing to DR. These authors found that using a pure O II ORLs T_e diagnostic it is clear that, at least for the extreme ADF PNe, the emission seems to come from a very low T_e region. On the other hand, other authors have a different point of view. Peimbert et al. (2014) found for a sample of ∼20 PNe, that the average temperatures derived from H, He and O lines were consistent with a chemically homogeneous gas with temperature fluctuations. However, they could not rule out chemical inhomogeneities for 4 objects of their sample.

Another approach to search for evidence of different gas components is PNe is to study the kinematics of the gas. Richer et al. (2013), from a spatially-resolved high-resolution UVES spectra of the PN NGC 7009 found that the kinematics of C II, N II, O II, and Ne II ORLs did not coincide with the kinematics of the [O III] and [Ne III] CELs, indicating that there is an additional plasma component where the ORLs are emitted which arises from a different volume to that giving rise of the CELs. Moreover, Richer et al. (2019) studied the temperature structure of NGC 7009 using the same data set and found large differences between O II-based T_e and CELs-based T_e (by more than 6000 K) in some parts of the nebula, strengthening the hypothesis of the existence of two plasma components in NGC 7009. Similar results have been found by Peña et al. (2017). These authors studied the expansion velocities (V_{exp}) in 14 PNe from O^{2+} ORLs and CELs and found that, in general, if the gas is in ionization equilibrium, ORLs have lower V_{exp} than CELs for a given ion, which means that ORLs are emitted by a gas component located closer to the central star. Finally, from a statistical study of the kinematics of the C II 6578 permitted line in 83

lines of sight in 76 PNe, Richer et al. (2017) found that the kinematics of this line was not that expected if the line arose from the recombination of C^{2+} ions or the fluorescence of C^{+} ions in ionization equilibrium in a chemically homogeneous nebula, but instead its kinematics were appropriate for a more internal volume than expected.

3.1. The link between close binary central stars and large ADFs

Wesson et al. (2003) proposed for the first time that PNe exhibiting particularly large ADFs, including those 'born-again' PNe, could be related to the phenomenon of novae and, therefore, host a central binary star. Liu et al. (2006) support this scenario as they found an extreme ADF ($\sim$70) in the PN Hf 2-2 which is known to host a close binary system that has been suggested to result from a common envelope (CE) event. Inspired by these findings, Corradi et al. (2015) analysed the nebular spectra of 3 PNe (Abell 46, Abell 63, and Ou 5) known to host post-CE close central binary stars, and they found extreme ADFs (ADF>10) in two of them and a very high value (ADF$\sim$10) in the third one. Furthermore, spatially-resolved analysis revealed that the ADFs were centrally peaked (reaching up to 300 in the central part of Abell 46). These results along with those obtained by Jones et al. (2016) for NGC 6778, another PN with a post-CE binary central star and a high ADF$\sim$20, confirm that the ADF is strongly centrally peaked in these objects. However, this result is not restricted only to PNe with high-ADFs and known binary central stars, and can be found in low-ADF PNe (see Garnett & Dinerstein, 2001, and Section 3). In an attempt to shed light on this issue, García-Rojas et al. (2016) obtained unprecedented tunable filter imaging of the emission coming from O II ORLs and compared it with narrow-band imaging in the [O III] λ5007 CEL in NGC 6778; these authors discovered that the spatial distribution of the O^{2+} ions producing the O II ORLs does not match that of the O^{2+} ions emitting in the [O III] CELs. This is a clear indication of the presence of two separate plasmas that are not well mixed, perhaps because they were produced in distinct ejection events. These results confirm the hypothesis that large ADFs in PNe and low-to-moderate ADFs in H II regions and PNe probably have different physical origins (García-Rojas & Esteban, 2007).

In a recent paper, Wesson et al. (2018) give extra support to the link between large ADFs and binarity of the central star from the analysis of a larger sample of PNe with known post-CE central stars, which present, in all the cases ADFs ranging from 10 to 80. These authors have also confirmed an anti-correlation between abundance discrepancies and nebular n_e. On the other hand, central star binarity seems to be a necessary but not sufficient condition for having a large ADF. Manick et al. (2015) discovered significant periodic variability of the central star of PN NGC 5189 that revealed a close binary with an orbital period of $\sim$4.04 days. However, García-Rojas et al. (2013) found an ADF of 1.6 for this object. Sowicka et al. (2017) computed and ADF of 1.75 for the PN IC 4776 and reported that the central star was a binary system with a period of $\sim$9 days, although in this case, the period is poorly constrained. Additionally, Corradi et al. (2015) reported that the lack of detection of O II ORLs in deep spectra of PNe sets a low upper limit to the ADF; this is the case of the Necklace nebula, a well known post-CE object with an orbital period of its central system

of 1.16 days, where no ORLs were detected in very deep spectra obtained by Corradi et al. (2011). Taking all these results and the available observations into account, Wesson et al. (2018) concluded that all nebulae with a binary central star with a period of less than 1.15 days have large ADFs (ADF≥10 and low electron densities (n_e < 1000 cm^{-3}). Moreover, these authors also reported for the first time that [O II] density diagnostic lines can be strongly enhanced by recombination excitation, while [S II] lines are not, suggesting that in the PNe where n_e([O II]) signifficantly exceeds n_e([S II]) this can be used as an additional diagnostic to infer an extreme-ADF PN and hence, the presence of a close binary star, even if ORLs lines are not detected. Finally, the evidence found in their study led Wesson et al. (2018) to support the idea that extreme ADFs are caused by nova-like eruptions from the central system, occuring soon after the CE phase, which ejects material depleted in H and enhanced in C, N, O and Ne, but not in third-row elements.

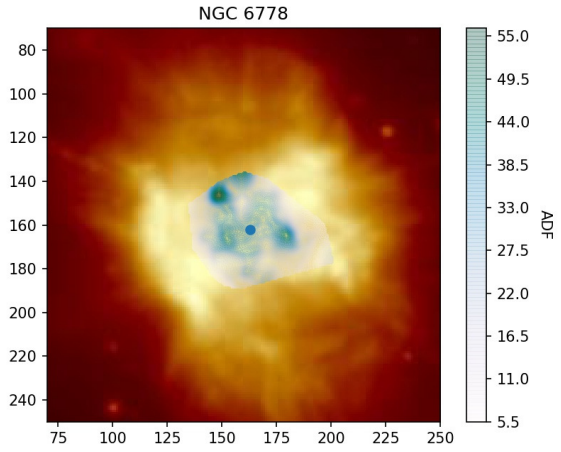

Figure 1. Preliminary results of the ADF spatial distribution in the PN NGC 6778 from our MUSE data. Background image is the Hα emission map. ADF map covers only the zones were O II ORLs were detected. It can be seen that the ADF peaks in regions close to the center of the nebula, reaching values higher than 50.

Our group has taken advantage of the high spatial-resolution of the 2D spectrograph MUSE at VLT to confirm that in several high-ADF PNe, the ORL emission is more centrally concentrated than the emission of the strongest [O III] λ4959 CEL (see Fig. 1 of García-Rojas & et al., 2017). As pointed out above, this is very frequently related with the presence of a confirmed post-CE binary central star, but sometimes it can be a signal of binarity of a still unconfirmed binary central star. This result, together with the presence of a high-ADF, can be a signal of binarity of a still unconfirmed binary central star. In Fig. 1 we also show a preliminary computation of the spatial distribution of the ADF in NGC 6778, showing that the value clearly peaks in the central regions of the PN.

A detailed analysis of the spatial distribution of the physical conditions and ionic abundances, from both CELs and ORLs line ratios is underway.

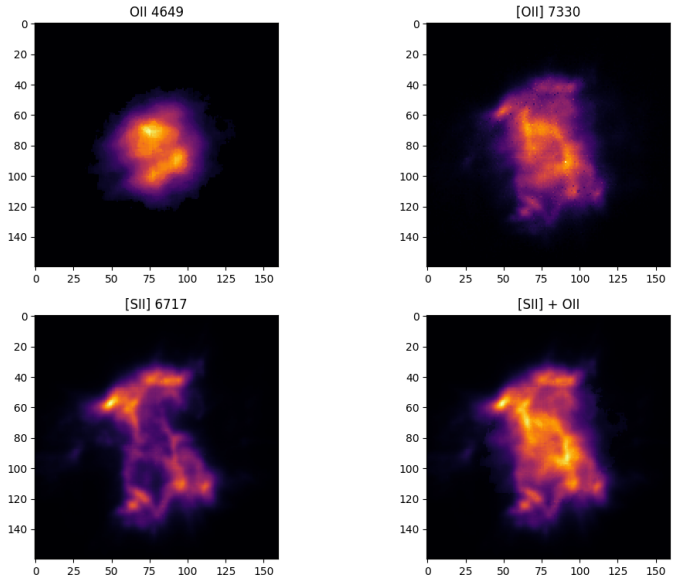

Figure 2. MUSE emission line maps of PN NGC 6778. From left to right and upper to down: O II λ4649+50 ORL, [O II] λ7330 CEL, [S II] CEL and a composite image of [S II]+O II emission maps (see text).

Another possibility to explain the behavior of the high-ADF PNe has been recently proposed by Ali & Dopita (2019). Using IFU data of the PN PB 4, these authors found strong O II ORL emission lines and a similar spatial distribution of O II λ4649 ORL and [O II] $\lambda\lambda$7320 CEL and proposed that the O II ORLs do not arise from recombination at all, but from fluorescent pumping of excited states in the O^+ ion caused by the extreme UV continuum of an interacting binary central star. We investigated the behavior of O II ORLs and [O II] CELs in our MUSE data of NGC 6778 and found that [O II] emission is much more extended than O II emission (see Fig 2) and that the possible similarities found in the emission distribution comes from the fact that [O II] λ7320+30 lines are strongly affected by recombination contribution. Strong recombination line enhancements are seen in second-row elements but not third-row ones (Wesson et al., 2018, and references therein) If O^{2+} is strongly affected by recombination but S^{2+} is not, then, as the two ions have similar ionisation potEntials, the Spatial distribution Of of [O II] should consist of a collisional component resembling [S II], and a recombination component resembling O II ORLs. In Fig. 2, we compare a map of NGC 6778 in the [O II] λ7330 CEL with with a composite image created by adding a map of [S II] emission (scaled to the same peak flux as the [O II] image) and a map of the O II λ4649+50 ORL. This composite image indeed strongly resembles the [O II] image. Moreover, if fluorescent pumping is affecting the emission of O II ORLs, it should also affect in a similar way the emission of C/N/Ne ORLs that are also strongly enhanced in extreme ADF PNe. Given

the different atomic configurations for these elements, it is hard to reconcile the scenario proposed by Ali & Dopita (2019) with observations.

4. Conclusions

In the last 15 years significant advances have been made in the field of the AD problem. Deep high-quality spectra have revealed to be crucial to advance understanding of this problem. Close binary evolution has been shown to be linked with the high ADFs found in PNe, opening a research line encouraging observational and theoretical astronomers to look for additional probes that can help to understand the CE process in close binary stars and the AD phenomenon. In particular, high-spatial and -spectral resolution 2D spectroscopy with MEGARA at GTC and FLAMES at VLT will be crucial to obtain detailed information about the spatial distribution and kinematics of the two gas components. Finally, the combination of these data with more refined models of the CE process and 3D photoionization models have the potential to revolutionize the way we can tackle this fundamental problem.
On the other hand, the solution to AD problem in H II regions and in the bulk of PNe is still far from being understood. Additional spatially-resolved observations with high-spectral resolution covering morphological structures in H II regions and PNe like high-velocity ionized flows of gas or proplyds would, for sure, give precious information to study the impact of these structures in the integrated spectrum of the nebulae.

Acknowledgments. JGR acknowledges support from an Advanced Fellowship from the Severo Ochoa excellence program (SEV-2015-0548). This work was supported by the State Research Agency (AEI) of the Spanish Ministry of Science, Innovation and Universities (MCIU) and the European Regional Development Fund (FEDER) under grants AYA2015-65205-P and AYA2017-83383-P. RW was supported by European Research Grant SNDUST 694520.

References

Ali A., Dopita M. A., 2019, *MNRAS*, **484**, 3251
Bautista M. A., Ahmed E. E., 2018, *ApJ*, **866**, 43
Binette L., Ferruit P., Steffen W., Raga A. C., 2003, *RevMexAA*, **39**, 55
Bresolin F., Kudritzki R.-P., Urbaneja M. A., et al., 2016, *ApJ*, **830**, 64
Corradi R. L. M., García-Rojas J., Jones D., et al., 2015, *ApJ*, **803**, 99
Corradi R. L. M., Sabin L., Miszalski B., et al., 2011, *MNRAS*, **410**, 1349
Draine B. T., Kreisch C. D., 2018, *ApJ*, **862**, 30
Ercolano B., 2009, *MNRAS*, **397**, L69
Escalante V., Morisset C., Georgiev L., 2012, *MNRAS*, **426**, 2318
Esteban C., García-Rojas J., Carigi L., et al., 2014, *MNRAS*, **443**, 624
Esteban C., Toribio San Cipriano L., García-Rojas J., 2018, G. F. Hägele, M. V. Cardaci, and E. Pérez-Mpntero (eds.), *Chemical Abundances in Gaseous Nebulae*, Vol. 10 of *AAA Workshop Serie*, p. 23
Ferland G. J., Henney W. J., O'Dell C. R., et al., 2016, *RevMexAA*, **52**, 261
García-Rojas J., Corradi R. L. M., Monteiro H., et al., 2016, *ApJL*, **824**, L27

García-Rojas J., Esteban C., 2007, *ApJ*, **670**, 457
García-Rojas J., et al., 2017, X. Liu, L. Stanghellini, and A. Karakas (eds.), *Planetary Nebulae: Multi-Wavelength Probes of Stellar and Galactic Evolution*, Vol. 323 of *IAU Symposium*, pp 65–69
García-Rojas J., Peña M., Morisset C., et al., 2013, *A&A*, **558**, A122
Garnett D. R., Dinerstein H. L., 2001, *ApJ*, **558**, 145
Giammanco C., Beckman J. E., 2005, *A&A*, **437**, L11
Guseva N. G., Izotov Y. I., Papaderos P., Fricke K. J., 2007, *A&A*, **464**, 885
Guseva N. G., Izotov Y. I., Thuan T. X., 2006, *ApJ*, **644**, 890
Henney W. J., Stasińska G., 2010, *ApJ*, **711**, 881
Huggins P. J., Frank A., 2006, M. J. Barlow and R. H. Méndez (eds.), *IAU Symp. 234, Planetary Nebulae in our Galaxy and Beyond (San Francisco: ASP)*, pp 271–276
Jones D., Wesson R., García-Rojas J., Corradi R. L. M., Boffin H. M. J., 2016, *MNRAS*, **455**, 3263
Liu X.-W., Barlow M. J., Zhang Y., Bastin R. J., Storey P. J., 2006, *MNRAS*, **368**, 1959
Liu X.-W., Storey P. J., Barlow M. J., Danziger I. J., Cohen M., Bryce M., 2000, *MNRAS*, **312**, 585
Maciejewski W., Mathis J. S., Edgar R. J., 1996, *ApJ*, **462**, 347
Manick R., Miszalski B., McBride V., 2015, *MNRAS*, **448**, 1789
Mendoza C., Bautista M. A., 2014, *ApJ*, **785**, 91
Mesa-Delgado A., Esteban C., García-Rojas J., 2008, *ApJ*, **675**, 389
Mesa-Delgado A., Esteban C., García-Rojas J., Luridiana V., Bautista M., Rodríguez M., López-Martín L., Peimbert M., 2009, *MNRAS*, **395**, 855
Mesa-Delgado A., Núñez-Díaz M., Esteban C., García-Rojas J., Flores-Fajardo N., López-Martín L., Tsamis Y. G., Henney W. J., 2012, *MNRAS*, **426**, 614
Nicholls D. C., Dopita M. A., Sutherland R. S., 2012, *ApJ*, **752**, 148
Núñez-Díaz M., Mesa-Delgado A., Esteban C., López-Martín L., García-Rojas J., Luridiana V., 2012, *MNRAS*, **421**, 3399
Peña M., Ruiz-Escobedo F., Rechy-García J. S., García-Rojas J., 2017, *MNRAS*, **472**, 1182
Peimbert M., 1995, R. Williams and M. Livio (eds.), *The Analysis of Emission Lines*, p. 165
Peimbert A., Peimbert M., Delgado-Inglada G., García-Rojas J., Peña M., 2014, *RevMexAA*, **50**, 329
Peimbert M., 1967, *ApJ*, **150**, 825
Peimbert M., Costero R., 1969, *Boletin de los Observatorios Tonantzintla y Tacubaya*, **5**, 3
Peimbert M., Storey P. J., Torres-Peimbert S., 1993, *ApJ*, **414**, 626
Raga A. C., Reipurth B., 2004, *RevMexAA*, **40**, 15
Richer M. G., Georgiev L., Arrieta A., Torres-Peimbert S., 2013, *ApJ*, **773**, 133
Richer M. G., Guillén Tavera J. E., Arrieta A., Torres-Peimbert S., 2019, *ApJ*, **870**, 42
Richer M. G., Suárez G., López J. A., García Díaz M. T., 2017, *AJ*, **153**, 140
Rodríguez M., García-Rojas J., 2010, *ApJ*, **708**, 1551
Sowicka P., Jones D., Corradi R. L. M., Wesson R., García-Rojas J., Santander-García M., Boffin H. M. J., Rodríguez-Gil P., 2017, *MNRAS*, **471**, 3529

Stasińska G., Szczerba R., 2001, *A&A*, **379**, 1024
Stasińska G., Tenorio-Tagle G., Rodríguez M., Henney W. J., 2007, *A&A*, **471**, 193
Storey P. J., Sochi T., 2014, *MNRAS*, **440**, 2581
Storey P. J., Sochi T., Bastin R., 2017, *MNRAS*, **470**, 379
Toribio San Cipriano L., Domínguez-Guzmán G., Esteban C., García-Rojas J., Mesa-Delgado A., Bresolin F., Rodríguez M., Simón-Díaz S., 2017, *MNRAS*, **467**, 3759
Toribio San Cipriano L., García-Rojas J., Esteban C., Bresolin F., Peimbert M., 2016, *MNRAS*, **458**, 1866
Torres-Peimbert S., Peimbert M., Daltabuit E., 1980, *ApJ*, **238**, 133
Torres-Peimbert S., Peimbert M., Pena M., 1990, *A&A*, **233**, 540
Tsamis Y. G., Péquignot D., 2005, *MNRAS*, **364**, 687
Tsamis Y. G., Walsh J. R., Vílchez J. M., Péquignot D., 2011, *MNRAS*, **412**, 1367
Viegas S. M., Clegg R. E. S., 1994, *MNRAS*, **271**, 993
Wesson R., Jones D., García-Rojas J., Boffin H. M. J., Corradi R. L. M., 2018, *MNRAS*, **480**, 4589
Wesson R., Liu X.-W., Barlow M. J., 2003, *MNRAS*, **340**, 253
Wyse A. B., 1942, *ApJ*, **95**, 356
Yuan H.-B., Liu X.-W., Péquignot D., Rubin R. H., Ercolano B., Zhang Y., 2011, *MNRAS*, **411**, 1035
Zhang Y., Ercolano B., Liu X.-W., 2007, *A&A*, **464**, 631
Zhang Y., Liu X.-W., Liu Y., Rubin R. H., 2005, *MNRAS*, **358**, 457
Zhang Y., Liu X.-W., Wesson R., Storey P. J., Liu Y., Danziger I. J., 2004, *MNRAS*, **351**, 935
Zhang Y., Zhang B., Liu X.-W., 2016, *ApJ*, **817**, 68

Chemical Abundances in Gaseous Nebulae:
Open problems in Nebular astrophysics
AAA Workshop Series NN, 2019
M. Cardaci, G. Hägele & E. Pérez-Montero, eds.

Invited Paper

Primordial Helium Abundance

A. Peimbert[1]

[1]*Instituto de Astronomía, Universidad Nacional Autónoma de México, Mexico City, 04510, Mexico*

Abstract. This is a brief review of the background and present situation of the determination of the primordial helium abundance. A comparison is made between derivations from space and ground observations.

Key words: early universe — galaxies: abundances — ISM : abundances

1. Introduction

It is well known that the determination of the helium to hydrogen ratio for low metallicity HII regions can help us to determine the primordial helium abundance. Both the helium and the heavy element determinations have been under discussion for what is known as the abundance discrepancy factor, ADF. In this case we will focus on the importance of temperature inhomogeneities in the helium determination. The proposal of the importance of temperature inhomogeneities within the observed slit in gaseous nebulae was first presented and developed by Peimbert (1967), and Peimbert & Costero (1969).

2. Temperature inhomogeneities and emission line intensities

As it has been explained the temperatures derived from collisionally excited, CEL, lines are significantly higher than those from recombination lines, RL.

$$I(CELs) \propto T_e^{-1/2} exp(-\Delta E/kT_e)\Upsilon_1(T_e), \tag{1}$$

while

$$I(RLs) \propto T_e^{-1}\Upsilon_2(T_e), \tag{2}$$

where $\Upsilon(T_e) \propto T_e^{\beta}$, with $\mid \beta \mid \leq 0.1$.
For the case of the collisionally excited lines these relations are given by

$$I(CELs) \propto T_e^{-1/2} exp(-\Delta E/kT_e), \tag{3}$$

while

$$I(RLs) \propto T_e^{-1}\Upsilon_2(T_e) \propto T_e^{-k}, \tag{4}$$

where $0.9 \leq \mid k \mid \leq 1.1$.

For helium the temperature can be derived from two well measured lines, but if there are more HeI lines available, for example up to ten lines, the determination can be obtained with higher precision. In this case, $I(\text{HeI}) = f(T_e, n_e, \tau_{3889})$. The results in general yield $T_e(\text{HeI}) \ll T_e[\text{OIII}]$, which again indicates the presence of temperature inhomogeneities. We derive this temperature applying a maximum likelihood method, searching for the best fit to all observed $I(\text{HeI})$ and $I(H\beta)$ line intensity ratios to the theoretical ones. The output provides the best solution for T_e, n_e, τ_{3889}, and He/H simultaneously.

In addition we need to model a distribution of temperatures. Since we don't know the temperature at each point of the nebula, we can try to make a model with a very large number of gas parcels. It would be a very artificial distribution without much astrophysical meaning. We simplify the problem assuming small deviations of temperature from the mean value.

The problem arises because the traditional calculations assume a uniform temperature across the whole region. While Peimbert's formalism (Peimbert, 1967), (Peimbert & Costero, 1969) can be described as a "Simplified Taylor Expansion of the Temperature Distribution (t^2)".

3. Simplified Taylor expansion of the temperature distribution

Astronomers that prefer t^2 models (and therefore RL abundances), where most of the object (weighted by emission measure) is chemically homogeneous. We must consider that there are many physical processes going on that destroy thermal homogeneity (shockwaves, shadows, X-rays, cosmic rays, moving ionisation fronts, etc.); for a review of these processes see Peimbert et al. (2017). In any case, CELs are expected to be brighter in regions that are slightly hotter than the average (this effect depends on the excitation energy and is larger for auroral than for nebular lines), while RLs are brighter in regions that are slightly cooler than the average. The difference strongly affects temperature determinations, and necessarily the derived chemical abundances.

This effect can be modeled as a Taylor expansion of an arbitrary temperature distribution. It can be shown that for "moderate" thermal inhomogeneities the zeroth and 2nd order terms in the expansion are the most important ones, hence the mean temperature, T_0, and t^2 formalism are given by

$$T_0 = \langle T(r) \rangle; \tag{5}$$

$$t^2 = \langle [T(r) - T_0]^2 / T_0^2 \rangle. \tag{6}$$

4. t^2 and helium abundance determinations

These determinations traditionally compare the [OIII] nebular and auroral lines with either the temperature from the ratio of the Balmer Jump to the Balmer lines, the intensity ratios of the OII multiplet 1 lines, or from the intensity ratios of the HeI lines.

In many circumstances the quality of these last determinations is similar and they often agree. However, the one from HeI lines is more robust, while the one

from OII lines requires echelle spectra, and the one from the Balmer Jump is often polluted by underlying stellar light.

For our case, from a crude approximation of the temperature distribution we can extend the solution of the maximum likelihood method described above. In this case, we propose a temperature distribution in 3 phases, where 66% of the volume is at T_0, and 17% of the volume is at a temperature $T_0 + 1.7\sigma_T$ higher, and 17% of the volume is at a temperature $T_0 - 1.7\sigma_T$ lower; where σ_T is the mean uncertainty of the derived T_0. From this distribution we select the best $\chi 2$ fit. The input values are trial T_0, t^2, n_e and He/H, where we compare the model intensities for the set of lines under consideration, with the observed ones; the best fit yields the final T_0, t^2, n_e and He/H values.

Not much attention has been paid to the temperature inhomogeneities problem in deriving helium abundances. The reason is that the helium derivation is not very sensitive to temperature. Typically the final value, taking all the lines into account, depends on $I(\mathrm{HeI}) \propto T^{\langle\beta\rangle}$, with $\langle\beta\rangle \approx -0.92$. That is, if either the wrong temperature, or the wrong t^2, is used, the derived value changes very slightly, by about 1% to 2% of the helium abundance. This effect does not seem important. In fact, there are no measurements of O/H with a $\leq 2\%$ error. However for the fraction of primordial mass in helium, Y_P, it is important to achieve a much higher precision. We wish to derive precisions of $\sim 2\%$ to be competitive, or $\sim 1\%$ to be a leading group, and "theoretically" $\sim 0.1\%$ to be able to fully constrain some physical parameters related to the Big Bang, BB.

5. Primordial helium

The importance of the determination of Y_P is manyfold. One of the reasons is that it is a very important parameter to understand the chemical evolution of galaxies. In fact, we need a starting point in our modeling; similarly it is important to understand the ratio of the helium production over the heavy element production, $\Delta Y/\Delta Z$.

The Standard Big Bang Theory, SBB, aims to understand the Universal Constants. Historically, constants like η, and the baryon/photon ratio, were determined from Y_P. Now, studies of the CMB carried out by Planck, and previously by WMAP, can directly determine η with extremely high precision (but only assuming SBB). At present, extremely high precision determinations of Y_P can set independent restrictions on the neutron mean lifetime, τ_n and the number of neutrino families, N_ν (e.g. Valerdi et al., 2019).

We can ask ourselves whether the BB and Big Bang Nucleosynthesis, BBN, are standard. The answer depends on the number of neutrino families. However, other questions have been raised: (a) are there fractional neutrino families? (b) are there any alternate options, for example, were there any exotic decaying particles present during BBN? (c) is the gravitational constant, G, really constant? and (d) have any other fundamental constants been constant at all times?

6. The derivation of primordial helium

The determination of Y_P has been attempted following three different types of studies: (a) by the results of WMAP and Planck satellites through studies of the CMB anisotropies, CMB, (b) by studies of D_P and HeI absorption lines along lines of sight to distant quasars, since BBN predicts that the initial ^{2}H, ^{3}H, ^{3}He, ^{4}He, and ^{7}Li should be correlated to each other, and (c) the determinations of Y_P, through studies of low and very low metallicity HII regions.

The derivation of Y_P from CMB satellites. The result from WMAP assuming SBBN was $Y_P = 0.2457 \pm 0.0004$ (Coc et al., 2005), and the estimated result from Planck amounts to $Y_P = 0.24672 \pm 0.00061$ (Planck Collaboration et al., 2018). These results have been obtained assuming that Big Bang is SBB. But even within the SBB scenario: they assume that some physical constants are known perfectly well, which is not necessarily valid. In addition, an important uncertainty not included in the claimed error comes from uncertainties in the determination of the neutron mean lifetime, τ_n. A recent result assigns a value of $\tau_n = 879.5 \pm 0.8$ from ultracold neutron measurements (Serebrov et al., 2017). In addition, we must point out that if BB is not SBB, e.g. if there is a fourth neutrino family, this is equivalent to $\Delta Y_P \approx 0.01400$ (Peimbert, 2008) (Peimbert 2008). In total, we are concerned that the accuracy of the Y_P determinations are lower than presented.

If we turn our attention to the neutron mean lifetime determinations, we can see that depending on the method of determination of the τ_n the results yield two different families of values, the bottle method gives a significantly lower value for the mean life than the beam method, 879.4 ± 0.6 and 887.7 ± 3.1, respectively (Wietfeldt et al., 2014) . We take this as an indication that at present this value is not well determined, and can certainly affect the final results of Y_P. That is, the previous determination assumes that all the physical constants are exactly known; and from the determined Ω_m, Ω_b, and H_0, it is possible to determine exactly the evolution of the SBBN, and thus Y_P. Once that this problem is considered, it is possible to relax the previous assumption, and from fits to the 5th and 6th maxima in the CMB anisotropy function they conclude that $Y_P = 0.2430 \pm 0.0240$ (Planck Collaboration et al., 2018).

The derivation of Y_P from intergalactic gas cloud absorption lines. D_P and Y_P have been determined from studies of intergalactic clouds near pristine absorptions system along the line of sight of bright distant quasars. Cooke & Fumagalli (2018) determined D_P from the presence of deuterium lines in Lyman HI systems located at high redshifts toward the several quasars. From these measurements they derived a value of $log(\mathrm{D/H})_P = -4.622 \pm 0.015$, which corresponds to $10^5(D_P) = 2.26 \pm 0.030$.These primordial helium determinations are not very restrictive since they suffer from the complication of astration, relative ionization compared to H, and possible preferential depletion of deuterium onto dust grains. In addition, Cooke et al. (2018) have determined an upper limit for $Y_P = 0.250^{+0.033}_{-0.025}$ directly from HeI absorption lines in the near-ultraviolet from partial Lyman limit systems against the light of a bright background quasar.

Determinations from HII regions in metal poor galaxies. This research was started by Peimbert & Torres-Peimbert (1974) who presented the first Y_P

determination. The value obtained was based on the strategy still used today. These studies have been pursued by many authors. In particular, there are three groups that have repeatedly worked on the HII regions determination: (a) Peimbert, Peimbert, Luridiana, et al., (b) Izotov, Thuan, Stasinska, Guseva, et al., and (c) Skillman, Olive, Aver, et al. The group of Izotov et al. has been very active observing metal poor galaxies. Starting in 1994, they have observed and studied over a hundred objects. The second group (Olive et al., 1997; Aver et al., 2015), relies on fewer number of regions. All their objects have also been observed by Izotov et al. We can also point out that 60% of the objects in our sample are included in the sample by Izotov et al. (2014).

The work by Olive et al. (1997) updated the analysis of helium in low-metallicity extragalactic HII regions. Although the observations were mostly from the data by Izotov et al. (1997) they combined several sets of observations and analyzed 62 HII regions. Their best estimate for the primordial abundance of ^{4}He assuming a linear relation between ^{4}He and O/H is based on the subset of HII regions with the lowest metallicity. They considered that Izotov et al. (1997) used too many simplifications and were overly optimistic in the error bars they presented. Olive et al. (1997) proposed that better determinations can be obtained with these data and thus obtained a different result for the Y_P value.

Later, the first group rejoined the discussion with observations of NGC 346 (Peimbert et al., 2000). Our approach differs greatly from that of the group of (Izotov et al., 1997, 2014) in that we believe that extremely careful studies of a few select objects (5 or less)are better than studies of a large group. Instead of relying on a large quantity of observed galaxies, we rely on observational data reduction, and statistical analysis. We believe that select observations, applying the CLOUDY code by Ferland et al. (2017), and carrying our chemical comparison with different objects improve the results.

In our case, our sample was based on five objects, NGC 346 (SMC N66A), Haro 29 (Mrk 209), NGC 2363, I Zw 18, and SBS 0335-052. A detailed study of uncertainties was presented by Peimbert et al. (2016), where the possible sources of uncertainties in the Y_P determination were considered individually (collisional excitation of HI lines, temperature inhomogeneities, $Z_0(\Delta Y/\Delta Z)$ correction, HI and HeI recombination coefficients, HI and HeI underlying absorption, reddening correction, He ionization correction factor, density structure, HeI triplet lines optical depth and HI and HeI line intensities); for these parameters the statistical and systematic errors were listed. For our observations of 5 objects we derive a $Y_P = 0.2446 \pm 0.0029$ with a value of 0.0019 for the statistical uncertainties, and a value of 0.0021 for the systematic ones. Based on additional observations of NGC 346, Valerdi et al. (2019) have presented a new determination of Y_P.

The value of Y_P depends on the determination of the oxygen abundance in each region. It is well established that in the presence of thermal inhomogeneities the direct method underestimates the real oxygen abundances by a factor of ~ 2, and thus introduces another small change in the Y_P determination. For hot objects (of low metallicity), $t^2 \neq 0.00$ the oxygen abundances can be ~ 1.5 higher than $t^2 = 0.00$ abundances, this implies changes of $\sim 1\%$ in the Y_P determination.

I would like to point out that from observations and chemical evolution models of low metallicity galaxies Peimbert et al. (2007a,b) find a general value of

$\Delta Y/\Delta Z_O = 3.3 \pm 0.7$, where Z_O is the O abundance by unit mass, which is in agreement with the results of Peimbert (2003) from NGC 346, 30 Dor, and M17.

7. Comparison of results by different authors

In Table 1 a comparison of the result of Y_P determinations by different groups is presented. Izotov et al. (2014) from the observations of 28 objects determined $\Delta Y/\Delta Z_O$; they used $T_e(He^+) \sim T_e$[OIII]; however, they ignore the ionization correction factor due to the presence of neutral helium inside the He^+ zone, ICF(He^+), the fluorescent effects for HI lines, and the effect of thermal inhomogeneities, deriving $Y_P = 0.2551 \pm 0.0022$. Aver et al. (2015) from the observations of 15 objects determined $\Delta Y/\Delta Z_O$; they used $T_e(He^+) = T_e$(HeI), included statistical corrections for the fluorescent HI lines and derived a value of $Y_P = 0.2449 \pm 0.0040$. Other Y_P determinations are also included in Table 1.

Table 1. Y_P, D_P and equivalent number of neutrino families.

Source	10^5 (D/H)$_P$	Y_P	N$_\nu$
Izotov et al. (2014)	...	0.2551 ± 0.0022	3.58 ± 0.25
Aver et al. (2015)	...	0.2449 ± 0.0040	2.91 ± 0.30
Peimbert et al. (2016)	...	0.2446 ± 0.0029	2.90 ± 0.22
Fernández et al. (2018)	...	0.245 ± 0.007	2.92 ± 0.55
Valerdi et al. (2019)	...	0.2451 ± 0.0026	2.92 ± 0.20
Cooke & Fumagalli (2018)	2.527 ± 0.030	...	3.41 ± 0.45
Cooke et al. (2018)	...	$0.250^{+0.033}_{-0.025}$	...

The corresponding values for the helium to oxygen enrichment ratio, $\Delta Y/\Delta Z_O$, by different groups are not in agreement; Izotov et al. (2014) find $\Delta Y/\Delta Z_O = 0.93 \pm 0.82$, while Aver et al. (2015) find $\Delta Y/\Delta Z_O = 6.5 \pm 3.5$. That is, the slopes derived by these two groups are very different.

Our concern has been to improve on the primordial helium determination, there are several approaches. One of them is to add more observations of similar quality. For example, if we are able to obtain a factor of 6 more observations, in principle the statistical errors in the Y_P value could be reduced to 0.0007. We point out that the inclusion of a factor of 6 more observations of lower quality can reduce some of the statistical errors , but it may also increase some of the uncertainties (temperature structure, underlying absorption of the He lines, He ionization correction factor) yielding a value of 0.0024 for the statistical uncertainties, and similarly for the systematic ones which yields a value of 0.0045. We consider that by including a single observation of extremely high quality (see Valerdi et al.2019) we can decrease our uncertainties to 0.0018 for the statistical, and to 0.0019 for the systematic ones. A comparison of the primordial values of Y_P, D_P and equivalent number of neutrino families derived by different groups is also presented in Table 1.

From the CMB observations from WMAP and Planck they derive Y_P with great accuracy by assuming SBB and SBBN. We would like to point out that this procedure can be turned around and instead try to compare HII region Y_P determinations with CMB determinations to ascertain the validity of the assumptions that BB and BBN are indeed SBB and SBBN.

8. Summary

We consider that: (a) Temperature inhomogeneities are present in low metallicity HII regions. (b) Temperature inhomogeneities should be taken into account to obtain high precision chemical abundances, (c) Helium lines provide the best available determinations of the amplitude of the thermal inhomogeneities, t^2. (d) The determination of Y_P requires the acknowledgment of the presence of important thermal inhomogeneities. (e) Y_P is deeply interlaced with the determination of other fundamental physical parameters, like the number of neutrino families and the neutron mean life.

Acknowledgments. I am grateful to S. Torres-Peimbert who presented this work in my absence to this meeting. I am also grateful to CONACyT for Grant 241732 and to DGAPA-UNAM for Grant PAPIIT IG100319.

References

Aver E., Olive K. A., Skillman E. D., 2015, *J. Cosmology Astropart. Phys.*, **2015(7)**, 011

Coc A., Angulo C., Vangioni-Flam E., Descouvemont P., Adahchour A., 2005, *NuPhA*, **752**, 522

Cooke R. J., Fumagalli M., 2018, *NatAs*, **2**, 957

Cooke R. J., Pettini M., Steidel C. C., 2018, *ApJ*, **855(2)**, 102

Ferland G. J., Chatzikos M., Guzmán F., Lykins M. L., van Hoof P. A. M., Williams R. J. R., Abel N. P., Badnell N. R., Keenan F. P., Porter R. L., 2017, *RevMexAA*, **53**, 385

Fernández V., Terlevich E., Díaz A. I., Terlevich R., Rosales-Ortega F. F., 2018, *MNRAS*, **478(4)**, 5301

Izotov Y. I., Thuan T. X., Guseva N. G., 2014, *MNRAS*, **445(1)**, 778

Izotov Y. I., Thuan T. X., Lipovetsky V. A., 1997, *ApJS*, **108(1)**, 1

Olive K. A., Steigman G., Skillman E. D., 1997, *ApJ*, **483(2)**, 788

Peimbert A., 2003, *ApJ*, **584(2)**, 735

Peimbert A., Peimbert M., Luridiana V., 2016, *RevMexAA*, **52**, 419

Peimbert M., 1967, *ApJ*, **150**, 825

Peimbert M., 2008, *Current Science*, **95**, 1165

Peimbert M., Costero R., 1969, *Boletin de los Observatorios Tonantzintla y Tacubaya*, **5**, 3

Peimbert M., Luridiana V., Peimbert A., 2007a, *ApJ*, **666(2)**, 636

Peimbert M., Luridiana V., Peimbert A., Carigi L., 2007b, A. Vallenari, R. Tantalo, L. Portinari, and A. Moretti (eds.), *From Stars to Galaxies: Building the Pieces to Build Up the Universe*, Vol. 374 of *Astronomical Society of the Pacific Conference Series*, p. 81

Peimbert M., Peimbert A., Delgado-Inglada G., 2017, *PASP*, **129(978)**, 082001

Peimbert M., Peimbert A., Ruiz M. T., 2000, *ApJ*, **541(2)**, 688

Peimbert M., Torres-Peimbert S., 1974, *ApJ*, **193**, 327

Planck Collaboration, Aghanim N., Akrami Y., Ashdown M., Aumont J., Baccigalupi C., Ballardini M., Banday A. J., Barreiro R. B., Bartolo N., 2018, *arXiv e-prints*, p. arXiv:1807.06209

Serebrov A. P., Kolomensky E. . A., Fomin A. K., Krasnoschekova I. A., Vassiljev A. V., Prudnikov D. M., Shoka I. V., Chechkin A. V., Chaikovskiy M. E., Varlamov V. E., 2017, *arXiv e-prints*, p. arXiv:1712.05663
Valerdi M., Peimbert A., Peimbert M., Sixtos A., 2019, *ApJ*, **876(2)**, 98
Wietfeldt F. E., Darius G., Dewey M. S., Fomin N., Greene G. L., Mulholland J., Snow W. M., Yue A. T., 2014, *Physics Procedia*, **51**, 54

Chemical Abundances in Gaseous Nebulae:
Open problems in Nebular astrophysics
AAA Workshop Series 11, 2019
M. Cardaci, G. Hägele & E. Pérez-Montero, eds.

Invited Review

Constraining the observational uncertainties of nebular abundances

Mónica Rodríguez

Instituto Nacional de Astrofísica, Óptica y Electrónica, Luis Enrique Erro 1, 728400 Tonantzintla, Puebla, Mexico

Abstract. I explore the effects of observational uncertainties in the calculation of nebular abundances. The results are based on the analysis of 180 optical spectra of 42 planetary nebulae (PNe) compiled from the literature. A score is assigned to each spectrum according to its quality, and the comparison between the abundances derived using the best spectrum of each object and those implied by other spectra are used to assess the uncertainties introduced by observational problems. The observational uncertainties are below or around 0.2 dex in most cases, but can reach 0.6 dex in extreme cases. Since the PNe analyzed here are representative of those nebulae that can be most easily observed, observational uncertainties are likely to be larger for fainter and extragalactic objects.

Key words: ISM: abundances — planetary nebulae: general — H II regions

1. Introduction

The calculation of chemical abundances in gaseous nebulae is relatively straightforward, but in order to get meaningful interpretations of the derived nebular abundances, we need to understand and constrain all the sources of uncertainty, namely, those introduced by observations, atomic data, and the different assumptions made about the nebular structure. The uncertainties introduced by departures from the commonly assumed structure in electron density and temperature, in metallicity, and in the degree of ionization of different elements (i.e., the ionization correction factors) have been explored in previous works (e.g., Peimbert & Costero, 1969; Liu et al., 2000; Stasińska, 2005; Delgado-Inglada et al., 2014). The uncertainties introduced by atomic data have also been recently explored and turn out to be especially important, since the use of different sets of data can introduce differences larger than 0.6 dex in several abundance ratios (Juan de Dios & Rodríguez, 2017). Observational uncertainties might be equally important, but their effects have not been much explored.
There are various possible sources of observational problems, which can arise during the observations, in the reduction process, or when the final data are transcribed into tables: atmospheric differential refraction (Filippenko, 1982), telluric absorption and emission (e.g., Smette et al., 2015), problems with the flux calibration or the extinction correction, the presence of unrecognized blends

(e.g., Rodríguez & Delgado-Inglada, 2011), a poor signal to noise, typos, etc. Observers usually provide error estimates for the line ratios used to derive physical conditions and chemical abundances, and these estimates can be used to assign uncertainties to the derived quantities. However, one or several of the possible sources of error are likely to go unnoticed or unconstrained by the observers, and will not be included in their error estimates. Hence, another approach is necessary.

The approach used here is to explore the effects of observational uncertainties in the derived chemical abundances by analyzing in a homogeneous way sets of different spectra of the same object. The differences in the chemical abundances implied by the different observations of the same object are used to constrain the uncertainties introduced by observational effects. All the objects analyzed are planetary nebulae (PNe), but most of the results will hold for H II regions.

2. Sample

The sample comprises 180 optical spectra of 42 PNe, each with three to eight spectra that have: (i) one or more density diagnostics ([S II] λ6716/λ6731, [O II] λ3726/λ3729, [Cl III] λ5518/λ5538, and/or [Ar IV] λ4711/λ4740), (ii) two temperature diagnostics, [O III] λ4363/(λ4959+λ5007) and [N II] λ5755/(λ6548+λ6583), and (iii) a measurement of the [O II] λ3726 + λ3729 lines. The [O II] lines are needed to calculate the O^+ abundance, which is used to derive not only the total abundance of oxygen but also the total abundances of other elements, since most ionization correction factors are based on the relative abundances of O^+ and O^{++}.

The requirement that the spectra include a measurement of the blue [O II] lines leaves out of the sample spectra that do not reach the blue spectral range but that have measurements of the red [O II] lines at $\lambda \sim 7325$ Å. Both sets of lines have their disadvantages. The blue [O II] lines are in a spectral region where many instruments have a low efficiency and they are very sensitive to the effects of atmospheric differential refraction, the flux calibration and the extinction correction. On the other hand, the red lines are weaker, can be heavily affected by telluric emission, and are more sensitive to electron density and to the contribution of recombination (see Section 4). The disadvantages of the red [O II] lines are likely to outweigh the disadvantages of the blue lines, and requirement (iii) above is based on this consideration.

The PNe in the sample are extended sources, and the spectra were taken at different positions, which may vary in their physical conditions and degree of ionization. This can introduce differences in the calculated abundances that are not due to observational uncertainties, but the effects are likely to be minor.

Further details on the sample and the references for the spectra will be presented elsewhere (Rodríguez, 2019, in prep.).

3. Method

Most of the calculations of physical and conditions and ionic abundances have been performed with PyNeb (Luridiana et al., 2015) using the extinction-corrected

line ratios provided by the different authors. I use atomic data that can be considered optimal or that have no apparent problems (Juan de Dios & Rodríguez, 2017, 2019, in prep.). The [N II] and [O III] temperatures are used in the calculations performed for low- and high-ionization ions, respectively. The electron density is obtained by averaging the logarithmic values of the available diagnostics. Ionic abundances are calculated for He^+, He^{++}, O^+, O^{++}, N^+, S^+, S^{++}, Cl^{++}, Ar^{++}, and Ne^{++}, although some spectra do not have the lines needed to calculate all these ionic abundances. The ionization correction factors are from Delgado-Inglada et al. (2014), except for nitrogen, where I use $N/O{=}N^+/O^+$ (see Delgado-Inglada et al., 2015).

The contribution of recombination to the [O II] blue and red emission lines was calculated by introducing the recombination coefficients of Storey et al. (2017) in the equations of statistical equilibrium for O^+. With this approach, the recombination contribution is proportional to the O^{++}/O^+ ratio, and in some cases the change in the O^+ abundance introduced by the correction makes it necessary to do up to five iterations when solving the statistical equilibrium equations. The alternative approach used by Liu et al. (2000), based on calculating the contribution of recombination to the emission lines without taking into account the effects of recombination on the level populations, does not lead to the same results. For this reason, and because no collisionally excited lines of [O IV] and [N III] are observed in the optical, I did not use the formulae provided by Liu et al. (2000) to correct the [O III] λ4363 and [N II] λ5755 lines for the effects of recombination.

4. Results

Figure 1 shows the differences in O^+/H^+ introduced by the correction for recombination as a function of the degree of ionization, O^+/O^{++}, implied by the corrected blue [O II] lines. The results are shown for the abundances calculated with the red and blue [O II] lines (plotted with squares and circles, respectively). The calculations are based on case B, which is usually assumed to hold for PNe (Storey et al., 2017). The corrections can be seen to be larger for the red [O II] lines, are significant only for objects with $O^+/O^{++} < 1$, and grow for lower values of the [N II] temperature. The effects of recombination on the densities derived from the [O II] $\lambda3726/\lambda3729$ are small, leading to changes in the electron density lower than 0.02 dex in all cases.

The correction for recombination of the O^+ abundances introduces changes in the derived total abundances of oxygen and, through the use of ionization correction factors, in the total abundances of nitrogen, sulfur, chlorine, argon, and neon. The changes are small, below 0.1 dex, in most cases, but reach values of up to 0.4 (0.6) dex in the total abundances of nitrogen and sulfur when the blue (red) [O II] lines are used to calculate the O^+ abundance.

Even though the effects of the correction for recombination are small in most cases, the effects of using either the blue or the red lines of [O II] to perform the calculations are not small. This is due to the fact that the O^+/H^+ abundances implied by the red and blue [O II] lines differ by almost a factor of 6 in either direction for some spectra, indicating that the relative flux calibration of the blue and red ends of the spectrum can go seriously wrong. Figure 2 shows histograms

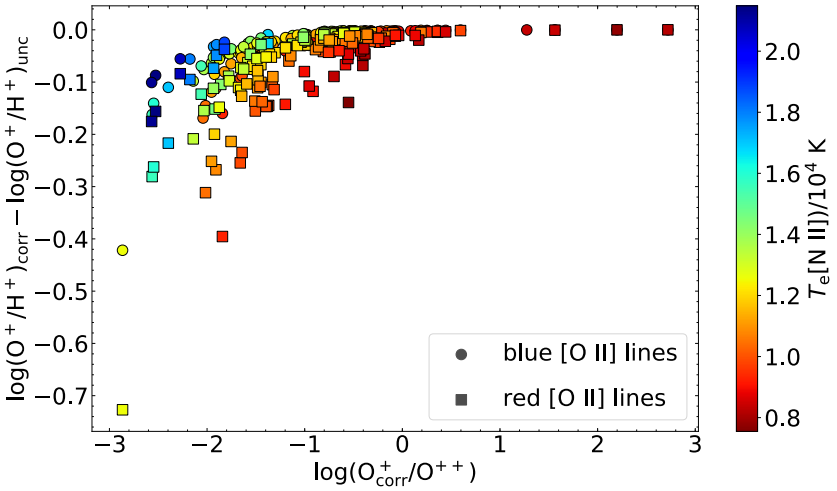

Figure 1. Differences in the values of O^+/H^+ introduced by the correction for recombination for abundances based on the blue (circles) and red (squares) lines of [O II]. The results are presented as a function of the degree of ionization given by O^+/O^{++}. The colors illustrate the dependence of the correction on the [N II] temperature.

of the differences between the total abundances of oxygen, nitrogen, chlorine and sulfur implied by the blue and red [O II] lines. The effects can be seen to be important for the abundance ratios that are more sensitive to the O^+/O^{++} ratio, namely N/H and S/H.

These results illustrate the importance of having assessments of the spectra quality along with estimates of the uncertainties introduced by the use of spectra of different quality. There are several ways to assess the quality of a given spectrum and they can be used to complement each other. First, if the observed spectrum includes more than one density diagnostic, the differences in the densities implied by the available diagnostics can be used to assign some initial score to the spectrum. Second, most observed spectra provide measurements of the [O III] λ4959, λ5007 and [N II] λ6548, λ6583 lines. These lines arise from transitions that have the same upper level and their relative intensities should have fixed values. Departures from these values can be used to assign scores to be added to the previous, density-based one. Third, the relative intensities of several He I lines can be compared with their expected values and used to provide one more score. Finally, for those spectra that allow the measurement of several H I Balmer and Paschen recombination lines, a comparison of their relative intensities with the expected ones can be used to provide another score.

The He I lines used to grade the spectra must be chosen with care, since some He I lines will depart from their expected values because of optical depth effects. I calculated several simple photoionization models with Cloudy (Ferland et al., 2017) characterized by different effective temperatures of the ionizing source (assumed to be a blackbody) and different densities. I increased the number of resolved He I levels in the manner described by Ferland et al. (2017) to obtain

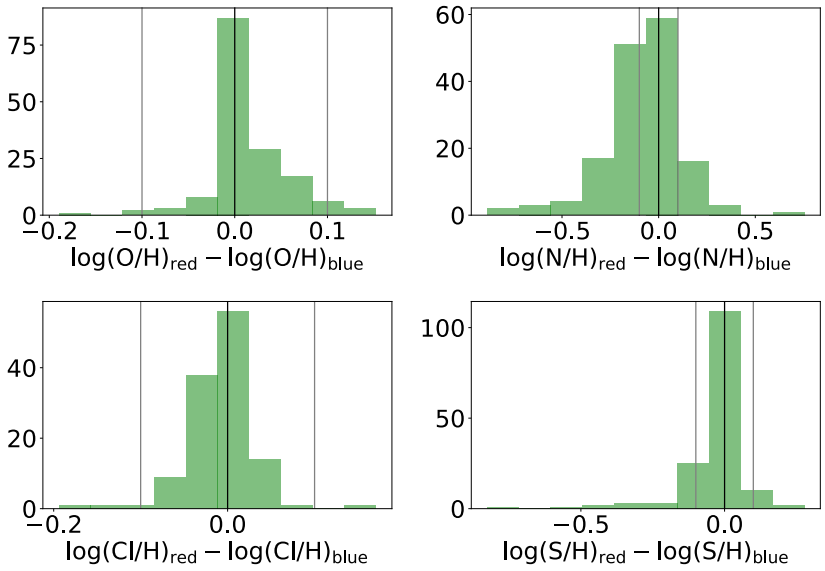

Figure 2. Histograms of the differences between the values of several abundance ratios calculated using the blue and red lines of [O II]. Vertical black lines indicate zero differences; gray lines show the locations of differences of ±0.1 dex.

more reliable line intensities and varied the optical depths of the models by including turbulence or excluding the outer layers of the model. The comparison between the model-predicted intensities of the He I lines and their predicted case B values (Porter et al., 2012, 2013) indicates that the lines at 4026, 4388, 4471, 4922, 5876, and 6678 Å are not sensitive to optical depth effects and can be used to evaluate the quality of spectra. These lines are produced by transitions that go from the d levels to the $2p$ levels of He I. A revision of the relative intensities of the He I lines in those spectra that received the highest scores from other spectral features suggests that this is a good approach.

On the other hand, there is evidence that the H I Balmer and Paschen lines can depart from their predicted case B values (Storey & Hummer, 1995), especially at large values of the principal quantum number n (Mesa-Delgado et al., 2009). In order to circumvent this problem, the assignation of scores can be based on the comparison of the departures of the Balmer and Paschen lines from their expected values as a function of n. This is based on the assumption that, at a given n, the Balmer and Paschen lines will have similar deviations from their case B predicted values.

The criteria described above were used to assign a preliminary score to each of the 180 spectra analyzed here. The resulting scores are in the range 4–18, with only six spectra achieving the highest scores (16–18). Figure 3 shows the behavior of the H I and He I lines for one spectrum with a relatively low score (the one by Hyung et al., 2001, for IC 5217, with a score of 7, represented by crosses) and for another spectrum with one of the highest scores (García-Rojas et al., 2012, for PC 14, with a score of 18, represented by circles). The top panel

of Figure 3 shows the values of $R_1 = [I(\mathrm{H}n)/I(\mathrm{H}\beta)]/[I(\mathrm{H}n)/I(\mathrm{H}\beta)]_{\mathrm{Case\ B}}$ as a function of the principal quantum number n for the Balmer (blue symbols) and Paschen (red symbols) lines. The bottom panel of Figure 3 shows the results for the He I lines, with $R_2 = [I(\lambda)/I(\lambda4471)]/[I(\lambda)/I(\lambda4471)]_{\mathrm{Case\ B}}$ plotted as a function of wavelength. The $nd - 2p$ transitions, whose intensities relative to He I λ4471 are expected to be independent of the optical depth, are shown in green; other transitions are shown in cyan.

Since the differences in the O^+ abundances implied by the blue and red [O II] lines have not been used so far to assign scores to the spectra, they can now be used to check whether the scores are reflecting the spectra quality. Figure 4 shows a histogram of these differences, with the correction for recombination already included, for the 156 spectra that have measurements of both the blue and the red lines. The colors indicate three ranges of scores, with the lowest and highest ones shown in red and blue, respectively. The vertical dashed line in the figure shows the position of the median at -0.075 dex (the median was -0.12 dex before the correction for recombination). There are spectra with low scores that show small differences, but this is to be expected since many spectra only report the intensities of a few lines. The measurements of these lines can be reliable, but the spectra do not provide enough information to evaluate their quality. On the other hand, the spectra with the highest scores do not show extreme differences in the values of O^+/H^+. These results suggest that the differences in O^+/H^+ can also be used in future assessments of the quality of the spectra (Rodríguez, 2019, in prep.).

The current scores can be used to provide estimates of the uncertainties introduced by observations in the derived abundances. The spectrum with the highest score for each PN (in the range 10–18) can be used as a reference, and the differences in the chemical abundances implied by the reference spectrum and the other available spectra (all but one of them in the range 4–14, with the exception having a score of 16) provide estimates of the observational uncertainties. Figure 5 shows these differences for oxygen, nitrogen, chlorine, and sulfur (note that the sample is smaller for sulfur and, especially, for chlorine, since not all spectra report measurements of [S III] and [Cl III] lines). The results presented in Figure 5 indicate that the observational uncertainties are ~ 0.2 dex for the sample PNe, though they can reach 0.6 dex for the poorest spectra. Since these 42 PNe can be considered objects that can be easily observed, because each of them has at least three spectra with measurements of enough lines to do the basic analysis performed here (see Section 2), observational uncertainties are likely to be larger for other samples.

5. Summary and conclusions

I have presented an analysis of 180 optical spectra of 42 PNe, each of them with at least three spectra that have measurements of [O II] $\lambda3726 + \lambda3729$, the lines needed to calculate the electron density, those required to derive the [N II] and [O III] temperatures, and the lines used to derive the abundances of several elements. The spectra, obtained from the literature, have been analyzed in a homogeneous way. The analysis includes a correction of O^+/H^+ for the effects

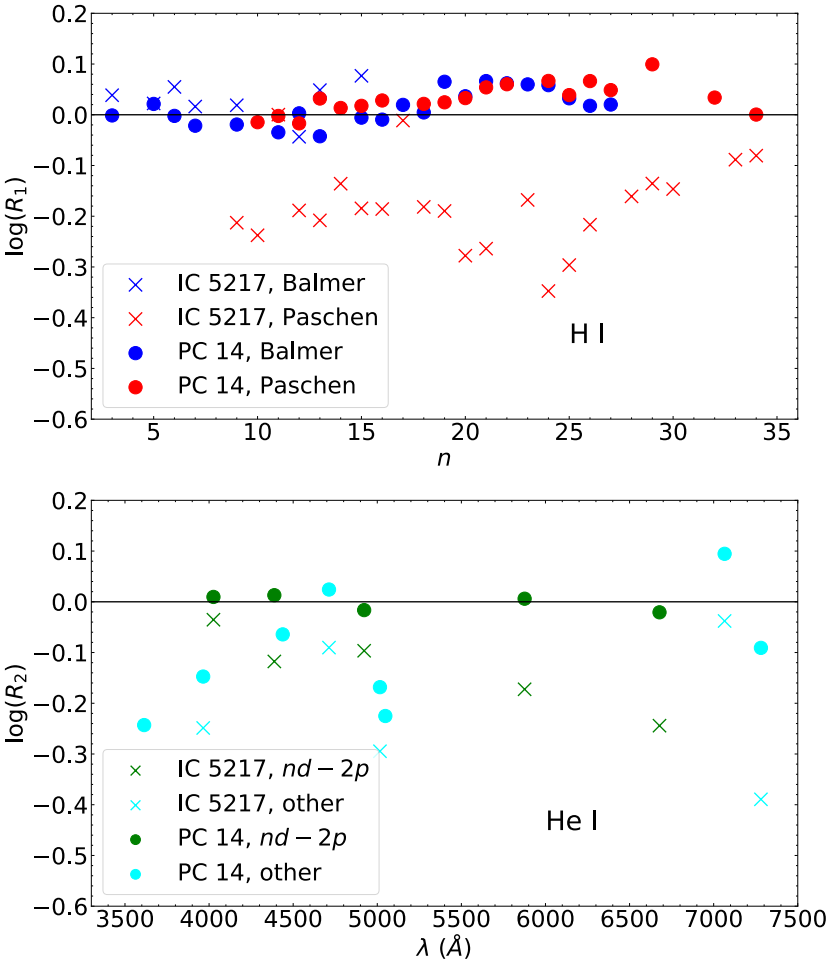

Figure 3. *Top:* Comparison between the extinction corrected Balmer (blue) and Paschen (red) lines and their expected values as a function of the principal quantum number n, with $R_1 = [I(\mathrm{H}n)/I(\mathrm{H}\beta)]/[I(\mathrm{H}n)/I(\mathrm{H}\beta)]_{\mathrm{Case\ B}}$, for the spectrum of Hyung et al. (2001) for IC 5217 (crosses) and the one of García-Rojas et al. (2012) for PC 14 (circles). *Bottom:* Comparison between the extinction corrected He I lines and their predicted values, with $R_2 = [I(\lambda)/I(\lambda4471)]/[I(\lambda)/I(\lambda4471)]_{\mathrm{Case\ B}}$, for the spectra of Hyung et al. (2001) for IC 5217 (crosses), and García-Rojas et al. (2012) for PC 14 (circles). The lines shown in green are expected to be insensitive to optical depth effects.

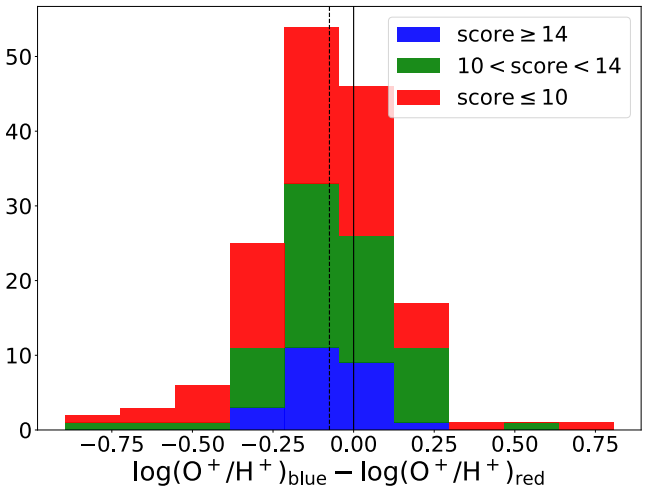

Figure 4. Differences between the values of O^+/H^+ obtained with the blue and red lines of [O II] for 156 spectra with measurements of both features. The colors illustrate the scores of the spectra. The vertical black line is at zero; the dashed line shows the median value at -0.075 dex.

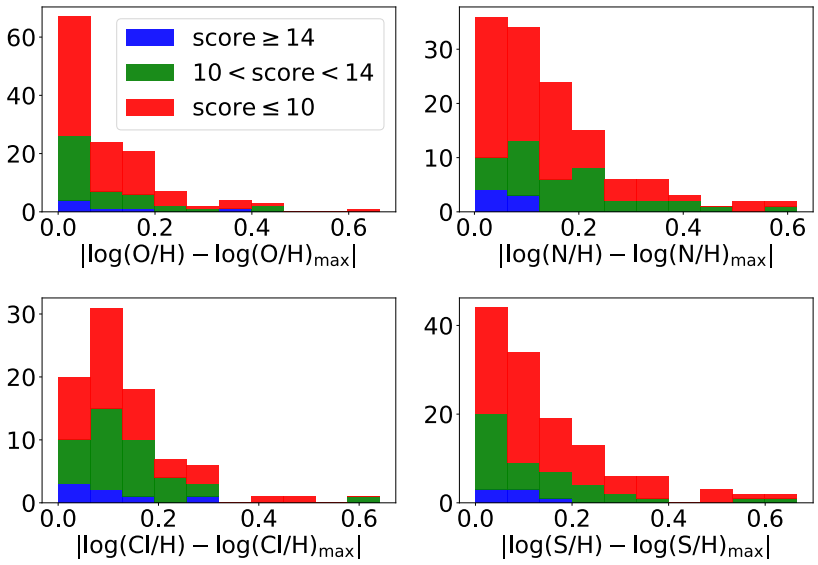

Figure 5. Absolute differences between the values of O/H, N/H, Cl/H, and S/H implied by different spectra (with their scores in colors) and those derived with the spectrum with the maximum score for each PN.

of recombination based on the recent calculations of recombination coefficients of Storey et al. (2017).
The correction for recombination of O^+/H^+ is smaller than 0.2 dex in most cases, but can go up to ~ 0.7 dex for the red [O II] lines, which could be analyzed in 156 of the 180 spectra. The correction affects the total oxygen abundance and, because most ionization correction factors use the ratio O^+/O^{++}, the abundances of nitrogen, chlorine, sulfur, argon, and neon. The effects are small in most cases, but can lead to changes of 0.5–0.6 dex in the abundances of nitrogen and sulfur when $\log(O^+/O^{++}) < -2.8$.
The differences in the O^+ abundances derived with either the blue or the red [O II] lines are larger than those introduced by the corrections for recombination, reaching factors of 6 in either direction. This indicates that the relative intensities of the blue and red lines are seriously wrong in some spectra. The differences in total abundances introduced by the use of the blue or the red [O II] lines are larger than the ones produced by the correction of recombination, especially for N/H, where they can easily reach a factor of 2 or more.
A score that should reflect the quality of the spectra has been assigned to each spectrum using the available density diagnostics, the [N II] $\lambda6583/\lambda6548$ and [O III] $\lambda5007/\lambda4959$ line ratios, and the behavior of the H I and He I lines. The disagreement between the O^+ abundance implied by the blue and red [O II] lines is shown to reflect and complement the scores derived using the previous considerations and will be added to the score-assignment scheme in the future.
A comparison between the abundances implied by the spectra with the highest score for each object and those implied by the other available spectra indicates that the observational uncertainties are near or below 0.2 dex in most cases, but can reach 0.6 dex or more. Since the PNe of this sample are the ones that can be most easily observed, the uncertainties will be larger for other samples.
Further results and more details on the procedure will be presented in Rodríguez (2019, in prep.).

Acknowledgments. I thank L. Juan de Dios, G. Domínguez Guzmán, J. Reyes Pérez, and K. Z. Arellano Córdova for their help at some stages of these calculations. I acknowledge support from Mexican CONACYT grant CB-2014-240562.

References

Delgado-Inglada G., Morisset C., Stasińska G., 2014, *MNRAS*, **440**, 536
Delgado-Inglada G., Rodríguez M., Peimbert M., Stasińska G., Morisset C., 2015, *MNRAS*, **449**, 1797
Ferland G. J., Chatzikos M., Guzmán F., Lykins M. L., van Hoof P. A. M., Williams R. J. R., Abel N. P., Badnell N. R., Keenan F. P., Porter R. L., Stancil P. C., 2017, *RevMexAA*, **53**, 385
Filippenko A. V., 1982, *PASP*, **94**, 715
García-Rojas J., Peña M., Morisset C., Mesa-Delgado A., Ruiz M. T., 2012, *A&A*, **538**, A54
Hyung S., Aller L. H., Feibelman W. A., Lee S.-J., 2001, *ApJ*, **563**, 889
Juan de Dios L., Rodríguez M., 2017, *MNRAS*, **469**, 1036

Liu X.-W., Storey P. J., Barlow M. J., Danziger I. J., Cohen M., Bryce M., 2000, *MNRAS*, **312**, 585
Luridiana V., Morisset C., Shaw R. A., 2015, *A&A*, **573**, A42
Mesa-Delgado A., Esteban C., García-Rojas J., Luridiana V., Bautista M., Rodríguez M., López-Martín L., Peimbert M., 2009, *MNRAS*, **395**, 855
Peimbert M., Costero R., 1969, *Boletín de los Observatorios Tonantzintla y Tacubaya*, **5**, 3
Porter R. L., Ferland G. J., Storey P. J., Detisch M. J., 2012, *MNRAS*, **425**, L28
Porter R. L., Ferland G. J., Storey P. J., Detisch M. J., 2013, *MNRAS*, **433**, L89
Rodríguez M., Delgado-Inglada G., 2011, *ApJL*, **733**, L50
Smette A., Sana H., Noll S., Horst H., Kausch W., Kimeswenger S., Barden M., Szyszka C., Jones A. M., Gallenne A., Vinther J., Ballester P., Taylor J., 2015, *A&A*, **576**, A77
Stasińska G., 2005, *A&A*, **434**, 507
Storey P. J., Hummer D. G., 1995, *MNRAS*, **272**, 41
Storey P. J., Sochi T., Bastin R., 2017, *MNRAS*, **470**, 379

Chemical Abundances in Gaseous Nebulae:
Open problems in Nebular astrophysics
AAA Workshop Series 11, 2019
M. Cardaci, G. Hägele & E. Pérez-Montero, eds.

Invited Review

Ionization correction factors for ionized nebulae

G. Delgado-Inglada[1], A. Medina-Amayo[1], and G. Stasińska[2]

[1]*Instituto de Astronomía, Universidad Nacional Autónoma de México, Mexico (email: gdelgado@astro.unam.mx)*
[2]*LUTH, Observatoire de Paris, CNRS, UniversitÈ Paris Diderot; Place Jules Janssen, F-92190 Meudon, France*

Abstract. In this paper we discuss the calculation of chemical abundances in planetary nebulae and H II regions through ionization correction factors (ICFs). We review the first ICFs proposed in the literature based on ionization potential similarities and we present the most recent ICFs derived from large sample of photoionization models. We also discuss some of the considerations that have to be kept in mind when using ICFs to compute the chemical composition of ionized nebulae.

Key words: galaxies: abundances — galaxies: ISM — ISM: abundances — planetary nebulae: general — H II regions

1. Introduction

The chemical abundances of planetary nebulae (PNe) and H II regions may be computed using different approaches (see, e.g., Stasińska, 2002; Peimbert et al., 2017). The so-called direct method consists of adding up all the ionic abundances of the ions present in the nebulae:

$$\frac{\mathrm{X}}{\mathrm{H}} = \frac{\mathrm{X}^{+}}{\mathrm{H}^{+}} + \frac{\mathrm{X}^{++}}{\mathrm{H}^{+}} + \frac{\mathrm{X}^{+3}}{\mathrm{H}^{+}} + ..., \tag{1}$$

and it requires to know the physical conditions: the electron temperature and density (T_e and n_e, respectively) in the regions where the different lines are emitted. When one cannot observe all the ions present in a nebula (either because the emission lines are too weak or because the observed wavelength range does not include all the involved lines), a correction must be made using ionization correction factors (ICFs):

$$\frac{\mathrm{X}}{\mathrm{H}} = \Sigma_{\mathrm{obs.}} \frac{\mathrm{X}^{+i}}{\mathrm{H}^{+}} \times \mathrm{ICF}, \tag{2}$$

where $\Sigma_{\mathrm{obs.}}$ represents the sum of all the ionic abundances that can be computed from observations. Therefore, ICFs account for the contribution of unobserved ions and they may be obtained from ionization potential similarities or from photoionization models (see Sections 2 and 3).

2. ICFs based on ionization potential similarities

The first ICFs were proposed 50 years ago. In the paper we are celebrating in this meeting, (Peimbert & Costero, 1969), the authors computed the total abundances of various elements in Orion, M8, and M17 based on ionization potential similarities. Three of the expressions proposed by these authors that are still commonly used to derive nitrogen, neon, and sulfur abundances are:

$$\mathrm{N/O} = \mathrm{N^+/O^+}, \tag{3}$$

$$\mathrm{Ne/O} = \mathrm{Ne^{++}/O^{++}}, \tag{4}$$

and

$$\mathrm{S/O} = (\mathrm{S^+ + S^{++}})/\mathrm{O^+}. \tag{5}$$

The ionization potentials of N^+, Ne^{++}, S^{++} are 29.6, 63.4, and 34.8 eV, and those of O^+ and O^{++} are 35.1 eV and 54.9 eV, respectively. The fact that N^+ and O^+, Ne^{++} and O^{++}, and S^{++} and O^+ have similar ionization potentials has been used to propose these simple ICFs.

Peimbert & Costero (1969) argued that the correction scheme was correct because the derived abundances in the three regions of Orion nebula studied by them were similar. But the observational basis was scarce at that time. Using recent photoionization models one finds that these simple expressions are not always valid and that new ICFs are needed to obtain more reliable abundances. Figure 1 illustrates this for neon and sulfur. It is obvious that the ICFs based on ionization potential similarities (represented by the solid line) lead to incorrect values of Ne/O and S/O in most of the cases. In particular, Equation 5 systematically overestimates S/O values whereas Equation 4 only provide reliable values of Ne/O for objects with $O^{++}/(O^+{+}O^{++}) \geq 0.6$.

3. ICFs based on photoionization models

The ICFs derived from photoionization models are, in principle, more reliable because photoionization codes include the physics involved in ionized nebulae (proper photoionization and recombination rates, charge transfer reactions) that may change the distributions of ions in nebulae. However, one must remember that the atomic physics included in photoionization codes can be incorrect and also that some of the assumptions made to construct the models may be too simplistic (for example, the real structure of nebulae may be different than the one assumed). ICFs from photoionization models have been derived by Kingsburgh & Barlow (1994); Delgado-Inglada et al. (2014) for planetary nebulae and by Mathis (1985); Stasińska (1978); Mathis & Rosa (1991); Gruenwald & Viegas (1992); Izotov et al. (2006); Dors et al. (2016) for H II regions.

A few years ago we started a project to obtain new ICFs for H II regions and PNe from large grids of photoionization models computed with CLOUDY (Ferland et al., 2013). The database generated is available at the web page `https://sites.google.com/site/mexicanmillionmodels/` and it was presented and described with detailed by Morisset et al. (2015).

Our approach is to compute analytical expressions for the ICFs that depend on $O^{++}/(O^+{+}O^{++})$ (and $He^{++}/(He^+{+}He^{++})$ for planetary nebulae). We have

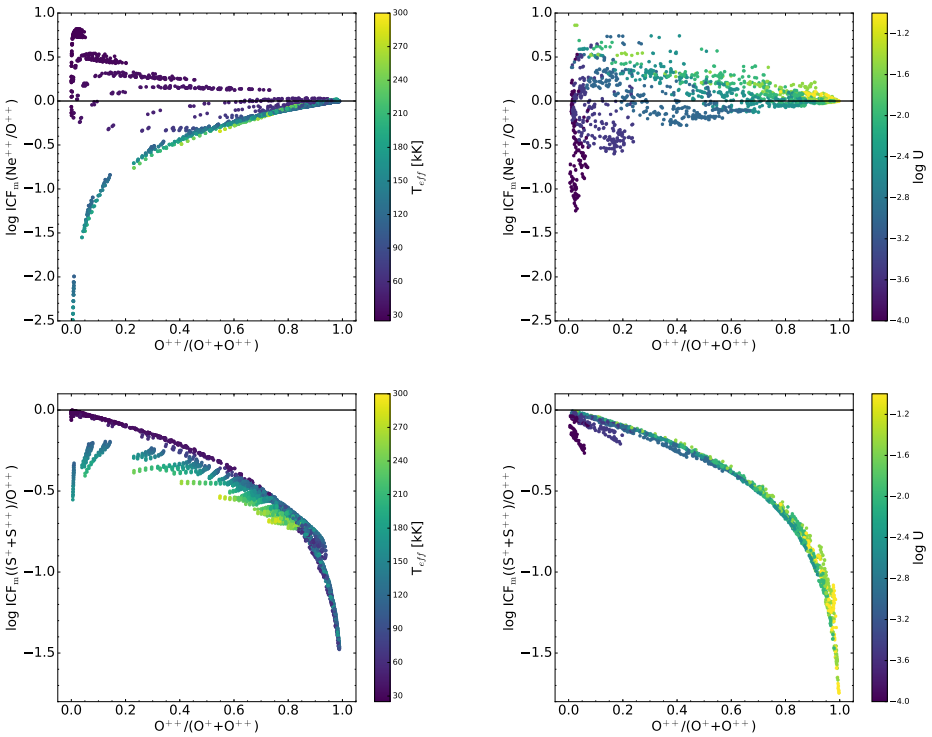

Figure 1. Values of $x(O^{++})/x(Ne^{++})$ (upper panels) and $x(O^+)/(x(S^+)+x(S^{++}))$ (lower panels) as a function of $O^{++}/(O^+{+}O^{++})$ for our sample of photoionization models representative of PNe (left panels) and extragalactic H II regions (right panels). The colorbars run from low lo high values of the effective temperature of the central star (for the PN models) and of the ionization parameter (for the extragalactic H II regions).

chosen these abundance ratios because they can be easily computed from strong emission lines. In total we computed ICFs for He, C, N, O, Ne, S, Cl, Ar, Ni, Na, K, and Ca to be used in PNe (Delgado-Inglada et al. 2014, 2016, Medina-Amayo et al. 2019a, in prep.) and for C, N, O, Ne, S, Cl, Ar to be used in extragalactic H II regions (Medina-Amayo et al. 2019b, in prep.).

4. ICFs for PNe

Delgado-Inglada et al. (2014) described the grid of photoionization models that has been used to derive new ICFs in PNe. The input parameters of the models cover a wide range of values so that the grid is representative of many observed PNe. For example, the grid covers from 25000 to 300000 K in effective temperature, from 3×10^{15} to 3×10^{18} cm in inner radius, from 30 to 300000 cm^{-3} in hydrogen density, and from 200 to 17800 $L_\odot$ in stellar luminosity. We have also

checked that changes in e.g., the chemical composition of the nebula, the density law of the gas, or the presence or absence of dust did not affect the ICFs derived. One strength of the ICFs derived by Delgado-Inglada et al. (2014) is that together with the analytical expressions of the ICFs we provide analytical expressions for the uncertainties associated with each ICF. In general these uncertainties are not taken into account and they may be not negligible. For example, the uncertainty in log(O/H), log(N/O), and log(Ar/H) associated to the ICF are ∼0.1, ∼0.2, and $\sim^{+0.18}_{-0.30}$ dex, respectively.

However, it must be noted that the grid of photoionization models considered was probably too extended for commonly observed planetary nebulae and the procedure to derive the uncertainties can be improved. A future study will revise the work by Delgado-Inglada et al. (2014).

5. ICFs for extragalactic H II regions

Medina-Amayo et al. (2019, in prep.) present new ICFs for C, N, Ne, S, Cl, and Ar adequate to compute chemical abundances in extragalactic H II regions. The sample of models was selected from the grid of photoionization models computed by Vale Asari et al. (2016) for giant H II regions. A large set of observations of extragalactic H II regions were used to constrain the sample of models from which the ICFs have been derived. It includes blue compact galaxies, giant H II regions, and galaxies from the Sloan Digital Sky Survey (Strauss et al., 2002). The data were taken from the same references used by Vale Asari et al. (2016) and also from Berg et al. (2013), Bresolin (2011a) and Bresolin (2011b). According to those observations, the sample was restricted in the N/O vs. O/H plane, the ionization parameter vs. O/H plane and the [O III] λ5007/Hβ vs. [N II] λ6584/Hβ plane. Fig. 2 shows the BPT diagram ([O III] λ5007/Hβ vs [N II] λ6584/Hβ) for the sample of models from Vale Asari et al. (2016, color dots, 31500 models) and for the sample of observations used by Medina-Amayo et al. (black dots, ∼133500 objects).

Medina-Amayo et al. performed fits to obtain the best possible ICFs. One improvement with respect to the ICFs obtained by Delgado-Inglada et al. (2014) is that Medina-Amayo et al. associated a weight to each model. To do this, the parameter space of Fig. 2 was divided in cells and a weight was associated to each model according to the number of observations in each cell (see Fig. 3). For example, a model located in a cell where there are no observations will have a very low weight whereas a model located in a cell where there are many observations will have a high weight.

The ICFs were computed by fitting analytical expressions to the models taking into account their weights. The use of the weights not only allows one to obtain a value of the ICFs more representative of the bulk of the observations but also to obtain more realistic expressions for their uncertainties. In principle, the weighted ICFs should be more adequate to obtain total abundances. Figure 4 shows the values of $x(O^{++})/x(Ne^{++})$ as a function of $O^{++}/(O^{+}+O^{++})$ for the weighted models.

The whole analysis and results for C, N, O, Ne, S, Cl, Ar will be presented by Medina-Amayo et al. (2019, in prep.).

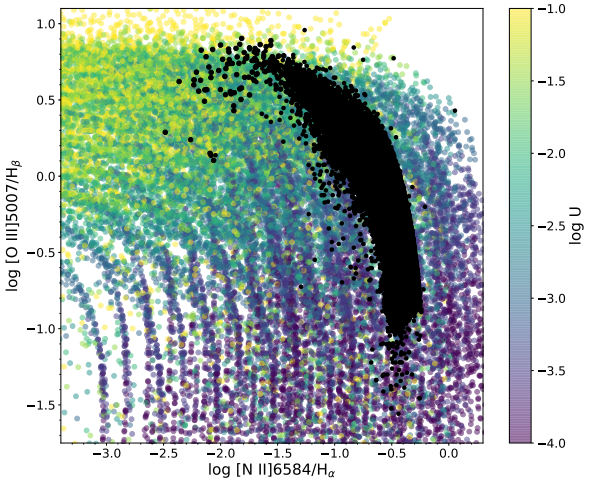

Figure 2. Values of [O III] λ5007/Hβ as a function of [N II] λ6584/Hβ (the BPT diagram). The color dots represent the initial sample of 31500 models from Vale Asari et al. (2016) whereas the black dots represent the observational sample of extragalactic H II regions (see the text for more details).

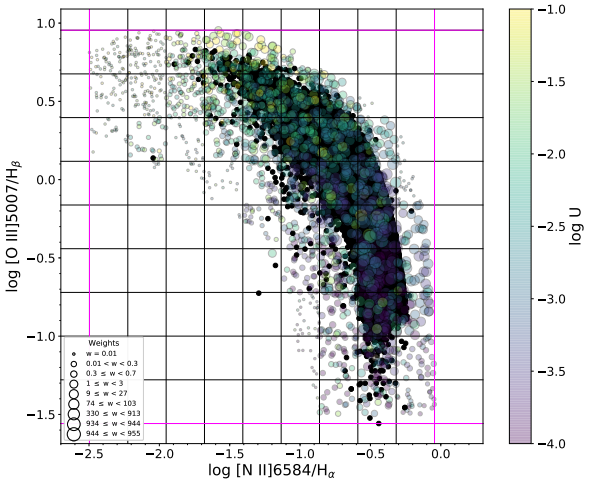

Figure 3. Values of [O III] λ5007/Hβ as a function of [N II] λ6584/Hβ (the BPT diagram). The parameter space is divided in cells. The color dots represent the weighted models (the size of the point is related to the weight) whereas the black dots represent the observed extragalactic H II regions.

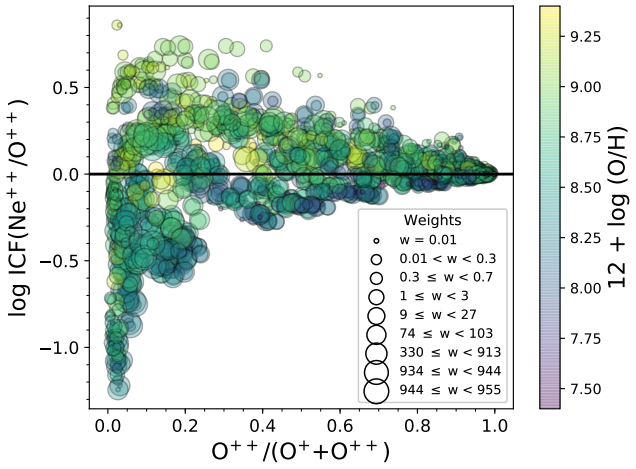

Figure 4. Values of $x(O^{++})/x(Ne^{++})$ as a function of $O^{++}/(O^{+}+O^{++})$ for our sample of weighted photoionization models representative of extragalactic H II regions. The colorbar runs from low lo high values of the O/H value. The black line represents where $x(O^{++})/x(Ne^{++}) = 1$ as assumed by the classical expression $Ne/O = Ne^{++}/O^{++}$.

6. Discussion about ICFs

A good ICF is one that does not introduce any bias or spurious trend in the derived abundances. One can use photoionization models to explore possible biases introduced by empirical ICFs based on ionization potential considerations. For example, from the grid of models presented in Sections 4 and 5 we obtain that using the expression $C/O = C^{++}/O^{++}$ may overestimate C/O values in up to 2.3 and 1.5 dex in PNe and H II regions, respectively, in low ionization nebulae (see Fig. 5).

Sometimes there is no obvious trend between the total abundances and the degree of ionization but an unexpected trend appears while using the derived abundances. This is the case for N/O. The ICF proposed by Delgado-Inglada et al. (2014) does not introduce any trend between N/O and $O^{++}/(O^{+}+O^{++})$. However, Delgado-Inglada et al. (2015) found that this ICF seems to introduce an artificial trend between N/O and He/H values in PNe and thus, it is preferable not to use it.

The ICF may be wrongly invoked as responsible for unexplained results. For example, Henry et al. (2004) suggested that the ICF is the most likely cause of the sulfur anomaly: the fact that, for the same O/H value, PNe systematically show lower S abundances than H II regions. However, Fig. 6 shows that using a different ICF (the one proposed by Delgado-Inglada et al. 2014) does not solve this problem so the explanation is likely different. This group of objects include Galactic PNe with C-rich dust, Galactic PNe with oxygen-rich dust, and a group of Galactic H II regions.

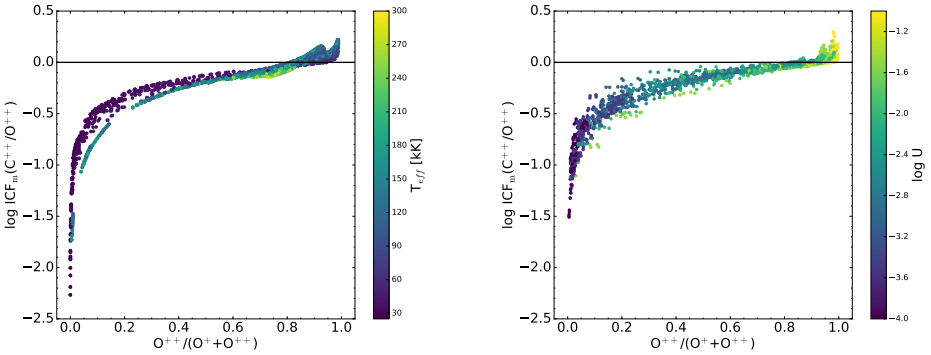

Figure 5. Values of $x(O^{++})/x(C^{++})$ as a function of $O^{++}/(O^{+}+O^{++})$ for our sample of photoionization models representative of PNe (left panel) and extragalactic H II regions (right panel). The colorbars run from low lo high values of the effective temperature of the central star (for the PN models) and of the ionization parameter (for the extragalactic H II regions).

In some cases one can compare abundances obtained using ICFs with those obtained by summing up all the ionic abundances of a given element. S. R. Pottasch and J. Bernard-Salas have done a lot of work in computing chemical abundances by directly adding individual ionic abundances (without using an ICF) of PNe from infrared, ultraviolet, and optical spectra (see, e.g., Pottasch & Bernard-Salas, 2008; Pottasch et al., 2009a,b, 2011). However, uncertainties associated with corrections for aperture effects may not be negligible.

Rodríguez & Rubin (2005) computed iron abundances in a group of PNe and H II regions by 1) adding up the ionic abundances of Fe^{+}, Fe^{++}, and Fe^{+3} obtained from the emission lines of [Fe II] (in some cases), [Fe III], and [Fe IV] and 2) by using Fe^{+} and Fe^{++} abundances and a theoretical ICF derived by them from photoionization models. They found a significant discrepancy between the empirical and theoretical ICF and concluded that the most likely explanation for this discrepancy is the inadequacy of some of the atomic data of iron.

Esteban et al. (2015) computed chlorine abundances in a group of Galactic H II regions directly by adding up the abundances of Cl^{+}, Cl^{++}, and Cl^{+3} and provide an empirical ICF. We illustrate in Figure 7 the values of $x(O^{+})/x(Cl^{++})$ as a function of $O^{++}/(O^{+}+O^{++})$ for our sample of extragalactic H II region models (color dots) and also for the group of H II regions studied by Esteban et al. (2015) (red stars). It is clear that a fit to the models will lead to an ICF (and hence, a Cl/O value) somewhat higher than a fit to the observations. One possibility is that photoionization models are not completely adequate to describe ionization structure of Galactic H II regions but another possibility is that the ionic abundances computed from observations are not correct (for example, because of using an incorrect T_e, see papers by Rodríguez and Domínguez-Guzmán et al. in these proceedings). Therefore, still some work has to be done with models and observations to find the best ICF for each element.

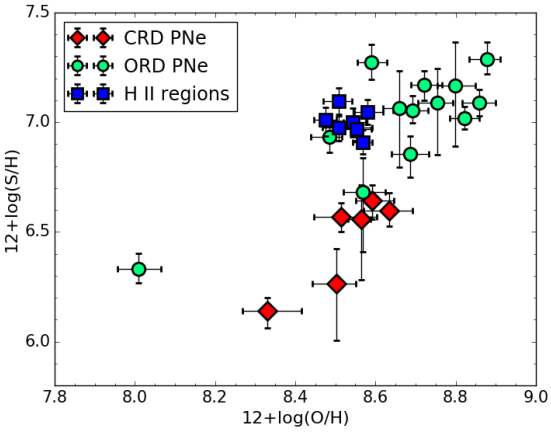

Figure 6. Values of S/H as a function of O/H for the sample of PNe and H II regions studied by (Delgado-Inglada et al., 2015). The red diamonds represent PNe with C-rich dust, the green circles represent those with oxygen-rich dust, and the blue squares represent a group of Galactic H II regions.

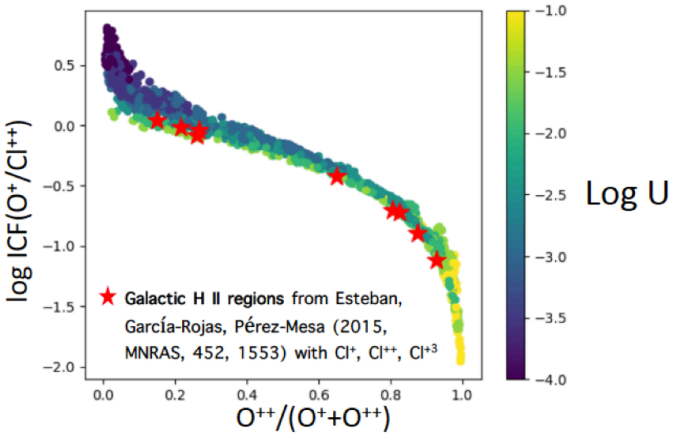

Figure 7. Values of $x(O^+)/x(Cl^{++})$ as a function of $O^{++}/(O^+{+}O^{++})$ for the sample of models representative of extragalactic H II regions (color dots). The red stars represent a group of Galactic H II regions observed by Esteban et al. (2015) where Cl^+, Cl^{++}, and Cl^{+3} can be computed to obtain the empirical ICF for chlorine. The colorbar runs from low lo high values of the ionization parameter.

7. Conclusions

We want to end by mentioning again that ICFs are essential to compute the abundances of many elements (the only alternative is to compute a detailed photoionization model). In principle, ICFs derived from photoionization models should be better than empirical ones based on ionization potential considerations because photoionization codes include all the relevant physics involved in ionized nebulae. However, there are a few considerations that have to be kept in mind. Theoretical ICFs rely on idealized photoionization models whose structure may be different from real objects, on atomic data which may be incomplete and sometimes incorrect, and on a description of the ionizing radiation field which relies on stellar atmosphere models and hypotheses regarding the distribution of stellar masses and ages in the case of giant H II regions. Observations may help to test and refine theoretical ICFs. However, the ionic abundances derived from observations have their own problems, as shown in several contributions to these proceedings.

Acknowledgments. G. D. I. wants to thank the organizers of this event for inviting her to give this talk and to all the participants for making this workshop very fruitful. The authors would like to thank support from PAPIIT (DGAPA-UNAM) grant no. IA-101517 and CONACyT grants 241732 and 254132.

References

Berg D. A., Skillman E. D., Garnett D. R., Croxall K. V., Marble A. R., Smith J. D., Gordon K., Kennicutt Jr. R. C., 2013, *ApJ*, **775**, 128
Bresolin F., 2011a, *ApJ*, **729**, 56
Bresolin F., 2011b, *ApJ*, **730**, 129
Delgado-Inglada G., Mesa-Delgado A., García-Rojas J., Rodríguez M., Esteban C., 2016, *MNRAS*, **456**, 3855
Delgado-Inglada G., Morisset C., Stasińska G., 2014, *MNRAS*, **440**, 536
Delgado-Inglada G., Rodríguez M., Peimbert M., Stasińska G., Morisset C., 2015, *MNRAS*, **449**, 1797
Dors O. L., Pérez-Montero E., Hägele G. F., Cardaci M. V., Krabbe A. C., 2016, *MNRAS*, **456**, 4407
Esteban C., García-Rojas J., Pérez-Mesa V., 2015, *MNRAS*, **452**, 1553
Ferland G. J., Porter R. L., van Hoof P. A. M., Williams R. J. R., Abel N. P., Lykins M. L., Shaw G., Henney W. J., Stancil P. C., 2013, *RevMexAA*, **49**, 137
Gruenwald R. B., Viegas S. M., 1992, *ApJS*, **78**, 153
Henry R. B. C., Kwitter K. B., Balick B., 2004, *AJ*, **127**, 2284
Izotov Y. I., Stasińska G., Meynet G., Guseva N. G., Thuan T. X., 2006, *A&A*, **448**, 955
Kingsburgh R. L., Barlow M. J., 1994, *MNRAS*, **271**, 257
Mathis J. S., 1985, *ApJ*, **291**, 247
Mathis J. S., Rosa M. R., 1991, *A&A*, **245**, 625
Morisset C., Delgado-Inglada G., Flores-Fajardo N., 2015, *RevMexAA*, **51**, 103
Peimbert M., Costero R., 1969, *Boletin de los Observatorios Tonantzintla y Tacubaya*, **5**, 3

Peimbert M., Peimbert A., Delgado-Inglada G., 2017, *PASP*, **129(8)**, 082001
Pottasch S. R., Bernard-Salas J., 2008, *A&A*, **490**, 715
Pottasch S. R., Bernard-Salas J., Roellig T. L., 2009a, *A&A*, **499**, 249
Pottasch S. R., Surendiranath R., Bernard-Salas J., 2011, *A&A*, **531**, A23
Pottasch S. R., Surendiranath R., Bernard-Salas J., Roellig T. L., 2009b, *A&A*, **502**, 189
Rodríguez M., Rubin R. H., 2005, *ApJ*, **626**, 900
Stasińska G., 1978, *A&A*, **66**, 257
Stasińska G., 2002, *arXiv Astrophysics e-prints*
Strauss M. A., Weinberg D. H., Lupton R. H., Narayanan V. K., Annis J., Bernardi M., Blanton M., Burles S., Connolly A. J., Dalcanton J., Doi M., Eisenstein D., Frieman J. A., Fukugita M., Gunn J. E., Ivezić Ž., Kent S., Kim R. S. J., Knapp G. R., Kron R. G., Munn J. A., Newberg H. J., Nichol R. C., Okamura S., Quinn T. R., Richmond M. W., Schlegel D. J., Shimasaku K., SubbaRao M., Szalay A. S., Vanden Berk D., Vogeley M. S., Yanny B., Yasuda N., York D. G., Zehavi I., 2002, *AJ*, **124**, 1810
Vale Asari N., Stasińska G., Morisset C., Cid Fernandes R., 2016, *MNRAS*, **460**, 1739

Chemical Abundances in Gaseous Nebulae:
Open problems in Nebular astrophysics
AAA Workshop Series 11, 2019
M. Cardaci, G. Hägele & E. Pérez-Montero, eds.

Invited Review

Can we believe the strong-line abundances in giant H II regions and emission-line galaxies?

Grażyna Stasińska [1]

[1] *LUTH, CNRS, Observatoire de Paris, PSL University, France*

Abstract. This review is not a compendium of strong-line methods to derive abundances in giant H II regions. It is mostly intended for readers who wish to use such methods but do not have a solid background on the physics of H II regions. It is also meant to encourage those using abundance results published in the literature to think more thoroughly about the validity of these results.

Key words: galaxies: abundances — galaxies: ISM — techniques: spectroscopy

1. Introduction

The knowledge of the chemical composition of the interstellar medium of galaxies is fundamental for our understanding of their chemical evolution. The royal way to derive the chemical abundances of the elements is considered to be the use of the so-called direct method, which is based on the use collisionally excited emission lines to compute the gaseous elemental abundances with respect to hydrogen. It involves the measurement of the physical conditions (temperature and electron density distribution) in the emitting plasma. This method requires accurate measurements of weak temperature-sensitive lines, reliable atomic data involved in the procedure, reliable ionisation correction factors for unobserved ions and an estimate of the element depletion in dust grains. The major problem lies in the fact that abundances derived from optical recombination lines in H II regions are larger than those derived from collisionally excited lines typically by a factor of two. This decades-old problem has so far no generally accepted solution. Until it is solved, element abundances in H II regions cannot be regarded as completely secure, even if important progress has been achieved at all steps of the procedure to derive them.

The so-called strong line methods to determine abundances in giant H II regions appeared in 1979. Pagel et al. (1979) and Alloin et al. (1979) were the first to propose quantitative estimates of the oxygen abundance in absence of detailed plasma diagnostics, by extrapolating observed trends between strong line ratios and oxygen abundance using the few relevant photoionisation models available at that time. Since then, with the help of extent photoionisation model grids, nu-

merous high quality observations confirmed that giant H II regions form basically a one-parameter sequence driven by their 'metallicity'[1].
One could have thought that, with the continuously improving quality of H II region spectra, strong-line methods would become obsolete. The reverse is happening, due to the deluge of spectroscopic data for H II regions in close-by galaxies as well as in high-redshift galaxies. Most of the time, these data either are of insufficient spectral resolution and signal-to-noise to provide a reliable determination of electron temperatures (especially at high metallicities) or they cover a very limited wavelength range allowing the measurement of only a few selected strong lines.
The purpose of this presentation is not to review the many strong-line methods that are nowadays available as these have been amply presented in the literature (see e.g. Stasińska et al., 2012; Bianco et al., 2016; Maiolino & Mannucci, 2019), but rather to draw attention to problems worth remembering. Due to space limitations, references in this text are kept to a minimum, and I apologise to all those who contributed to the subject and do not have their work quoted here. More complete sets of references are given in the papers mentioned above.

2. Strong line methods: the idea

Since, in giant H II regions, strong-line intensity ratios have been shown to present some trends with abundances derived from temperature-based methods, the idea came up that strong lines alone would be sufficient to derive the metallicities[2]. This is true – only statistically, of course – provided some caution is exercised. The first difficulty is that *any* ratio of the kind I_C/I_R where I_C is the intensity of a collisionally excited line and I_R that a hydrogen recombination line is double-valued with respect to metallicity. One thus has to choose which of the two regimes – high or low metallicity – is appropriate for the object under study. The choice is either based on external arguments (e.g. H II regions in the central parts of galaxies are supposed to be metal-rich, low-mass star-forming galaxies are supposed to be metal-poor, etc.) or on an argument based more or less directly on the N/O ratio (expected to be large at high metallicities). The second difficulty is that H II regions do not strictly form a one-parameter sequence. While it has been shown that there is a relation between the metallicity, the hardness of the ionising radiation field and the mean ionisation parameter of the H II regions – which are the main parameters determining their spectrum – the relation likely suffers some dispersion. For example, giant H II regions of same metallicity can be ionised by star clusters of different ages. In addition, other parameters (nebular geometry, dust content, ionising photon leakage, etc.) also play a role, even if not dominant. Their role should be evaluated, especially when one is looking for metallicity differences between two classes of similar objects. For example H II regions in spiral arms versus H II regions between spiral arms.

---

[1]In the following, the term 'metallicity' will be used to designate the oxygen abundance, as is ubiquitously the case in the literature on the subject.

[2]We neglect the issue of reddening which can easily be accounted for if both Hα and Hβ are measured.

3. The importance of calibration

Any strong-line method needs to be calibrated, either using data sets with abundances from direct methods, or using photoionisation models, or a combination of both.

If based on observations, the calibrating sample must represent well the *entire* family of H II regions to be studied. For example, calibrations based on local, high-density H II regions should no be used for giant H II regions. Calibrations based on giant H II regions should not be used to derive the global metallicity of large portions of galaxies, such as observed in the Sloan Digital Sky Survey.

One of the drawbacks of observational calibrations is that the weak emission lines needed to determine the electron temperature cannot be observed at very high metallicities because of their strong dependence on the excitation energy[3]. In addition, it is likely that the calibration samples are biased towards the highest temperatures at a given metallicity. The recent use of stacked spectra of emission-line galaxies allows one to obtain high signal-to-noise ratios even for very weak lines (Liang et al., 2007; Andrews & Martini, 2013; Curti et al., 2017; Bian et al., 2018) and opens the way to observational calibrations for high metallicities but the results may depend on the stacking parameters, which have to be carefully chosen, as shown by Brown et al. (2016).

Using model grids, one is free from the selection biases mentioned above since photoionisation models can be produced at any metallicity. But photoionisation models are a simplified representation of reality and require ingredients that are not fully known. For example, the spectral energy distribution of the ionising radiation relies on stellar atmosphere models which are difficult to validate observationally, as well as on a correct description of the stellar initial mass function and stellar evolution, for which rotation and the effect of binarity have been introduced only recently. The geometrical distribution of the nebular gas does play a role which is generally ignored. The ratios of elemental abundances with respect to oxygen are not constant: some dispersion is expected, especially for nitrogen and carbon, since their production sites are not identical. The presence of dust grains affects both the chemical composition of the gas phase and the line emission – either directly (because of depletion) or indirectly (because of the effect of grains on the ionization structure and on the nebular temperature). Calibrations based on different grids of models may lead to different results.

Finally, the role of atomic data cannot be ignored. They play a crucial role in direct abundance determinations as well as in photoionisation models. Even recently, some important atomic data have suffered changes (e.g. the collision strengths for [O III] by Palay et al. (2012), later revised by Storey et al. (2014) and Tayal & Zatsarinny (2017).

[3]Even when [O III]λ4363 can be measured but is very weak, it may lead to a completely wrong temperature diagnostic for the entire O^{++}zone, as shown by Stasińska (2005).

4. Various approaches

4.1. Indices

The easiest way to obtain metallicities from strong lines is to use analytic expressions based on some indices, such as the famous ([O III] + [O II])/Hβ (Pagel et al., 1979) or [O III]/[N II] (Alloin et al., 1979) (which have been recalibrated many times). This method is still being used because of its simplicity and minimal observational requirements. Other indices have been also proposed since then. However, it must be kept in mind that methods based on indices are especially prone to biases which may lead to erroneous astronomical inferences.
This method has been extended to the use of two indices to account for a second parameter (namely the ionisation level) that influences the H II regions spectra (McGaugh, 1994; Pilyugin, 2001). It is customary to compute the error bars taking into account *only* the uncertainties in the line intensities and not the intrinsic statistical uncertainty of the method.

4.2. Interpolation

A more elaborate way to obtain abundances from strong lines is to use an iterative approach to interpolate in a grid of models (e.g. Kewley & Dopita, 2002). In this very paper, the uncertainties are evaluated by comparison of results using several methods.
An even more sophisticated approach is to interpolate within a grid by χ^2 minimization or a related technique using selected line ratios (e.g. Charlot et al., 2002; Pérez-Montero, 2014).
Instead of a grid of models, one can also use real objects for which direct abundances are available, based on the assumption that 'H II regions with similar intensities of strong emission lines have similar physical properties and abundances' (Pilyugin et al., 2012) – which is not entirely true.

4.3. Bayesian methods

A common belief is that, when many lines are used (i.e. not only the few classical strong lines such as [O III], [O II], [N II] with respect to Hα or Hβ) the resulting abundances will be more accurate. This is not necessarily correct. Considering additional lines from other elements may give more information on the physical conditions of the nebulae, but at the same time introduce a dependence on abundance ratios that are not varied in the reference grid of models. In addition, lines such as [S II], [Ne III], [Ar III], [S III] being often relatively weak may add noise or biases to the procedure. Nevertheless, a treatment of the available information in a Bayesian framework may lead to reliable inferences Chevallard & Charlot (2016). Bayesian methods are becoming more and more popular to determine chemical abundances (Blanc et al., 2015; Vale Asari et al., 2016; Thomas et al., 2018). However it is important to realise that each author uses his own philosophy and the results – including the characterisation of the uncertainties – depend on the priors.

4.4. Machine learning

The next step, which has already been taken, is to use machine learning techniques to derive abundances – together with other properties (Ucci et al., 2017, 2018, 2019; Ho, 2019). Such techniques try to make the best use of the information encoded in the observational data by considering not only some pre-selected emission lines, but the entire observation set – without necessarily understanding the underlying physics. Machine learning techniques are widely used in many areas of science – including human sciences – when analysing huge amounts of data which depend on a large number of parameters whose role is not fully understood and which are sometimes not even identified. It is not clear what is their advantage in the case of abundance determinations except, perhaps, their ability to treat a colossal amount of data in a short time. Regarding nebulae and their chemical composition, we know, in principle, what governs the production of the emission lines and even what are the steps undergone by the photons generated in the nebulae before being recorded by our observational devices. In fact, machine learning approaches which ignore the physics of the studied phenomena may lead to very strange inferences. For example in the on-line accompanying data of the study by Ucci et al. (2018), it is stated that 'the 6 most informative features are lines connected to H and He transitions (i.e. Hβ, Hδ, He Iλ5876) and 3 metals lines (i.e. [O II]λ3726 + λ3729, [Ne III]λ3869, and [Ar III]λ7135). [...] the two most informative lines, Hδ and [Ar III]λ7135, sum up to over 40% of the total feature importance'. Such a statement will of course puzzle anyone familiar with the physics of nebulae!

5. Biases, misinterpretations and mistakes

The fact that strong-line methods have become more and more sophisticated over the years should not prevent us from keeping a critical eye on their results and on their astrophysical inferences: a blind confidence is not recommended.

5.1. Very indirect abundance estimates

The real relation between N/O and O/H is the interstellar medium of galaxies is in itself important to know for understanding the production conditions of nitrogen and the chemical history of galaxies Mollá & Gavilán (2010). But it is also critical for a proper determination of the oxygen abundance in most strong-line methods. For example, the [N II]/[O II] index promoted by Kewley & Dopita (2002) to estimate O/H is actually directly related to N/O. The same is true for the [O III]/[N II] index, although the latter is also linked to the excitation state of the nebula which, empirically, is linked to metallicity. Even in the case when the metallicity derivation is based on a library of models, the assumed N/O versus O/H relation plays an important role. This has already been mentioned (Section 5.3) for the oxygen abundances based on the grid of Charlot & Longhetti (2001) but is also true for many other works (Dopita et al., 2016, see e.g.). So far, N and O are considered independently only in the grids of Pérez-Montero (2014) and Vale Asari et al. (2016).

5.2. Models are not perfect

Photoionisation models composing the grids are based on very simple geometries for the gas and the dust. Their predicted [O III]λ4363/[O III]λ5007 line ratios are often smaller than observed (this explains why strong-line methods often give larger abundances that temperature-based methods). This may be due to a density distribution that is too schematic, but also to an input assumed spectral energy distribution (SED) of the ionising photons that is too soft, or to the presence of temperature inhomogeneities of unknown nature. Note that the long-lasting problem of the presence of He II lines in metal-poor H II regions seems to be solved by the presence of high-mass X-ray binaries (not yet routinely considered in most models for giant H II regions) although contributions from shocks are not excluded (Schaerer et al., 2019).
Another problem is that, so far, strong-line methods based on model grids consider only ionisation-bounded cases while photon leakage from star-forming complexes is now well-documented. This issue should be considered for giant H II regions although, in the case of integrated observations of emission-line galaxies, one also need to consider the diffuse ionised medium (see Sect. 6).

5.3. Gigantic grids are not sufficient

In methods based on large model grids, one may think that the grids are so extensive that they encompass all the possible situations. This is far from true. If the grid does not include a reasonable representation of *all* that is seen in nature, the abundance results may be biased.
For example, the oxygen abundances derived by Tremonti et al. (2004) based on a library of 2×10^5 models by Charlot & Longhetti (2001) were shown by Liang et al. (2007) to be strongly overestimated at the high metallicity end. Their library assumed a unique value of N/O for all metallicities and the fitting was made with a χ^2 technique summing on all the available strong lines, so that a mismatch of the [N II]/Hα ratio between observations and models required a modification of the O/H ratio.
Abundances derived from model grids can be incorrect just because the method is inadequate. For example, Fig. C4 in Vale Asari et al. (2016) demonstrates that the HII-CHI-MISTRY code by Pérez-Montero (2014) may give erroneous oxygen abundances when excluding [O III]λ4363 from the fitting procedure.

5.4. Fake relations

Empirical expressions to derive abundances from line ratios can artificially reduce an intrinsic scatter. This is exemplified in Fig. C5 of Vale Asari et al. (2016) in the case of the ON calibration from Pilyugin et al. (2012). When applied to a sample models where N/O and O/H are loosely correlated, the ON calibration tightens the resulting relation significantly.
Using the HII-CHI-MISTRY code for spaxel-analysis of integral-field spectroscopic observations of the blue compact dwarf galaxy NGC 4670 Kumari et al. (2018) find that N/O anti-correlates with O/H. This result is in clear contrast with previous studies on the behaviour of N/O versus O/H, and likely stems from the fact that the observational uncertainties are very large leading to an apparent anti-correlation between N/O and O/H.

As a matter of fact, some of the methods to obtain the metallicity are *only indirectly* linked to this parameter. They work just because, in astrophysical situations, other parameters are related to metallicity. This is the case of the [N II]/[O II] ratio mentioned above, or of [N II]/Hα (Denicoló et al., 2002). The latter is very convenient because it requires only a very narrow spectral range and does not depend on reddening. But its is essentially driven by N/O and the nebular excitation – which both happen to be astrophysically related to the metallicity.

5.5. Degeneracies

Because the ratio of collisional and recombination lines is degenerate with respect to metallicity, a way must be found to distinguish high metallicity from low metallicity objects. As mentioned in Section 2, this is generally done using arguments of astrophysical nature. The fact that N and O follow a different chemical evolution in galaxies is obviously of great help. However, there may be outliers, and those can be of particular astrophysical interest. In their bayesian approach BOND, Vale Asari et al. (2016) devised a way to find whether an object is oxygen-rich or oxygen-poor, independently of N/O. It relies on the semi-strong lines [Ne III]λ3869 and [Ar III]λ7135 whose ratio depends strongly on the electron temperature and weakly on ionisation conditions and abundance ratio. Indeed, the [Ar III]λ7135 and [Ne III]λ3869 lines have different excitation thresholds (1.7 and 3.2 eV, respectively), therefore different dependencies on the electron temperature; argon and neon are two primary elements and both are rare gases not suspected of dust depletion, so their abundance ratio in the gas phase is expected to be constant. The [Ar III]λ7135 and [Ne III]λ3869 lines do not arise exactly from the same zone, the ionisation potentials of the parent ions being different, but the [O III]/[O II] ratio helps figuring out what the ionisation is. BOND allows for a possible small deviation of Ne/Ar from the standard cosmic value by applying appropriate weights to their lines.
It must be noted, however, that BOND will probably not work correctly in the case of large observational errors in the strong line fluxes (say 20 percent).

5.6. The problem when comparing two samples and the role of the hardness of the SED

Some claims about the metallicity and its connexion with other galaxy properties could be wrong by actually arising from the fact that different physical conditions in the galaxies – not accounted for in the method used to obtain the metallicity – mimic a change in abundance. Such could be the case for the surprising finding by Sánchez Almeida et al. (2009) that oxygen abundances are larger in galaxies with older starbursts. As showed by Stasińska (2010) this could be due to a wrong interpretation of the [N II]/Hα index in terms of just oxygen abundance while it is primarily dependent on the hardness of the ionising radiation field which softens with age due to the gradual disappearance of the most massive stars. Similarly, the claim that luminous infrared galaxies (LIRGs) have smaller metallicities than local star-forming galaxies (Rupke et al., 2008) should be reexamined having in mind that the hardness of the ionising radiation is likely different in the two categories of galaxies. The same can be said about the claim that metallicity gradients flatten in colliding systems (see e.g. Kewley et al., 2010). So far, only

the BOND method of Vale Asari et al. (2016) determines the oxygen abundance trying to account for the characteristics of the ionising radiation field. The semi-strong line He Iλ5876 plays a key role in the process.

5.7. Do we get what we want?

In a recent study using neural networks to obtain galaxy metallicity from three-colour images, Wu & Boada (2019) suggest that their approach has 'learned a representation of the gas-phase metallicity, from the optical imaging, beyond what is accessible with oxygen spectral lines'. This *a priori* surprising statement is based on the fact that with their method they find a mass-metallicity relation for galaxies that is tighter than the one derived by Tremonti et al. (2004). They further comment that possibly their method 'is measuring some version of metallicity that is more fundamentally linked to the stellar mass, rather than [the metallicity] derived from oxygen spectral lines'. Indeed, galaxy colours are not only determined by the metallicities of their stellar populations (which are different from the metallicities of their interstellar medium) but also by their ages, and both are known to be correlated with stellar mass. This interesting case should incite us to remain cautious about the interpretation of the oxygen abundance determined by any method: is it really the present-day oxygen abundance that is being measured or something else related to it?

6. Metallicities of entire galaxies and the importance of the DIG

While the methods to derive the chemical composition of the ionised interstellar medium were developed for giant H II regions, they are often applied to entire galaxies or, at least, to a large fraction of their volume (e.g Tremonti et al., 2004; Mannucci et al., 2010). This is not only because observations are now available for galaxies at high redshifts. The 'characteristic' metallicity of a galaxy is an important constraint for chemical evolution models. Past studies have tried to determine it in nearby galaxies from the study of their H II regions (Zaritsky et al., 1994; Moustakas & Kennicutt, 2006).

Integrated spectra of galaxies combine the spectra of hundreds of H II regions of various sizes, ages and metallicities. They also contain emission from the diffuse ionized gas (DIG), whose characteristics are different from those of *bona fide* H II regions (Lacerda et al., 2018). Integral field spectroscopy of nearby galaxies (etc CALIFA, MANGA, SAMI, MUSE) now allow one to investigate these issues and try to find ways to account for them for a proper characterisation of the metallicity of nearby and distant galaxies.

The existence of a diffuse component in the ionised medium of galaxies has been acknowledged several decades ago (Reynolds, 1990; Hoopes et al., 1999). On the basis of a sample of about 100 H I selected galaxies it has been claimed that diffuse Hα emission constitutes roughly 60 per cent of the total Hα emission, irrespective of the Hubble type (Oey et al., 2007). In a more detailed study of 391 galaxies from the CALIFA survey (Sánchez, 2012), Lacerda et al. (2018) have shown that the DIG is quite complex. Regions with the lowest equivalent widths of Hα (called hDIG) are likely ionised by hot low-mass evolved stars (HOLMES) while diffuse zones with Hα equivalent widths between 3 and 14 Å (dubbed mDIG) are rather ionised by radiation leaking out from star-forming complexes

(SFc). The hDIG, mDIG, and SFc contributions to the total Hα luminosity vary systematically along the Hubble sequence, ranging from about (100, 0, 0) per cent in ellipticals and S0's to (9, 60, 31) per cent in Sa–Sb's and (0, 13, 87) per cent in later types.
Based on resolved spectroscopic observations of nearby galaxies, a few studies are starting to investigate the effect of the DIG on the abundance determination from emission lines in galaxies (Sanders et al., 2017; Kumari et al., 2019; Erroz-Ferrer et al., 2019).

7. Conclusion

While strong-line methods are routinely used to estimate the metallicities of giant H II regions as well as the characteristic of metallicities of local and high-redshift emission-line galaxies, one can easily be fooled by their apparent simplicity. Even the latest more sophisticated approaches involve a certain degree of approximation. The purpose of this text was to draw attention to some pitfalls and to encourage astronomers to consider their results with appropriate caution.

Acknowledgments. I thank the organisers for their kind invitation and deeply acknowledge financial support from FAPESP (processo 11/51680-6) which allowed me to participate in the workshop.

References

Alloin D., Collin-Souffrin S., Joly M., Vigroux L., 1979, *A&A*, **78**, 200
Andrews B. H., Martini P., 2013, *ApJ*, **765(2)**, 140
Bian F., Kewley L. J., Dopita M. A., 2018, *ApJ*, **859(2)**, 175
Bianco F. B., Modjaz M., Oh S. M., Fierroz D., Liu Y. Q., Kewley L., Graur O., 2016, *Astronomy and Computing*, **16**, 54
Blanc G. A., Kewley L., Vogt F. P. A., Dopita M. A., 2015, *ApJ*, **798(2)**, 99
Brown J. S., Martini P., Andrews B. H., 2016, *MNRAS*, **458(2)**, 1529
Charlot S., Kauffmann G., Longhetti M., Tresse L., White S. D. M., Maddox S. J., Fall S. M., 2002, *MNRAS*, **330(4)**, 876
Charlot S., Longhetti M., 2001, *MNRAS*, **323(4)**, 887
Chevallard J., Charlot S., 2016, *MNRAS*, **462(2)**, 1415
Curti M., Cresci G., Mannucci F., Marconi A., Maiolino R., Esposito S., 2017, *MNRAS*, **465(2)**, 1384
Denicoló G., Terlevich R., Terlevich E., 2002, *MNRAS*, **330(1)**, 69
Dopita M. A., Kewley L. J., Sutherland R. S., Nicholls D. C., 2016, *Ap&SS*, **361**, 61
Erroz-Ferrer S., Carollo C. M., den Brok M., Onodera M., Brinchmann J., Marino R. A., Monreal-Ibero A., Schaye J., Woo J., Cibinel A., Debattista V. P., Inami H., Maseda M., Richard J., Tacchella S., Wisotzki L., 2019, *MNRAS*, **484(4)**, 5009
Ho I. T., 2019, *MNRAS*, **485(3)**, 3569
Hoopes C. G., Walterbos R. A. M., Rand R. J., 1999, *ApJ*, **522(2)**, 669
Kewley L. J., Dopita M. A., 2002, *ApJS*, **142(1)**, 35

Kewley L. J., Rupke D., Zahid H. J., Geller M. J., Barton E. J., 2010, *ApJ*, **721(1)**, L48
Kumari N., James B. L., Irwin M. J., Amorín R., Pérez-Montero E., 2018, *MNRAS*, **476(3)**, 3793
Kumari N., Maiolino R., Belfiore F., Curti M., 2019, *MNRAS*, **485(1)**, 367
Lacerda E. A. D., Cid Fernandes R., Couto G. S., Stasińska G., García-Benito R., Vale Asari N., Pérez E., González Delgado R. M., Sánchez S. F., de Amorim A. L., 2018, *MNRAS*, **474(3)**, 3727
Liang Y. C., Hammer F., Yin S. Y., Flores H., Rodrigues M., Yang Y. B., 2007, *A&A*, **473(2)**, 411
Maiolino R., Mannucci F., 2019, *A&A Rev.*, **27(1)**, 3
Mannucci F., Cresci G., Maiolino R., Marconi A., Gnerucci A., 2010, *MNRAS*, **408(4)**, 2115
McGaugh S. S., 1994, *ApJ*, **426**, 135
Mollá M., Gavilán M., 2010, *MemASI*, **81**, 992
Moustakas J., Kennicutt Robert C. J., 2006, *ApJ*, **651(1)**, 155
Oey M. S., Meurer G. R., Yelda S., Furst E. J., Caballero-Nieves S. M., Hanish D. J., Levesque E. M., Thilker D. A., Walth G. L., Bland-Hawthorn J., Dopita M. A., Ferguson H. C., Heckman T. M., Doyle M. T., Drinkwater M. J., Freeman K. C., Kennicutt R. C. J., Kilborn V. A., Knezek P. M., Koribalski B., Meyer M., Putman M. E., Ryan-Weber E. V., Smith R. C., Staveley-Smith L., Webster R. L., Werk J., Zwaan M. A., 2007, *ApJ*, **661(2)**, 801
Pagel B. E. J., Edmunds M. G., Blackwell D. E., Chun M. S., Smith G., 1979, *MNRAS*, **189**, 95
Palay E., Nahar S. N., Pradhan A. K., Eissner W., 2012, *MNRAS*, **423(1)**, L35
Pérez-Montero E., 2014, *MNRAS*, **441(3)**, 2663
Pilyugin L. S., 2001, *A&A*, **369**, 594
Pilyugin L. S., Grebel E. K., Mattsson L., 2012, *MNRAS*, **424(3)**, 2316
Reynolds R. J., 1990, S. Bowyer and C. Leinert (eds.), *The Galactic and Extragalactic Background Radiation*, Vol. 139 of *IAU Symposium*, p. 157
Rupke D. S. N., Veilleux S., Baker A. J., 2008, *ApJ*, **674(1)**, 172
Sánchez S. F. e. a., 2012, *A&A*, **538**, A8
Sánchez Almeida J., Aguerri J. A. L., Muñoz-Tuñón C., Vazdekis A., 2009, *ApJ*, **698(2)**, 1497
Sanders R. L., Shapley A. E., Zhang K., Yan R., 2017, *ApJ*, **850(2)**, 136
Schaerer D., Fragos T., Izotov Y. I., 2019, *A&A*, **622**, L10
Stasińska G., 2005, *A&A*, **434(2)**, 507
Stasińska G., 2010, G. R. Bruzual and S. Charlot (eds.), *Stellar Populations - Planning for the Next Decade*, Vol. 262 of *IAU Symposium*, pp 93–96
Stasińska G., Prantzos N., Meynet G., Simón-Díaz S., Chiappini C., Dessauges-Zavadsky M., Charbonnel C., Ludwig H. G., Mendoza C., Grevesse N., Arnould M., Barbuy B., Lebreton Y., Decourchelle A., Hill V., Ferrand o P., Hébrard G., Durret F., Katsuma M., Zeippen C. J., 2012, *Oxygen in the Universe*, EAS Publications Series
Storey P. J., Sochi T., Badnell N. R., 2014, *MNRAS*, **441(4)**, 3028
Tayal S. S., Zatsarinny O., 2017, *ApJ*, **850(2)**, 147
Thomas A. D., Dopita M. A., Kewley L. J., Groves B. A., Sutherland R. S., Hopkins A. M., Blanc G. A., 2018, *ApJ*, **856(2)**, 89

Tremonti C. A., Heckman T. M., Kauffmann G., Brinchmann J., Charlot S., White S. D. M., Seibert M., Peng E. W., Schlegel D. J., Uomoto A., Fukugita M., Brinkmann J., 2004, *ApJ*, **613(2)**, 898
Ucci G., Ferrara A., Gallerani S., Pallottini A., 2017, *MNRAS*, **465**, 1144
Ucci G., Ferrara A., Gallerani S., Pallottini A., Cresci G., Kehrig C., Hunt L. K., Vilchez J. M., Vanzi L., 2019, *MNRAS*, **483**, 1295
Ucci G., Ferrara A., Pallottini A., Gallerani S., 2018, *MNRAS*, **477**, 1484
Vale Asari N., Stasińska G., Morisset C., Cid Fernandes R., 2016, *MNRAS*, **460(2)**, 1739
Wu J. F., Boada S., 2019, *MNRAS*, **484(4)**, 4683
Zaritsky D., Kennicutt Jr. R. C., Huchra J. P., 1994, *ApJ*, **420**, 87

Chemical Abundances in Gaseous Nebulae:
Open problems in Nebular astrophysics
AAA Workshop Series 11, 2019
M. Cardaci, G. Hägele & E. Pérez-Montero, eds.

Invited Review

Galactic abundance gradients from deep spectra of H II regions

C. Esteban[1,2], J. García-Rojas[1,2], K. Z. Arellano-Córdova [1,2,3] and J.E. Méndez-Delgado[1,2]

[1]*Instituto de Astrofísica de Canarias, E-38200 La Laguna, Spain*
[2]*Departamento de Astrofísica, Universidad de La Laguna, E-38206, La Laguna, Spain*
[3]*Instituto Nacional de Astrofísica, Óptica y Electrónica, Apdo. Postal 51 y 216, Puebla, Mexico*

Abstract. We present some results of an ongoing project devoted to reassess the radial abundance gradients in the disc of the Milky Way based on deep spectroscopy of H II regions. The data have been taken with large aperture telescopes, mainly with the GTC and VLT. The sample contains about 35 objects located at Galactocentric distances from 5 to 17 kpc. We determine the electron temperature for all nebulae, allowing the precise calculation of chemical abundances. In this paper, we present and discuss results mostly concerning the radial gradients of O, N and C.

Key words: ISM: abundances — Galaxy: abundances — Galaxy: disc — Galaxy: evolution — H II regions.

1. Introduction

Since decades ago, we know that chemical abundances in spiral galaxies show well defined radial gradients (e.g. Searle, 1971; Pagel & Edmunds, 1981). These gradients trace the spatial distribution and temporal evolution of star formation history and the effects of gas flows and other processes over the chemical composition of the galaxies. H II regions can be used as probes of the present-day composition of the interstellar medium in the zone of the hosting galaxy where they are located. The emission-line spectrum of H II regions can be used to determine the gas-phase abundance of several elements, especially of O – the proxy of metallicity in the analysis of ionized nebula – but also of He, C, N, Ne, S, Cl, Ar and Fe.

In the late seventies, several works investigated the radial abundance gradients in the Milky Way based on optical spectroscopy of a small number of H II regions (e.g. Peimbert et al., 1978; Hawley, 1978; Talent & Dufour, 1979). Until recently, the number of Galactic H II regions with direct determination of the electron temperature, T_e, from optical spectra has been rather limited. In fact, the classic work on the subject by Shaver et al. (1983), who observed a larger sample of H II regions in a wider range of Galactocentric distances, used optical spectra to measure the collisionally excited lines (hereinafter CEL) of heavy-element

ions but radio recombination line measurements to derive the T_e of the nebulae. Optical and radio observations were not co-spatial and the aperture sizes of both kinds of data were very different. Deharveng et al. (2000) also combined non-co-spatial optical spectra and radio observations to derive T_e for most of the 34 H II regions of their sample. The studies of the radial abundance gradients based on far infrared, FIR, observations (e.g. Rudolph et al., 2006) combine measurements of CELs from FIR spectra and T_e determined from radio observations with also different apertures.

As we have said above, the O/H ratio is the proxy of metallicity in nebular abundance studies. In normal H II regions, O abundance can be derived simply adding the O^+ and O^{2+} abundances, that can be obtained from the intensity of bright optical CELs. The paucity of abundance determinations based on co-spatial direct determinations of T_e for H II regions, especially at both extremes of the Galactic disc – central zones and anticentre – has been an enduring problem in the exploration of the true shape of the Galactic O gradient. Those distant nebulae are usually faint and heavily reddened and the direct determinations of T_e – essential for determining reliable abundances – is very difficult (see Peimbert et al., 1978; Esteban et al., 2005).

2. The sample and methodology

The aim of our ongoing project is to obtain very deep spectroscopy of a sizable sample of H II regions covering the largest possible fraction of the Galactic disc. By now, the observed sample covers 35 objects located at Galactocentric distances, R_G, between 5 and 17 kpc. The preliminary results concerning the O and N gradients have been published in Esteban et al. (2017) and Esteban & García-Rojas (2018). Thirteen objects of the sample are located beyond the isophotal radius of the Milky Way (R_{25} = 11.5 kpc, de Vaucouleurs & Pence, 1978) and have been selected to explore the shape of the radial abundance gradients at the Galactic anticentre. Almost all the spectra have been taken with high or intermediate-resolution spectrographs attached to 8 - 10 m telescopes (GTC and VLT). In all the H II regions the T_e-sensitive auroral [O III] 4363 Å and/or [N II] 5755 Å lines have been measured, allowing us to obtain a precise determination of T_e and the ionic abundances and avoiding uncertainties due to the combination of non-co-spatial data.

We have been especially careful in selecting appropriate values of R_G for the objects. For each H II region, we have assumed the mean values of the kinematic and stellar distances given in different published references (see Esteban et al., 2017; Esteban & García-Rojas, 2018, for details). We have associated an uncertainty for each distance, which corresponds to the standard deviation of the values used for the mean. In contrast to what is customary in many previous works, we include the errors in R_G when calculating the linear fits of the gradients. We have assumed the Sun located at R_G = 8.0 kpc (Reid, 1993).

We have derived the electron density, n_e, and T_e using the density and temperature-sensitive emission line ratios of the CELs observed in each spectrum. Using these lines, we can also derive ionic and total abundances of several elements as He, C, N, O, Ne, S, Cl, Ar and Fe. We use the same methodology and atomic dataset to derive physical conditions and abundances for all the objects.

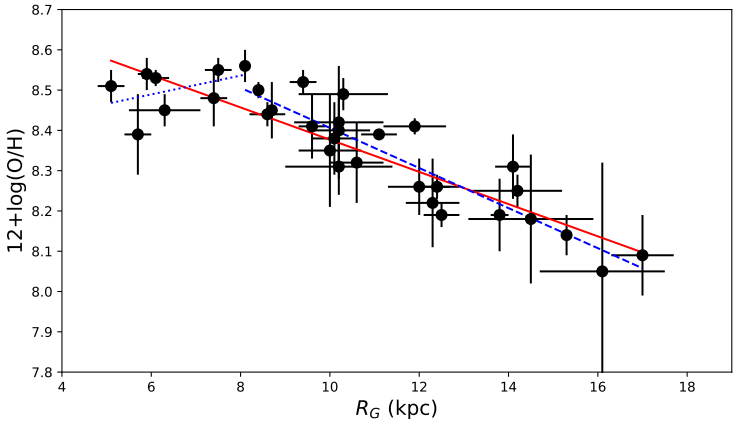

Figure 1. Radial distribution of the O abundance – in units of 12+log(O/H) – as a function of the Galactocentric distance, $R_{\rm G}$, for our sample of Galactic H II regions. The solid red line represents the least-squares fit to all objects. The dashed blue line corresponds to the least-squares fit to the H II regions located at $R_{\rm G} > 8$ kpc and the dotted blue line to those with $R_{\rm G} < 8$ kpc.

3. The O/H gradient

In Fig. 1 we present the spatial distribution of the O/H ratio for the H II regions of our sample (a first version of this graph was published in Esteban & García-Rojas, 2018). The least-squares linear fit to the $R_{\rm G}$ and the O abundances, gives the following radial gradient :

$$12 + \log({\rm O/H}) = 8.80(\pm0.09) - 0.041(\pm0.006) R_{\rm G}; \quad (1)$$

valid for $R_{\rm G}$ from 5.1 to 17.0 kpc. The slope of the gradient is consistent with other previous determinations, as those obtained by Deharveng et al. (2000) or Esteban et al. (2005). As it was reported by Esteban et al. (2017), the slope of the radial O abundance gradient does not change for objects located beyond R_{25}. This fact demonstrates the absence of flattening of the O gradient in the outer Milky Way, at least up to $R_{\rm G} \sim 17$ kpc, contrary to what was claimed in previous works (e. g. Fich & Silkey, 1991; Vilchez & Esteban, 1996; Maciel et al., 2006). In Fig. 1, we can note that the radial distribution of the O/H ratio seems to change its slope for objects located at $R_{\rm G} < 8$ kpc. In fact, this zone shows a drop or flattening of the O gradient. We have made a double linear fit of the spatial distribution of the O abundances. Firstly, we made a least-squares linear fit to the $R_{\rm G}$ and the O/H ratios for objects with $R_{\rm G} > 8$ kpc (represented by a dashed blue line in Fig. 1):

$$12 + \log({\rm O/H}) = 8.90(\pm0.11) - 0.050(\pm0.010) R_{\rm G}; \quad (2)$$

which is somewhat stepper than the fit we obtain for the whole sample but still consistent within the errors. The least-squares linear fit for the objects located

in the inner part of the Galactic disc, with $R_G < 8$ kpc, is (represented by a dotted blue line in Fig. 1):

$$12 + \log(O/H) = 8.35(\pm 0.13) + 0.023(\pm 0.019) R_G. \quad (3)$$

The presence of a drop or flattening of the O/H ratio in the inner zones of the Galactic disc may have important implications for chemical evolution models. There are previous works that have found indications of a change on the abundance distribution of O, Fe and α-elements in Cepheids in the inner Galactic disc (Martin et al., 2015; Andrievsky et al., 2016). Another evidence can be found in metallicity gradients derived from SDSS-III/APOGEE observations of red giants by Hayden et al. (2014). These authors find an apparent flattening at $R_G < 6$ kpc, especially evident for low-$[\alpha/Z]$ stars. The flattening found with Cepheids or red giants begins at somewhat smaller distances (at $R_G \sim$ 5-6 kpc) than suggested by our H II region data, but the results seem to be qualitatively consistent considering the uncertainties. Andrievsky et al. (2016) proposed that this change of slope could be due to a decrease or quenching of the star formation rate produced by gas flows towards the Galactic Centre induced by the presence of the Galactic bar. On the other hand, Haywood et al. (2016) and Khoperskov et al. (2018) propose that a quenching of the star formation may be produced by the increasing of turbulence in the gas due to the stellar bar. A third evidence of a drop of O/H ratios at inner parts of the Milky Way comes from abundance studies of planetary nebulae, PNe, in the Galactic bulge. Using mid-infrared *Spitzer* spectra, Gutenkunst et al. (2008) found that the mean O abundance of these PNe – located at R_G between 0 and 3 kpc – do not follow the trend of the disc and is about or even slightly lower than solar. The effect of the Galactic bar has also been advocated as the possible origin of this behavior (Pottasch & Bernard-Salas, 2015).

Inner drops in the radial O abundance distribution have been reported in several spiral galaxies (e.g. Belley & Roy, 1992; Rosales-Ortega et al., 2011; Sánchez-Menguiano et al., 2018). In all the cases, these features have been obtained from abundance analysis based on strong-line methods and not on direct determinations of T_e of the H II regions. Sánchez-Menguiano et al. (2018) have found that about 35% of a sample of about 100 galaxies show an inner drop located about half of the effective radius, R_e, of the galaxy. Considering that R_e is between 4-5 kpc in the Milky Way (de Vaucouleurs & Pence, 1978), the position of our change of slope is located at a considerably larger distance than expected if the behavior found by Sánchez-Menguiano et al. (2018) is extrapolated to our Galaxy.

The mean difference of the O abundance of the H II regions represented in Fig. 1 and the abundance given by Eq. 1 at their corresponding distance is $\pm$0.05 dex, of the order of the typical abundance uncertainties. That low dispersion indicates that O is well mixed in the interstellar gas along the observed section of the Galactic disc. This result contrast dramatically, for example, with the large scatter shown in the data by Shaver et al. (1983) (Fig. 2).

In Fig. 2 we also show the comparison between the radial O gradient obtained for our sample objects when using CELs or RLs of O^{2+}. The gradient obtained from RLs includes the objects studied in Esteban et al. (2005, 2013) and Sh 2-100, which data are described in Esteban et al. (2017). As we can see, both gradients are almost parallel, in fact the slope obtained from RLs is -0.033 ± 0.009 dex

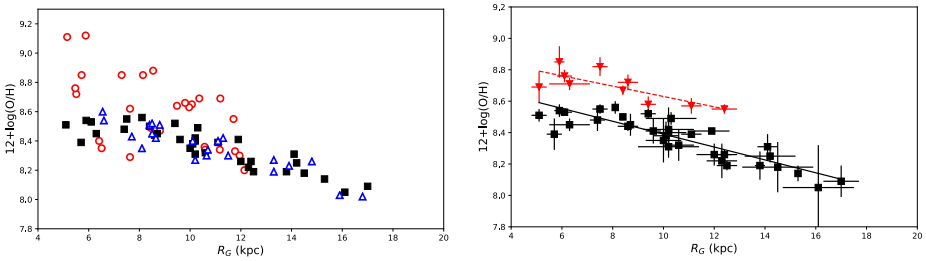

Figure 2. *Left:* Radial distribution of the O abundance as a function of R_G including our sample of Galactic H II regions (black squares); the blue empty triangles represent data from Deharveng et al. (2000) and the red empty circles include data from Shaver et al. (1983); Peimbert et al. (1978); Hawley (1978) and Talent & Dufour (1979). *Right:* Comparison of the radial gradient of O/H obtained from CELs (black squares and continuous line) and RLs (red triangles and dashed line).

kpc^{-1}. The mean offset between both gradient lines is of the order of 0.2 dex, the typical value of the abundance discrepancy factor for H II regions (see paper by García-Rojas et al. in these proceedings or García-Rojas & Esteban, 2007).

4. The N/H and N/O gradients determined without ICF

In Fig. 3 we show the spatial distribution of N abundances of the very low-ionization H II regions of our sample. In these objects we can assume that N/H $\approx$ N$^+$/H$^+$. Therefore, an ICF is not necessary for estimating the N/H ratio (see Esteban & García-Rojas, 2018). The least-squares linear fit to the R_G of the objects and their N abundance gives the following radial N abundance gradient:

$$12 + \log(\mathrm{N/H}) = 8.21(\pm0.09) - 0.059(\pm0.009) R_G. \quad (4)$$

As in the case of the O/H gradient, the mean difference of the N abundance of the H II regions and the linear fit at their corresponding distance is $\pm$0.06 dex, of the order of the average uncertainty of the abundance determinations, which is about $\pm$0.05 dex. This result indicates that the amount of N in the ISM of the Galactic disc is fairly homogeneous and that any possible local inhomogeneity is not substantially larger than the observational uncertainties. All previous determinations of the radial abundance gradient of N from H II regions have been calculated using ICFs, and give slopes stepper than ours (Eq. 4). For example, Shaver et al. (1983) obtain -0.073 ± 0.013 dex kpc^{-1} and Rudolph et al. (2006) – using FIR observations – obtain -0.085 ± 0.020 dex kpc^{-1}.
In the right panel of Fig. 3 we show the radial distribution of log(N/O) as a function of R_G for the same objects. The least-squares linear fit to the data (represented by the red solid line) is:

$$\log(\mathrm{N/O}) = -0.63(\pm0.17) - 0.012(\pm0.018) R_G, \quad (5)$$

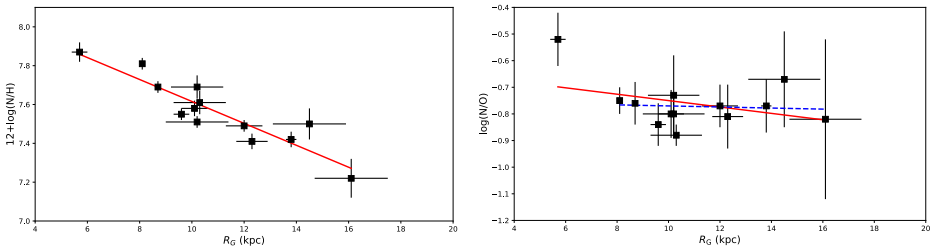

Figure 3. *Left:* Radial distribution of the N abundance as a function of R_G for our low-ionization sample of Galactic H II regions. In these objects $N/H \approx N^+/H^+$. The solid red line represents the least-squares fit to all objects. *Right:* Radial distribution of log(N/O) as a function of R_G, for the same objects shown in the left panel. The solid red line represents the least-squares fit to all the objects. The dashed blue line corresponds to the fit excluding the innermost object, Sh 2-61, that shows a much higher N/O ratio.

which slope is rather small and can even be considered flat within the uncertainties. As it can be seen, the slope of the N/O gradient depends strongly on the innermost object – Sh 2-61 – that shows the highest N/O ratio. Recalculating the fit excluding that object the slope becomes virtually flat (blue dashed line in Fig. 3).

$$\log(N/O) = -0.79(\pm0.22) + 0.002(\pm0.021)R_G. \quad (6)$$

The flatness of the radial distribution of the N/O ratio between 8 and 16 kpc, permits to assume a constant mean value of $\log(N/O) = -0.77 \pm 0.04$ for that range of R_G. All previous determinations of the radial N/O gradient from H II region spectra have been obtained assuming an ICF scheme to determine the N abundance. Using optical data and an ICF(N^+), Shaver et al. (1983) obtained a rather flat slope of -0.006 dex kpc^{-1}, in good agreement with our results. Other determinations of the N/O gradient use FIR spectra, are based on an assumed ICF(N^{2+}) because [N III] CELs are the only N lines observable in the FIR range. With these kinds of observations, Simpson et al. (1995) obtained a gradient of log(N/O) with a slope of -0.04 ± 0.01 dex kpc^{-1}. However, they find a significantly better result using a step fit with two levels, an inner constant value of $\log(N/O) = -0.49$ for objects located at $R_G < 6$ kpc and and external one of $\log(N/O) = -0.74$ for 6 kpc $< R_G <$ 11 kpc. Rudolph et al. (2006), also based on FIR spectra and assuming an ICF(N^{2+}) from photoionisation models, obtained similar results. The results based on FIR observations indicate an enhancement of the N/O ratio in the inner part of the Galactic disc but no strong evidence for an overall linear radial gradient of this quantity. The almost flat N/O gradient we see in Fig. 3 indicates that the bulk of the N is not formed by standard secondary processes at least in most part of the Galactic disc. Further deep optical spectra of low-ionization H II regions located at $R_G < 8$ kpc are necessary to confirm if other H II regions apart from Sh 2-61 show the enhancement of N/O that FIR data suggest.

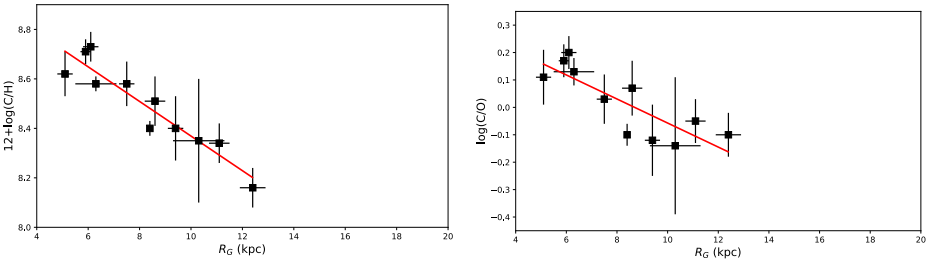

Figure 4. *Left:* Radial distribution of the C abundance as a function of R_G for our sample of Galactic H II regions. The solid red line represents the least-squares fit to all objects. *Right:* Radial distribution of log(C/O) as a function of R_G for our Galactic H II region where C and O abundances have been derived from RLs. The solid red line represents the least-squares fit.

5. The C/H and C/O gradients

The C/H and C/O gradients of the Milky Way determined from H II region spectra were studied by Esteban et al. (2005, 2013). In this paper we show a revision of those results including determinations of C/H ratios for two additional objects: Sh 2-100 and Sh 2-152, which data are presented in Esteban et al. (2017) and Esteban & García-Rojas (2018), respectively. The C abundances have been derived from measurements of the faint RL of C II 4267 Å and the application of an ICF(C^{2+}) due to the absence of C^+ lines in the optical. We have used the mean value of three different estimations of ICF(C^{2+}) based on the results of photoionization models: the relation found by Garnett et al. (1999) and the recent ones by Berg et al. (2019) and Medina-Amayo et al. (in preparation). In Fig. 4 we show the spatial distribution of the resulting C abundances for the H II regions of our sample. The least-squares linear fit to the data (represented by the red solid line) is:

$$12 + \log(\mathrm{C/H}) = 9.07(\pm0.11) - 0.070(\pm0.014)R_\mathrm{G}, \tag{7}$$

which is stepper than the O gradient or even the N one. Again, the dispersion of the individual C/H ratios with respect to the fit is rather small – 0.05 dex – and of the order of the uncertainties, indicating the absence of substantial chemical inhomogeneities along the Galactic disc. In Fig. 4 we show the radial distribution of log(C/O) as a function of R_G for those objects where we detect both C II and O II RLs in their spectra. This group includes the H II regions studied in Esteban et al. (2005, 2013) and Sh 2-100. The least-squares linear fit to the data (represented by the red solid line in Fig. 4) is:

$$\log(\mathrm{C/O}) = 0.38(\pm0.11) - 0.044(\pm0.014)R_\mathrm{G}. \tag{8}$$

Toribio San Cipriano et al. (2017) determined the C/H gradients for two nearby low-mass spiral galaxies, NGC 300 and M33, finding also that the C/H gradients are steeper than those of O/H, leading to negative C/O gradients. On the other

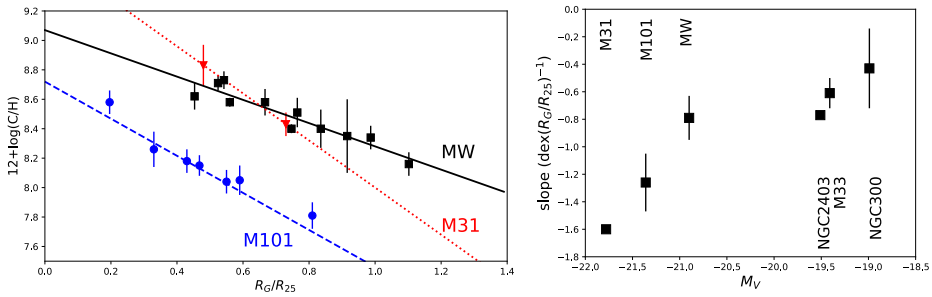

Figure 5. *Left:* C radial abundance gradients normalized to galactic isophotal radius R_{25} obtained from H II region spectra of the Milky Way (black squares, this work) and M101 and M31 (blue circles and red triangles, respectively, data taken from Esteban et al., in preparation). Lines represent the least-squares linear fits for the Milky Way (black solid line), M101 (blue dashed line) and M31 (red dotted line). *Right:* Slope of C radial abundance gradients *vs.* absolute magnitude, M_V for several spiral galaxies (see text for details).

hand, Esteban et al. (in preparation) are studying the C and O abundance gradients of M31 and M101, which are nearby spiral galaxies more massive than the Milky Way. In Fig. 5 we compare the C/H gradients of these three galaxies as a function of the fractional galactocentric distance of the H II regions, R/R_{25}, inside each galaxy. In Fig. 5 we also represent the slope of the C/H gradient of several spiral galaxies with respect to their M_V including the data of Toribio San Cipriano et al. (2017) for NGC 300 and M33; of Esteban et al. (2009) for NGC 2403, of Esteban et al. (in preparation) for M101 and M31 and of this work for the Milky Way. In the figure we can see that both quantities are clearly correlated, a result that was firstly reported by Toribio San Cipriano et al. (2017). There are two galaxies without errorbars in their C/H slope represented in the right panel of Fig. 5. The gradient of M31 is based only on two observational points, so we cannot assign a formal error. In the case of NGC 2403, the individual determinations of C/H of the H II regions have large errors and the estimation of the slope is rather uncertain. In the light of the results by Carigi et al. (2005), Toribio San Cipriano et al. (2017) propose that the correlation between the slope of the C/H gradient and M_V may be the product of metallicity-dependent yields of C. At high metallicities, 12+log(O/H) $\geq$ 8.5, the main contributors to C should be massive stars. However, at intermediate metallicities, 8.1 $\leq$ 12+log(O/H) $\leq$ 8.5, the main contributors to C are low metallicity low-mass stars. On the other hand, the behaviour of the C/O radial abundances gradients are consistent with an "inside-out" formation scenario. In the inner parts of galaxies, the low- and intermediate-mass stars had enough time to inject C into the ISM. The newborn massive stars formed in more metal-rich environments can further enrich the ISM via their stellar winds. Therefore, this behavior would certainly produce different C/H gradients in galaxies of different luminosities and average metallicities. Further analysis of the C/H and C/O gradients in the Milky Way will be presented in Arellano-Córdova et al. (in preparation).

6. Other elements

Our deep spectra allow to explore the radial gradients of other elements as He, Ne, S, Cl or Ar. He is the second most abundant element in the Universe but there are rather few works that have tried to determine its gradient in the Milky Way (e.g. Peimbert et al., 1978; Shaver et al., 1983; Fernández-Martín et al., 2017). Thanks to the depth of our spectra, we can measure a large number of He I lines in most H II regions of our sample. The atomic levels of He I have two possible quantum states, singlet and triplet. Lines from triplet levels are comparatively much more affected by collisional excitation and radiative transfer effects, so singlet lines are more suitable for obtaining precise abundances of the He^+/H^+ ratio. In the paper authored by Méndez-Delgado et al. of these proceedings we describe the methodology and our preliminary determination of the radial He abundance gradient of the Milky Way. A final study will be presented in Méndez-Delgado et al. (in preparation).
Some preliminary results on the gradients of Ne, S and Cl abundances – especially of Cl/H and Cl/O ratios – can be found in the paper by Arellano-Córdova et al. of these proceedings. In a future paper (Arellano-Córdova et al., in preparation) we will explore in depth the behavior of Ne, S, Cl and Ar abundance gradients – as well as their ratios with respect to O – carrying out a detailed analysis of the most appropriate ICF schemes for each element and discussing the implications on the chemical evolution of the Milky Way.

Acknowledgments. This research is funded by the State Research Agency (AEI), Spanish Ministry of Science, Innovation and Universities (MCIU) and the European Regional Development Fund (ERDF) under grant AYA2015-65205-P. JG-R acknowledges support from an Advanced Fellowship from the Severo Ochoa excellence program (SEV-2015-0548). KZA-C acknowledges support from Mexican CONACYT grant 711183.

References

Andrievsky S. M., Martin R. P., Kovtyukh V. V., Korotin S. A., Lépine J. R. D., 2016, *MNRAS*, **461**, 4256
Belley J., Roy J.-R., 1992, *ApJS*, **78**, 61
Berg D. A., Erb D. K., Henry R. B. C., Skillman E. D., McQuinn K. B. W., 2019, *ApJ*, **874**, 93
Carigi L., Peimbert M., Esteban C., García-Rojas J., 2005, *ApJ*, **623**, 213
de Vaucouleurs G., Pence W. D., 1978, *AJ*, **83**, 1163
Deharveng L., Peña M., Caplan J., Costero R., 2000, *MNRAS*, **311**, 329
Esteban C., Bresolin F., Peimbert M., García-Rojas J., Peimbert A., Mesa-Delgado A., 2009, *ApJ*, **700**, 654
Esteban C., Carigi L., Copetti M. V. F., García-Rojas J., Mesa-Delgado A., Castañeda H. O., Péquignot D., 2013, *MNRAS*, **433**, 382
Esteban C., Fang X., García-Rojas J., Toribio San Cipriano L., 2017, *MNRAS*, **471**, 987
Esteban C., García-Rojas J., 2018, *MNRAS*, **478**, 2315
Esteban C., García-Rojas J., Peimbert M., Peimbert A., Ruiz M. T., Rodríguez M., Carigi L., 2005, *ApJL*, **618**, L95

Fernández-Martín A., Pérez-Montero E., Vílchez J. M., Mampaso A., 2017, *A&A*, **597**, A84
Fich M., Silkey M., 1991, *ApJ*, **366**, 107
García-Rojas J., Esteban C., 2007, *ApJ*, **670**, 457
Garnett D. R., Shields G. A., Peimbert M., Torres-Peimbert S., Skillman E. D., Dufour R. J., Terlevich E., Terlevich R. J., 1999, *ApJ*, **513**, 168
Gutenkunst S., Bernard-Salas J., Pottasch S. R., Sloan G. C., Houck J. R., 2008, *ApJ*, **680**, 1206
Hawley S. A., 1978, *ApJ*, **224**, 417
Hayden M. R., Holtzman J. A., Bovy J., Majewski S. R., Johnson J. A., Allende Prieto C., Beers T. C., Cunha K., Frinchaboy P. M., García Pérez A. E., Girardi L., Hearty F. R., Lee Y. S., Nidever D., Schiavon R. P., Schlesinger K. J., Schneider D. P., Schultheis M., Shetrone M., Smith V. V., Zasowski G., Bizyaev D., Feuillet D., Hasselquist S., Kinemuchi K., Malanushenko E., Malanushenko V., O'Connell R., Pan K., Stassun K., 2014, *AJ*, **147**, 116
Haywood M., Lehnert M. D., Di Matteo P., Snaith O., Schultheis M., Katz D., Gómez A., 2016, *A&A*, **589**, A66
Khoperskov S., Haywood M., Di Matteo P., Lehnert M. D., Combes F., 2018, *A&A*, **609**, A60
Maciel W. J., Lago L. G., Costa R. D. D., 2006, *A&A*, **453**, 587
Martin R. P., Andrievsky S. M., Kovtyukh V. V., Korotin S. A., Yegorova I. A., Saviane I., 2015, *MNRAS*, **449**, 4071
Pagel B. E. J., Edmunds M. G., 1981, *ARA&A*, **19**, 77
Peimbert M., Torres-Peimbert S., Rayo J. F., 1978, *ApJ*, **220**, 516
Pottasch S. R., Bernard-Salas J., 2015, *A&A*, **583**, A71
Reid M. J., 1993, *ARA&A*, **31**, 345
Rosales-Ortega F. F., Díaz A. I., Kennicutt R. C., Sánchez S. F., 2011, *MNRAS*, **415**, 2439
Rudolph A. L., Fich M., Bell G. R., Norsen T., Simpson J. P., Haas M. R., Erickson E. F., 2006, *ApJS*, **162**, 346
Sánchez-Menguiano L., Sánchez S. F., Pérez I., Ruiz-Lara T., Galbany L., Anderson J. P., Krühler T., Kuncarayakti H., Lyman J. D., 2018, *A&A*, **609**, A119
Searle L., 1971, *ApJ*, **168**, 327
Shaver P. A., McGee R. X., Newton L. M., Danks A. C., Pottasch S. R., 1983, *MNRAS*, **204**, 53
Simpson J. P., Colgan S. W. J., Rubin R. H., Erickson E. F., Haas M. R., 1995, *ApJ*, **444**, 721
Talent D. L., Dufour R. J., 1979, *ApJ*, **233**, 888
Toribio San Cipriano L., Domínguez-Guzmán G., Esteban C., García-Rojas J., Mesa-Delgado A., Bresolin F., Rodríguez M., Simón-Díaz S., 2017, *MNRAS*, **467**, 3759
Vilchez J. M., Esteban C., 1996, *MNRAS*, **280**, 720

Chemical Abundances in Gaseous Nebulae:
Open problems in Nebular astrophysics
AAA Workshop Series 11, 2019
M. Cardaci, G. Hägele & E. Pérez-Montero, eds.

Invited Review

Galactic radial abundance gradients: cepheids and photoionized nebulae

W.J. Maciel[1], S. Andrievsky[2]

[1] *Astronomy Department, University of São Paulo, São Paulo, Brazil*
[2] *Odessa National University, Ukraine*

Abstract.
Radial abundance gradients are observed in the Galaxy and other galaxies as well, and include several chemical elements in different stellar systems. Possibly the most accurate gradients in the Galaxy are those determined from chepheid variable stars. These objects have very accurate abundances for many elements and are generally considered as standard candles, so that their galactocentric distances are very well determined. These stars are relatively young, with ages between the main types of photoionized nebulae, namely the younger HII regions and the older planetary nebulae. In this paper we consider the O/H and Fe/H gradients based on a large sample of galactic cepheids, and compare the results with recent determinations from photoionized nebulae.

Key words: galaxies: abundances — galaxies: ISM — stars: cepheids

1. Introduction

Radial abundance gradients are increasingly important as a constraint of chemical evolution models both for the Galaxy and other galaxies as well. They can be measured using a variety of objects, such as HII regions, cepheid variables, planetary nebulae, open clusters, etc. Since these objects comprise a large range of ages, from a few million years to several Gyr, the gradients can also give some information on the time variation of the abundances in several galactic systems. It is generally believed that the gradients derived from young objects, such as HII regions and cepheid stars are somewhat different from those measured in older systems, such as planetary nebulae and open clusters. However, the interpretation of the data is complex, in view of the different elements that can be studied and of the considerable uncertainties in assigning a definite age to each object, especially in the case of the older systems. Some references include Anders et al. (2017); Mollá et al. (2018); Mollá et al. (2019); Maciel & Costa (2014, 2013); Maciel et al. (2012); Cavichia et al. (2014, 2011). Some recent results obtained by our group suggest that the gradients have not appreciably changed in the past 3-5 Gyr, although these results are dependent on relatively uncertain age estimates (Maciel et al., 2012; Maciel & Costa, 2013).
Another source of uncertainties are possible space variations of the gradients, such as the proposed flattening at large galactocentric distances, the behaviour

of the gradients in the inner Galaxy, which can be affected by the presence of bars, and near the solar galactocentric distance, where a large amount of data is available. The simplest models assume a unique linear gradient throughout the galactic disk, but more complicated variations have also been considered, such as multiple linear gradients in different parts of the disk and non linear variations (see for example, Maciel et al., 2015; Davies et al., 2009; Ivezić et al., 2008; Esteban et al., 2017).

In this paper, we consider the O/H and Fe/H radial gradients in the galactic disk as measured by cepheid variable stars. There is a large amount of data for these stars, including the results of the group by S. Andrievsky and collaborators (Andrievsky et al., 2016, 2014, 2013, 2004, 2002b,a,c; Luck et al., 2013, 2011, 2006, 2003; Luck & Lambert, 2011; Korotin et al., 2014; Martin et al., 2015), as well as by other groups, (Genovali et al., 2015b,a, 2014, 2013; Lemasle et al., 2018, 2013, 2015; Pedicelli et al., 2009). Our goal is to consider the largest possible sample of reliable spectroscopic abundances as well as accurate galactocentric distances. It is expected that the use of a nearly complete sample may lead to an accurate determination of the gradients, so that the non-homogeneity of the data may be counterbalanced. We will analyze several possibilities of the abundance variations in the disk, such as a unique linear gradient, multiple gradients, and non-linear variations. The results can then be compared with the results from other young and older systems, such as HII regions, planetary nebulae and open clusters.

2. Cepheid gradients: O/H and Fe/H

2.1. The data

The basic sample comes from the work by Korotin et al. (2014), who have presented a NLTE analysis of the oxygen abundance distribution in the thin disk based on infrared data from two telescopes: the Hobby-Eberly Telescope (HET) and the Max Planck Gesellschaft Telescope (MPG). The lines used are the triplet 777.1 - 777.4 nm. The HET data are described by Luck & Lambert (2011), whereas the MPG data are from Luck et al. (2013) with atmospheric parameters from Luck et al. (2011). Fe/H data are also included from Luck & Lambert (2011) and Luck et al. (2013). The lowest uncertainties in the O/H abundances are in the range 0.05 to 0.08 dex, and an average uncertainty is 0.12. The data by Luck & Lambert (2011) include Fe abundances with errors and oxygen abundances, but not distances. The average uncertainties for the Fe/H data are 0.141 dex for FeI and 0.119 dex for FeII, with a standard deviation of 0.047 dex, considering all. We adopt the FeII data when possible, so that we can assume and average uncertainty of 0.12 dex for the Fe/H abundances, which is the same as the O/H uncertainties in the data by Korotin et al. (2014). The distances and galactocentric distances of the objects in the sample by Luck & Lambert (2011) are given in Luck et al. (2013).

Martin et al. (2015) presented chemical abundances for a sample of galactic cepheids, including also the elements O/H and Fe/H. The galactocentric distances range mostly from 5 to 7 kpc, adopting $R_0 = 7.9\,\mathrm{kpc}$ for the solar galactocentric distance, that is, the objects are generally closer to the galactic centre than in the previous samples. A combination of the previous data

with the present results suggests a plateau in the chemical abundances closer to the galactic centre. The observations were secured with the 3.6 CFHT telescope, the VLT, and the MPG telescope as in Korotin et al. (2014). Stellar atmosphere parameters are presented, as in the previous samples. Fe abundances are from LTE analysis, while for O/H NLTE is used. The uncertainties in the abundances are small, similar or lower than in Korotin et al. (2014). A value of 0.12 dex can be estimated both for O/H and Fe/H, being usually an upper limit.
More recently, Andrievsky et al. (2016) presented a detailed study of a cepheid variable star located closer to the galactic bulge than the previous samples. It is the object ASAS 181024-2049.6, for which they derive R_G = 2.53 kpc, ϵ(O) = 9.17 and ϵ(Fe) = 7.94, corresponding to [O/H] = 0.46 and [Fe/H] = 0.44. The data were obtained with the CFHT telescope and a selection of 4 candidate stars was considered in the literature, one of which satisfied the usual criteria to distinguish Cepheid variables from W Vir stars. Andrievsky et al. (2016) included this object in order to obtain a more complete sample than the one by Martin et al. (2015). This sample emphasized the objects closer to the galactic centre in order to investigate an apparent flattening in the gradients in this region, possibly as a consequence of the existence of a bar. Such a suggestion had already been made in the literature based on theoretical models and planetary nebula data (see for example Cavichia et al., 2014, 2011). In the paper, Andrievsky et al. consider a large number of elements such as Mg, Si, S, Ca, and Ti, all of which share the same characteristics.
Genovali et al. (2015b,a) presented Fe/H abundances of a sample of galactic cepheids with data analyzed by Genovali et al. (2014). Some of the stars in their sample are also presented in the previous samples, so that they have not been considered. The data are based on high-resolution UVES spectra collected at ESO VLT (Cerro Paranal, Chile). The abundances are based essentially on the equivalent widths of FeI and FeII lines. The galactocentric distances are based on NIR photometry together with reddening-free Period-Wesenheit relations, with R_0 = 7.94 kpc. Some results by Lemasle et al. (2018) have also been taken into account (see also Lemasle et al., 2013, 2015). This work includes double-mode cepheids from the Gaia Data Release (DR2). The metallicity is derived from the ratio of the first overtone and fundamental periods by Gaia DR2 and the parallaxes are used to determine the Galactocentric distances of the stars. The derived abundances are then used to investigate the effects on the galactic [Fe/H] gradient.

2.2. Results

We have analyzed a large sample of galactic cepheids with accurate abundances and distances. In this paper we report some results for a total sample of 361 independent stars with Fe/H abundances, and 331 stars with O/H abundances. The main results are shown in Figures 1ab, 2ab, 3ab, and 4ab, and in Tables 1 and 2. We adopt an average uncertainty of 0.12 dex both for O/H and Fe/H. From the discussion by Groenewegen (2013) the uncertainty in the galactocentric distances is very small, as cepheids are considered as standard candles. The average uncertainty in the distance for the 128 galactic cepheids of Groenewegen (2013) is about 5.38%, and in the case of the galactocentric distance R_G it is 0.79%. Very few stars have uncertainties higher than 1%, so that we adopted

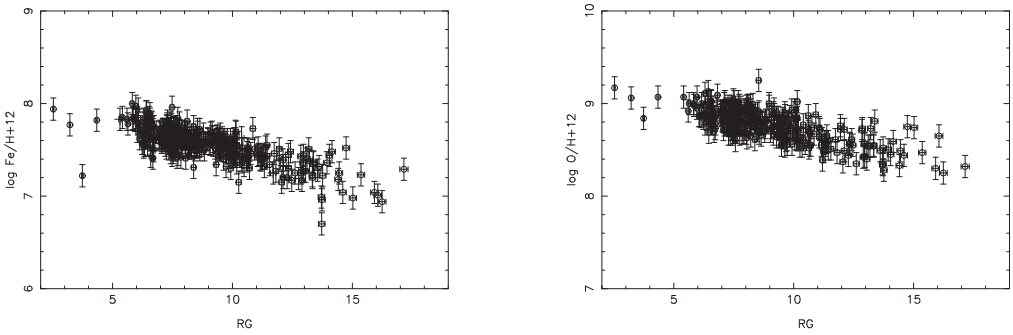

Figure 1. Fe/H and O/H abundances functions of the galactocentric distance for galactic cepehids with the adopted error bars.

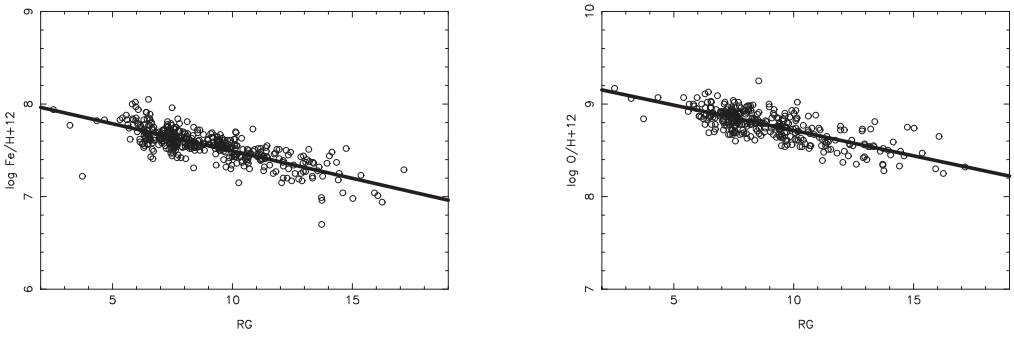

Figure 2. Same as Figure 1 including the linear fits.

here an average uncertainty of 1%. Figure 1a and 1b show the data with error bars for Fe/H and O/H, respectively. Figure 2ab includes linear fits, and the corresponding coefficients are given in Table 1, where we have

$$\log \mathrm{X/H} + 12 = A + B\ R_G \tag{1}$$

We notice that the O/H slope is very similar to the gradient found by Korotin et al. (2014), namely −0.058 dex/kpc, although we have used a larger sample. It can also be seen that both the Fe/H and O/H gradients are essentially the same within the uncertainties. From Figure 1ab there is some indication of a flattening in the inner Galaxy, where $R \leq 5$ kpc, but the number of stars in this range is very small. Furthermore, the star with the lowest abundances at $R \simeq 3.6$ kpc is probably a W Vir star, so that this possibility should be viewed with caution.

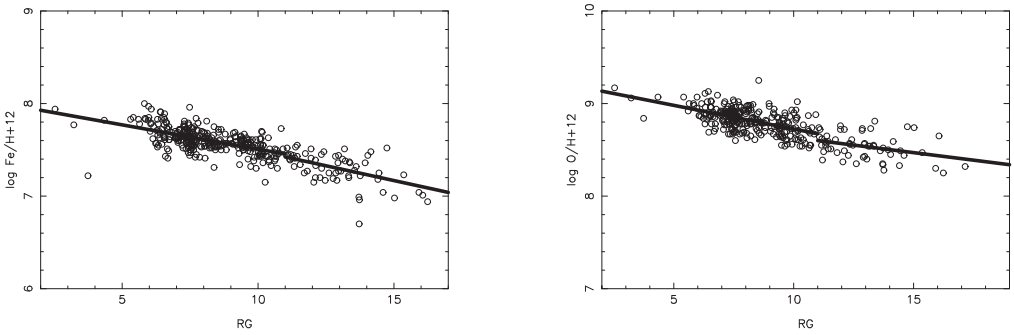

Figure 3. Same as Figure 1 including double linear fits.

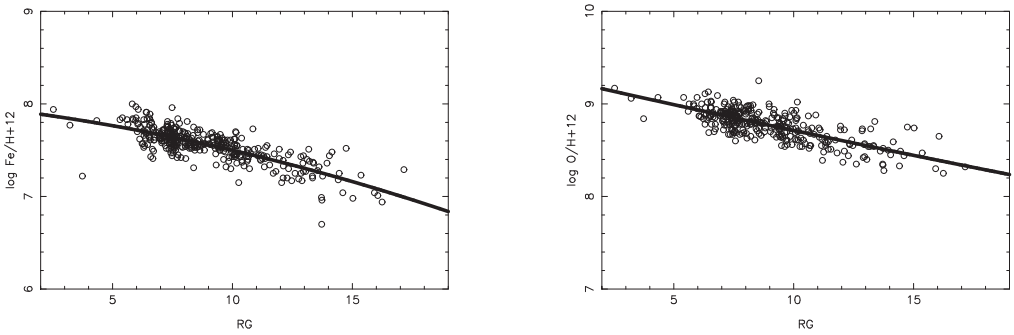

Figure 4. Same as Figure 1 including quadratic polynomial fits.

As a second possibility, we have considered a double linear fit, in the ranges 4-11 kpc and 11-19 kpc, respectively, in agreement with the discussion by Korotin et al. (2014). The adoption of different ranges leads to slightly different results. The results of the fits are also given in Table 1 and Figures 3a and 3b. It can be seen that the correlation becomes less accurate for both segments, in view of the lower correlation coefficients r. For O/H there seems to exist some flattening in the outer galaxy, while for Fe/H the inner gradient is slightly flatter, but the difference is small, so that the gradient can be considered as essentially constant. As a third possibility, we have considered a quadratic polynomial fit, which in principle could take into account any detailed space variations of the gradients, especially in the outer galaxy. The equation used is

$$\log \mathrm{X/H} + 12 = A + B\ R_G + C\ R_G^2 \qquad (2)$$

The results are shown in Figures 4ab, and are essentially indistinguishable from the unique gradient shown in Figures 2ab. For example, at $R_G = 7.9$ kpc we have -0.056 dex/kpc and -0.054 dex/kpc for the O/H and Fe/H gradients, respectively. The coefficients are given in Table 2. Again the correlations seem less accurate. For O/H the gradient is essentially constant, with maybe a slight flattening at large distances. For Fe/H there is a slight steepening in the outer galaxy, but again the difference is small. It should be mentioned that the results for the samples containing all variability phases and only one phase are similar, since the abundances in different phases are essentially the same.

Table 1 - Linear fits of O/H and Fe/H gradients for galactic cepheids.

element	n	A	B	r
Single linear fits				
O/H	331	9.26 ± 0.02	-0.055 ± 0.003	-0.75 ± 0.11
Fe/H	361	8.09 ± 0.02	-0.060 ± 0.003	-0.77 ± 0.11
Double linear fits				
O/H: $R_G < 11$ kpc	273	9.24 ± 0.04	-0.051 ± 0.005	-0.56 ± 0.10
O/H: $R_G > 11$ kpc	58	8.96 ± 0.15	-0.033 ± 0.011	-0.35 ± 0.13
Fe/H: $R_G < 11$ kpc	298	8.03 ± 0.04	-0.053 ± 0.004	-0.58 ± 0.11
Fe/H: $R_G > 11$ kpc	63	8.13 ± 0.17	-0.064 ± 0.013	-0.53 ± 0.15

Table 2 - Quadratic fit of O/H and Fe/H gradients for galactic cepheids.

element	n	A	B	C	χ^2
O/H	331	9.281	-0.05889	-0.0002061	0.0122
Fe/H	361	7.957	-0.03114	-0.001462	0.0130

3. Gradients of photoionized nebulae

Photoionized nebulae, namely HII regions and planetary nebulae are favourite objects to study radial gradients, especially for element ratios such as O/H, Ne/H, Ar/H and S/H, which are usually more difficult to determine in stars. On the other hand, Fe/H abundances are hardly measured in the nebulae, since most Fe is probably condensed in solid grains, so that the interpretation of the iron lines is more complex.

3.1. HII regions

Since the study by Shaver et al. (1983), many papers have dealt with the determination of radial gradients from HII regions, especially for O/H, on the basis of optical or infrared data (see for example Esteban & García-Rojas, 2018; García-Rojas, 2018; Esteban et al., 2017; Balser et al., 2011; Rudolph et al., 2006; Quireza et al., 2006; Deharveng et al., 2000). These papers are based on rather small samples compared with the cepheid samples. Recent work suggests a constant gradient of about -0.04 to -0.05 dex/kpc for O/H and no flattening at large galactocentric distances (Esteban & García-Rojas, 2018). The data are based on a sample with 35 objects with 10.4 GTC observations, for which electron temperatures have been measured. An inverse temperature gradient is also apparent. Some flattening has been pointed out in the inner Galaxy ($R_G \leq 5\,\mathrm{kpc}$), a result also suggested on the basis of planetary nebulae (see for example Gutenkunst et al., 2008; Cavichia et al., 2011). This feature is also observed in our data, as mentioned in section 2.2. A compilation of recent determinations from photoionized nebulae can be found in Mollá et al. (2019).

3.2. Planetary Nebulae

Planetary nebulae can be compared with HII regions, taking into account their different ages and also the fact that some elements have their abundances changed by the evolution of the progenitor stars, such as He and N. The determination of PN ages is a very difficult problem, which certainly affects the interpretation of the gradients (see for example Stanghellini & Haywood, 2018; Maciel et al., 2011, 2010, for some recent discussions on the age problem).

Recent determinations of the abundance gradients include mainly the ratios O/H, Ne/H, S/H and Ar/H, with particular emphasis on the possible variations along the galactocentric distance and also relative to the distance from the galactic plane (see for example Stanghellini & Haywood, 2018; Pagomenos et al., 2018; Maciel et al., 2015; Maciel & Costa, 2013). A detailed study of distance-independent abundance correlations between Ne/H, S/H and Ar/H with O/H has been recently presented by Maciel et al. (2017) for photoionized nebulae of the Local Group, showing that these elements are well correlated in HII regions and also in PN, albeit with a larger dispersion. The O/H radial gradients of PN are usually in the range -0.02 to -0.05 dex/kpc, and most recent papers favour the lowest gradients. However, the interpretation of these results is complex for a variety of reasons. First, the PN distances are not as well known as in the case of cepheids and even HII regions. Second, the (in)famous discrepancy between the results of forbidden lines and recombination lines is still largely unresolved, affecting both PN and HII regions (cf. Carigi et al., 2018). Third, PN central stars have different ages, which are poorly known, especially for those objects older than about 4 Gyr. Fourth, radial migration has been recently found to be an important factor (see for example Minchev et al., 2018; Jia et al., 2018), which probably acts in order to flatten the gradients. This may explain some of the shallow gradients found in the literature, affecting the comparison between the gradients derived from young and old objects. Therefore the uncertainties of the average gradients are probably higher than generally assumed, and any spatial and temporal variations of the gradients based on PN should be viewed with care.

4. Some Conclusions

• The radial gradients from cepheids are reasonably well represented by a unique gradient of about −0.05 dex/kpc, which is essentially the same both for Fe/H and O/H. This is probably the best estimate of the radial gradient at the present time. A double linear fit does not seem likely, although some flattening in the outer galaxy can be observed for O/H. The data are consistent with some flattening in the inner Galaxy, but this region is clearly not well covered in the present sample, since very few stars have galactocentric distances lower than about 5 kpc.

• O/H gradients from HII regions and cepheids are similar within the uncertainties. HII region abundances of O, Ne, S, and Ar show good correlations, and Ne, S, and Ar vary in lockstep with O, so that similar gradients can be expected for these elements.

• PN apparently have slightly flattened gradients of about −0.03 dex/kpc for O/H and Ne/H, but most samples probably include objects with different ages. The uncertainties in the age determination of the PN progenitor stars (and their distances) are very large for the older objects, with ages higher than about 5 Gyr. Radial migration makes things even more difficult, especially for older objects. These facts may explain the lower PN gradients compared with cepheids and HII regions.

• A comparison of the gradients derived from cepheids and photoionized nebulae shows as a first approximation that the gradients are similar, taking into account the uncertainties in the abundances, distances and, especially, the age determinations of PN. There are apparently no important temporal variations in the gradients in the last 3 to 5 Gyr for O/H. The distance-independent correlations for photoionized nebulae studied by Maciel et al. (2017) and stars (see for example Ramírez et al., 2007) suggest that the Fe/H gradients are only marginally different from the O/H gradients.

• Recent theoretical models are able to explain the average gradients based on a inside out formation scenario for the Galaxy. Some models can account for the inner flattening of the gradients, or predict some steepening at galactocentric distances larger than R_0 (see for example Mollá et al., 2019; Stanghellini & Haywood, 2018; Grisoni et al., 2018). These models consider the time variation of the gradients and the results are often conflicting. The idea of a nearly constant gradient in the last few Gyr is supported by several models, but the behaviour of the gradients at earlier epochs is largely controversial. More recently, studies of the variation of the gradients with redshift are also consistent with approximately constant gradients for $z \leq 2$, but again the behaviour at earlier epochs is not clear, and a steeper gradient for $z > 3$ cannot be ruled out (see for example Mollá et al., 2019; Stanghellini & Haywood, 2018).

Acknowledgments. This work was partially supported by CNPq (Process 302556/2015-0) and FAPESP (Process 2010/18835-3 and 2018/04562-7)

References

Anders F., Chiappini C., Minchev I., et al., 2017, *A&A*, **600**, A70
Andrievsky S. M., Bersier D., Kovtyukh V. V., et al., 2002a, *A&A*, **384**, 140
Andrievsky S. M., Kovtyukh V. V., Luck R. E., et al., 2002b, *A&A*, **381**, 32
Andrievsky S. M., Kovtyukh V. V., Luck R. E., et al., 2002c, *A&A*, **392**, 491
Andrievsky S. M., Lépine J. R. D., Korotin S. A., et al., 2013, *MNRAS*, **428**, 3252
Andrievsky S. M., Luck R. E., Korotin S. A., 2014, *MNRAS*, **437**, 2106
Andrievsky S. M., Luck R. E., Martin P., Lépine J. R. D., 2004, *A&A*, **413**, 159
Andrievsky S. M., Martin R. P., Kovtyukh V. V., et al., 2016, *MNRAS*, **461**, 4256
Balser D. S., Rood R. T., Bania T. M., Anderson L. D., 2011, *ApJ*, **738**, 27
Carigi L., Peimbert M., Peimbert A., 2018, *ApJ in press, arXiv:1802.09688*
Cavichia O., Costa R. D. D., Maciel W. J., 2011, *RevMexAA*, **47**, 49
Cavichia O., Mollá M., Costa R. D. D., Maciel W. J., 2014, *MNRAS*, **437**, 3688
Davies B., Origlia L., Kudritzki R.-P., et al., 2009, *ApJ*, **696**, 2014
Deharveng L., Peña M., Caplan J., Costero R., 2000, *MNRAS*, **311**, 329
Esteban C., Fang X., García-Rojas J., Toribio San Cipriano L., 2017, *MNRAS*, **471**, 987
Esteban C., García-Rojas J., 2018, *MNRAS*, **478**, 2315
García-Rojas J., 2018, *Astronomy in Focus, Vol. 12, ed. P. Benvenuti et al.*
Genovali K., Lemasle B., Bono G., et al., 2013, *A&A*, **554**, A132
Genovali K., Lemasle B., Bono G., et al., 2014, *A&A*, **566**, A37
Genovali K., Lemasle B., da Silva R., et al., 2015a, *A&A*, **580**, A17
Genovali K., Romaniello M., Lemasle B., et al., 2015b, *Mem. S. A. It.*, **86**, 340
Grisoni V., Spitoni E., Matteucci F., 2018, *MNRAS*, **481**, 2570
Groenewegen M. A. T., 2013, *A&A*, **550**, A70
Gutenkunst S., Bernard-Salas J., Pottasch S. R., et al., 2008, *ApJ*, **680**, 1206
Ivezić Ž., Sesar B., Jurić M., et al., 2008, *ApJ*, **684**, 287
Jia Y., Chen Y., Zhao G., et al., 2018, *ApJ*, **863**, 93
Korotin S. A., Andrievsky S. M., Luck R. E., et al., 2014, *MNRAS*, **444**, 3301
Lemasle B., François P., Genovali K., et al., 2013, *A&A*, **558**, A31
Lemasle B., Hajdu G., Kovtyukh V., et al., 2018, *A&A*, **618**, A160
Lemasle B., Kovtyukh V., Bono G., et al., 2015, *A&A*, **579**, A47
Luck R. E., Andrievsky S. M., Korotin S. N., Kovtyukh V. V., 2013, *AJ*, **146**, 18
Luck R. E., Andrievsky S. M., Kovtyukh V. V., et al., 2011, *AJ*, **142**, 51
Luck R. E., Gieren W. P., Andrievsky S. M., et al., 2003, *A&A*, **401**, 939
Luck R. E., Kovtyukh V. V., Andrievsky S. M., 2006, *AJ*, **132**, 902
Luck R. E., Lambert D. L., 2011, *AJ*, **142**, 136
Maciel W., Costa R. D. D., 2014, *Asymmetrical Planetary Nebulae VI Conference*, p. 55
Maciel W. J., Costa R. D. D., 2013, *RevMexAA*, **49**, 333
Maciel W. J., Costa R. D. D., Cavichia O., 2015, *RevMexAA*, **51**, 165
Maciel W. J., Costa R. D. D., Cavichia O., 2017, *RevMexAA*, **53**, 151
Maciel W. J., Costa R. D. D., Idiart T. E. P., 2010, *A&A*, **512**, A19
Maciel W. J., Rodrigues T., Costa R., 2012, *IAU Symposium*, Vol. 283 of *IAU Symposium*, pp 424–425

Maciel W. J., Rodrigues T. S., Costa R. D. D., 2011, *RevMexAA*, **47**, 401
Martin R. P., Andrievsky S. M., Kovtyukh V. V., et al., 2015, *MNRAS*, **449**, 4071
Minchev I., Anders F., Recio-Blanco A., et al., 2018, *MNRAS*, **481**, 1645
Mollá M., Díaz A. I., Acasibar Y., et al., 2018, *First Workshop on Chemical Abundances in Gaseous Nebulae, AAA Workshop Series 10, ed. G. Hägele et al.*, pp 81–90
Mollá M., Díaz Á. I., Cavichia O., et al., 2019, *MNRAS*, **482**, 3071
Pagomenos G. J. S., Bernard-Salas J., Pottasch S. R., 2018, *A&A*, **615**, A29
Pedicelli S., Bono G., Lemasle B., et al., 2009, *A&A*, **504**, 81
Quireza C., Rood R. T., Bania T. M., et al., 2006, *ApJ*, **653**, 1226
Ramírez I., Allende Prieto C., Lambert D. L., 2007, *A&A*, **465**, 271
Rudolph A. L., Fich M., Bell G. R., et al., 2006, *ApJS*, **162**, 346
Stanghellini L., Haywood M., 2018, *ApJ*, **862**, 45

Contributed Talks

Chemical Abundances in Gaseous Nebulae:
Open problems in Nebular astrophysics
AAA Workshop Series 11, 2019
M. Cardaci, G. Hägele & E. Pérez-Montero, eds.

Contributed Paper

A new determination of the primordial helium abundance based on the H II region NGC 346

M. Valerdi & A. Peimbert

[1]*Instituto de Astronomía, Universidad Nacional Autónoma de México, Apdo. Postal 70-264 Ciudad Universitaria, México*

Abstract. To understand the Universe a highly accurate ($\sim 1\%$) primordial helium abundance ($Y_{\rm P}$) determination plays an important role; it is extremely important to constrain: Big Bang Nucleosynthesis models, elementary particle physics, and the study of galactic chemical evolution. Low-metallicity H II regions have been used to estimate it since their statistical uncertainties are relatively small. We present a new determination of the primordial helium abundance, based on long-slit spectra of the H II region NGC 346 in the small Magellanic cloud. We found that for NGC 346: $X = 0.7465$, $Y = 0.2505$ and $Z = 0.0030$. By assuming $\Delta Y/\Delta O = 3.3 \pm 0.7$ we found that the primordial helium abundance is $Y_{\rm P} = 0.2451 \pm 0.0026$ (1σ).

Key words: ISM: abundances — galaxies: ISM — primordial nucleosynthesis — H II regions — Magellanic Clouds

1. Introduction

According to the Big Bang model, the universe expanded rapidly from a highly compressed primordial state, which resulted in a significant decrease in density and temperature. After a few seconds, the universe cooled enough to allow the formation of certain nuclei. The Standard Big Bang Nucleosynthesis (SBBN) theory predicts that definite amounts of hydrogen, helium, and lithium were produced. If the BB was not standard some variations on these abundances is expected. Primordial nucleosynthesis is believed by most cosmologists to have taken place in the interval from roughly 10s to 20m after the Big Bang. Most of the helium as the isotope ^{4}He was formed, along with small amounts of the hydrogen isotope ^{2}H or D, the isotope ^{3}He, and a very small amount of the isotope ^{7}Li. Determination of $Y_{\rm P}$ imposes constraints the BB model on galaxy evolution models, and shows the composition of the universe when it was less that 1 Gyr old. ^{4}He is very stable, and neither decays nor combines easily to form heavier nuclei.

Thus, one seeks astrophysical objects with low metal abundances, in order to measure light element abundances that are closer to primordial. Low-metallicity H II regions have been used to estimate it since they are very bright and emit the relevant lines in the visual region of the spectrum. The first determination of $Y_{\rm P}$ based on observations of H II regions was carried out by Peimbert & Torres-

Peimbert (1974) and several dozens have followed. Using several low-metallicity H II regions has permitted to estimate the primordial helium abundance with very small statistical errors ($\lesssim 1\%$) (e.g. Izotov et al., 2014; Aver et al., 2015; Peimbert et al., 2016); nevertheless, due to the numerous systematic uncertainties, obtaining better than 1% precision for individual objects remains a challenge.
The Small Magellanic Cloud hosts the H II region NGC 346, arguably the best H II region to determine the primordial helium abundance. Its low metallicity $Z \sim 0.003$ ($\sim 20\%$ of solar) requires a relatively small extrapolation to obtain $Y_{\rm P}$. NGC 346 has many advantages with respect to other H II regions: the underlying absorption correction for the helium lines can be reduced by at least an order of magnitude, the determination of the ICF(He) can be estimated by observing different lines of sight of a given H II region, the accuracy of the determination can be estimated by comparing the results derived from different points in a given H II region, overall there is no H II region that is simultaneously at least as close, as large, and with a metallicity as low as NGC 346.
To obtain the value for $Y_{\rm P}$ it is necessary to use the correlation between the helium mass fraction Y and the metal abundance Z. The correlation is then extrapolated to zero metallicity to estimate the primordial mass fraction of helium $Y_{\rm P}$. Since the universe was born with no heavy elements, $Y_{\rm P} = Y(Z = 0)$. This method has been modified to use the O abundance instead of Z, because measuring other chemical elements becomes impractical. Although some groups seek alternatives to O, like using N or S (e.g. Pagel et al., 1992; Fernández et al., 2018).

2. Observations

We analyzed the H II region NGC 346 of the Small Magellanic Cloud. We obtained the long-slit spectra with FORS1, at the VLT located at Melipal, Chile. We used IRAF to reduce the spectra, following the standard procedure. We also corrected for underlying absorption and reddening correction, as well as a renormalization of Hβ. For further information please see Valerdi et al. (2019).

3. Physical Conditions

We used optical collisional excitation lines (CELs) to calculated physical conditions, which were determined fitting the line intensities with `PyNeb` by Luridiana et al. (2003). The temperature and density were determined using the conventional sets of intensity ratios from the auroral to the nebular lines. Electron temperatures were determined using [O III] $\lambda4363/(\lambda4959 + \lambda5007)$, [O II] $(\lambda7320 + \lambda7330)/(\lambda3726 + \lambda3729)$, and [N II] $\lambda5755/\lambda6584$. Electronic densities were determined from the [O II] $\lambda3726/\lambda3729$, and [S II] $\lambda6731/\lambda6716$ ratios, which are strongly density dependent. In addition, we obtained the [Fe III] density from the computations by Keenan et al. (2001), using the $I(\lambda4986)/I(\lambda4658)$ ratio. The temperatures and densities are presented in Table 1.
We also obtain values for the temperature and density from He I lines. We used the program `Helio14`, which is an extension of the maximum likelihood method presented by Peimbert et al. (2000) to obtain these values. By using ten He I lines, we obtained a temperature T_e(He I) and a density n_e(He I).

Table 1. Temperature and density from CELs.

Temperature (K)	[OIII]	[OII]	[NII]	HeI
NGC 346	12871±98	12445±464	10882±767	11400±550
Density (cm^{-3})	[OII]	[SII]	[FeIII]	HeI
NGC 346	23.7±8.2	32±21	101 ± 17	<10

4. Chemical Abundances

We obtained ionic abundances using both: the direct method and the t^2 formalism. We first used `PyNeb` to perform the computations $t^2 = 0.00$. To obtain the ionic abundance using $t^2 \neq 0.00$, we used the equation 11 by Peimbert et al. (2004). To obtain the t^2 value, we combining results from CELs and values from He I and using the `Helio14` code we found that the maximum likelihood values are: $t^2(He^+) = 0.033 \pm 0.017$ and $T_0 = 11900 \pm 450$ K. The ionic abundance of He^{++} was obtained from the λ4686 line and using the recombination coefficients given by Storey & Hummer (1995). The Table 2 shows the ionic abundances for $t^2 = 0.00$ as well as for $t^2 = 0.033 \pm 0.017$.

Table 2. Ionic abundances for the H II region NGC 346.

Ion	$t^2 = 0.000$	$t^2 = 0.033 \pm 0.017$
He^+	10.917±0.004	10.915±0.004
He^{++}	8.30±0.04	8.30±0.04
N^+	5.87±0.02	5.97±0.06
O^+	7.41±0.05	7.54±0.08
O^{++}	7.93±0.01	8.04±0.06
Ne^{++}	7.22±0.01	7.33±0.06
S^+	5.55±0.03	5.65±0.06
S^{++}	6.18±0.02	6.24±0.04
Ar^{++}	5.54±0.01	5.60±0.03
Ar^{+3}	5.11±0.02	5.22±0.06
Cl^{++}	4.37±0.03	4.47±0.06

In units of $12 + \log n(X^{+i})/n(H)$.

To establish the total abundance of an element, one must account for the unobserved ionization stages, by means of introducing an Ionization Corrector Factor (ICF). The functional forms of those ICFs frequently depend on the depth, quality, and coverage of the spectra.

For H II regions with a high degree of ionization, we can consider that the presence of neutral helium within is negligible, and $\mathrm{ICF}(He^0) \simeq 1$. To obtain the abundance of helium we used:

$$\frac{N(He)}{N(H)} = \mathrm{ICF}(He^0) \left[\frac{N(He^+) + N(He^{++})}{N(H^+)} \right], \quad (1)$$

previous computations by Luridiana et al. (2003), Peimbert et al. (2002), Peimbert et al. (2007), and Relaño et al. (2002) showed that the ICF(He^0)= 1.00 for NGC 346.

Table 3. Total abundances for the H II region NGC 346.

Element	$t^2 = 0.000$	$t^2 = 0.033 \pm 0.017$
He	10.918±0.004	10.916±0.004
N	6.50±0.03	6.61±0.07
O	8.05±0.02	8.19±0.08
Ne	7.33±0.02	7.48±0.08
S	6.40±0.03	6.44±0.08
Ar	5.70±0.02	5.82±0.07
Cl	5.37±0.04	5.47±0.07

In units of $12 + \log n(X)/n(\mathrm{H})$.

For oxygen, to obtain the total abundance, we considered that $N(O^{3+})/N(O) = N(He^{++})/N(He)$ (Peimbert & Costero, 1969), therefore:

$$\frac{N(\mathrm{O})}{N(\mathrm{H})} = \mathrm{ICF}(\mathrm{O}^+ + \mathrm{O}^{++}) \left[\frac{N(\mathrm{O}^+) + N(\mathrm{O}^{++})}{N(\mathrm{H}^+)}\right], \tag{2}$$

where

$$\mathrm{ICF}(\mathrm{O}^+ + \mathrm{O}^{++}) = \frac{N(\mathrm{O}^+) + N(\mathrm{O}^{++}) + N(\mathrm{O}^{3+})}{N(\mathrm{O}^+) + N(\mathrm{O}^{++})}. \tag{3}$$

For nitrogen, and neon we obtained the total abundances using the ICFs by Peimbert & Costero (1969). We observed the auroral lines of [S II] and [S III]. To obtain the total sulphur abundance we used the ICF proposed by Stasińska (1978). For the case of argon, we have measurements for lines of [Ar III] and [Ar IV]; we used the calculations by Pérez-Montero et al. (2007). Finally for chlorine, we have measurements for lines of [Cl III], and to obtain the total abundance we used the ICF proposed by Delgado-Inglada et al. (2014). In Table 3 we present the results for $t^2 = 0.00$ as well as for $t^2 = 0.033 \pm 0.017$.

5. Primordial helium abundance

Through the chemical abundances of NGC 346, we computed the primordial helium abundance. To obtain this value, we need to calculate the fraction of helium by mass. For low metallicity objects such as NGC 346, its oxygen is expected to represent $O/Z \approx 0.55$ of the total mass of heavy elements (Peimbert et al., 2007). In this way, the chemical composition of NGC 346 is $X = 0.7465$, $Y = 0.2505$ and $Z = 0.0030$.
To compute Y_P, we assumed that:

$$Y_\mathrm{P} = Y - O\ \frac{\Delta Y}{\Delta O}, \tag{4}$$

and we adopted $\Delta Y/\Delta O = 3.3 \pm 0.7$ (Peimbert et al., 2016), this value derived from metal-poor extragalactic H II regions with different O and Y values.
Through the low-metallicity H II region NGC 346 we have determined $Y_{\rm P}$. By measuring its He I line intensities, we determined a primordial helium abundance $Y_{\rm P} = 0.2451 \pm 0.0026$. Our determination is consistent with literature values, but our error bar is smaller. For further discussion on the determination of this value, and its error bars please see Valerdi et al. (2019).
Table 4, shows $Y_{\rm P}$ measurements reported in the literature. We note that our result is consistent with the results by Aver et al. (2015), Peimbert et al. (2016), and Fernández et al. (2018). However we note that the Izotov et al. (2014) determination differs significantly from the other values. We consider that they have some systematic errors that they are ignoring; for example, part of this difference is due to the adopted temperature structure.

Table 4. $Y_{\rm P}$ values basen on H II regions.

$Y_{\rm P}$ source	$Y_{\rm P}$
Izotov et al. (2014)	0.2551 ± 0.0022
Aver et al. (2015)	0.2449 ± 0.0040
Peimbert et al. (2016)	0.2446 ± 0.0029
Fernández et al. (2018)	0.245 ± 0.007
This work	0.2451 ± 0.0026

Through our determination of $Y_{\rm P}$, as a complement, we estimated the number of neutrino families and neutron half-life value. Using the $Y_{\rm P}$ value reported, and assuming a neutron half-life value $\tau_n = 880.2$ s (Tanabashi et al., 2018), we obtained that $N_\nu = 2.92 \pm 0.20$. As expected our result is consistent with Aver et al. (2015), Peimbert et al. (2016), and Fernández et al. (2018); these results agree with the presence of three families of neutrinos, which is consistent with laboratory determinations (e.g., Mangano et al., 2005; Mangano & Serpico, 2011). While the $Y_{\rm P}$ result by Izotov et al. (2014) suggests the presence of a fourth neutrino family (see Table 5).

Table 5. Predicted equivalent number of neutrino families, N_ν and the neutron half-life, τ_ν.

$Y_{\rm P}$ source	$Y_{\rm P}$	[a] N_ν	[b] τ_ν (s)
Izotov et al. (2014)	0.2551 ± 0.0022	3.58 ± 0.16	921 ± 11
Aver et al. (2015)	0.2449 ± 0.0040	2.91 ± 0.30	872 ± 19
Peimbert et al. (2016)	0.2446 ± 0.0029	2.89 ± 0.22	870 ± 14
Fernández et al. (2018)	0.245 ± 0.007	2.92 ± 0.55	872 ± 33
This work	0.2451 ± 0.0026	2.92 ± 0.20	873 ± 13

[a]Assuming $\tau_\nu = 880.2$ s by Tanabashi et al. (2018).
[b]Assuming $N_\nu = 3.046$ by Mangano et al. (2005).

We also estimated the value of the neutron half-life using the value of $N_\nu = 3.046$ (Mangano et al., 2005), and we obtained $\tau_n = 873 \pm 13$ s. Our result together with

the results obtained from Aver et al. (2015), Peimbert et al. (2016), Fernández et al. (2018), are within 1σ from the value presented by Tanabashi et al. (2018), and they are in agreement with the τ_n laboratory determinations (see Table 5). However, the results obtained by Izotov et al. (2014) differs by more than 3σ from the laboratory determination.

References

Aver E., Olive K. A., Skillman E. D., 2015, *JCAP*, **7**, 011
Delgado-Inglada G., Morisset C., Stasińska G., 2014, *MNRAS*, **440**, 536
Fernández V., Terlevich E., Díaz A. I., Terlevich R., Rosales-Ortega F. F., 2018, *MNRAS*, **478**, 5301
Izotov Y. I., Thuan T. X., Guseva N. G., 2014, *MNRAS*, **445**, 778
Keenan F. P., Aller L. H., Ryans R. S. I., Hyung S., 2001, *Proceedings of the National Academy of Science*, **98**, 9476
Luridiana V., Peimbert A., Peimbert M., Cerviño M., 2003, *ApJ*, **592**, 846
Mangano G., Miele G., Pastor S., Pinto T., Pisanti O., Serpico P. D., 2005, *Nuclear Physics B*, **729**, 221
Mangano G., Serpico P. D., 2011, *Physics Letters B*, **701**, 296
Pagel B. E. J., Simonson E. A., Terlevich R. J., Edmunds M. G., 1992, *MNRAS*, **255**, 325
Peimbert A., Peimbert M., Luridiana V., 2002, *ApJ*, **565**, 668
Peimbert A., Peimbert M., Luridiana V., 2016, *RMxAA*, **52**, 419
Peimbert M., Costero R., 1969, *Boletin de los Observatorios Tonantzintla y Tacubaya*, **5**, 3
Peimbert M., Luridiana V., Peimbert A., 2007, *ApJ*, **666**, 636
Peimbert M., Peimbert A., Ruiz M. T., 2000, *ApJ*, **541**, 688
Peimbert M., Peimbert A., Ruiz M. T., Esteban C., 2004, *ApJS*, **150**, 431
Peimbert M., Torres-Peimbert S., 1974, *ApJ*, **193**, 327
Pérez-Montero E., Hägele G. F., Contini T., Díaz Á. I., 2007, *MNRAS*, **381**, 125
Relaño M., Peimbert M., Beckman J., 2002, *ApJ*, **564**, 704
Stasińska G., 1978, *A&A*, **66**, 257
Storey P. J., Hummer D. G., 1995, *MNRAS*, **272**, 41
Tanabashi M., Hagiwara K., Hikasa K., Nakamura K., Sumino Y., Takahashi F., Tanaka J., Agashe K., Aielli G., Amsler C., et al., 2018, *Phys. Rev. D*, **98(3)**, 030001
Valerdi M., Peimbert A., Peimbert M., Sixtos A., 2019, *arXiv e-prints*

Chemical Abundances in Gaseous Nebulae:
Open problems in Nebular astrophysics
AAA Workshop Series 11, 2019
M. Cardaci, G. Hägele & E. Pérez-Montero, eds.

Contributed Paper

Chemical abundances and temperature structure of HII regions

G. Domínguez-Guzmán[1], M. Rodríguez[1], C. Esteban[2,3] and J. García-Rojas[2,3]

[1]*Instituto Nacional de Astrofísica, Óptica y Electrónica, Apdo. Postal 51 y 216, Puebla, Mexico*
[2]*Instituto de Astrofísica de Canarias, E-38200, La Laguna, Tenerife, Spain*
[3]*Departamento de Astrofísica, Universidad de La Laguna, E-38206, La Laguna, Tenerife, Spain*

Abstract. We use a sample of 37 HII regions with high quality spectra to study the behavior of the relative abundances of several elements as a function of metallicity. The sample includes spectra for eight HII regions of the Magellanic Clouds, obtained with UVES/VLT; the rest are gathered from the literature. We find that if we use the traditional two-zone scheme of temperature for the observed ions, the S/O, Cl/O and Ar/O abundance ratios increase with metallicity. However, with slight changes in the temperature structure, which include the use of intermediate temperatures, these ratios are constant with metallicity, as expected. Therefore, high quality observations allow us to deepen our understanding of the temperature structure of HII regions.

Key words: HII regions: chemical abundances

1. Introduction

The Magellanic Clouds (MCs) are nearby, low-metallicity galaxies, that provide an excellent opportunity to explore in detail the behavior of the chemical composition of HII regions as a function of metallicity. However, it is difficult to obtain reliable optical spectra of HII regions in the MCs since these galaxies are generally observed at high airmasses, making the observations very sensitive to the effects of atmospheric differential refraction (Filippenko, 1982). In fact, of all the available spectra of MC HII regions (Peimbert & Torres-Peimbert, 1974; Dufour, 1975; Pagel et al., 1978; Dufour et al., 1982; Stasińska et al., 1986; Tsamis et al., 2003; Nazé et al., 2003; Peimbert, 2003), only the spectrum of 30 Doradus presented by Peimbert (2003) can be considered of high quality since it is a deep spectrum with high wavelength coverage and relatively high spectral resolution that was obtained using an atmospheric dispersion corrector. Here we present eight new spectra of HII regions in the MCs of comparable quality, which, along with a sample of high quality spectra compiled from the literature, allow us to

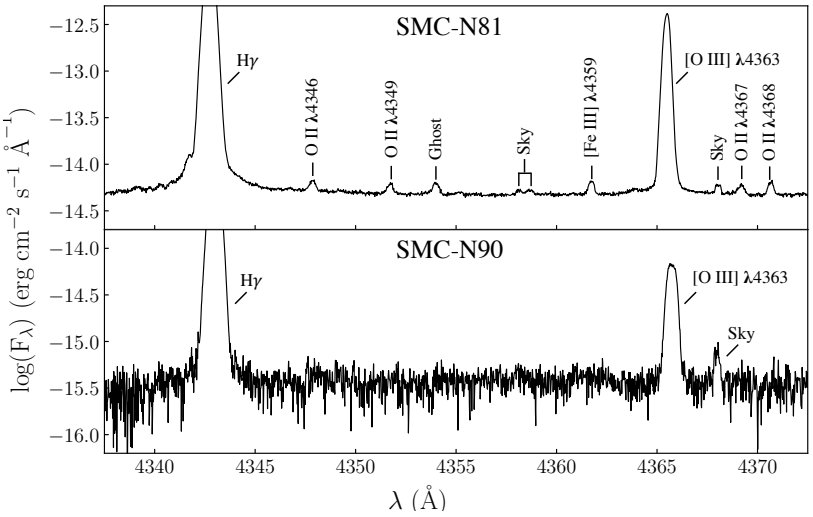

Figure 1. Part of our best (top panel, SMC-N81) and worst (bottom panel, SMC-N90) spectra. The [OIII] λ4363 line used to estimate the electron temperature can be easily measured in both cases.

explore different issues related to the analysis of the chemical composition of HII regions at different metallicities.

2. Observational data

We obtained echelle spectra of eight HII regions in the MCs, four in the Small Magellanic Cloud (SMC) and four in the Large Magellanic Cloud (LMC). The data were taken with UVES/VLT (Cerro Paranal Observatory, Chile). The spectral range 3100-10400 Å was covered with a resolution of $\Delta\lambda \sim \lambda/11600$. The atmospheric dispersion corrector was used to keep the same observed region within the slit at different wavelengths, since the MCs are observed at high airmasses (between 1.35 and 1.88). Figure 1 shows the wavelength range that includes the Hγ and [OIII] λ4363 lines for our best (SMC-N81) and worst spectrum (SMC-N90).

The reddening coefficient, $c(\mathrm{H}\beta)$, is determined by comparing the intensities of several Balmer and Paschen lines relative to Hβ with their case B values (Storey & Hummer, 1995). We use lines whose upper levels have principal quantum numbers $n \leq 7$, since for $n > 7$ the lines depart from their expected case B values (see the empty symbols in Figure 2). This behavior was previously found in the Orion Nebula by Mesa-Delgado et al. (2009), who argue that it could arise from collisions that change the quantum number l by more than ± 1 or from the pumping of the HI lines by absorption of the stellar continuum.

We use the reddening law of Howarth (1983), which has a ratio of total to selective extinction $R_{\mathrm{V}} = 3.1$ and is commonly used for the MCs, for all objects excepting

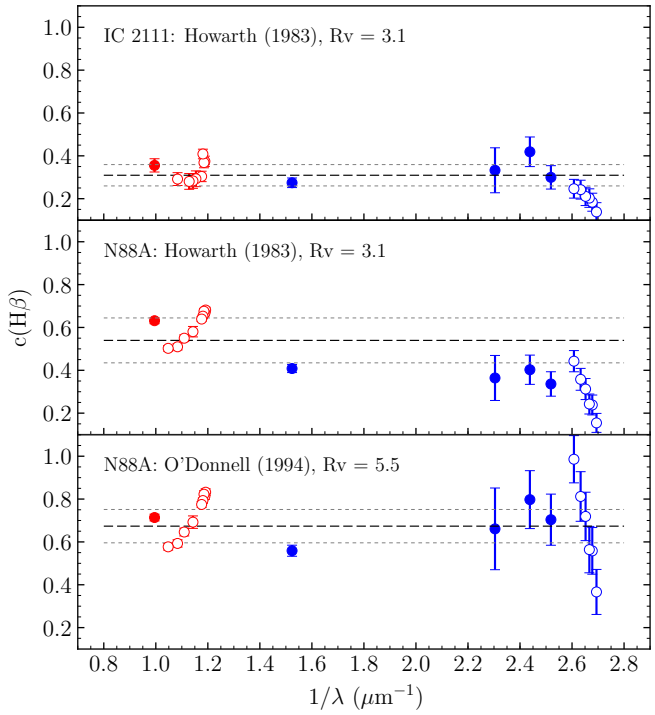

Figure 2. Reddening coefficient $c(\mathrm{H}\beta)$ as a function of the inverse wavelength in μm. Blue circles show the results obtained with the Balmer lines and the red circles those implied by the Paschen lines. The filled circles are those values we use to estimate the weighted mean (long dashed line) and the standard deviation (small dashed lines).

N88A and N90. In these two regions, the law of O'Donnell (1994) for $R_{\mathrm{V}} = 5.5$ provided a better fit. Figure 2 illustrates these results for IC 2111 and N88A. To this sample of eight MC HII regions, we have added 29 HII regions from the literature that have spectra of similar quality (García-Rojas et al., 2004, 2005, 2006, 2007; Esteban et al., 2004, 2009, 2014, 2017; Toribio San Cipriano et al., 2016; Peimbert, 2003).

3. Results

We have performed a homogeneous analysis of all regions in the sample. The calculations of physical conditions and ionic abundances are carried out with PyNeb (Luridiana et al., 2015). We use the density diagnostics n_{e}([OII]), n_{e}([SII]), n_{e}([ClIII]), and n_{e}([ArIV]), and the temperature diagnostics T_{e}([NII]) and T_{e}([OIII]) to characterize the gas of the nebula. We estimate the ionic abundances assuming a scheme of two temperatures; T_{e}([NII]) for S^{+}, O^{+}, and N^{+}; and T_{e}([OIII]) for S^{++}, Cl^{++}, O^{++}, and Ne^{++}. We do not use the other available temperature diagnostics, T_{e}([OII]), T_{e}([SIII]), and T_{e}([ArIII]), because they are

affected by different problems (recombination effects, telluric absorption) and have higher uncertainties than T_e([NII]) and T_e([OIII]).
The total abundance of nitrogen is obtained using the classical ionization correction factor (ICF), $N/O = N^+/O^+$. For the rest of the elements we use the ICFs provided by Delgado-Inglada et al. (2014). These ICFs were derived using photoionization models tailored for planetary nebulae, but they work better than those provided by Izotov et al. (2006) for HII regions, leading to somewhat lower dispersions. Besides, the photoionization models for HII regions of Reyes-Pérez et al. (2019, in preparation) confirm their validity.
The methodology described above, the most used in the literature, gives us as a result that the Cl/O, Ar/O, and S/O abundance ratios increase with metallicity (left panels in Figure 3 for Cl/O and S/O). On the other hand, if we use T_e([NII]) to calculate Cl^{++} and the mean of T_e([NII]) and T_e([OIII]) for S^{++} and Ar^{++}, we find that Cl/O, Ar/O, and S/O are approximately constant with metallicity (right panels in Figure 3), as expected. In the case of Ne^{++}, we find that the use of T_e([OIII]) to calculate its abundance is appropriate, but we find a large dispersion in the values derived for Ne/O (see the left panel in Figure 4). However, this dispersion is due to the behavior of the ICF for Ne, since it is also found when the spectra predicted by the photoionization models of Reyes-Pérez et al. (2019, in preparation) are analyzed in the same way as the observed spectra (right panel of Figure 4).

4. Conclusions

We present new determinations of chemical abundances of eight HII regions in the MCs based on deep echelle spectra taken with UVES/VLT. The quality of the spectra allows us to explore which extinction law is working better for each object. We have extended the sample including spectra with the same quality as the main sample. We find that if we use the traditional two-zone scheme of temperature, the abundance ratios Cl/O, S/O and Ar/O increase with metallicity. However, with slight changes in the temperature structure, these abundance ratios are constant with metallicity, as expected.

Acknowledgments. We acknowledge support from Mexican CONACYT grant CB-2014-240562 and from MINECO under grant AYA2015-65205-P. G.D.-G. acknowledges support from CONACYT grant 297932.

References

Delgado-Inglada G., Morisset C., Stasińska G., 2014, *MNRAS*, **440**, 536
Dufour R. J., 1975, *ApJ*, **195**, 315
Dufour R. J., Shields G. A., Talbot Jr. R. J., 1982, *ApJ*, **252**, 461
Esteban C., Bresolin F., Peimbert M., García-Rojas J., Peimbert A., Mesa-Delgado A., 2009, *ApJ*, **700**, 654
Esteban C., Fang X., García-Rojas J., Toribio San Cipriano L., 2017, *MNRAS*, **471**, 987
Esteban C., García-Rojas J., Carigi L., Peimbert M., Bresolin F., López-Sánchez A. R., Mesa-Delgado A., 2014, *MNRAS*, **443**, 624

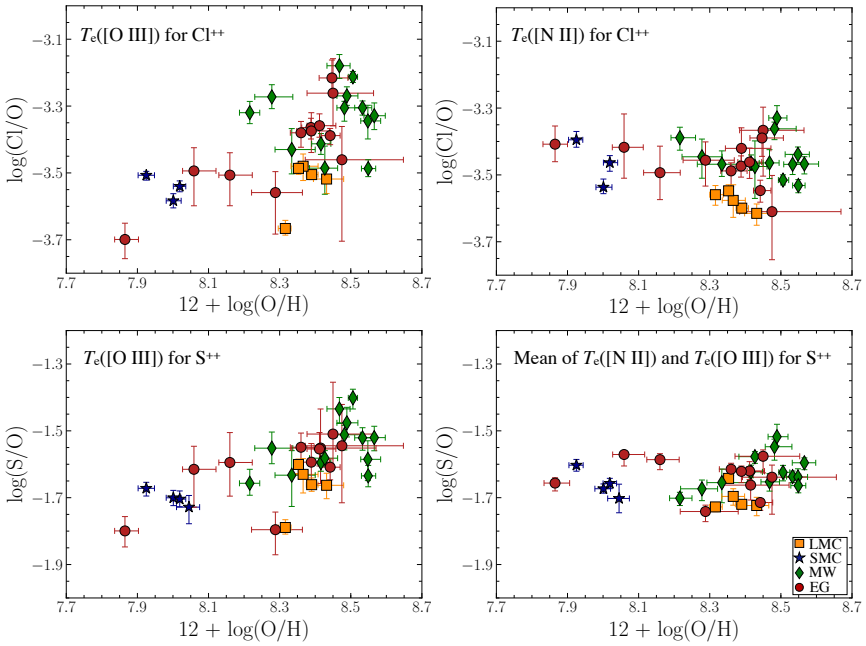

Figure 3. Cl/O and S/O abundance ratios as a function of O/H. The orange squares are LMC HII regions, the blue stars are SMC HII regions, the green diamonds are Galactic HII regions (MW), and the red circles are extragalactic HII regions (EG). The left plots use the traditional method to estimate the total abundance. In the right plots we use T_e([NII]) to calculate Cl^{++} and the mean of T_e([NII]) and T_e([OIII]) to determine S^{++}.

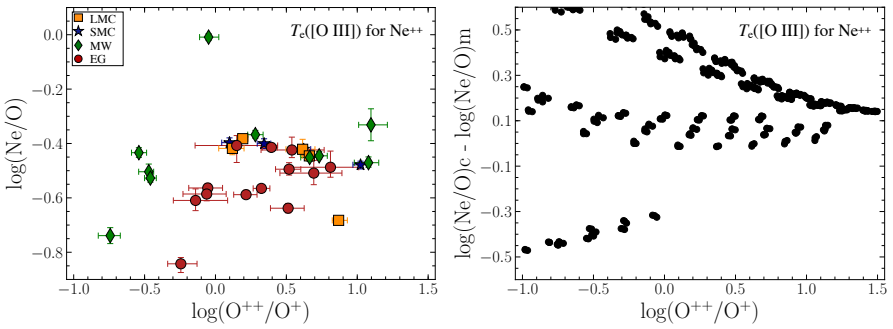

Figure 4. Left panel: Ne/O as a function of the degree of ionization. The color code is the same as in Figure 3. Right panel: differences between the values of Ne/O obtained from the analysis of the spectra predicted by photoionization models and the input abundance of the models (Reyes-Pérez et al., 2019, in preparation).

Esteban C., Peimbert M., García-Rojas J., Ruiz M. T., Peimbert A., Rodríguez M., 2004, *MNRAS*, **355**, 229
Filippenko A. V., 1982, *PASP*, **94**, 715
García-Rojas J., Esteban C., Peimbert A., Peimbert M., Rodríguez M., Ruiz M. T., 2005, *MNRAS*, **362**, 301
García-Rojas J., Esteban C., Peimbert A., Rodríguez M., Peimbert M., Ruiz M. T., 2007, *RevMexAA*, **43**, 3
García-Rojas J., Esteban C., Peimbert M., Costado M. T., Rodríguez M., Peimbert A., Ruiz M. T., 2006, *MNRAS*, **368**, 253
García-Rojas J., Esteban C., Peimbert M., Rodríguez M., Ruiz M. T., Peimbert A., 2004, *ApJS*, **153**, 501
Howarth I. D., 1983, *MNRAS*, **203**, 301
Izotov Y. I., Stasińska G., Meynet G., Guseva N. G., Thuan T. X., 2006, *A&A*, **448**, 955
Luridiana V., Morisset C., Shaw R. A., 2015, *A&A*, **573**, A42
Mesa-Delgado A., Esteban C., García-Rojas J., Luridiana V., Bautista M., Rodríguez M., López-Martín L., Peimbert M., 2009, *MNRAS*, **395**, 855
Nazé Y., Rauw G., Manfroid J., Chu Y.-H., Vreux J.-M., 2003, *A&A*, **408**, 171
O'Donnell J. E., 1994, *ApJ*, **422**, 158
Pagel B. E. J., Edmunds M. G., Fosbury R. A. E., Webster B. L., 1978, *MNRAS*, **184**, 569
Peimbert A., 2003, *ApJ*, **584**, 735
Peimbert M., Torres-Peimbert S., 1974, *ApJ*, **193**, 327
Stasińska G., Testor G., Heydari-Malayeri M., 1986, *A&A*, **170**, L4
Storey P. J., Hummer D. G., 1995, *MNRAS*, **272**, 41
Toribio San Cipriano L., García-Rojas J., Esteban C., Bresolin F., Peimbert M., 2016, *MNRAS*, **458**, 1866
Tsamis Y. G., Barlow M. J., Liu X.-W., Danziger I. J., Storey P. J., 2003, *MNRAS*, **338**, 687

Chemical Abundances in Gaseous Nebulae:
Open problems in Nebular astrophysics
AAA Workshop Series 11, 2019
M. Cardaci, G. Hägele & E. Pérez-Montero, eds.

Contributed Paper

The kinematic behaviour of optical recombination lines and collisionally excited lines in Galactic planetary nebulae

F. Ruiz-Escobedo[1], M. Peña[1], J. S. Rechy-García[1] and J. García-Rojas[2,3]

[1] *Instituto de Astronomía, Universidad Nacional Autónoma de México Apdo. Postal 70264, Ciudad de México, 04510, Mexico*
[2] *Instituto de Astrofísica de Canarias (IAC), E-38200, La Laguna, Tenerife, Spain*
[3] *Universidad de La Laguna, Dept. Astrofísica. E-38206, La Laguna, Tenerife, Spain*

Abstract.
In this work, we present some of the results from an analysis of the expansion velocities (v_{exp}) of Collisionally Excited Lines (CELs) and Optical Recombination Lines (ORLs) from a sample of 14 PNe with different characteristics (central stars types, ADFs, etc.), aiming to explore the possibility that these lines being emitted by a gas at different conditions inside each object.

Key words: galaxies: abundances — galaxies: ISM — techniques: imaging spectroscopy

1. Introduction

Planetary Nebulae (PNe) are one of the latest evolutionary stages of the low-intermediate mass stars. These objects are constituted by a hot evolved central star which is ionizing an expanding shell of gas, which was part of the stellar atmosphere and was ejected during the Asymptotic Giant Branch (AGB) phase. Because this gas is a low-density plasma, emission of collisionally excited lines (CELs) of heavy elements (C, N, O, Ne and others) and optical recombination lines (ORLs) of H, He and heavy elements can be found. In these objects it can be found an ionization structure, in which the highly ionized species are near to the central star and the lowly ionized species are farther away (Osterbrock & Ferland, 2006), and a velocity field, in which the expansion velocity increases with the distance to the central star, in agreement with hydrodynamical models (Schönberner & Steffen, 1999, 2000).
From photoionized regions spectra, physical conditions (electronic temperature and density) and ionic and total abundances can be derived. A well-known problem in the physics of photoionized regions is the existence of the Abundance Discrepancy Factor (ADF): for ions like O^{+2}, abundances derived using ORLs are larger than those derived using CELs. Typical values of ADF are of 2 for H

II and 3 for PNe (García-Rojas & Esteban, 2007), nevertheless, there are PNe in which the ADF may reach values up to 100 (McNabb et al., 2013; Wesson et al., 2018).
The origin of ADF is still an open problem, some of the proposals to explain it are the existence of temperature fluctuations in the plasma (Peimbert, 1967, 1971) and the presence of tiny metal-rich inclusions in a H-rich plasma (Liu et al., 2006, and references therein). Both proposals would imply that these lines are being emitted in different zones of the nebulae, because CELs have a stronger dependence of electronic temperature than ORLs, CELs are emitted in higher-temperature zones while ORLs emission arises from lower-temperature zones. Recent works by García-Rojas et al. (2016); Peña et al. (2017); Richer et al. (2013, 2017) have showed that CELs and ORLs have different spatial distribution and kinematical behaviour inside the PNe, expansion velocities of ORLs are lower than CELs, and ORLs emission seems to arises from inner parts of the nebulae.

2. Procedure

In this work, we performed an analysis of the nebular structure of a sample of 14 PNe, with different ADFs ($1.5 - 5.0$) and central stars types ([WC], *wels* and normal), to explore the possibility that CELs and ORLs being emitted by gas at different conditions. In this contribution, we present partial results of those presented during the Workshop, the complete results and a deeper analysis are presented in Peña et al. (2017).
We analysed the kinematical behaviour of both lines from high-resolution spectra. The spectra of 12 PNe were obtained with the Magellanic Inamori Kyocera Echelle (MIKE) spectrograph (Bernstein et al., 2003) attached to the 6.5 m Magellan telescope Clay at Las Campanas Observatory (LCO), Chile. MIKE provides a spectral resolution R$\sim$28,000 for a 1" slit width. These same data were used to derive the physical conditions, ionic abundances, total abundances and ADFs for these objects (García-Rojas et al., 2009, 2012, 2013). Data used for the rest of the sample, NGC 7009 and NGC 3918, were obtained from Richer et al. (2013) and García-Rojas et al. (2015), respectively.
Given the high resolution of our spectra, the emission lines are resolved. In several cases the lines are split, allowing us to observe the blue and red components from the front and back zones of the expanding shells of the nebula (see Figure 1 *Left*); in other cases, the line profiles present a single component or show evidence of the presence of several overlapped components. From all the spectra in the sample, we used IRAF task SPLOT to determine the observed central wavelength and the Full-Width Half Maximum (FWHM) of several CELs and ORLs by adjusting a Gaussian profile to each line, or two, to deblend the components of split lines. Line widths were corrected by effects of the instrumental widths, considering that they add in quadrature. Thermal broadening was not corrected, thus, the lines include the contributions of thermal broadening, turbulence and physical structure of the nebulae along the line of view.
For every split line, the velocities of the red and the blue components were calculated using the Doppler effect, then the expansion velocities v_{exp} were calculated as half of the difference between both components. In the case of lines with a

single profile, the FWHM was transformed into v_{exp} by multiplying it by the half of the light speed.
Expansion velocities were measured for all the available CELs and ORLs (e.g., O^{+}, N^{+}, Ne^{+2}, etc.) in each spectrum, and the average v_{exp} values were calculated for CELs and ORLs separately. The reported errors correspond to 1σ deviation from average. Finally, we constructed plots comparing v_{exp} of the ions as a function of the Ionization Potential (IP), which is representative of the distance of the ion relative to the central star (Figure 1 *Right*).

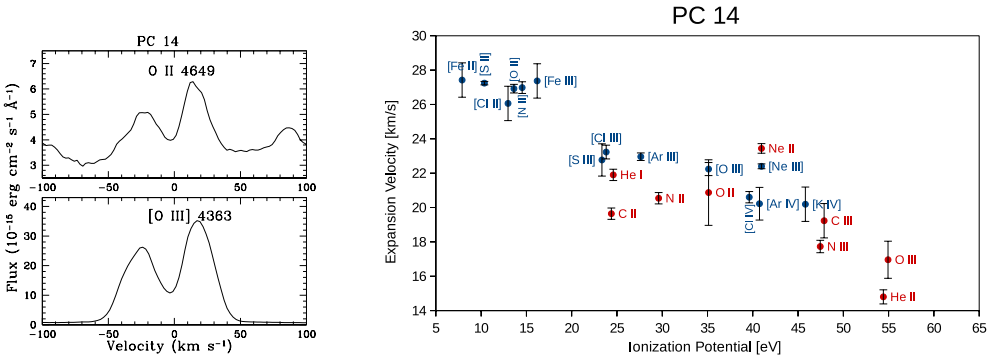

Figure 1. *Left:* Line profiles of O II λ4649 (*up*) and [O III] λ4363 (*below*) lines of PC 14. Al line profiles in this PN are split (from Figure 1 by Peña et al. (2017)). *Right:* v_{exp} as a function of IP for all CELs (blue dots) and ORLs (red) available in PC 14 (from Figure 3 by Peña et al. (2017)).

3. Results and discussion

Figure 1 *Right* shows the existence of a structure in the velocity field inside an expanding nebula, PN PC 14: ions with lower IP have higher v_{exp} than those ions with higher IP. In this object, this gradient of expansion velocities is clearly visible with the CELs (blue dots), the low ionized species like [O II], [Fe II], [Cl II], [N II] and [S II] present $v_{exp} \sim 27$ km s^{-1}; meanwhile the high ionized species like [Ar IV], [Cl IV] and [K IV] present $v_{exp} \sim 20$ km s^{-1}. In the other side, there is not a clear gradient in expansion velocities derived from ORLs (red dots): their v_{exp} lies between $22 - 15$ km s^{-1}, however, their velocities are systematically lower than CELs.
It was possible to compare the v_{exp} of CELs and ORLs of O^{+2} in all the PNe of the sample. In most of cases, they do not match: in 7 objects v_{exp}([O III]) $>$ v_{exp}(O II) , in 3 objects v_{exp}([O II]) $<$ v_{exp}(O II) and in 4 objects v_{exp}([O III]) $=$ v_{exp}(O II), within the errors (Table 1). The average difference between v_{exp}([O III]) and v_{exp}(O II) in the whole sample is about 2.70 km s^{-1}.

Name	C. Star	ADF	v_{exp}([O III])	v_{exp}(O II)
Cn 1-5	[WO 4]p	1.90	26.45±1.18	11.22 ±0.23
Hb 4	[WO 3]	3.70	16.04±1.04	11.22±0.23
M1-25	[WC 5-6]	1.51	19.17±0.30	20.16±0.29
M3-15	[WC 4]	2.34	11.93±0.41	14.20±1.00
M1-32	[WO 4]p	2.34	12.53±0.68	8.39±0.26
M1-61	wels	1.66	15.03±0.39	14.66±0.90
NGC 7009	pn	5.00	19.08±0.74	18.03±0.39
NGC 2867	[WO 2]	1.58	27.29±0.30	24.50±0.04
Pe 1-1	[WO 4]	1.70	11.18±0.08	10.89±0.10
PB 8	[WC/WN]	2.19	14.53±0.16	12.79±1.06
NGC 3918	pn	1.80	13.93±0.41	15.23±0.09
He 2-86	[WC 4]	1.95	7.86±0.30	7.51±0.85
PC 14	[WO 4]	1.94	22.24±0.38	20.87±1.91
M1-30	wels	2.14	10.30±0.02	9.24±0.45

Table 1. Characteristic of the PNe of the sample (central star type and ADF) and differences between v_{exp} of CELs and ORLs for O^{+2}.

4. Conclusions

We performed a kinematical analysis of CELs and ORLs from a sample of 14 PNe with different characteristics. We found that in almost all cases CELs and ORLs do not have the same kinematical behaviour: CELs present a gradient in velocity as a function of the distance to the central star, given by the ionization potential (IP), which is expected for an expanding plasma in ionization equilibrium. The velocity field also is accelerating outwards, in agreement with hydrodynamical models. ORLs do not present this behaviour, in almost all cases they have lower v_{exp} than CELs even for the same ion, which indicates that they are being emitted in inner zones of the nebulae. It was also found that, in general, FWHM of CELs are larger than FWHM of ORLs; this can be interpreted as ORLs being emitted in zones of lower temperature than CELs.
The results of our work, together with the results from Richer et al. (2013, 2017), support the idea of the existence of two different plasmas in the PNe with different physical conditions and abundances: one gas, H-rich, emitting CELs and another gas, cooler and H-poor, emitting ORLs.

Acknowledgments. This work has received financial support from grant UNAM-PAPIIT IN103117. FRE acknowledges the recipt of a schoolarship from CONACyT, México.

References

Bernstein R., Shectman S. A., Gunnels S. M., Mochnacki S., Athey A. E., 2003, M. Iye and A. F. M. Moorwood (eds.), *Instrument Design and Performance for Optical/Infrared Ground-based Telescopes*, Vol. 4841 of *Proc. SPIEJ*, pp 1694–1704

García-Rojas J., Corradi R. L. M., Monteiro H., Jones D., Rodríguez-Gil P., Cabrera-Lavers A., 2016, *ApJL*, **824**, L27
García-Rojas J., Esteban C., 2007, *ApJ*, **670**, 457
García-Rojas J., Madonna S., Luridiana V., Sterling N. C., Morisset C., Delgado-Inglada G., Toribio San Cipriano L., 2015, *MNRAS*, **452**, 2606
García-Rojas J., Peña M., Morisset C., Delgado-Inglada G., Mesa-Delgado A., Ruiz M. T., 2013, *A&A*, **558**, A122
García-Rojas J., Peña M., Morisset C., Mesa-Delgado A., Ruiz M. T., 2012, *A&A*, **538**, A54
García-Rojas J., Peña M., Peimbert A., 2009, *A&A*, **496**, 139
Liu X.-W., Barlow M. J., Zhang Y., Bastin R. J., Storey P. J., 2006, *MNRAS*, **368**, 1959
McNabb I. A., Fang X., Liu X.-W., Bastin R. J., Storey P. J., 2013, *MNRAS*, **428**, 3443
Osterbrock D. E., Ferland G. J., 2006, *Astrophysics of gaseous nebulae and active galactic nuclei*
Peña M., Ruiz-Escobedo F., Rechy-García J. S., García-Rojas J., 2017, *MNRAS*, **472**, 1182
Peimbert M., 1967, *ApJ*, **150**, 825
Peimbert M., 1971, *Boletin de los Observatorios Tonantzintla y Tacubaya*, **6**, 29
Richer M. G., Georgiev L., Arrieta A., Torres-Peimbert S., 2013, *ApJ*, **773**, 133
Richer M. G., Suárez G., López J. A., García Díaz M. T., 2017, *AJ*, **153**, 140
Schönberner D., Steffen M., 1999, E. Guenther, B. Stecklum, and S. Klose (eds.), *Optical and Infrared Spectroscopy of Circumstellar Matter*, Vol. 188 of *Astronomical Society of the Pacific Conference Series*, p. 281
Schönberner D., Steffen M., 2000, J. H. Kastner, N. Soker, and S. Rappaport (eds.), *Asymmetrical Planetary Nebulae II: From Origins to Microstructures*, Vol. 199 of *Astronomical Society of the Pacific Conference Series*, p. 59
Wesson R., Jones D., García-Rojas J., Boffin H. M. J., Corradi R. L. M., 2018, *MNRAS*, **480**, 4589

Chemical Abundances in Gaseous Nebulae:
Open problems in Nebular astrophysics
AAA Workshop Series 11, 2019
M. Cardaci, G. Hägele & E. Pérez-Montero, eds.

Contributed Paper

The internal kinematic of star-forming regions in interacting galaxies

V. Firpo[1,2], D. Muthukrishna[3], F. Campuzano-Castro[4,5], G. Bosch[4,5], G. Hägele[4,5], S. Torres-Flores[2], & M. Cardaci[4,5]

[1]*Gemini Observatory, Southern Operations Centre,La Serena, Chile.*
[2]*Universidad de La Serena, La Serena, Chile.*
[3]*Institute of Astronomy, University of Cambridge, UK.*
[4]*Instituto de Astrofísica de La Plata, CONICET–UNLP, Argentina.*
[5]*Facultad de Ciencias Astronómicas y Geofísicas, Universidad Nacional de La Plata, Argentina.*

Abstract. Star formation processes can be found in colliding galaxies, where the gas compression can trigger the formation of giant star-forming regions. We present the results from a detailed kinematic analysis in a sample of HII regions located in three strongly interacting galaxies. The velocity dispersion and the luminosity of the multiple-components analyzed in the emission-line profiles suggest that these star-forming objects correspond to giant complexes. In addition, the star formation rates and the ionization state in these regions revealed the presence of ongoing star formation events.

galaxies: kinematics — star formation — ISM

1. Introduction

Interacting galaxies give us a laboratory to study star formation at different levels, ranging from small stellar clusters to Giant HII Regions (GHIIR). The interaction of galaxies increases the turbulence in HIIRs due to the continued accretion of gas onto the HIIRs plus the feedback through stellar winds and supernova explosions (Zaragoza-Cardiel et al., 2015). The knowledge of GHIIR currently remains poor. The early stages of the massive star-forming regions are short-lived, leaving little time for the study of their evolution. Furthermore, there are very few GHIIR per galaxy. Therefore, it is necessary to analyze in detail the few regions available in nearby galaxies and to link the global parameters of these regions with properties such as its gas kinematics, chemical abundances, evolutionary state, and stellar population, which will allow us to expand the study of the GHIIR. In this way, the observations of nearby GHIIRs, with large spectral range and high spectral resolution, provide an excellent laboratory for the study of the important feedback between these regions and their environment.

2. Observation

We have high-resolution spectroscopic from MIKE/echelle, Magellan Telescope (LCO). The spectral ranges (Blue: 3300 Å - 5100 Å, and Red: 4500 Å - 9300 Å) guarantee the measurement of [OII] 3727,29 Å to [SIII] $\lambda\lambda$9069,9532 Å. Resolution obtained at ∼6000 Å is 11∼ km/s (Blue: R∼25000 and Red: R∼20000).

3. Overview and Methodology

We analyze a sample of star-forming regions located in three strongly interacting galaxies NGC 6845, Ap 314, HGC 31.
The analysis of the ionized gaseous component is divided in two parts:

1) kinematical properties (following Firpo et al. (2005, 2010, 2011)): to study line profile asymmetries and multiple components present in the emission lines profiles, determine the radial velocities and the velocity dispersion, estimate luminosities and SFR, and verify the supersonic nature of the ionized gas.
2) physical properties (following Hägele et al. (2006, 2008, 2012)): we estimate electron density and temperature, chemical abundances, reddening, and ionization structure.

The detailed analysis after merging chemical and kinematical information obtained for the gaseous component is called *Chemodynamic* (Esteban & Vilchez, 1992). This analysis is done in the global emission and in the different kinematical components present in all emission-line profiles.

In this work, we present the preliminary results of the first part, where we study the internal kinematic of the ionized gas in six regions by analyzing the multiple kinematical components and the global emission, and confirming (or not) whether these regions have supersonic velocity dispersion.

We developed a complete Python code that automatically models all emission-lines (more-less 30) for all different regions. This code allow us to fit the emission-lines profiles calling the Non-Linear Least-Square Minimization and Curve-Fitting (LMFIT) Python package (Newville et al., 2014). Python's LMFIT iterates over solutions a few hundred times and allow us to obtain better solutions. To determine what is the maximum number of component to fit in the profiles, we use an Akaike Information Criterion indicator (AIC, Akaike, 1974) which allows testing the quality of the statistical model by comparing several models with different Gaussian components, and with different numbers of free parameters.

In summary, this code allows us:

- to find multiple components and/or asymmetric wings in the emission-line profiles,

- to obtain the radial velocities, velocity dispersion, fluxes, emission measure (EM) relative to the total line flux, and the global flux.
- to verify the supersonic nature of the ionized gas for the global and multiple components, and classify the regions as GHIIRs or not.
- to estimate Hα luminosity and Star Formation Rate (Kennicutt, 1998),
- to analyze the ionization source of the objects using the BPT diagnostic diagram (Baldwin et al., 1981),

4. Preliminary Results

High-resolution data are essential to study in detail the internal kinematic and the physical properties of these star forming regions. This data allow us to perform a multiple component analysis on the emission-lines (Firpo et al., 2019 in prep.), which will be enable us to develop a chemodynamical analysis of the strongest star-forming regions located in a sample of interacting systems.
The validity of the profile multiplicity and broadening is checked over the different emission lines. In Figure 4, left panels, we show the plots of the Hα multiple components fit. In the right panels we show the plots of the strongest emission-lines fit. The evident similarity among the different fits in the emission-lines profiles confirms the presence of a complex kinematic structure in all regions.
The width of the emission line profiles give us information regarding supersonic motions. Table 1 shows the average radial velocities and velocity dispersion for the six regions. The velocity dispersion was corrected by instrumental and termal dispersion. Taking account the uncertainties, the global component and the different kinematical components in all regions present supersonic velocity dispersion, typically found in GHIIRs. The exception is the Narrow 1 component in HCG 31-C region, that we have estimated a velocity dispersion of 7.1 ± 4.2 km s^{-1}.

Table 1. Average radial velocities and velocity dispersion for different components in all regions.

	v_r (km s^{-1})	σ (km s^{-1})	v_r (km s^{-1})	σ (km s^{-1})
	HCG31-A		HCG31-C	
Narrow 1	4023.0 ± 1.5	16.3 ± 2.7	3918.3 ± 3.3	7.1 ± 4.2
Narrow 2	4001.7 ± 3.1	40.5 ± 2.3	3975.2 ± 2.0	40.4 ± 2.2
Broad	3977.9 ± 4.6	94.2 ± 4.1	4006.9 ± 2.3	87.6 ± 6.6
	NGC6845-7		NGC6845-26	
Narrow 1	6312.4 ± 2.4	16.7 ± 1.5	6169.2 ± 1.2	14.7 ± 2.5
Narrow 2	6348.1 ± 2.8	11.8 ± 1.5	6192.4 ± 3.2	49.7 ± 2.7
Broad	6327.6 ± 1.8	55.2 ± 1.9	6195.8 ± 5.3	125.4 ± 10.6
	Arp314-NED02		Arp314-NED02-off	
Narrow 1	3651.3 ± 1.5	35.7 ± 3.5	3655.8 ± 1.9	37.0 ± 2.7
Narrow 2	3663.5 ± 2.0	13.1 ± 2.3	3663.9 ± 2.2	15.9 ± 2.5
Broad	3644.9 ± 8.9	71.3 ± 7.8	3651.9 ± 7.6	71.0 ± 3.4

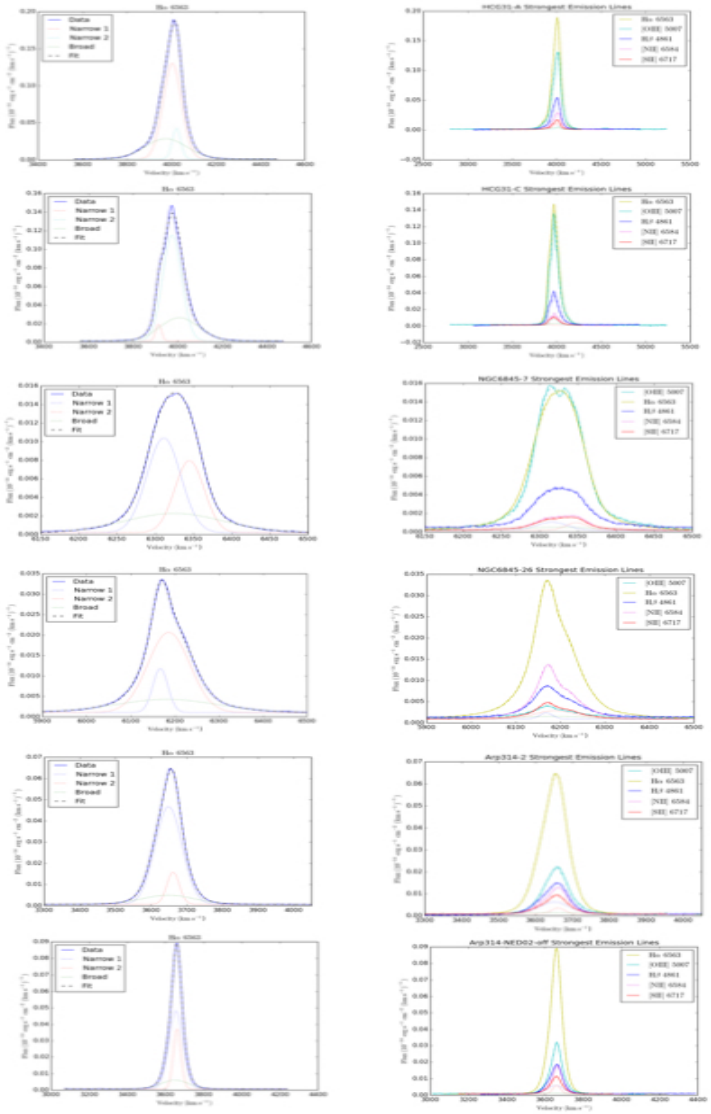

Figure 1. Left panels: Hα multiple components fit. Right panels: The strongest emission-lines fit.

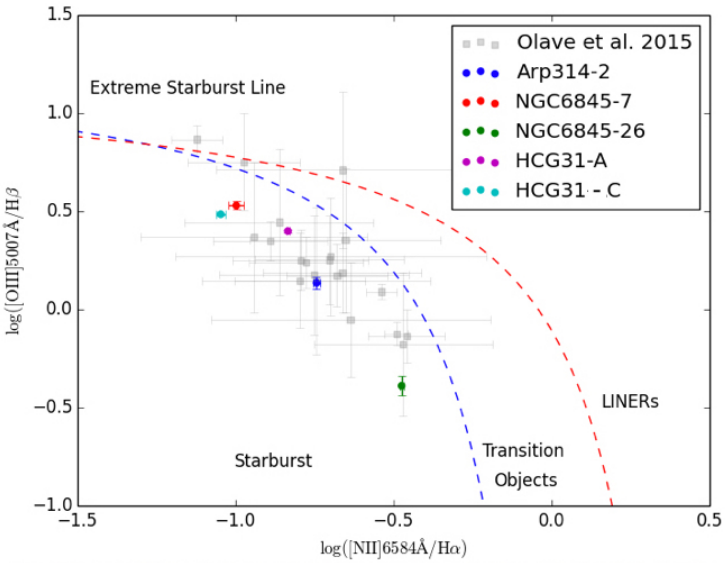

Figure 2. BPT diagnostic diagram for the global Gaussian component of each star-forming region. The regions studied in Olave-Rojas et al. (2015) are overlapped in grey squares.

In Figure 4, we show the BPT diagnostic diagram for the global Gaussian component of each star-forming region. This diagnostic diagram shows that all studied regions are ionized by massive stars.
In table 2, we show the SFR and Hα luminosities for all regions. This values are typical of giant star-forming complexes.

Table 2. SFR and logaritm of Hα luminosities for the six regions.

Region Name	SFR ($M_\odot$ yr^{-1})	log(L(Hα)) ($ergs^{-1}$)
HCG31-A	0.42 ± 0.003	40.9 ± 0.003
HCG31-C	0.35 ± 0.004	40.8 ± 0.005
NGC6845-7	0.04 ± 0.001	39.9 ± 0.006
NGC6845-26	0.08 ± 0.000	40.2 ± 0.002
Arp314-NED02	0.11 ± 0.001	40.3 ± 0.003
Arp314-NED02-off	0.13 ± 0.001	40.4 ± 0.005

Acknowledgments. VF acknowledges support from CONICYT Astronomy Program-2015 Research Fellow GEMINI-CONICYT (32RF0002).

References

Akaike H., 1974, *IEEE Transactions on Automatic Control*, **19**, 716
Baldwin J. A., Phillips M. M., Terlevich R., 1981, *PASP*, **93**, 5
Esteban C., Vilchez J. M., 1992, *ApJ*, **390**, 536
Firpo V., Bosch G., Hägele G. F., Díaz Á. I., Morrell N., 2011, *MNRAS*, **414**, 3288
Firpo V., Bosch G., Hägele G. F., Morrell N., 2010, *MNRAS*, **406**, 1094
Firpo V., Bosch G., Morrell N., 2005, *MNRAS*, **356**, 1357
Hägele G. F., Díaz Á. I., Terlevich E., Terlevich R., Pérez-Montero E., Cardaci M. V., 2008, *MNRAS*, **383**, 209
Hägele G. F., Firpo V., Bosch G., Díaz Á. I., Morrell N., 2012, *MNRAS*, **422**, 3475
Hägele G. F., Pérez-Montero E., Díaz Á. I., Terlevich E., Terlevich R., 2006, *MNRAS*, **372**, 293
Kennicutt Jr. R. C., 1998, *ARA&A*, **36**, 189
Newville M., Stensitzki T., Allen D. B., Ingargiola A., 2014, *LMFIT: Non-Linear Least-Square Minimization and Curve-Fitting for Python*
Olave-Rojas D., Torres-Flores S., Carrasco E. R., Mendes de Oliveira C., de Mello D. F., Scarano S., 2015, *MNRAS*, **453**, 2808
Zaragoza-Cardiel J., Beckman J. E., Font J., García-Lorenzo B., Camps-Fariña A., Fathi K., James P. A., Erroz-Ferrer S., Barrera-Ballesteros J., Cisternas M., 2015, *MNRAS*, **451**, 1307

Chemical Abundances in Gaseous Nebulae:
Open problems in Nebular astrophysics
AAA Workshop Series 11, 2019
M. Cardaci, G. Hägele & E. Pérez-Montero, eds.

Contributed Paper

Exploring the electron density in planetary nebulae

L. Juan de Dios[1] and M. Rodríguez[1]

[1]*Instituto Nacional de Astrofísica, Óptica y Electrónica (INAOE), Apdo. Postal 51 y 216, Puebla, Mexico*

Abstract. We explore several issues related to the determination of the electron density and the density structure of planetary nebulae (PNe). We use a sample of 46 objects with deep spectra that allow the calculation of the electron density from four diagnostics based on ions that predominate in different areas of the nebula: [SII], [OII], [ClIII], and [ArIV]. We compare our results with those obtained from photoionization models characterized by different density structures. We also explore the impact that different atomic data have on the results. The final objectives are determining what density structures can be used to characterize PNe and which atomic data are working better.

Key words: planetary nebulae — atomic data

1. Introduction

The electron density is a fundamental parameter needed to characterize a planetary nebula (PN) and to derive its chemical composition. In the optical range the density diagnostics more commonly used are [SII] λ6716/λ6731, [OII] λ3726/λ3729, [ClIII] λ5518/λ5538, and [ArIV] λ4711/λ4740. These diagnostics sample different zones of the PN and can give us a rough idea of the density structure of these objects.

Past determinations of electron density using different samples of PNe have found different density structures (e.g. Saraph & Seaton, 1970; Aller & Epps, 1976; Stanghellini & Kaler, 1989; Copetti & Writzl, 2002; Wang et al., 2004). This can be attributed in part to the different procedures followed by different authors, but also to changes in the atomic data used in the calculations since, as shown in Juan de Dios & Rodríguez (2017), the selection of transition probabilities and collision strengths has a significant impact on the values derived for the physical conditions. However, the available studies use fixed sets of atomic data, or explore the effect of changing the data for just one of the ions.

Even if we had a perfect knowledge of the atomic data, the electron densities obtained from different diagnostics will not arise only from the real density structure in the objects. The results will also be affected by the uncertainties in the line ratios, which introduce biases for densities near the limits of validity of the diagnostics. This is especially important at high densities, where the diagnostics are very sensitive to small variations in the line ratio. Another thing to take

into account is the effect of the critical densities of the upper levels of the lines used in the diagnostic (Rubin, 1989). In the presence of density variations, the emission of those lines that have low critical densities will arise mostly from the regions of lower density.
Here we use a sample of 46 PNe whose available spectra have the four density diagnostics listed above, along with photoionization models with different density structures to explore these issues.

2. Method

We have selected a sample of 46 PNe with available optical spectra from the literature. We used as selection criteria the presence in the published spectra of lines belonging to the four most used density diagnostics, [SII], [OII], [ClIII], and [ArIV], and the two most used temperature diagnostics, [NII] $\lambda5755/(\lambda6548+\lambda6583)$ and [OIII $\lambda4363/(\lambda4959+\lambda5007)$. The sample objects cover a wide range in characteristics such as excitation degree and electron density, and in that sense can be considered representative of the population of ionized nebulae.
We have also constructed a grid of photoionization models with different neutral hydrogen density structures using the photoionization code Cloudy (Ferland et al., 2017). The free parameters are the effective temperature (for which we use several values in the range $T_{\rm eff}$ = 30000–240000 K) and the luminosity (values in the range $L_{\odot}$ = 36.88–37.588) of the central star, the inner nebular radius (R_{in}[cm] = 16.70–18.00), and the hydrogen density of the gas ($n_{\rm H}$). We use $n_{\rm H} = 10^2$–10^5 cm^{-3} for the constant density models and an initial $n_{\rm H} = 10^2$–10^4 cm^{-3} with exponents from -1.5 to 4 for the power law models.
We change the transition probabilities and collision strengths that Cloudy uses by default since we want to explore the effects of changes in the atomic data in our determinations of the electron density. Besides we have also detected some problems with the atomic data used by default (Juan de Dios & Rodríguez, 2019, in prep.). We have selected two sets of transition probabilities that do not seem to have problems according to Juan de Dios & Rodríguez (2017) to compute the models and analyze our results. Table 1 shows the atomic data used in the calculations. We change only the transition probabilities since these are the most critical atomic data in the density calculations. To analyze the models we extract the lines needed to determine the electron density and temperature and perform the calculations using Pyneb (Luridiana et al., 2015) following the same procedure that we use for the objects.

3. Results

For each PN and each model, we calculate an average density using the four diagnostics. Figure 1 shows the differences from the mean implied by the four density diagnostics plotted against the mean density when the calculations are performed with the atomic data sets A (left panels) and B (right panels). The top panels show the results obtained for the objects in the sample, the middle panels the results obtained for the constant density models and the bottom panels the results obtained for the power law models. We can see that the density structure of the objects changes slightly with the two sets of atomic data, especially for

Table 1. Atomic data sets used in our calculations.

Ion	Transition probabilities		Collision strengths
	Set A	Set B	Sets A & B
S^{+}	PKW09	VVF96-MZ82	TZ10
O^{+}	FFT04	Z82-WFD96	P76-McLB93-v1
Cl^{++}	M83	Fal99	BZ89
Ar^{+3}	MZ82	MZ82	RB97

BZ89: Butler & Zeippen (1989), Fal99: Fritzsche et al. (1999), FFT04: Fischer & Tachiev (2004), M83: Mendoza (1983), McLB93: McLaughlin & Bell (1993), MZ82a: Mendoza & Zeippen (1982), P76:Pradhan (1976), PKW09: Podobedova et al. (2009), RB97: Ramsbottom & Bell (1997) TZ10: Tayal & Zatsarinny (2010), VVF96: Verner et al. (1996), WFD96: Wiese et al. (1996).

[SII], but the models lead to very similar 'observed' structures with the two data sets for both types of density structures. On the other hand, none of the models reproduce the behavior observed in the objects.

We have also interchanged the atomic data sets used to model and analyze the results, so that the models computed with set A are analyzed with set B and vice versa. This is equivalent to having observations, resulting from the real atomic data, which are analyzed using a set of calculated atomic data. Figure 2 shows the results. We can see that in this case, the behavior of the models is very similar to the one found for the objects when the same atomic data is used for the analysis in both observations and models. This implies, on the one hand, that the density structure derived for the objects depends strongly on the atomic data used in the calculations, and, on the other hand, that the density structures obtained from models of different characteristics might be used to determine which sets of available atomic data lead to reasonable results.

The effects of observational uncertainties can be explored by introducing errors in the line intensities predicted by the models. We are also exploring the density structures implied by photoionization models that include density variations by combining models that have different input densities. These results and more details on the ones shown here will be presented elsewhere (Juan de Dios & Rodríguez, 2019, in prep.).

4. Conclusions

We study different issues related to the density structures of PNe using a sample of objects from the literature whose observed spectra provide measurements of four density diagnostics along with photoionization models characterized by different density structures. Observations and models are both analyzed in the same way and using the same atomic data. We find that the models lead to similar density structures independently of the atomic data used in the calculations, but do not reproduce the behavior shown by the objects. However, when different data sets are used in the computation of the models and in the analysis of their predicted spectra, the density structures found for the models change sig-

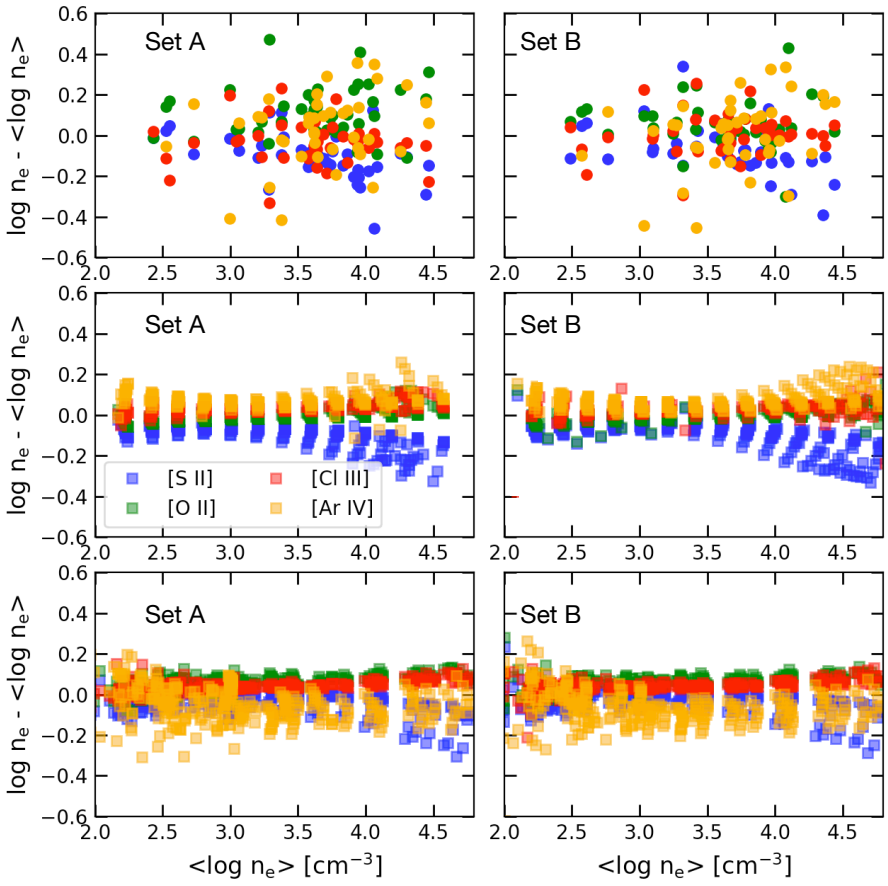

Figure 1. Differences from the mean density of the four density diagnostics plotted as a function of the mean density. The calculations use set A of atomic data (left panels) and set B (right panels). Top panels: results obtained for the objects in the sample; middle panels: results obtained for the constant density models; bottom panels: results obtained for the power law models.

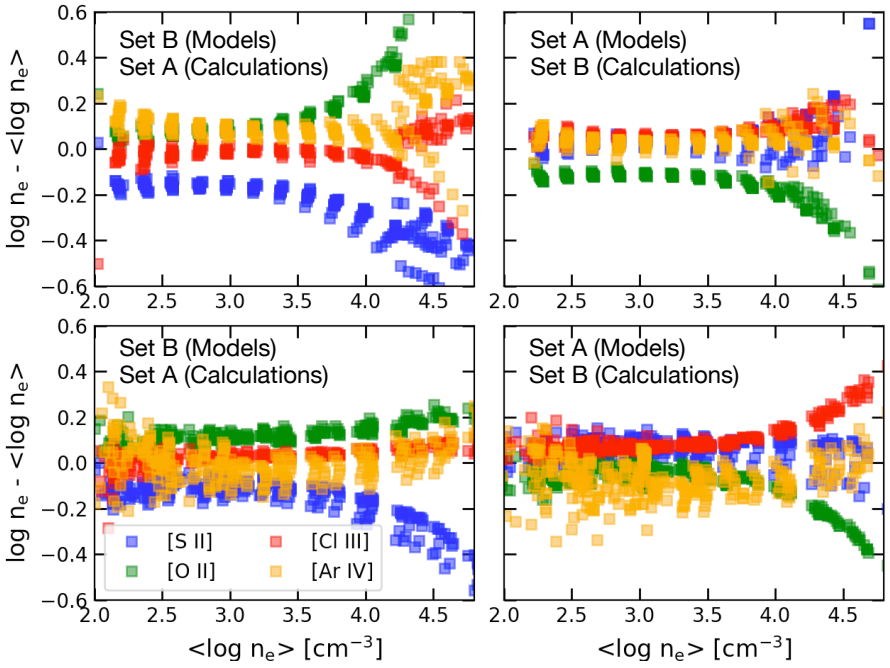

Figure 2. Differences from the mean of the four density diagnostics plotted against the mean electron density when the atomic data used in the models and in the analysis of their spectra are interchanged. Top panels: results obtained for the constant density models; bottom panels: results obtained for the power law models.

nificantly and resemble the ones derived for the objects analyzed with the same atomic data. We conclude that the density structures observed in the objects depend strongly on the atomic data used in the calculations. We will explore more complex structures by combining models with different densities. These results will allow us to know more about the density structures of the objects and to determine which atomic data are working better.

Acknowledgments. We acknowledge support from Mexican CONACYT grant CB-2014-240562. LJdD acknowledges support from CONACYT grant 298356.

References

Aller L. H., Epps H. W., 1976, *ApJ*, **204**, 445
Butler K., Zeippen C. J., 1989, *A&A*, **208**, 337
Copetti M. V. F., Writzl B. C., 2002, *A&A*, **382**, 282
Ferland G. J., Chatzikos M., Guzmán F., Lykins M. L., van Hoof P. A. M., Williams R. J. R., Abel N. P., Badnell N. R., Keenan F. P., Porter R. L., Stancil P. C., 2017, *RevMexAA*, **53**, 385
Fischer C. F., Tachiev G., 2004, *At. Data and Nucl. Data Tables*, **87(1)**, 1
Fritzsche S., Fricke B., Geschke D., Heitmann A., Sienkiewicz J. E., 1999, *ApJ*, **518**, 994
Juan de Dios L., Rodríguez M., 2017, *MNRAS*, **469**, 1036
Luridiana V., Morisset C., Shaw R. A., 2015, *A&A*, **573**, A42
McLaughlin B. M., Bell K. L., 1993, *ApJ*, **408**, 753
Mendoza C., 1983, D. R. Flower (ed.), *Planetary Nebulae*, Vol. 103 of *IAU Symposium*, pp 143–172
Mendoza C., Zeippen C. J., 1982, *MNRAS*, **198**, 127
Podobedova L. I., Kelleher D. E., Wiese W. L., 2009, *Journal of Physical and Chemical Reference Data*, **38(2)**, 171
Pradhan A. K., 1976, *MNRAS*, **177**, 31
Ramsbottom C. A., Bell K. L., 1997, *At. Data and Nucl. Data Tables*, **66**, 65
Rubin R. H., 1989, *ApJS*, **69**, 897
Saraph H. E., Seaton M. J., 1970, *MNRAS*, **148**, 367
Stanghellini L., Kaler J. B., 1989, *ApJ*, **343**, 811
Tayal S. S., Zatsarinny O., 2010, *ApJS*, **188**, 32
Verner D. A., Verner E. M., Ferland G. J., 1996, *At. Data and Nucl. Data Tables*, **64**, 1
Wang W., Liu X.-W., Zhang Y., Barlow M. J., 2004, *A&A*, **427**, 873
Wiese W. L., Fuhr J. R., Deters T. M., 1996, *Journal of Physical and Chemical Reference Data*, **Monograph 7**, 403

Chemical Abundances in Gaseous Nebulae:
Open problems in Nebular astrophysics
AAA Workshop Series 11, 2019
M. Cardaci, G. Hägele & E. Pérez-Montero, eds.

Contributed Paper

Oxygen abundance gradients in nearby galaxies and the performance of strong-line methods

K. Z. Arellano-Córdova[1,2,3] and M. Rodríguez[1]

[1] *Instituto Nacional de Astrofísica, Óptica y Electrónica (INAOE), Apdo. Postal 51 y 216, Puebla, Mexico*
[2] *Instituto de Astrofísica de Canarias, E-38200 La Laguna, Tenerife, Spain*
[3] *Departamento de Astrofísica, Universidad de La Laguna, E-38206 La Laguna, Tenerife, Spain*

Abstract.
We explore the sensitivity to observational problems of the direct method and the P, ONS, C, O3N2 and N2 strong-line methods by analyzing the dispersions around the metallicity gradient implied by these methods using a large sample of HII regions from nearby galaxies. For each galaxy, we use observations of different authors that are likely to be affected by observational effects in different ways. Our results show that the direct method and the P method introduce large dispersions around the metallicity gradient, of 0.11-0.21 dex, whereas the ONS, C, O3N2, and N2 methods lead to lower dispersions, in the range of 0.06-0.11 dex. We also explore the performance of strong-line methods using a sample of 154 spectra of HII regions with measurements of T_e[NII] and T_e[OIII] compiled from the literature. We find that the P method provides differences in O/H with respect to the direct method that go up to 0.66 dex. The ONS, C, O3N2, and N2 methods lead to differences that reach 0.4 dex.

Key words: ISM: abundances — HII regions — galaxies

1. Introduction

Strong-line methods are used to calculate the oxygen abundance in HII regions when the weak lines needed to derive electron temperatures, such as [OIII] λ4363 or [NII] λ5755, are not available, making it impossible to use the direct method. Such methods are calibrated using observational data, photoionization models or a combination of both (see, e.g., López-Sánchez & Esteban 2010, and references therein). There are potential problems related to the calibration and application of strong-line methods, for instance, their dependence on the degree of ionization and the N/O abundance ratio, their reliance on temperature relations, mainly between T_e[NII] and T_e[OIII], the fact that the calibration sample might not cover a wide range of physical properties of HII regions, and the observational uncertainties in the line intensity ratios. The effects of some of these problems

can be explored by comparing the abundances implied by strong-line methods with those derived with the direct method using a large sample of HII regions. On the other hand, the observational uncertainties are generally assumed to be small for strong-line methods, but their effects can be important and can be studied by analyzing the dispersion that the methods introduce around the oxygen abundance gradient in spiral galaxies when observations obtained by different authors are used in the calculations. Arellano-Córdova et al. (2016) use different observations of HII regions in M81 and find that the direct method and the P method (Pilyugin & Thuan 2005) lead to the highest dispersions around the metallicity gradient in comparison with other strong-line methods like the C and N2 methods of Pilyugin et al. (2012) and Marino et al. (2013), respectively. Arellano-Córdova et al. (2016) argue that this high dispersion can be explained by the sensitivity of the methods to the line ratios that are more likely affected by observational problems. For example, the [OII] $\lambda3727/\mathrm{H}\beta$ line ratio can be easily affected by problems with the flux calibration, atmospheric differential refraction or the extinction correction. The [NII] $(\lambda6548 + \lambda6584)/\lambda5755$ and [OIII] $(\lambda4959 + \lambda5007)/\lambda4363$ line ratios will be affected by problems with the measurement of the weak [OIII] $\lambda4363$ and [NII] $\lambda5755$ lines.
Here we expand on the work of Arellano-Córdova et al. (2016) by applying the same analysis to four other spiral galaxies. We also study the perfomance of several strong-line methods by comparing their results with those implied by the direct method.

2. Sample and methodology

In order to study the sensitivity of the direct method and some strong-line methods to observational problems, we have compiled a large number of spectra of HII regions obtained by different authors in nearby galaxies. The sample comprises 132 HII regions in M31, 63 in M33, 110 in M101 and 50 in NGC 300. The sample objects cover different ranges of galactocentric distances: 4–20 kpc in M31, 0.2–8 kpc in M33, 2–33 kpc in M101, and 2–33 kpc in NGC 300. Most of the values of the galactocentric distances were taken from the literature, but we have recalculated the distances for some regions in order to have a homogenous determination for each galaxy. We have also gathered a sample of 154 observations of 131 HII regions with measurements of T_e[NII] and T_e[OIII] (Arellano-Córdova & Rodríguez, 2019, in prep.), which allow us to explore the performance of some strong-line methods.
We use the package PyNeb (Luridiana et al. 2015) to calculate the physical conditions and chemical abundances in a homogenous way and using the same atomic data. We determine the electron temperature using the line intensity ratios [NII] $(\lambda6548+\lambda6584)/\lambda5755$ and [OIII] $(\lambda4959+\lambda5007)/\lambda4363$ to calculate T_e[NII] and T_e[OIII]. To compute the total oxygen abundances, we adopt a two-zone ionization structure characterized by T_e[NII] for O^+ and by T_e[OIII] for O^{++}. We obtain the total oxygen abundances by adding the contribution of both ions: $\mathrm{O/H} = \mathrm{O}^+/\mathrm{H}^+ + \mathrm{O}^{++}/\mathrm{H}^+$. We have also calculated the metallicity for the two samples of objects using the P method of Pilyugin & Thuan (2005), the ONS method of Pilyugin et al. (2010), the C method of Pilyugin et al. (2012) and the O3N2 and N2 methods of Marino et al. (2013).

3. The dispersion around the metallicity gradient in nearby galaxies

Since the spectra we have gathered for HII regions in M31, M33, M101 and NGC 300 were observed by different authors, it is likely that they are affected by various observational problems in different amounts. This allows us to study the sensitivity of the direct method and some strong-line methods to potential observational problems. To do that, we study the dispersion around the metallicity gradient implied by the direct method and the P, ONS, C, O3N2 and N2 methods (Pilyugin & Thuan 2005; Pilyugin et al. 2010, 2012; Marino et al. 2013). In order to estimate the metallicity gradient, we fit straight lines with the least-squares method. In Figure 1, we show our results for the metallicity gradient as a function of the galactocentric distance for the sample of HII regions in NGC 300. Figure 1 displays the results implied by the direct method and the P, C, and N2 methods. The ONS and O3N2 methods behave in a similar way to the C and N2 methods. The different symbols indicate the references for the observational data. For NGC 300, we find that the direct method and the P method provide the largest dispersions around the gradient, 0.14 dex and 0.17 dex, respectively, whereas the ONS, C, O3N2, and N2 methods provide dispersions around the gradient ranging from 0.08 dex to 0.10 dex. Note that the different datasets of observations have in general different behaviors.

Our results for M31, M33 and M101 show similar dispersions around the gradient for the direct method and the P method, ranging from 0.11 dex to 0.21 dex. These results are in agreement with the one previously reported by Arellano-Córdova et al. (2016) for M81. This indicates that the quality of the spectra required to apply effectively these methods is sometimes underestimated. On the other hand, the methods most robust to observational problems are the ONS, C, O3N2, and N2 methods, with dispersion values ranging from 0.06 dex to 0.11 dex. However, this does not imply that these methods provide the best determinations of the oxygen abundance, since their performance depends on their calibration and on the effects of variations in the N/O abundance ratio.

3.1. The performance of the P, ONS, C, O3N2 and N2 methods

We use a sample of 154 observations of 131 HII regions with measurements of T_e[NII] and T_e[OIII] to study the performance of some strong-line methods. To do that, we calculate the differences between the metallicity derived with the strong-line methods and the one implied by the direct method and study their behavior as a function of the degree of ionization measured with P = [OIII] $\lambda\lambda$4959,5007/([OII] λ3727 + [OIII] $\lambda\lambda$4959,5007). Figure 2 shows the differences obtained for the P, C, and N2 methods as a function of the degree of ionization. The circles show our sample of extragalactic HII regions color-coded with their metallicity. We show with different symbols (stars) the results obtained for Galactic HII regions, since their spectra correspond to a small region of the nebula and they can behave in a different way. We find that the P method introduces metallicity differences of up to 0.66 dex, while the ONS and C methods show differences that go up to 0.4 dex. The O3N2 and N2 methods also provide differences that go up to 0.4 dex. Figure 2 also shows that the differences in the oxygen abundance have a slight dependence on the degree of ionization and on the metallicity.

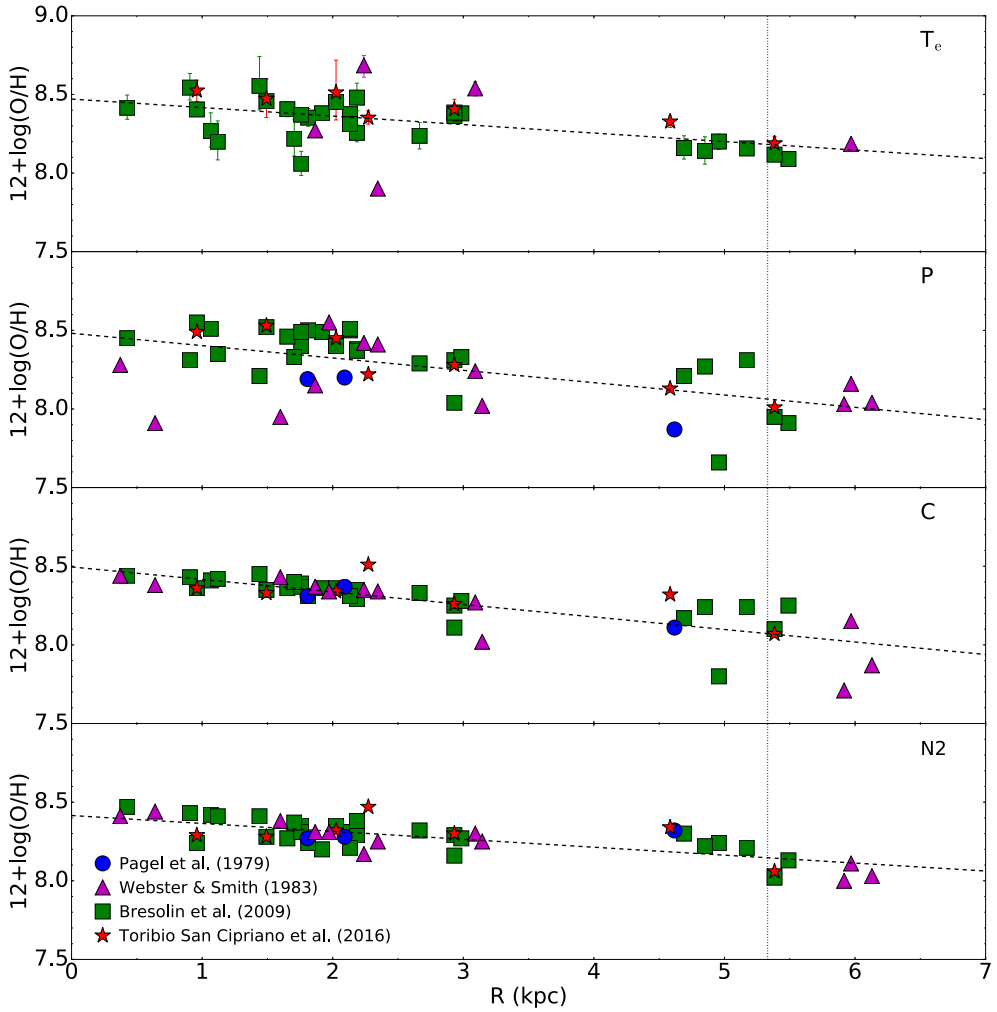

Figure 1. Oxygen abundances in HII regions of NGC 300 as a function of their galactocentric distances, along with the abundance gradients resulting from our fits. The panels show the results of the direct method, and the P, C, and N2 methods. The different symbols indicate the references for the observational data we used. All the panels are at the same scale. The vertical line represents the value of the isophotal radius, $R_{25} = 5.33$ kpc (Toribio San Cipriano et al. 2016).

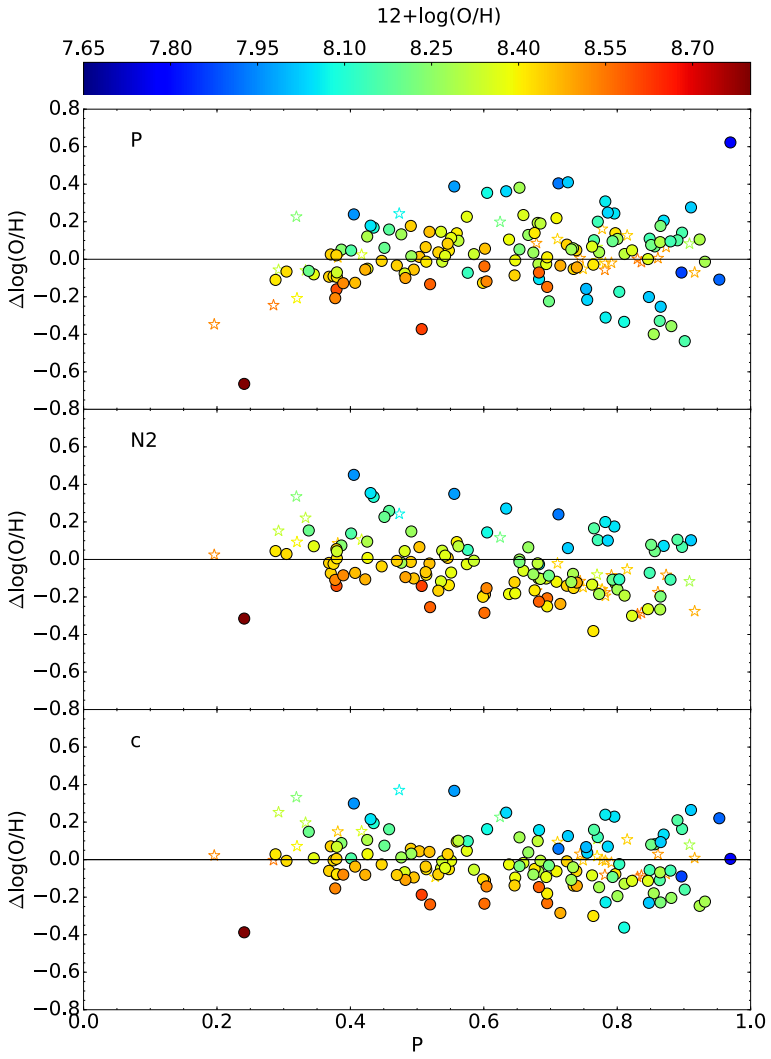

Figure 2. Differences between the oxygen abundances calculated using strong-line methods and those calculated using the direct method, as a function of the P parameter, color-coded with the metallicity given by O/H. The top panel shows the results for the P method; the middle panel those for the N2 method; and the bottom panel the results for the C method. The circles show our sample of extragalactic H II regions that have measurements of T_e[N II] and T_e[O III]. The empty stars show the results for the Galactic H II regions.

4. Summary and conclusions

We have compiled two samples of HII regions to study some problems related to the determination of chemical abundances. For both samples, we determine the physical conditions and chemical abundances in a homogenous way using the line intensities reported in the literature. We study the sensitivity to potencial observational problems of the direct method and some strong-line methods by analyzing the dispersion they introduce around the metallicity gradient. To do that, we use a sample of HII regions in M31, M33, M101 and NGC 300. We find that the direct method and the P method are very sensitive to observational problems and provide the highest dispersion values around the oxygen abundance gradients, 0.11-0.15 dex and 0.15-0.21 dex, respectively. These results are in agreement with the previous ones reported for M81 (Arellano-Córdova et al. 2016). Our results for the direct method do not imply that it is not working well, but that better spectra are required to measure properly the weak [OIII] λ4363 and [NII] λ5755 lines, so that we can get better estimates of the electron temperature and the chemical abundances. On the other hand, the ONS and C methods are the most robust methods in the presence of observational problems, showing dispersions around the metallicity gradient lower than 0.10 dex. This does not mean that these methods provide better estimates of the oxygen abundances since their performance depends on the validity of their calibration.
We also study the performance of the P, ONS, C, O3N2, and N2 methods using a sample of HII regions with measurements of T_e[NII] and T_e[OIII]. We compare the metallicity calculated using the strong-line methods with the one calculated using the direct method. We find that the ONS, C, O3N2, and N2 methods show differences in O/H with respect to the direct method that go up to 0.2-0.4 dex for most objects, whereas the P method provides differences of up to 0.66 dex. The differences show a dependence on the degree of ionization and on the metallicity.

Acknowledgments. We acknowledge support from Mexican CONACYT grant CB-2014-240562. KZA-C acknowledges support from Mexican CONACYT grant 351585 and 711183.

References

Arellano-Córdova K. Z., Rodríguez M., Mayya Y. D., Rosa-González D., 2016, *MNRAS*, **455**, 2627
López-Sánchez Á. R., Esteban C., 2010, *A&A*, **517**, A85
Luridiana V., Morisset C., Shaw R. A., 2015, *A&A*, **573**, A42
Marino R. A., Rosales-Ortega F. F., Sánchez S. F., Gil de Paz A., Vílchez J., et al., 2013, *A&A*, **559**, A114
Pilyugin L. S., Grebel E. K., Mattsson L., 2012, *MNRAS*, **424**, 2316
Pilyugin L. S., Thuan T. X., 2005, *ApJ*, **631**, 231
Pilyugin L. S., Vílchez J. M., Thuan T. X., 2010, *ApJ*, **720**, 1738
Toribio San Cipriano L., García-Rojas J., Esteban C., Bresolin F., Peimbert M., 2016, *MNRAS*, **458**, 1866

Chemical Abundances in Gaseous Nebulae:
Open problems in Nebular astrophysics
AAA Workshop Series 11, 2019
M. Cardaci, G. Hägele & E. Pérez-Montero, eds.

Contributed Paper

Chemical evolution models for the Galactic disk based on HII region abundances derived from a direct method and a temperature independent method

L. Carigi[1], M. Peimbert[1], and A. Peimbert [1]

[1]*Instituto de Astronomía, Universidad Nacional Autónoma de México, Apdo. Postal 70-264, México, C.P. 04510, CdMx, Mexico*

Abstract.
We present two chemical evolution models of our galaxy, both models are built to fit the O/H ratios derived from HII regions, using two different methods. One model is based on abundances obtained from the [OIII] 4363/5007 temperatures (direct method, DM) and the other on abundances obtained from the recombination line ratios of [OII/HI] (temperature independent method, TIM). The differences between the O/H values obtained from these two methods are about 0.25 dex. We find that the model based on the TIM values produces an excellent fit to the observational stellar constraints (B-stars, Cepheids, and the Sun), while the model based on the DM fails to reproduce each of them. Moreover, the TIM model can explain the flattening of the O/H gradient observed in the inner disk due to the assumption of an inside-out star formation quenching, in the $3-6$ kpc galactocentric range, starting ~ 9 Gyr ago.

Key words: HII regions — ISM: abundance — Galaxy: abundances — Galaxy: evolution

1. Introduction

A chemical evolution model (CEM) computes the chemical abundances of the gas mass in a Galactic zone and the predicted evolution can be tested by comparing it with the chemical abundances of no polluted stars which ages are known. The inferred chemical history of the Galactic zone will be more reliable, when the observational constraints become more precise.
In this work, we present two CEMs for the Galactic disk obtained using the CHEVOL code that considers ingredients dependent on time, t(Gyr), galactocentric distances, R(kpc), and metallicity of the gas, Z: such as galactic flows, star formation laws, initial mass functions, and stellar properties of each formed star. The code considers the lifetime of each star, independently of it mass.
For more details of these CEMs and their observational constraints, see Carigi et al. (2019, CPP19).

2. Ingredients of the Chemical Evolution Models

The main characteristics of our CEMs are: i) The Galaxy is assembled with primordial infalls but without any type of outflows. During the first Gyr the halo formed efficiently, then the disk formed with R-dependent efficiencies following an inside-outside scenario. The amount of accreted gas for each R is chosen to reproduce $M_{tot}(R)$. ii) The star formation rate is the well known law $SFR(R,t) \propto M^{1.4}_{gas}(R,t)$ by Kennicutt & Evans (2012). The proportionality coefficient is a spatial and temporal function, $\nu(M_{gas}+M_{star})^{0.4}$, and ν is obtained to fit the general behavior of $M_{gas}(R)$ and the flattening of the O/H gradient for $R <$ 6 kpc. iii) The initial mass function is that by Kroupa et al. (1993) in the $0.08-Mup$ $M_\odot$ range. Mup is a free parameter of the models, that is obtained to match the absolute value of the preset-day O/H gradient. iv) Each star enriches the interstellar medium when it leaves the main sequence, depending of its initial stellar mass and metallicity. Moreover, SNIa are taken into account. v) The age of the models is 13 Gyr and the Sun is located in an orbit of 8-kpc-medium radius. vi) Radial flows of gas or stars are not included.

3. Observational data to built the CEMs

The models are built to reproduce the following observational radial distributions along the Galactic disk: i) the total baryonic mass, $M_{tot}(R)$, ii) the gas mass, $M_{gas}(R)$, and iii) the O/H values from HII regions. For $M_{tot}(R)$, we adopt an exponential profile with a disk scale length ~ 4 kpc, and for $M_{gas}(R)$, we take into account the distribution by Kennicutt & Evans (2012). Regarding the O/H(R), we consider O/H gaseous values determined from the direct method (DM) and the temperature independent method (TIM), and we include the fraction of O atoms trapped in dust grains.

For the DM, we consider the O/H gaseous values for 21 HII regions derived from the forbidden lines (FLs) of O^{++} under the assumption that there are no temperature inhomogeneities; see Esteban & García-Rojas (2018) and Table 1 by CCP19. The dust contribution used depends slightly on Z and is in the $0.10-0.11$ dex range (Peimbert & Peimbert, 2010).

For the TIM, the O/H values are determined from the recombination lines (RLs) of O^{++} and H^+ (10 HII regions, see Table 2 by CCP19) and we used the Peimbert & Peimbert (2010) dust correction. For objects where no RLs are available (11 HII regions, see Table 3 by CCP19) we correct $(O/H)_{FL}$ values due to temperature inhomogeneities and presence of dust by adopting the calibration by Peña-Guerrero et al. (2012).

4. Observational data to test the CEMs

Early B type stars are very young objects, with ages less than ~ 100 Myr and their abundances can be considered as good representatives of the present-day abundances. In this work, we consider the mean O/H value of 13 B-stars of the Orion OB 1 association by Nieva & Przybilla (2012), located at distances from the Sun smaller than 350 pc. Moreover, we take into account a set of 18 O/H values in the $6-18$ kpc range obtained from 51 early type B-stars of Galactic

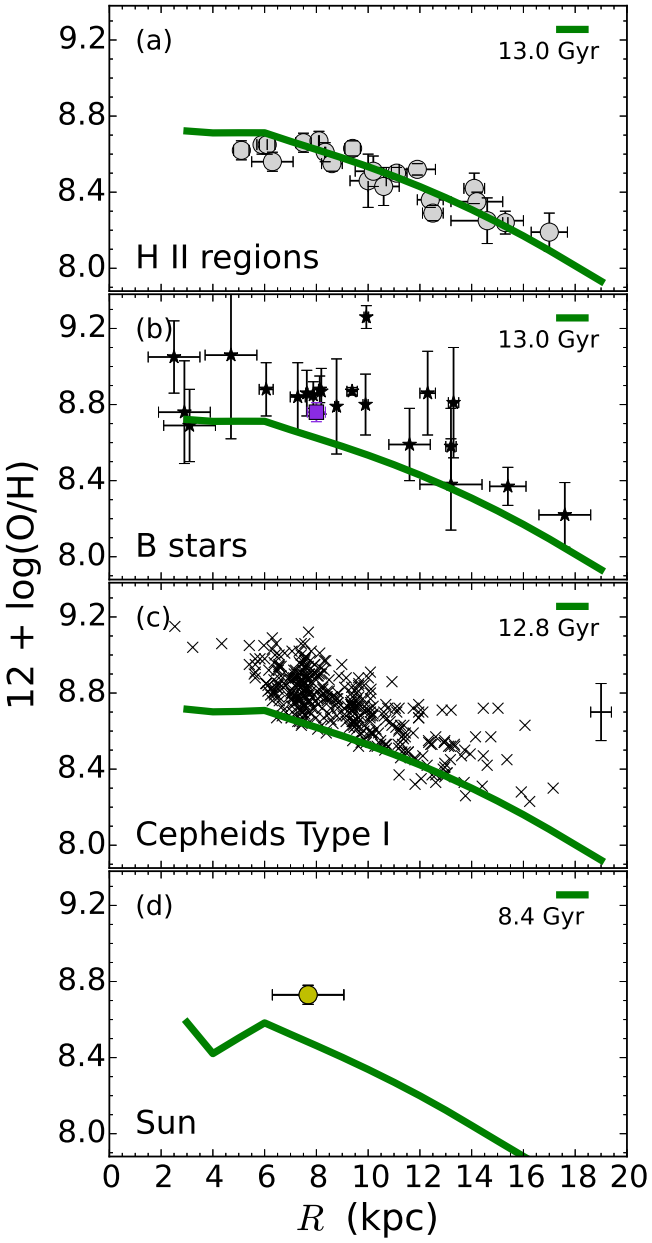

Figure 1. Radial distribution of O/H obtained by the DM model at different evolutionary times (green lines). Panel (a): HII regions. Gaseous values obtained with the Direct Method plus dust corrections. Panel (b): B-stars. Black stars: values by Rolleston et al. (2000) and Smartt et al. (2001). Violet square: the average value by Nieva & Przybilla (2012). Panel (c): Cepheids of Type I. Error bars: uncertainties for the typical Cepheid. Panel (d): Initial solar value by Asplund et al. (2009). The horizontal error bar: average migration of the Sun computed by Martinez-Medina et al. (2017).

open cluster associations by Rolleston et al. (2000). We also present 4 B-stars in the $2-5$ kpc range, studied by Smartt et al. (2001).
Cepheids of Type I are younger than 200 Myr, and consequently their O/H values can be compared with the predicted O/H values at 12.8 Gyr. We considered a set of 397 disk Cepheids located in the $3-17$ kpc range compiled by Martin (private communication, 2017).
The age of the Sun is ~ 4.6 Gyr and the protosolar abundance ($12 + \log(\mathrm{O/H}) = 8.73$ dex, Asplund et al., 2009) would represent the O/H of the ISM at 8.4 Gyr. However, its birth galactocentric distance could be different than the current one, because the Sun might have migrated. In this work, we take into account the dynamic models by Martinez-Medina et al. (2017) that indicate that the Sun may have been born in the $6.3-9.1$ kpc range.

5. The Direct-Method model

The DM model is built to fit the O/H values of the HII regions derived from the direct method. These values are reproduced by considering $Mup = 40$ $\mathrm{M}_\odot$. Moreover, the model requires that $\nu = 0.019$ to match the general behavior of $M_{gas}(R)$, however with this constant ν this model predicts an O/H gradient steeper than observed for $R < 6$ kpc. To reproduce the O/H flattening for $R < 6$ kpc, we assume a unit step function, such that diminishes abruptly the *SFR(R)* at specific quenching times as a function of R. Then we adopt the current star formation rate observed at these radii (Kennicutt & Evans, 2012) for the rest of the evolution. Specifically, to reproduce the $12+\log(\mathrm{O/H}) \sim 8.70$ value for R =3, 4, and 5 kpc, the quenching times are 3.30, 3.50, and 5.40 Gyr, and the present-day SFR is equal to 0.45, 0.55, and 0.65 $\mathrm{M}_\odot\mathrm{pc}^{-2}\mathrm{Gyr}^{-1}$, respectively. We ran several models, testing different quenching times, where we chose the highest times that match the 8.70 dex value.
In Fig.1 we present the results of this model built to fit the O/H values of the HII regions from the DM (panel a) and we test it with O/H stellar abundances (panels b, c, and d). In Fig.1(b, c), we compare the predicted value of the O/H(R) for the present time and for 0.2 Gyr ago with the values from B-stars and Cepheids, respectively. It can be noted that the agreement is poor, being the predicted values ~ 0.25 dex lower than observed. In Fig.1(d), we present the predicted O/H(R) at 8.4 Gyr, the protosolar O/H value, and the initial solar orbit. The predicted initial solar value is in the 8.40 to 8.56 range, about 0.25 dex smaller than the inferred one. No stellar migration (outward or inward) can explain the O/H solar value.

6. The Temperature-Independent-Method model

The TIM model is built to reproduce the observed O/H values based on the temperature independent method. Since the $(\mathrm{O/H})_{TIM}$ values are higher by ~ 0.25 dex than $(\mathrm{O/H})_{DM}$, the TIM model needs more massive stars to produce O, consequently an $Mup = 80$ $\mathrm{M}_\odot$ is required. We apply the same idea and procedure of quenching that in the DM model, because the R behavior of the O/H values from both methods are very similar. To reproduce the $12+\log(\mathrm{O/H}) \sim 8.83$ value for R =3, 4, and 5 kpc, the quenching times are 4.08, 6.10, and 8.38

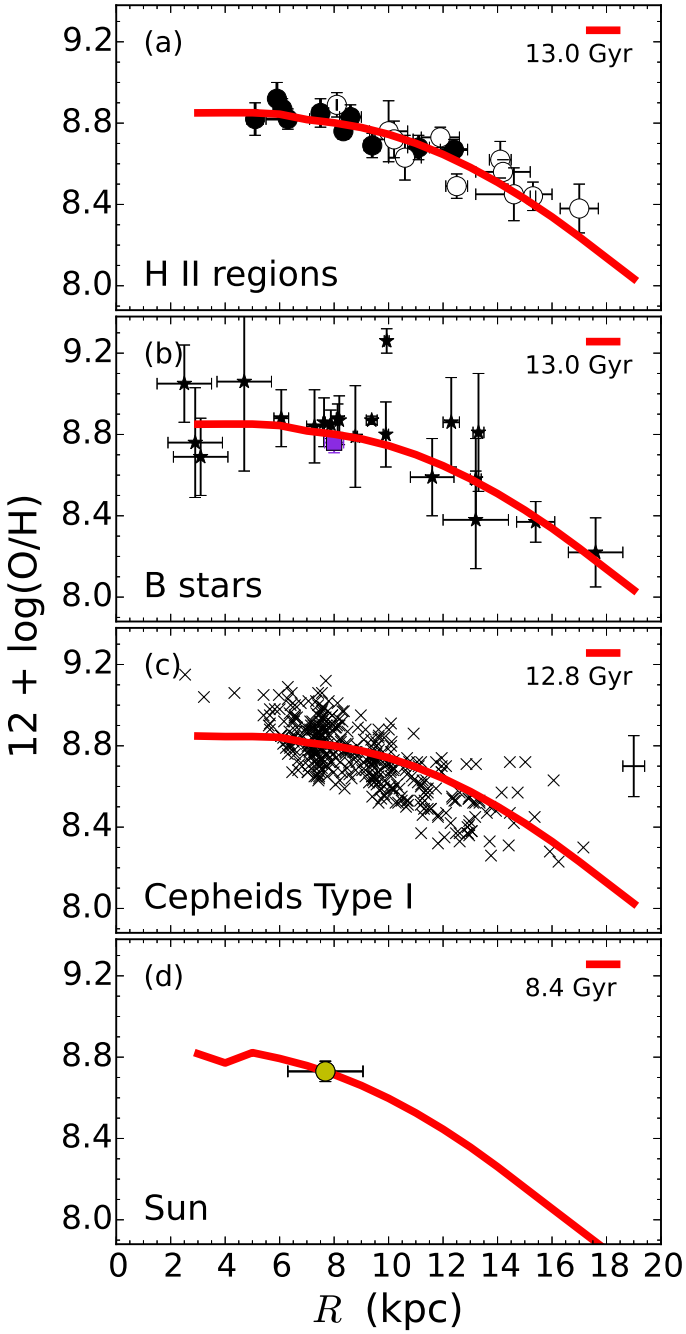

Figure 2. Radial distribution of O/H obtained by the TIM model at different evolutionary times (red lines). Panel (a): HII regions. Gaseous values obtained with the Temperature Independent Method plus dust corrections. The filled circles denote direct observations of the recombination lines, the empty circles use the calibration by Peña-Guerrero et al. (2012). Panels (b), (c), and (d) as Fig.1.

Gyr, respectively; later times than those inferred by the DM model, because the O/H flattening value from the TIM is higher.
In Fig.2(a) we present the model built to fit the O/H values of HII regions derived from the TIM. In Fig.2(b) we compare the predicted current O/H(R) with O/H values in B-stars at different R and we find that the model is in good agreement with these observations. In Fig.2(c) we test the predicted O/H(R) at 0.2 Gyr ago with the Cepheid data. The match is very good for $R > 6$ kpc, but for the inner disk more data are needed. In Fig.2(d) we present the predicted O/H radial distribution at 8.4 Gyr, the protosolar value and the possible Rs where the Sun was born. The spatial, temporal, and O/H agreements with the model are excellent, and consequently, the TIM model does not need to invoke a radial migration of the Sun to explain its chemical properties.

7. Conclusions

We present two galactic chemical evolution models: i) the Direct Method model (DM model), built to fit the O/H values in HII regions derived from the forbidden lines of O^{++}, dependent on temperature; and ii) the temperature-independent-method model (TIM model), built to fit the O/H values based on the recombination lines of $O^{++}$and H^{+}. Moreover corrections due to O embedded in dust grains are considered. The $(O/H)_{DM}$ values are smaller by ~ 0.25 dex than $(O/H)_{TIM}$.
The DM model cannot match either the early B-stars and the Cepheid data, or the solar O/H value, even considering an average migration for the Sun. In particular, the predicted O/H values are typically smaller, by ~ 0.25 dex, than the stellar chemical abundances.
The TIM model reproduces very well the O/H values from B and Cepheid stars. Moreover, the predicted O/H when the Sun was formed is in excellent agreement with the protosolar O/H value, without having to invoke stellar migration.
If the O/H flattening in the $3 - 6$ kpc range is corroborated, it would imply an inside-out star formation rate quenching in this range, that started ~ 9 Gyr ago.

Acknowledgments. L.C. thanks the support from CONACyT, grant 247132.

References

Asplund M., Grevesse N., Sauval A. J., Scott P., 2009, *ARA&A*, **47(1)**, 481
Carigi L., Peimbert M., Peimbert A., 2019, *ApJ*, **873(2)**, 107
Esteban C., García-Rojas J., 2018, *MNRAS*, **478(2)**, 2315
Kennicutt R. C., Evans N. J., 2012, *ARA&A*, **50**, 531
Kroupa P., Tout C. A., Gilmore G., 1993, *MNRAS*, **262**, 545
Martinez-Medina L. A., Pichardo B., Peimbert A., Carigi L., 2017, *MNRAS*, **468(3)**, 3615
Nieva M. F., Przybilla N., 2012, *A&A*, **539**, A143
Peña-Guerrero M. A., Peimbert A., Peimbert M., 2012, *ApJ*, **756(1)**, L14
Peimbert A., Peimbert M., 2010, *ApJ*, **724(1)**, 791
Rolleston W. R. J., Smartt S. J., Dufton P. L., et al., 2000, *A&A*, **363**, 537
Smartt S. J., Venn K. A., Dufton P. L., et al., 2001, *A&A*, **367**, 86

Chemical Abundances in Gaseous Nebulae:
Open problems in Nebular astrophysics
AAA Workshop Series 11, 2019
M. Cardaci, G. Hägele & E. Pérez-Montero, eds.

Contributed Paper

The Equivalent Width of the Hydrogen Emission Lines as HII Regions Age Indicators

H. Dottori

Astronomy Dpt. Instituto de Física, UFRGS, Av. Bento Goncalves 9500, Porto Alegre, Brazil

Abstract. I summarized in this talk the present status, the historical development and the reasons that led me in 1981 to propose the equivalent width of the ionized Hydrogen emission lines as a measure of the state of evolution or the age of HII regions. I will discuss the first determination of ages of HII regions in the Magellanic Clouds and other applications by myself and other authors, including our calibration of Brγ emission line in the arms of NGC 2997 as a age indicator in the study of the propagation of the density wave on the disk of this galaxy. Finally, an ongoing study of the HII regions on the disc NGC 7020, the clearest case known up to now of extremely populated 6:1 orbital resonance.

Key words: galaxies:ISM — galaxies: HII Regions — techniques: photometry, spectroscopy.

1. Introduction

We took as a basis for this contribution the revision of papers on H emission lines as HII regions age indicators accomplished by Levesque and Leitherer (Levesque & Leitherer, 2013). I proposed for the first time the use of equivalent width (W) of the Hidrogen lines in emission (WHβ in this case) as age indicator (Dottori, 1981). The guiding line behind this idea was somewhat similar to Sanstra's temperature, which would allow to compare star formation bursts of different intensity. In this sense, comparing the intensity of the line(s) in emission with the underlying continuum fulfills this role when stars form according to a IMF. I studied the fading of WHβ as a function of the more massive stars evolution. That time we considered the influence of the initial mass function (IMF) and mass upper mass limit (Mu) under case B of Baker & Menzel (1938) as the only variables influencing WHβ. Later Copetti, in his PhD thesis, developed more complete models (Copetti et al., 1986) taking into account a wider range of IMF, Mu, also restricted to Baker & Menzel (1938) case B but incorporating stars metallicity and mass loss. Other intensive parameters susceptible of being evolution indicators, such as [OIII]5007/Hβ, where analyzed in this paper. Later, many authors (e.g., Mas-Hesse & Kunth, 1991; García Vargas & Díaz, 1994; Mayya, 1995) confirmed WHβ as an important age indicator, although drawbacks have been raised, by example stars of a previous burst as well as others like leaks of ionizing photons, extintion by dust, etc. (e.g., García Vargas et al., 1995) In

the next Sections we discuss some examples and the set of parameters swept by different authors trying to fix how reliable WHβ and other lines W are to be used as age indicators.

2. Physical conditions influencing the emission lines equivalent width (W).

W evolution (WHβ in this example) is influenced by stellar as well as emitting gas properties. Stellar masses, metallicities, IMF, winds, etc. gas metallicity, temperature, density, spatial distribution, etc. are some of these properties. For this reason it is necessary to constrain the limits of each variable to run a given set of models. In Copetti et al. (1986) case, constrains were divided in:
(A) those of the stellar association; 1-stars form in a burst; the IMF is exponential with five different exponents, 2-four stellar upper mass limit were considered, 3-the lower mass limit is 0.5 $M_{\odot}$. 4-four different abundances and Kurucz (1979) stellar atmospheres models.
(B) those of the gas; 1-lines are formed according to case B of Baker & Menzel (1938), 2- dust influence is negligible. Other HII regions age indicators studied in this paper where the ratio between the He and H Stromgren's spheres and the ratio [OIII]5007A/Hβ. two of the many models derived in this paper are shown in Fig. 1. Stasińska & Leitherer (1996) developed photoionization models to study starburst galaxies. As known, these galaxies show strong signs of evolution, both in the stellar component and in the ionized gas. To accomplish their objectives the authors developed state of the art models at the epoch, including the effect of stellar winds produced by massive stars. Due to this fact their models were more restrictive than the previous ones. Since the authors aim was to study HII galaxies, they restricted metallicity to a half solar or lower. Under these conditions, there was found a small spread in free parameters needed to reproduce the emission-line properties of HII galaxies, which lead them to propose $W_{[OIII]5007}$ as a quite robust age indicator useful up to larger ages than WHβ does. Two important steeps were given by Fernandes et al. (2003) in the study of the last burst of star formation in composed stellar populations found in starburst and HII galaxies. Firstly, they assumed that star formation occurred in three cycles, an old one, an intermediate one and the last ionizing one which may happens in a burst or continuously. Secondly, they proposed to control the ages derived from WHβ through a second independent parameter. As a whole an important result derive from this work is that starburst nuclei are found to have a more even distribution of stellar ages in the 1 to 100 Myr range than HII galaxies, which are often dominated by the youngest star generations. The authors confirmed that after cleaning of older star formation cycles, WHβ as well as $W_{[OIII]}$ continue to be good age indicators for the youngest cycle of star formation. They also showed that emission lines ratio can be used as age indicators only for metal-poor objects, which are in their sample mostly HII galaxies. More metallic galaxies do not show a clear evolutionary trend of the lines ratios. So, Ws continue to be the most universal age indicator below 100 Myr. Nevertheless, for HII galaxies, Martín Manjón et al. (2008) carried out detailed models of composed stellar populations piling up succesive bursts with increasing metallicity. Their models show that the most informative data to uncover the presence of underlying pop-

ulations in HII galaxies consist of the combination of a line emission parameter, which characterizes the properties of the current burst of star formation, and a continuum colour which represents better the star formation history in longer time-scales. Their figure 13, clearly shows the changes of WHβ vs (U-V) along the evolution of the galaxy for succesive stellar burst. Processes than in the eighties were barely know, like massive stars mass loss (Meynet et al., 1994), rotation (Vanbeveren et al., 1998) and binarity (Georgy et al., 2013), in the nineties and later received increasing attention (Levesque et al., 2012; Levesque & Leitherer, 2013).

3. Results

Fig. 1 shows the time evolution of WH_α according to Starburst99 models (Leitherer et al., 1999, http://www.stsci.edu/science/starburst99/figs).
The very first result we obtained (Dottori & Bica, 1981) was the photoelectrical measurement of WHβ of 29 LMC and SMC HII regions.

$$WH\beta = -50 + 204 \times \log(R), \tag{1}$$

Equation 1 shows the relation we derived between WH$\beta \geq 10$, with log R, where $R = R_{\rm HII}/R_A$ is the ratio between the radius of the HII region and that of the ionizing association. R is a useful age indicator for ages ≤ 6 Myr. When compared to Starburst99 models, the groups of old and young HII regions do not change, but the detail of the individual ages changes.
The HII region evolutive models of Copetti et al. (1986) (Fig. 1) were improved by Starburst99 (Leitherer et al., 1999) Fig. 2. Nevertheless they were compared with observational data of HII regions in the Magellanic Clouds, M 33, M 101 and of "isolated extragalactic HII regions". The main results were Copetti et al. (1985) (1) IMF with $\chi = 3$ or 2.5 are inconsistent with a large number of HII regions; (2) The more uniform age distribution of isolated extragalactic HII regions obtained through an IMF with $\chi = 2$ suggests that this value is more realistic than $\chi = 1$ or 1.5; (3) The HII region age estimates indicate a burst of star formation about 5.5±1.0 Myr ago in the LMC and about 2.3±0.9 Myr ago in the SMC; (4) The observed [OIII]/Hβ gradient in M 33 and M 101 must be caused by color temperature variation of the radiation ionizing the HII regions; (5) The variation of WHβ; and [O III]/Hβ in M 33 and M 101 are explained qualitatively by metallicity gradients, but the values are only compatible with HII regions with ages between 2 and 5 Myr.
Many grand design spiral galaxies show strings of bright knots along their arms on near-infrared K-band images. A particularly interesting one is that of NGC 2997 southern arm Grosbøl et al. (2006) shown in Fig. 3b. The alignment of such knots (blue dots in Fig. 3a) suggests a relation to the spiral pattern (dashed line in the same figure) and possibly to a large-scale, star-forming associated with a density wave. Low resolution near-infrared K- and J-band spectra of the knots allowed to obtain H WBrγ for six HII regions and WPaβ for four, which were used to obtain ages through Starburst99 models (Leitherer et al., 1999). These set of regions where used to calibrate and validate determination of ages obtained from IR CCDs. That was necessary because of the large absorption shown accros the arm (Grosbøl & Dottori, 2009). These observations together

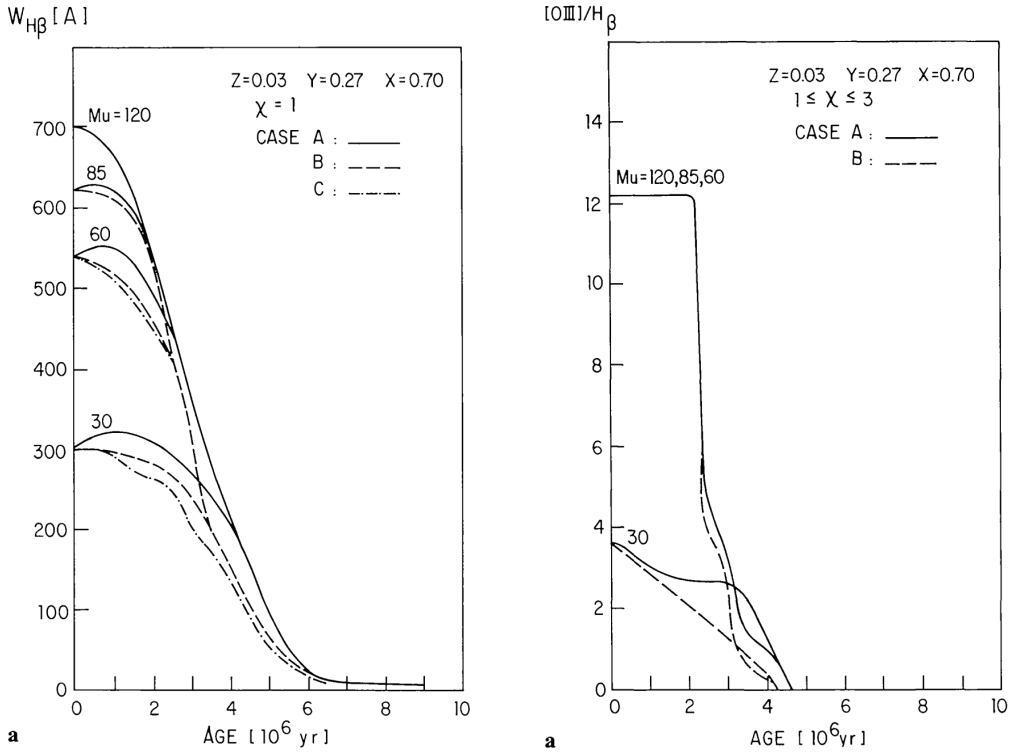

Figure 1. *Left:* WH_β vs age for metallicity z=0.03, Mu = 30, 60, 85 and 120 $M_\odot$; IMF $\chi = 1.0$, 1.5, 2.0, 2.5, 3.0; Mass-loss null(A), weak(B) and strong(C). (Fig. 1a; Copetti et al., 1986). *Right:* O[III]/H_β vs age, without mass-loss. (Fig. 7a; Copetti et al., 1986)

.

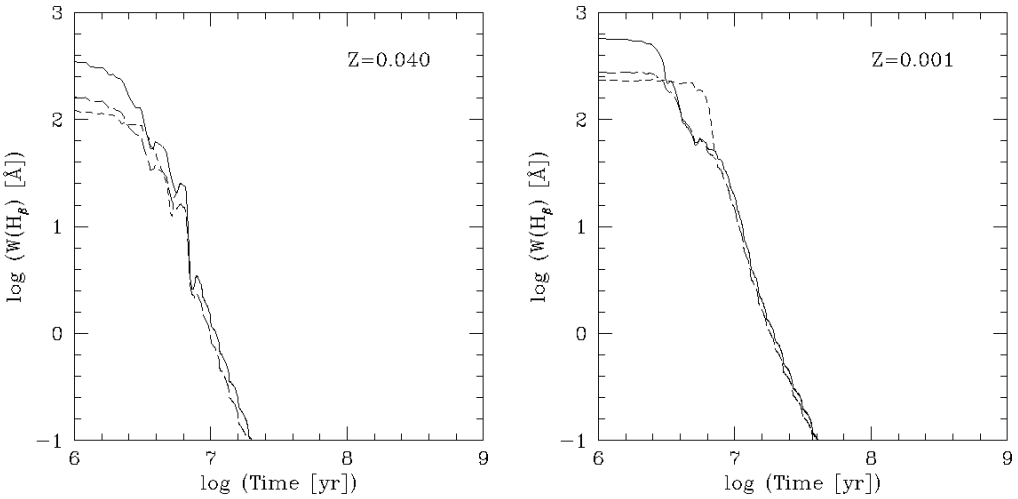

Figure 2. Starburst99 Models for WHβ.For IMF $\chi = 2.35$ (100 $M_\odot$ solid, 30 $M_\odot$ short dashed) and 3.30 (100 $M_\odot$ long-dashed).

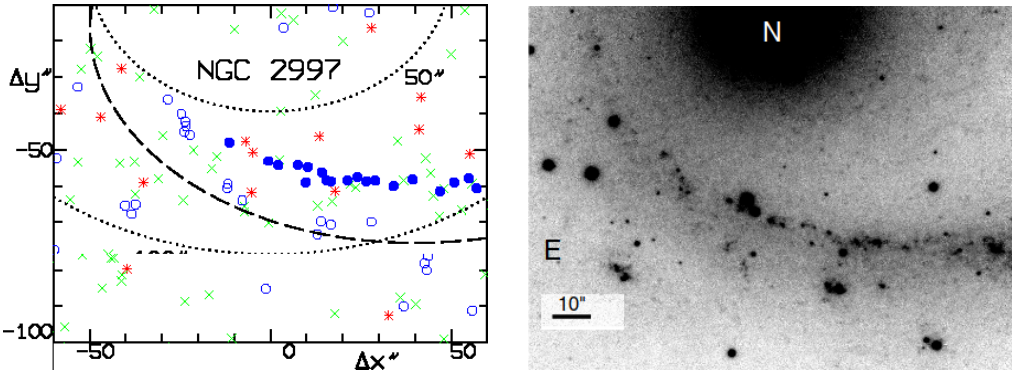

Figure 3. *left:* blue dots are the 19 brightest giants HII regions. Dashed line is the IR arm ridge determined by FFT. *right:* Image of NGC 2997 southern arm.

with the models show a trend of the brightest HII regions ($M_K \leq -12$ mag) age with the azimuthal departure from the IR arm (dashed line in Fig. 3a), if due to the transit of the density wave that formed the HII regions allowed us to determine an angular velocity of 16 km s^{-1} kpc^{-1} for the spiral pattern.

4. Conclusions

The brief synthesis that we made in this contribution allowed us to show that the equivalent width of the emission lines of the H in emission was consolidated over more than 30 years as a reliable indicator of the age of the giant HII regions, which can reach high precision, as in the chains of HII regions present in the arms of many grand design spiral galaxies.
The permanent and continuous concern of programs such as SB99 to improve their models as we better know the evolution of massive stars and the behavior of the ionized gas associated with them represent a great effort that needs to be valued and appreciated for the invaluable service they provide.
I can not close this work without remembering the two honorees in this workshop, my old friends Dres Manuel Peimbert and Rafael Costero, who 50 years ago, through their memorable contribution, broke a very important path in the study of abundances of HII regions. This is undoubtedly the basis of many achievements in the study of HII regions.

Acknowledgments. To Dr. Claus Leitherer of STScI, for kindly allowing the use of Figures from: (http://www.stsci.edu/science/starburst99/figs).

References

Baker J. G., Menzel D. H., 1938, *ApJ*, **88**, 52
Copetti M. V. F., Pastoriza M. G., Dottori H. A., 1985, *A&A*, **152**, 427
Copetti M. V. F., Pastoriza M. G., Dottori H. A., 1986, *A&A*, **156**, 111
Dottori H. A., 1981, *Ap&SS*, **80**, 267
Dottori H. A., Bica E. L. D., 1981, *A&A*, **102**, 245

Fernandes R. C., Leão J. R. S., Lacerda R. R., 2003, *MNRAS*, **340**, 29
García Vargas M. L., Bressan A., Díaz A. I., 1995, *A&AS*, **112**, 35
García Vargas M. L., Díaz A. I., 1994, *ApJS*, **91**, 553
Georgy C., Walder R., Folini D., Bykov A., Marcowith A., Favre J. M., 2013, *A&A*, **559**, A69
Grosbøl P., Dottori H., 2009, *A&A*, **499**, L21
Grosbøl P., Dottori H., Gredel R., 2006, *A&A*, **453**, L25
Kurucz R. L., 1979, *ApJS*, **40**, 1
Leitherer C., Schaerer D., Goldader J. D., Delgado R. M. G., Robert C., Kune D. F., de Mello D. F., Devost D., Heckman T. M., 1999, *ApJS*, **123**, 3
Levesque E. M., Leitherer C., 2013, *ApJ*, **779**, 170
Levesque E. M., Leitherer C., Ekstrom S., Meynet G., Schaerer D., 2012, *ApJ*, **751**, 67
Martín Manjón M. L., Mollá M., Díaz A. I., Terlevich R., 2008, *MNRAS*, **385**, 854
Mas-Hesse J. M., Kunth D., 1991, K. A. van der Hucht and B. Hidayat (eds.), *Wolf-Rayet Stars and Interrelations with Other Massive Stars in Galaxies*, Vol. 143 of *IAU Symposium*, p. 613
Mayya Y. D., 1995, *AJ*, **109**, 2503
Meynet G., Maeder A., Schaller G., Schaerer D., Charbonnel C., 1994, *A&AS*, **103**, 97
Stasińska G., Leitherer C., 1996, *ApJS*, **107**, 661
Vanbeveren D., De Donder E., Van Bever J., Van Rensbergen W., De Loore C., 1998, *New Astron.*, **3**, 443

Chemical Abundances in Gaseous Nebulae:
Open problems in Nebular astrophysics
AAA Workshop Series NN, 2019
M. Cardaci, G. Hägele & E. Pérez-Montero, eds.

Contributed Paper

Spatially resolve chemodynamics of Green Pea galaxies

G. F. Hägele[1], G. Bosch[1], R. Amorín[2,3], V. Firpo[4,3], M. V. Cardaci[1], J. M. Vílchez[5], E. Pérez-Montero[5], P. Papaderos[6], O. L. Dors[7], A. C. Krabbe[7] and F. Campuzano-Castro[1]

[1]*Instituto de Astrofísica de La Plata (UNLP - CONICET), La Plata, Argentina*
[2]*Instituto de Investigación Multidisciplinar en Ciencia y Tecnología, Universidad de La Serena, Raúl Bitrán 1305, La Serena, Chile*
[3]*Departamento de Física y Astronomía, Universidad de La Serena, Av. Juan Cisternas 1200 Norte, La Serena, Chile*
[4]*Gemini Observatory, Southern Operations Center, La Serena, Chile*
[5]*Instituto de Astrofísica de Andalucía - CSIC, Glorieta de la Astronomía s.n., E-18008 Granada, Spain*
[6]*Centro de Astrofísica and Faculdade de Ciências, Universidade do Porto, Rua das Estrelas, 4150-762, Porto, Portugal*
[7]*Universidade do Vale do Paraíba, Av. Shishima Hifumi, 2911, Cep 12244-000, São José dos Campos, SP, Brazil*

Abstract. Green Pea (GP) galaxies are the best local analogues of young high-redshift galaxies and ideal laboratories to study galaxy formation, reionization and feedback under extreme physical conditions. Complex emission line profiles for 6 GPs were observed using high-resolution spectroscopy at the WHT showing a very broad line underlying more than one narrower component. The broad components indicate large expansion velocities (full width zero intensity ∼1000km/s) probably showing the imprint of energetic outflows from supernovae. Using GMOS-IFU Gemini observations of a GP, we deconvolve the Hα, HeI5676Å, [OI]6300Å, [NII]6548, 6584Å, and [SII]6717, 6731Å emission-line profiles, as well as the temperature sensitive auroral emission line [OII]7325Å. This allow us to study the origin of the different emission line components and estimate the electron densities and the presence of shocks. This work present a new methodology for analyzing IFU observations of emission line spectra, considering the presence of multiple components, and preliminary physical conditions results.

Key words: galaxies: starburst — galaxies: kinematics and dynamics — techniques: imaging spectroscopy

1. Introduction

The discovery of extreme emission line galaxies at low redshift (z∼0.1-0.3), dubbed Green Peas (GPs; Cardamone et al., 2009; Amorín et al., 2010) due

to their unusually high emission line equivalent widths (EW([OIII]) 200-1500Å), paves the way to address pressing open questions in galaxy formation and reionization studies. GPs show physical properties closely resembling those inferred in young galaxies at high redshift (see Amorín et al., 2017). Thus, GPs are convenient laboratories to study in larger detail early galaxy build-up and feedback processes, and to test the production and escape of ionizing photons into the interstellar and intergalactic medium (see a detailed discussion in Bosch et al., 2019). Therefore, these low metallicity systems are likely to be local analogues of high redshift star-forming galaxies (see also Lofthouse et al., 2017).
Amorín et al. (2012) performed a kinematical study using the ISIS spectrograph at the WHT of a sample of six GPs at intermediate redshifts (z∼0.1-0.5), finding very complex emission-line profiles, consisting in the superposition, in a spatial extent of few kpc, of different kinematic components, similarly to some other compact starbursts in the local universe (see e.g. Hägele et al., 2007, 2009, 2010, 2012, 2013; Firpo et al., 2010, 2011). These deep high-dispersion ISIS spectra showed the first evidence of the presence of strong ionized outflows in GPs, with the narrower components showing high intrinsic velocity dispersions (σ ∼30-100km/s), suggesting clumpy and highly turbulent star formation, and the broader emission characterized by large expansion velocities (FWZI∼1000km/sec), suggesting the presence of fast ionized outflows driven by strong stellar winds and SNe remnants.

2. Observations

The Gemini GMOS-IFU is an ideal tool to perform high quality kinematical and spatial studies of this kind of galaxies. We performed 3D spectroscopic observations of the GP galaxy SDSSJ083843.63+385350.5 (hereafter SDSS J0839) already observed by Sloan, object that presents multi-components in its emission-line profiles in the Sloan spectrum. We used the GMOS-IFU at Gemini North as a pilot program (Proposal Id: GN-2014B-Q-20; PI: G. Hägele) and using the IFU 1-slit mode covering a FOV of $3.5 \times 5\,\mathrm{arcsec}^2$ and the R831 grating together with the OG515 filter to avoid second order contamination. This configuration yields a spectral range from 6500 to 8500 Å (from 5550 to 7250Å at the rest frame of the source). For details about the observations and data reduction process see Bosch et al. (2019).

3. Results and discussion

One of the aims of our work is to try to spatially identify the origin of the four different kinematical components already observed in its SDSS spectrum deconvolving the complex emission-line profile. However, our very deep intermediate spectral (R831 grating) and high spatial (∼0.4") resolution data reveal the presence of two or three Gaussian components for all the observed spaxels, and even four in the central ones.
In Fig. 1 we show the results for the single Gaussian fit and those performed using a three Gaussian fit, in decreasing dispersion order. The single Gaussian velocity map suggests evidence of galaxy rotation, which would be difficult to reconcile with the velocity dispersion which peaks off galaxy center. After being able to

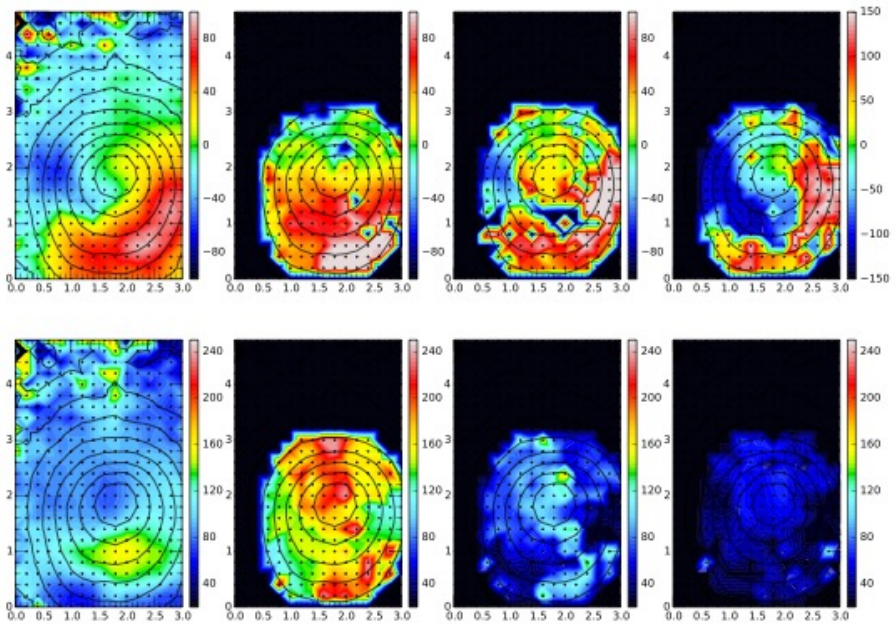

Figure 1. Hα gas kinematic maps. From left to right, the figure displays results for single Gaussian fit, and each component of a three Gaussian fit to the observed profiles, in decreasing dispersion order (BC, NC1 and NC2, respectively). Top row displays radial velocity, relative to galaxy average. Bottom row shows the corresponding values for the velocity dispersion.

split the observed profile in one broad and two relatively narrower components (BC, and NC1 and NC2, respectively), a completely different scenario arises. The broad component has a complex behavior: the spaxels that exhibit the largest velocity dispersion also seem to show the largest radial velocity deviations. The broad, low-surface brightness component is spatially extended ($\sim$7Kpc) and suggest the presence of strong outflows probably induced by violent star formation activity and the presence of SNe. The lower velocity dispersion components, NC1 and NC2, show different behaviours. The lowest velocity dispersion gas shows another strong polarized behaviour but with much larger velocity amplitude and extended along the 'x-axis', showing an almost constant velocity dispersion. It could be related with a kinematical signature of a rotating disk with relatively low velocity dispersion. It is noticeable that the velocity field of NC1 resembles the velocity pattern of NC2 with small deviations and its velocity dispersion resembles the general behaviour of BC.

A possible scenario to explain this behaviour is that NC1 is originated in the external layers of the gaseous material that seems to follow an overall rotational movement (NC2) and, therefore, both component shows similar velocity patterns. On the other hand, the velocity dispersion map of NC1 is similar to the one of BC, that could be the result of the interaction of the outflow that originates BC with the rotating gas. Thus, NC1 might be associated with the mixing

layer component such as those described by the scenarios proposed for M82 by Westmoquette et al. (2009) and for NGC2363 by Binette et al. (2009).
SDSS J0838 shows a complex gas kinematic behaviour very similar to what was found by Amorín et al. (2012) for a sample of 6 GPs using high resolution spectroscopy. Therefore, we are able to link our results to the hypothesis suggested by these authors that presented GPs as rapidly assembling galaxies.

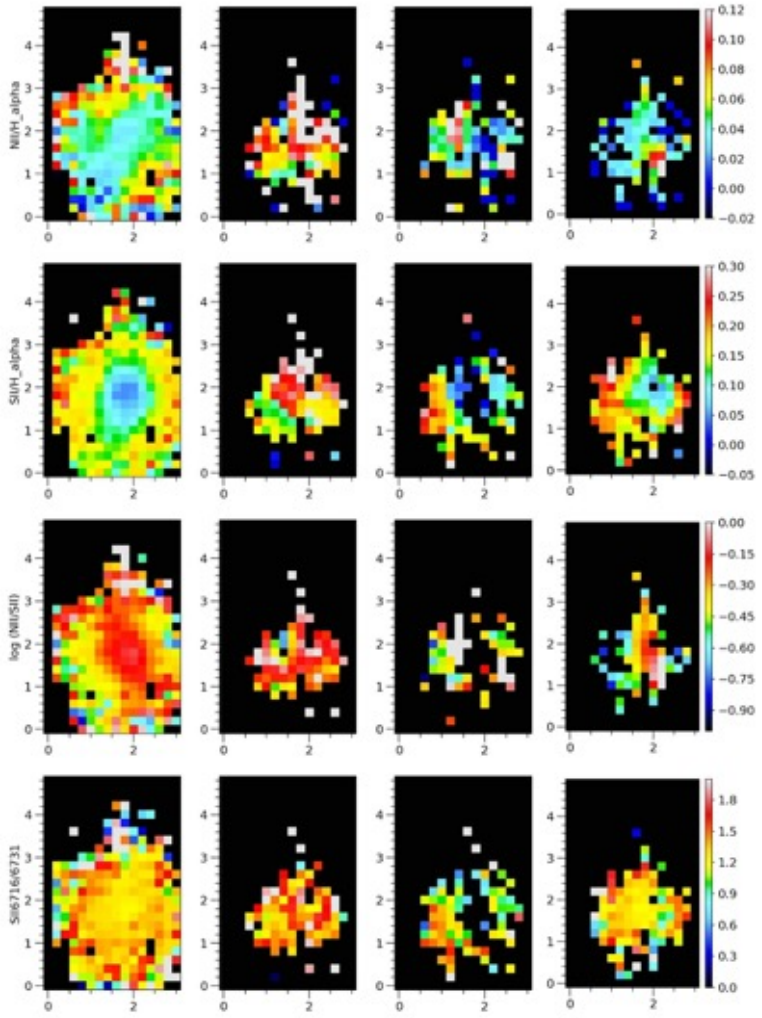

Figure 2. Different emission-line intensity ratio maps. From left to right, the figure displays results estimated from the single Gaussian fit, and from each component of a three Gaussian fit to the observed profiles, in decreasing dispersion order.

We are also able to deconvolve the profiles of several emission-lines: HeI5876, [OI]6300, [NII]6548, 6584, [SII]6717, 6731, [ArIII]7136Å. In Fig. 2 we show some emission line ratios from which we will be able to perform different oxygen abun-

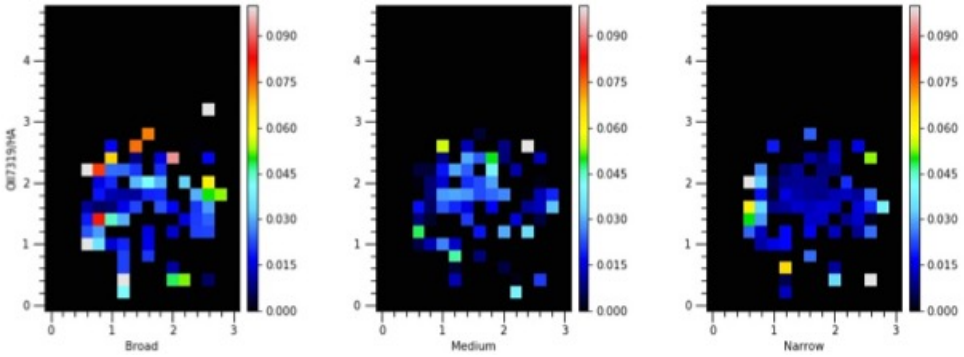

Figure 3. [OII]7325Å auroral emission-line flux maps for each component of a three Gaussian fit, in decreasing dispersion order.

dances estimations (Hägele et al. in prep.). We will also use the HII-CHI-MISTRY code Pérez-Montero (2014), which establishes a bayesian-like comparison between the relative observed optical line fluxes emitted by the ionized gas and the predictions from a grid of photoionization models covering a large range of input conditions to estimate O/H, N/O and ionization parameter (U).

We are also able to perform the spatial and kinematical decomposition of the weak temperature sensitive auroral [OII] emission-line at 7325Å. In Fig. 3 we can see the flux map for the different kinematic components of a three Gaussian fit. Observations using the GMOS-IFU with the B1200 grating, to observed the [OIII]4363 temperature sensitive auroral emission-line (among others) with enough spatial and spectral resolution to perform a complete spatial and chemodynamical study of this GP following the same procedure as in Hägele et al. (2012) are needed.

References

Amorín R., Fontana A., Pérez-Montero E., Castellano M., Guaita L., Grazian A., Le Fèvre O., Ribeiro B., Schaerer D., Tasca L. A. M., Thomas R., Bardelli S., Cassarà L., Cassata P., Cimatti A., Contini T., de Barros S., Garilli B., Giavalisco M., Hathi N., Koekemoer A., Le Brun V., Lemaux B. C., Maccagni D., Pentericci L., Pforr J., Talia M., Tresse L., Vanzella E., Vergani D., Zamorani G., Zucca E., Merlin E., 2017, *Nature Astronomy*, **1**, 0052

Amorín R., Vílchez J. M., Hägele G. F., Firpo V., Pérez-Montero E., Papaderos P., 2012, *ApJL*, **754**, L22

Amorín R. O., Pérez-Montero E., Vílchez J. M., 2010, *ApJL*, **715**, L128

Binette L., Flores-Fajardo N., Raga A. C., Drissen L., Morisset C., 2009, *ApJ*, **695**, 552

Bosch G., Hägele G., Amorín R., Firpo V., Cardaci M., Vílchez J. M., Pérez-Montero E., Papaderos P., Dors O. L., Krabbe A. C., Campuzano-Castro F., 2019, *MNRAS accepted*

Cardamone C., Schawinski K., Sarzi M., Bamford S. P., Bennert N., Urry C. M., Lintott C., Keel W. C., Parejko J., Nichol R. C., Thomas D., Andreescu D., Murray P., Raddick M. J., Slosar A., Szalay A., Vandenberg J., 2009, *MNRAS*, **399**, 1191

Firpo V., Bosch G., Hägele G. F., Díaz Á. I., Morrell N., 2011, *MNRAS*, **414**, 3288

Firpo V., Bosch G., Hägele G. F., Morrell N., 2010, *MNRAS*, **406**, 1094

Hägele G. F., Díaz Á. I., Cardaci M. V., Terlevich E., Terlevich R., 2007, *MNRAS*, **378**, 163

Hägele G. F., Díaz Á. I., Cardaci M. V., Terlevich E., Terlevich R., 2009, *MNRAS*, **396**, 2295

Hägele G. F., Díaz Á. I., Cardaci M. V., Terlevich E., Terlevich R., 2010, *MNRAS*, **402**, 1005

Hägele G. F., Díaz Á. I., Terlevich R., Terlevich E., Bosch G. L., Cardaci M. V., 2013, *MNRAS*, **432**, 810

Hägele G. F., Firpo V., Bosch G., Díaz Á. I., Morrell N., 2012, *MNRAS*, **422**, 3475

Lofthouse E. K., Houghton R. C. W., Kaviraj S., 2017, *MNRAS*, **471**, 2311

Pérez-Montero E., 2014, *MNRAS*, **441(3)**, 2663

Westmoquette M. S., Gallagher J. S., Smith L. J., Trancho G., Bastian N., Konstantopoulos I. S., 2009, *ApJ*, **706**, 1571

Chemical Abundances in Gaseous Nebulae:
Open problems in Nebular astrophysics
AAA Workshop Series 11, 2019
M. Cardaci, G. Hägele & E. Pérez-Montero, eds.

Contributed Paper

Metallicity Calibrations in High-Redshift Galaxies

F. Bian[1], L. J. Kewley[2], M. A. Dopita[2]

[1]*European Southern Observatory, Alonso de Córdova 3107, Casilla 19001, Vitacura, Santiago 19, Chile*
[2] *Research School of Astronomy and Astrophysics, Australian National University, Canberra, ACT 2611, Australia*

Abstract. The evolution of the ISM conditions suggests that the local metallicity calibrations would most likely not to be valid for high-redshift galaxies. Here we study the high-redshift metallicity calibrations using a sample of local analogs of high-redshift galaxies. These local analogs are selected in the same region as $z \sim 2$ star-forming galaxies on the BPT diagram. This type of analog share the same ionized interstellar medium (ISM) properties with high-redshift galaxies. We establish empirical metallicity calibrations between the direct gas-phase oxygen abundances and the $N2$ and $O3N2$ indices in our local analogs. We find significant systematic offsets between the metallicity calibrations for our local analogs of high-redshift galaxies and those derived from the local HII regions and a sample of local reference galaxies selected from the Sloan Digital Sky Survey (SDSS). The N2 and O3N2 metallicities will be underestimated by 0.05-0.1 dex relative to our calibration, if one simply applies the local metallicity calibration in previous studies to high-redshift galaxies. By comparing with MAPPINGs photoionization models, the different empirical metallicity calibration relations between the local analogs and the SDSS reference galaxies are primarily due to the change of ionized ISM conditions.

Key words: galaxies: abundances — galaxies: ISM

1. Introduction

The evolution of chemical abundances in galaxies provides insight into the key physical processes regulating the formation and evolution of galaxies. By comparing the evolution of chemical abundance depending on galaxy properties (such as stellar mass) with the cosmological galaxy evolution simulation, one can put strong constraints on galaxy build-up process and the stellar feedback models that drive galactic-scale outflows (e.g., Finlator & Davé, 2008; Davé et al., 2012). Therefore, it is essential to accurately measure the chemical abundance in galaxies at different epochs of the Universe.
Strong nebular emission-line ratios are commonly used to estimate the gas-phase oxygen abundance based on either photoionization models (e.g., Kewley & Dopita, 2002) or empirical calibrations (e.g., Pettini & Pagel, 2004, PP04 hereafter).

In particular, metallicity measurement in high-redshift galaxies relies heavily on the PP04 calibrations. PP04 compiled a sample of HII regions in nearby star-forming galaxies and established the relationship between the metallicities derived from direct temperature (T_e) method and $N2 = \log([\mathrm{NII}]\lambda6584/\mathrm{H}\alpha)$ and $O3N2 = \log[([\mathrm{OIII}]\lambda5007/\mathrm{H}\beta)/([\mathrm{NII}]\lambda6584/\mathrm{H}\alpha)]$ strong emission ratios. The $N2$ and $O3N2$ based on local HII regions have been widely used to study the metallicities in high-redshift galaxies (e.g., Erb et al., 2006; Hainline et al., 2009; Steidel et al., 2014; Sanders et al., 2015).

Photoionization models show that the $[\mathrm{NII}]\lambda6584/\mathrm{H}\alpha$ and $[\mathrm{OIII}]\lambda5007/\mathrm{H}\beta$ ratios depend not only on the metallicity but also on other effects, including the ionization parameter, the electron density, the nitrogen-to-oxygen ratio (N/O), and the spectral shape of the radiation field (e.g., Kewley & Dopita, 2002). Observations show that the interstellar medium (ISM) conditions changes significantly with redshift (e.g., Steidel et al., 2014). The ISM conditions in high-redshift star-forming galaxies are characterized by ~ 0.6 dex higher ionization parameters and an order of magnitude higher electron densities than their local counterparts (e.g., Bian et al., 2010; Nakajima & Ouchi, 2014). Such evolution also causes the different locations on the $[\mathrm{OIII}]\lambda5007/\mathrm{H}\beta$ vs $[\mathrm{NII}]\lambda6584/\mathrm{H}\alpha$ BPT diagram between the nearby and high-redshift star-forming galaxies.

These pieces of evidence raise questions on the applicability of local metallicity calibrations for high redshift galaxies. We approach this questions by recalibrating the $N2$ and $O3N2$ metallicity indicators in a sample of local analogs of high-redshift galaxies using the direct T_e method. We also compare the empirical calibrations derived from the local analogs with those derived from a sample of local reference galaxies to study how the empirical calibrations change with cosmic time.

2. Sample Selection

We adopt the emission line fluxes from the SDSS MPA-JHU catalog to select the local reference galaxies and local analogs based on their locations on the BPT diagram. The sample of local analogs of high-redshift galaxies are selected in the ±0.04 dex region of the $z \sim 2.3$ star-forming sequence defined by equation 9 in Steidel et al. (2014) on the BPT diagram (blue small data points in Figure 1). Studies have shown that local galaxies that shares the same region as high-redshift galaxies on the BPT diagram closely resemble the properties of the high-redshift galaxies (Bian et al., 2016, 2017).

The properties of these local analogs can be summarized as follows. The median stellar mass is $\log(M_*/M_\odot) = 8.8^{+0.06}_{-0.02}$. The median SFR and sSFR are $3.9^{+0.7}_{-0.2}\ M_\odot\ \mathrm{yr}^{-1}$ and $10.0^{+1.0}_{-0.5}\ \mathrm{Gyr}^{-1}$, respectively. The sSFR of the local analogs is comparable to that in $z \sim 2$ star-forming galaxies with similar stellar mass. Furthermore, these analogs closely resemble the ISM conditions in high-redshift galaxies, including high ionization parameters ($\log q \simeq 7.9\ \mathrm{cm}^{-1}$) and high electron densities ($n_e \simeq 120\ \mathrm{cm}^{-3}$). These properties are also comparable to those in the $z \sim 2-3$ galaxies (e.g., Nakajima & Ouchi, 2014; Sanders et al., 2016). To compare the metallicity calibration between the local analogs and nearby galaxies, we also select local reference galaxies located in the ±0.05 dex region of the local star-forming sequence on the BPT diagram.

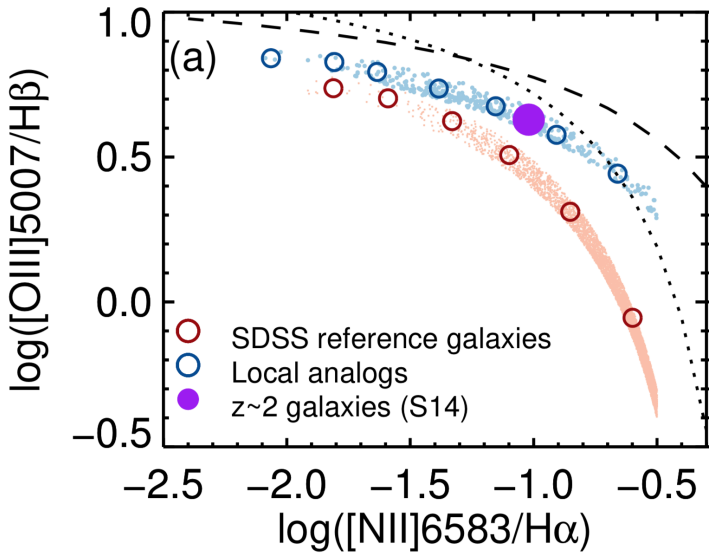

Figure 1. BPT diagrams of local analogs of high-redshift galaxies and SDSS reference galaxies. The small blue and red points represent the individual local analogs and SDSS reference galaxies, respectively, and the large open blue and red points represent the stacked spectra of the local analogs and SDSS reference galaxies, respectively. The large purple filled circle represents the stacked spectrum of a sample of $z \sim 2$ UV-selected galaxies adopted from Steidel et al. (2014, S14). The figure is adopted from Bian et al. (2018)

3. Analysis

We combine the spectra and generate stacked spectra for both our local analogs and SDSS reference galaxies to detect the weak [OIII]λ4363 line. We first correct the dust extinction of the reduced galaxy spectra from the SDSS DR9 using the Balmer decrement (Hα/Hβ). Then each of the spectra is shifted to the rest-frame wavelength based on their redshifts, resampled onto a grid of wavelength from 3700Å to 7300Å with $\Delta\lambda = 1$Å, and normalized using the the mean flux density in the $4400 - 4450$Å. We divide the local analogs and the SDSS redshift galaxies separately into 0.25 dex bins in [NII]λ6584/Hα from log([NII]λ6584/Hα)$= x$ to $x + 0.25$, where $x = [-2.25, -2.00, -1.75, -1.50, -1.25, -1.00, -0.75]$. At last, we stack the spectra within each of the [NII]λ6584/Hα bins using the mean flux density at each wavelength, and a total of fourteen stacked spectra are generated: seven spectra of local analogs of high-redshift galaxies and seven spectra of SDSS reference sample.

We subtract the stellar continuum from the stacked spectra using the STARLIGHT stellar population synthesis models. The flux of the following emission lines, [OII]$\lambda\lambda$3726,3729, Hγ, [OIII]λ4363, Hβ, Hα, [NII]$\lambda\lambda$6548,6584, and [SII]$\lambda\lambda$6717,6731, are measured by fitting the lines with Gaussian functions. To

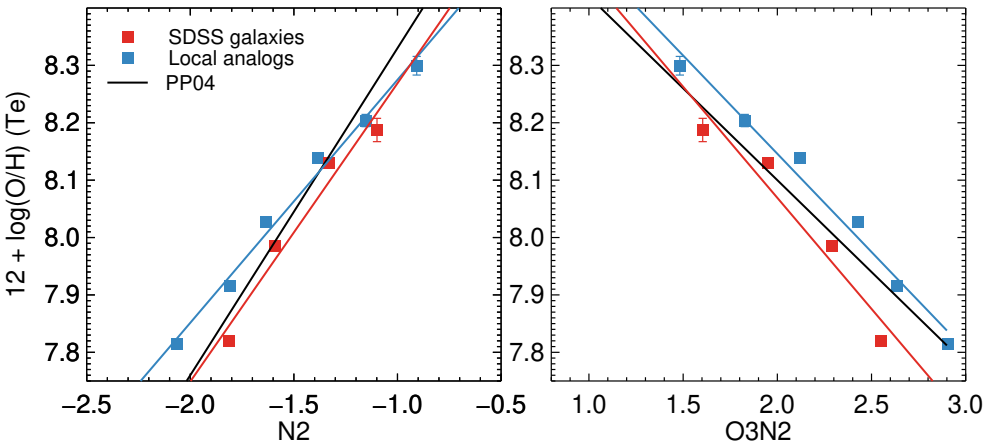

Figure 2. Calibrations of N2 (left) and O3N2 (right) metallicity indicators using direct T_e metaod in the local analogs of high-redshift galaxies and the SDSS reference galaxies. The figure is adopted from Bian et al. (2018).

get reliable direct T_e oxygen abundance measurements, we only adopt the stacked spectra with signal-to-noise ratios of [OIII]λ4363 greater than ten (S/N $>$ 10) for the our analysis.

The Izotov et al. (2006) recipe is used to estimate the direct T_e metallicity. We further adopt the following relation between T_e(OIII) and T_e(OII) from Garnett (1992): T_e(OII)=0.7T_e(OIII)+3000K. We estimate the O^{++} abundance by using the T_e(OIII) temperature and [OIII]$\lambda\lambda$4959,5007/Hβ ratio and O^{+} abundance using the T_e(OII) temperature, [OII]$\lambda\lambda$3726,3729/Hβ and electron density. The final oxygen abundance is the sum of the O^{++} abundance and the O^{+} abundance.

4. Results

We use the direct T_e metallicity and line ratios measured in the stacked spectra to calibrate the $N2$ and $O3N2$ metallicity indicators. We show the relations between the direct T_e oxygen abundance and the $N2$ and $O3N2$ indices in the local analogs of high-redshift galaxies (blue squares) and the local normal star-forming galaxies (red squares) in Figure 2. We fit the relation between the direct oxygen abundance and the N2 and O3N2 indices using a linear equation. The results to fit for our local analogs as follows (blue solid lines in Figure 2):

$$12 + \log(\mathrm{O/H}) = 8.82 + 0.49 \times \mathrm{N2}, \quad (1)$$

$$12 + \log(\mathrm{O/H}) = 8.97 - 0.39 \times \mathrm{O3N2}, \quad (2)$$

The results for the SDSS reference galaxies are as follows (red solid lines in Figure 2):

$$12 + \log(\mathrm{O/H}) = 8.98 + 0.63 \times \mathrm{N2}, \quad (3)$$

$$12 + \log(\mathrm{O/H}) = 9.05 - 0.47 \times \mathrm{O3N2}, \quad (4)$$

where $7.8 < 12 + \log(\mathrm{O/H}) < 8.4$
The metallicity will be underestimated by 0.05-0.1 dex, if one simply applies the local metallicity calibration to high-redshift galaxies.

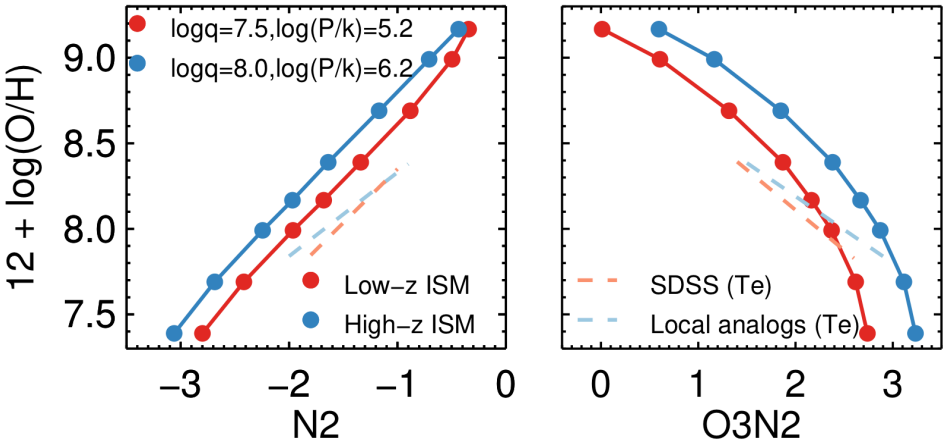

Figure 3. Relations between the strong emission-line ratios and oxygen abundance from MAPPINGs photoionization models. The figure is adopted from Bian et al. (2018).

5. Discussion

We establish the relation between the $N2$ and $O3N2$ diagnostic line ratios and the oxygen abundance for two cases using the MAPPINGs photoionization models: 1. The ionization parameter of $\log q = 7.5$ and the ISM pressure is $\log(P/k) = 5.2$ are comparable to those in the normal nearby galaxies (e.g., Bian et al., 2016). 2. The ionization parameter of $\log q = 8.0$ and the ISM pressure of $\log(P/k) = 6.2$ are consistent with those in $z \sim 2$ galaxies and our local analogs (e.g., Kaasinen et al., 2017). Figure 3 shows the relations between $N2$ and $O3N2$ diagnostic line ratios and the oxygen abundance derived from the photoionization models. Though there is a large offset on the absolute value of the metallicity estimation, the metallicity calibrations between the high-redshift and low-redshift conditions derived by the photoionization models (solid lines in Figure 3) follow the same trend as those between the local analogs and the SDSS reference galaxies (dashed lines in Figure 3). This suggests that the different metallicity calibration relations between the high- and low-redshift galaxies are due to the evolution of the ISM conditions.

Acknowledgments. I would like to give a special thank to my mother, Fengqing Cheng, who gave me life and brought me up. She just passed away, when I was writing this acknowledgement.

References

Bian F., Fan X., Bechtold J., McGreer I. D., Just D. W., Sand D. J., Green R. F., Thompson D., Peng C. Y., Seifert W., Ageorges N., Juette M., Knierim V., Buschkamp P., 2010, *ApJ*, **725**, 1877
Bian F., Kewley L. J., Dopita M. A., 2018, *ApJ*, **859**, 175
Bian F., Kewley L. J., Dopita M. A., Blanc G. A., 2017, *ApJ*, **834**, 51
Bian F., Kewley L. J., Dopita M. A., Juneau S., 2016, *ApJ*, **822**, 62
Davé R., Finlator K., Oppenheimer B. D., 2012, *MNRAS*, **421**, 98
Erb D. K., Shapley A. E., Pettini M., Steidel C. C., Reddy N. A., Adelberger K. L., 2006, *ApJ*, **644**, 813
Finlator K., Davé R., 2008, *MNRAS*, **385**, 2181
Garnett D. R., 1992, *AJ*, **103**, 1330
Hainline K. N., Shapley A. E., Kornei K. A., Pettini M., Buckley-Geer E., Allam S. S., Tucker D. L., 2009, *ApJ*, **701**, 52
Izotov Y. I., Stasińska G., Meynet G., Guseva N. G., Thuan T. X., 2006, *A&A*, **448**, 955
Kaasinen M., Bian F., Groves B., Kewley L. J., Gupta A., 2017, *MNRAS*, **465**, 3220
Kewley L. J., Dopita M. A., 2002, *ApJS*, **142**, 35
Nakajima K., Ouchi M., 2014, *MNRAS*, **442**, 900
Pettini M., Pagel B. E. J., 2004, *MNRAS*, **348**, L59
Sanders R. L., Shapley A. E., Kriek M., Reddy N. A., Freeman W. R., Coil A. L., Siana B., Mobasher B., Shivaei I., Price S. H., de Groot L., 2015, *ApJ*, **799**, 138
Sanders R. L., Shapley A. E., Kriek M., Reddy N. A., Freeman W. R., Coil A. L., Siana B., Mobasher B., Shivaei I., Price S. H., de Groot L., 2016, *ApJ*, **816**, 23
Steidel C. C., Rudie G. C., Strom A. L., Pettini M., Reddy N. A., Shapley A. E., Trainor R. F., Erb D. K., Turner M. L., Konidaris N. P., Kulas K. R., Mace G., Matthews K., McLean I. S., 2014, *ApJ*, **795**, 165

Chemical Abundances in Gaseous Nebulae:
Open problems in Nebular astrophysics
AAA Workshop Series 11, 2019
M. Cardaci, G. Hägele & E. Pérez-Montero, eds.

Contributed Paper

Exploring diffuse ionised gas using MUSE/VLT

Nimisha Kumari[1,2,3]

[1]*Kavli Institute for Cosmology, University of Cambridge, Cambridge CB3 0HA, UK*
[2]*Cavendish Laboratory, University of Cambridge, Cambridge CB3 0HE, UK*
[3]*Institute of Astronomy, University of Cambridge, Cambridge CB3 0HA, UK*

Abstract. We use integral field spectroscopic data taken with Multi-Unit Spectroscopic Explorer to analyse ionised gas in 24 nearby star-forming galaxies. For three metallicity calibrations of HII regions, O3N2 =log([OIII]/Hβ)-log([NII]/Hα), O3S2=log([OIII]/Hβ+[SII]/Hα) and N2S2Hα=log([NII]/[SII])+0.264log([NII]/Hα), we test whether these calibrations can be used to estimate metallicity for diffuse ionised gas (DIG) and/or low-ionisation emission region (LI(N)ER). To that end, we identify closeby HII-DIG/LIER pairs expected to have similar metallicities, and compare their metallicites estimated using above-mentioned diagnostics. We find that these calibrations over-/underestimate metallicities of DIG/LIERs with respect to the closeby HII regions, though O3N2 suffers the least from DIG contamination. We provide empirically-derived corrections to O3N2 and O3S2 calibrations in order to measure abundances of DIG/LIERs, and propose to use the new corrected O3N2 and O3S2 calibrations for measuring gas-phase metallicity in quiescent galaxies and quiescent regions within active star-forming galaxies.

Key words: galaxies: abundances — galaxies: ISM

1. Introduction

Chemical evolution of the Universe is one of the most explored topics in astrophysics, and requires accurate estimates of chemical abundances. The so-called direct T_e-method is deemed to provide robust measure of gas-phase abundance but relies on the use of weak auroral lines. Hence, several diagnostics using strong emission lines have been devised to estimate metallicity of the ionised gas (see e.g. Maiolino & Mannucci, 2019; Curti et al., 2017). All these metallicity calibrations, direct and indirect methods, have been devised to estimate the gas phase abundance of star-forming regions (HII regions), and not of the diffuse ionised gas (DIG), a lesser dense component of the interstellar medium.
The DIG was first discovered in the Milky Way off the disc (Reynolds, 1984), though it is also found in the disks and halos of spiral galaxies, and in passive galaxies (see e.g. Rossa & Dettmar, 2003; Belfiore et al., 2016). The DIG is

generally distinguished from the HII regions, on the basis of surface brightness of Hα (Zhang et al., 2017), equivalent width of Hα (Cid Fernandes et al., 2011), and the classical emission line diagnostic diagrams (BPT diagrams; Baldwin et al., 1981). On the [SII]-BPT and [NII]-BPT diagrams, the line ratios of DIG correspond to that of low ionisation nuclear emission or low ionsation emission regions (LIER, Belfiore et al., 2016) and may also spill into the region on the BPT diagrams occupied by the active galactic nuclei (AGNs) or Seyferts.

The effect of DIG contamination in abundance estimates have been recently studied by a few works (see e.g. Zhang et al., 2017; Yan, 2018). The present contribution is based on one such study, Kumari et al. (2019), where fine spatial resolution of Multi-Unit Spectroscopic Explorer (MUSE) is exploited to study the biases in gas-phase metallicity due to DIG contamination and to devise first-ever methods for estimating metallicities of DIG/LIERs.

The work is structured in the following way: Section 2 describes data observation, reduction and line fitting techniques to obtain emission line maps, the methodology to identify the HII-DIG/LIER/AGN pairs and the three metallicity diagnostics used in this work. In Section 3, we discuss the observed biases in metallicities of DIG/LIER/AGN with respect to the nearby HII regions, and provide novel empirical metallicity calibrations for DIG/LIERs.

2. Data & Methodology

The data: We used integral field spectroscopic data of 24 nearby star-forming galaxies taken with MUSE, observed as part of guaranteed time observation program (IDs 095.B-0532(A), 096.B-0309(A), 097.B-0165(A)). We used the reduced data cubes available at the ESO archive to create emission line maps of Hα, Hβ, [OIII] λ5007, [NII] λ6584 and [SII] $\lambda\lambda$6717,6731, by fitting a Gaussian profile to each line of interest, after subtracting continuum via a customised spectral-fitting routine using a set of simple stellar population templates from MIUSCAT library (Vazdekis et al., 2012). A Voronoi binning (Cappellari & Copin, 2003) scheme was used while fitting continuum as well as while fitting emission lines, in order to preserve the initial spatial resolution of high S/N regions and also analyse regions with low S/N at the original sampling.

HII-DIG/LIER pair selection: We first identify closeby HII-DIG/LIER pairs that are expected to be chemically-homogeneous due to the same level of chemical enrichment at small spatial scales (see Kumari et al., 2019, for details). We determine the spatial scale to be 500 pc using the catalogue of HII regions in NGC 0628 from Berg et al. (2013). We present two classification methods to separate HII regions and DIG/LIERs, i.e. [SII]-BPT and [NII]-BPT diagnostic diagrams. We use the maximum starburst line from Kewley et al. (2001) for this separation in [SII]-BPT classification. However for [NII]-BPT classification, we use the line from Kauffmann et al. (2003) as it was used to calibrate the metallicity diagnostics (O3N2 and O3S2) for HII regions followed in this work.

HII regions metallicity calibrators: We use three strong line metallicity diagnostics, O3N2, O3S2 and N2S2Hα, described below. They employ the ratios of closely-spaced emission lines, hence they do not require reddening correction.

1. O3N2 (= log([OIII]/Hβ) - log([NII]/Hα)) adopted here is the following empirical calibration derived by Curti et al. (2017) using stacked spectra of galaxies

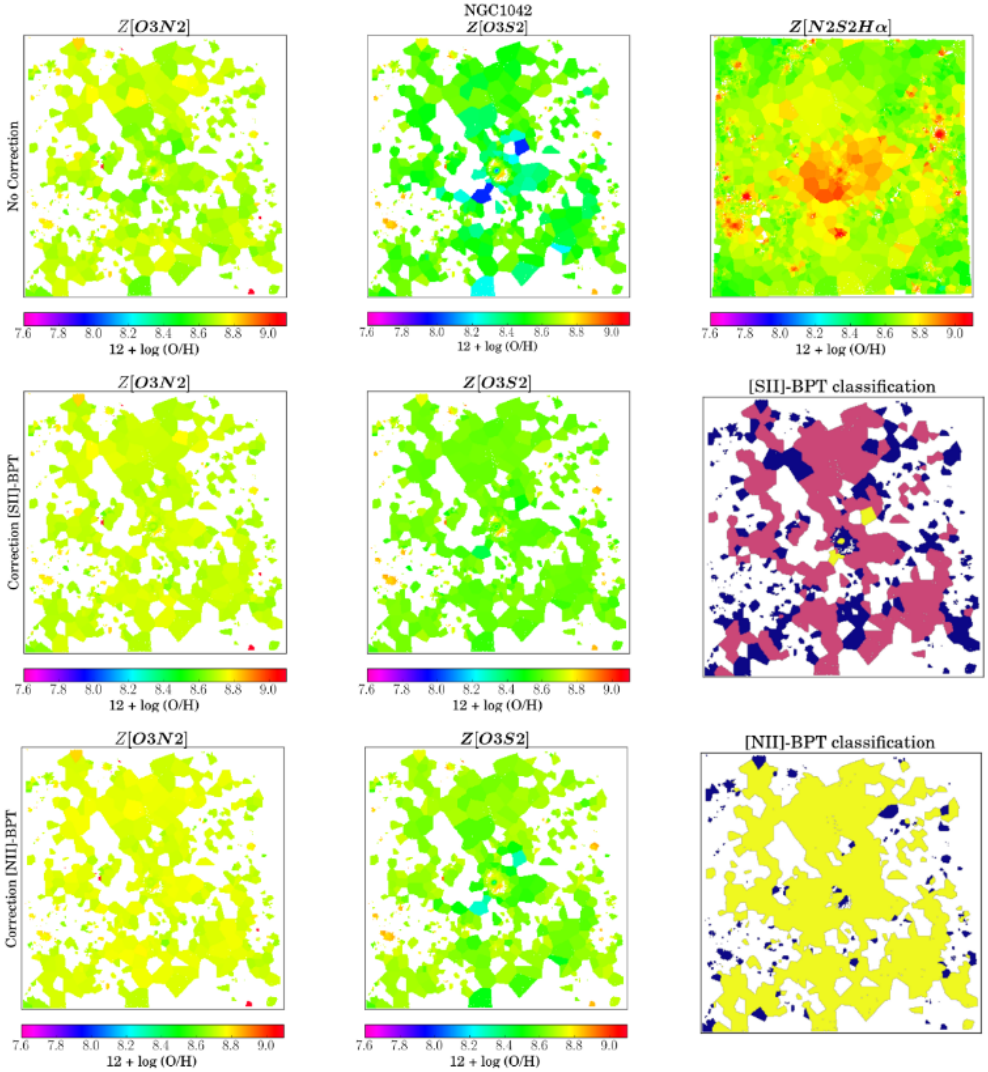

Figure 1. *Upper panel:* Metallicity maps of one of the sample galaxies, NGC 1042, using the metallicity diagnostics, O3N2 (upper-left panel), O3S2 (upper-central panel) and N2S2Hα (upper-right panel), before applying any corrections. *Middle panel:* Metallicity maps of the same galaxy NGC 1042 using metallicity diagnostics O3N2 (middle-left panel) and O3S2 (middle-central panel) after corrections derived in this work are applied to the DIG/LIER and Seyfert-like regions identified using [SII]-BPT diagnostic and are shown as pink (DIG/LIER) and yellow (Seyfert-like) regions in the spatially-resolved [SII]-BPT map of this galaxy (middle-right panel). *Lower panel:* Metallicity maps of the same galaxy NGC 1042 using metallicity diagnostics O3N2 (bottom-left panel) and O3S2 (bottom-central panel) after corrections derived in this work are applied to the DIG/LIER regions identified using [NII]-BPT diagnostic and are shown as yellow regions in the spatially-resolved [NII]-BPT map of this galaxy (bottom-right panel). The blue regions in the spatially-resolved BPT maps denote the HII regions. The scale and limits on all metallicity maps are set to be same for a better visual comparison. Figure reproduced from Kumari et al. (2019).

from the Sloan Digital Sky Survey (SDSS), and is valid in a wide metallicity range, $7.6 < 12 + \log(\mathrm{O/H}) < 8.85$:

$$\mathrm{O3N2} = 0.281 - 4.765\ \mathrm{x_{O3N2}} - 2.268\ \mathrm{x^2_{O3N2}}. \quad (1)$$

2. O3S2 (= $\log([\mathrm{O\,III}]/\mathrm{H}\beta + [\mathrm{S\,II}]/\mathrm{H}\alpha)$) used in this work is also based on same SDSS dataset and stacking technique used for O3N2 diagnostic in Curti et al. (2017), and is given below:

$$\mathrm{O3S2} = -0.046 - 2.223\ \mathrm{x_{O3S2}} - 1.073\ \mathrm{x^2_{O3S2}} + 0.534\ \mathrm{x^3_{O3S2}}, \quad (2)$$

In equations (1) & (2), $\mathrm{x_{O3N2}}$ and $\mathrm{x_{O3S2}}$ are oxygen abundances normalised to the solar value in the form $12 + \log(\mathrm{O/H})_\odot = 8.69$.

3. N2S2Hα (= $\log([\mathrm{N\,II}]/[\mathrm{S\,II}]) + 0.264 \log([\mathrm{N\,II}]/\mathrm{H}\alpha)$) was introduced as a metallicity diagnostic by Dopita et al. (2016) who gave two calibrations for metallicity as a linear and a polynomial function of N2S2Hα.

Figure 1 (upper panel) shows metallicity maps of a sample galaxy NGC 1042, obtained using O3N2 (left panel), O3S2 (middle panel) and N2S2Hα (right panel). The three metallicity maps of the same galaxy have different appearance, showing the inherent discrepancies between various metallicity calibrations discussed in several works (see e.g. Kumari et al., 2017; Maiolino & Mannucci, 2019).

3. Results

Biases in metallicities of DIG/LIER-dominated regions: Figure 2 shows the distribution of metallicity difference between the closeby H II-DIG/LIER pairs, ΔlogZ in all 24 galaxies. We estimate the mean ($\overline{\Delta\mathrm{logZ}}$) and standard deviation ($\sigma(\Delta\mathrm{logZ})$) of the differential metallicity distributions for each diagnostic and for both [S II]-BPT (left panel) and [N II]-BPT (right panel) classification. Assuming that the true metallicity of DIG counterpart within a H II-DIG/LIER pair is same as the metallicity of the adjacent H II region as measured from the strong line methods, we find that the metallicity of DIG/LIER determined from O3N2 shows little offset with respect to the expected metallicity, irrespective of the classification method used. Moreover, $\sigma(\Delta\mathrm{logZ})$ is also minimal for the O3N2 diagnostic. On the contrary, O3S2 diagnostic underestimates the metallicities of DIG/LIER counterpart and shows large dispersions for both [S II]-BPT and [N II]-BPT classification. N2S2Hα shows the largest $\sigma(\Delta\mathrm{logZ})$ among the three metallicity calibrators, though the offset is not as significant as O3S2 diagnostic.

New metallicity calibrations for DIG/LIER: Further analysis shows that ΔlogZ varies with ($\log([\mathrm{O\,III}]/\mathrm{H}\beta) = \mathrm{O3}$) for both O3N2 and O3S2 diagnostics. We use this observation to correct the biases in metallicities of DIG/LIERs and hence propose the following metallicity calibrations for DIG/LIERs.

1. For [S II]-BPT classification, the metallicities of DIG/LIER are given by:

$$12 + \log(\mathrm{O/H})_{\mathrm{DIG/LIER}} = \mathrm{x_{O3N2}} + 8.69 + 0.156\ \mathrm{O3}, \quad (3)$$

$$12 + \log(\mathrm{O/H})_{\mathrm{DIG/LIER}} = \mathrm{x_{O3S2}} + 8.765 + 0.309\ \mathrm{O3} + 0.208\ \mathrm{O3}^2. \quad (4)$$

2. For [N II]-BPT classification, the metallicities of DIG/LIER are given by:

$$12 + \log(\mathrm{O/H})_{\mathrm{DIG/LIER}} = \mathrm{x_{O3N2}} + 8.723 + 0.127\ \mathrm{O3}, \quad (5)$$

$$12 + \log(\mathrm{O/H})_{\mathrm{DIG/LIER}} = \mathrm{x_{O3S2}} + 8.803 + 0.229\ \mathrm{O3}, \quad (6)$$

where $\mathrm{x_{O3N2}}$ and $\mathrm{x_{O3S2}}$ in the above equations are same as defined in Section 2.

Figure 1 shows new metallicity maps of NGC 1042 from O3N2 (left-panel) and O3S2 (middle-panel) diagnostics, where HII and DIG/LIER have been identified using [SII]-BPT (central panel) and [NII]-BPT criteria (bottom panel). For obtaining these new metallicity maps, the HII region metallicity calibrations are applied to HII regions while new DIG/LIER calibrations are applied to DIG/LIER within the galaxy. For example, central-left panel shows the new metallicity map where original O3N2 calibration (i.e. equation 1) has been applied to HII regions and new O3N2 caibration (equation 3) has been applied to DIG/LIER. Hence, each of the new metallicity maps is obtained by a combination of original HII region calibrations (equations (1) & (2)) and the new DIG calibrations (equations (3)-(6)). The new metallicity maps (central and bottom panels) do not show the small scale metallicity variations seen in the original metallicity maps (upper-panel) from O3N2 and O3S2 diagnostics.

Using new metallicity maps obtained from O3N2 and O3S2 diagnostics, we again study the distribution of differential metallicities as done for original maps of all galaxies shown in Figure 2, and derive the $\overline{\Delta \log Z}$ and $\sigma(\Delta \log Z)$ of the new distributions for both [SII]-BPT and [NII]-BPT classification. The mean offsets are zero by construction, and $\sigma(\Delta \log Z)$ are reduced for both diagnostics. The new O3N2 calibration, in particular, results in $\sigma(\Delta \log Z)$ of only 0.04 and 0.03 for [SII]-BPT and [NII]-BPT classifications, respectively. Hence, we recommend using the new O3N2 calibration for estimating metallicities of DIG/LIER. However, the distribution of differential metallicities obtained from O3S2 diagnostic is bimodal in the case of [NII]-BPT classification. Hence, we do not recommend using O3S2 diagnostic when DIG/LIER is identified using [NII]-BPT. We also propose to use the new calibrations for the passive/quiescent galaxies. However, further studies need to be performed to test the applicability of these calibrations for Seyferts/AGNs. The new calibrations will be significantly useful to extend chemical evolution studies to passive/quiescent galaxies.

Acknowledgments. NK thanks co-authors of the publication, Kumari et al. (2019), on which the present contribution is based. NK also thanks Schlumberger Foundation, ERC Advanced Grant 695671 'QUENCH' and the Science and Technology Facilities Council (STFC) for supporting the travel to this conference.

References

Baldwin J. A., Phillips M. M., Terlevich R., 1981, *PASP*, **93**, 5

Belfiore F., Maiolino R., Maraston C., Emsellem E., Bershady M. A., Masters K. L., Yan R., Bizyaev D., Boquien M., Brownstein J. R., Bundy K., Drory N., Heckman T. M., Law D. R., Roman-Lopes A., Pan K., Stanghellini L., Thomas D., Weijmans A.-M., Westfall K. B., 2016, *MNRAS*, **461**, 3111

Berg D. A., Skillman E. D., Garnett D. R., Croxall K. V., Marble A. R., Smith J. D., Gordon K., Kennicutt Jr. R. C., 2013, *ApJ*, **775**, 128

Cappellari M., Copin Y., 2003, *MNRAS*, **342**, 345

Cid Fernandes R., Stasińska G., Mateus A., Vale Asari N., 2011, *MNRAS*, **413**, 1687

Curti M., Cresci G., Mannucci F., Marconi A., Maiolino R., Esposito S., 2017, *MNRAS*, **465**, 1384

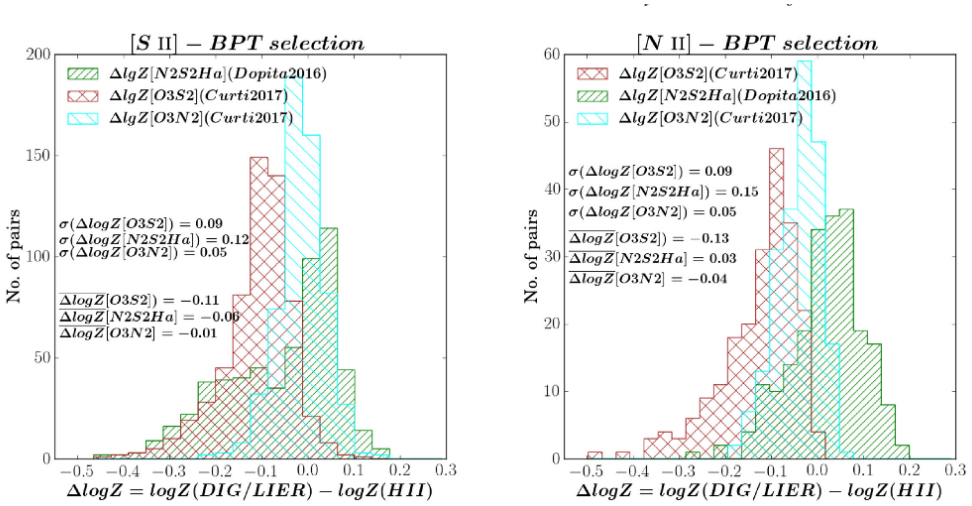

Figure 2. Distribution of metallicity difference (ΔlogZ) between closeby DIG/LIER (logZ(DIG/LIER)) and HII region (logZ(HII)) pairs based on [SII]-BPT (*left panel*) and [NII]-BPT (*right panel*) criteria. On both panels, cyan, brown and green represent the distribution of differential metallicities from O3N2, O3S2 and N2S2Hα diagnostics, respectively. $\overline{\Delta \log Z}$ and $\sigma(\Delta \log Z)$ correspond to the mean and standard deviation of the distributions, respectively, and are presented for each metallicity diagnostic. Figure adapted from Kumari et al. (2019).

Dopita M. A., Kewley L. J., Sutherland R. S., Nicholls D. C., 2016, *Ap&SS*, **361**, 61

Kauffmann G., Heckman T. M., Tremonti C., Brinchmann J., Charlot S., White S. D. M., Ridgway S. E., Brinkmann J., Fukugita M., Hall P. B., Ivezić Ž., Richards G. T., Schneider D. P., 2003, *MNRAS*, **346**, 1055

Kewley L. J., Dopita M. A., Sutherland R. S., Heisler C. A., Trevena J., 2001, *ApJ*, **556**, 121

Kumari N., James B. L., Irwin M. J., 2017, *MNRAS*, **470**, 4618

Kumari N., Maiolino R., Belfiore F., Curti M., 2019, *MNRAS*, **485**, 367

Maiolino R., Mannucci F., 2019, *A&A Rev.*, **27**, 3

Reynolds R. J., 1984, *ApJ*, **282**, 191

Rossa J., Dettmar R.-J., 2003, *A&A*, **406**, 493

Vazdekis A., Ricciardelli E., Cenarro A. J., Rivero-González J. G., Díaz-García L. A., Falcón-Barroso J., 2012, *MNRAS*, **424**, 157

Yan R., 2018, *MNRAS*, **481**, 476

Zhang K., Yan R., Bundy K., Bershady M., Haffner L. M., Walterbos R., Maiolino R., Tremonti C., Thomas D., Drory N., Jones A., Belfiore F., Sánchez S. F., Diamond-Stanic A. M., Bizyaev D., Nitschelm C., Andrews B., Brinkmann J., Brownstein J. R., Cheung E., Li C., Law D. R., Roman Lopes A., Oravetz D., Pan K., Storchi Bergmann T., Simmons A., 2017, *MNRAS*, **466**, 3217

Chemical Abundances in Gaseous Nebulae:
Open problems in Nebular astrophysics
AAA Workshop Series 11, 2019
M. Cardaci, G. Hägele & E. Pérez-Montero, eds.

Contributed Paper

The morphology and stellar populations in HII galaxies

Eduardo Telles
Observatório Nacional, Rua Gen. José Cristino, 77, Rio de Janeiro, RJ, 20921-400, Brasil

Abstract.
I briefly review some of our own work on the morphological properties of HII galaxies and their clumpy starbursts. I also present our recent results on the stellar populations from our SED fitting from UV to mid-IR. A simple three burst history of star formation seems to be enough to fit the photometric data. The bulk of stars in HII galaxies were formed in their early history. The *current* episode of star formation contributes to only a few per cent of the total stellar mass. However, this starburst is making stars at a maximum rate comparable to our best nearby laboratory of a massive star factory, the 30 Dor region in the LMC.

Key words: galaxies: abundances — galaxies: ISM — techniques: imaging spectroscopy

1. The looks of HII galaxies

Star formation (SF) is a temporal and spatial phenomenon in HII galaxies. We have to understand how it occurred along the history as well as its distribution over the extent of the galaxy. Imaging studies over the last decades have shown that recent SF dominates the optical emission over a large area of HII galaxies, shaping its overall morphology (Telles et al., 1997). Little is evident of the underlying galaxy. Surface photometry in the optical and near-IR studies however indicate that there must be a population of stars formed in previous episodes of SF (Telles & Terlevich, 1997; Telles, 2002). This seems to rule out the hypothesis that HII galaxies may be forming stars for the first time now. They are at least middle aged dwarf irregular galaxies with superposed recent starburst.

Figure 1 shows the images of a prototypical blue compact galaxy. Mrk 36 (Haro 4), at a distance of 9 Mpc, has once been known as one of the youngest galaxies in the local universe (Huchra et al., 1982). The superb image quality of GEMINI in the near-IR reveals that compactness is "in the eye of the beholder". Slit or fiber spectroscopy are usually placed on the brightest knot. As can be seen in the figure, a $2''$-$3''$aperture will cover a number of massive clusters, even in the nearest HII galaxies.

The starbursts in HII galaxies are composed of knots of recent SF with typical sizes of a few tens of parsecs spread over galactic scales. These knots, in turn, are ensembles of massive young ionizing clusters of a few parsecs in size (Lagos et al.,

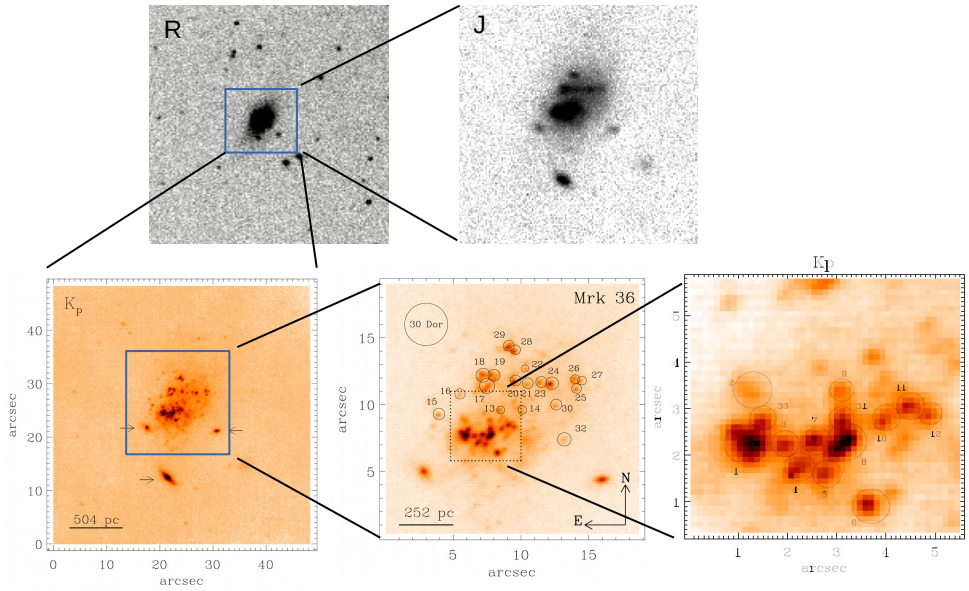

Figure 1. Mrk 36 a prototypical young blue compact galaxy. The images show increasing spatial resolution from the optical to near-IR. Upper Panels: The R-band image is from Lowell observatory (NED). The J-band image is from UKIRT (Telles, 2002). Bottom Panels: The K-band images are from GEMINI (Lagos et al., 2011).

2011; Torres-Campos et al., 2017). This scenario disfavors the hypothesis that SF propagates in galactic scales. Instead, SF may be stochastic and synchronized within the time scales of the lifetime of the knots of SF ($< 10^8$yrs). HII galaxies form stars like pop-corn in a pan! The result of this scenario is that the starbursts in HII galaxies have irregular structures and are very clumpy (Lagos et al., 2007). The clumpiness and extent of the starbursts allied with the orientation of the galaxy in the sky may make them look like your favorite vegetable, fruit, or animal. But in the end they are the same class of objects. Spatially resolved spectroscopy also have helped us draw this picture of the general properties and homogeneous physical conditions in HII galaxies (see e.g Cresci et al., 2017; Telles et al., 2014; Lagos et al., 2009, 2012, 2016, 2018; Lagos & Papaderos, 2013, and references therein).

2. HII galaxies are old

Despite the progress from increasingly detailed studies of prototypical HII galaxies, in times of large surveys, we return to their most basic spectroscopic properties in order to select a large sample from SDSS DR13 for a re-analysis of their stellar population. HII galaxies will fall into the category of "extreme" star forming galaxies, selected for their intense line emission. By selecting objects in the upper-left wing of the BPT diagram we pick the high excitation, low metallicity objects. In addition, the choice of large equivalent widths of Hβ (> 30Å)

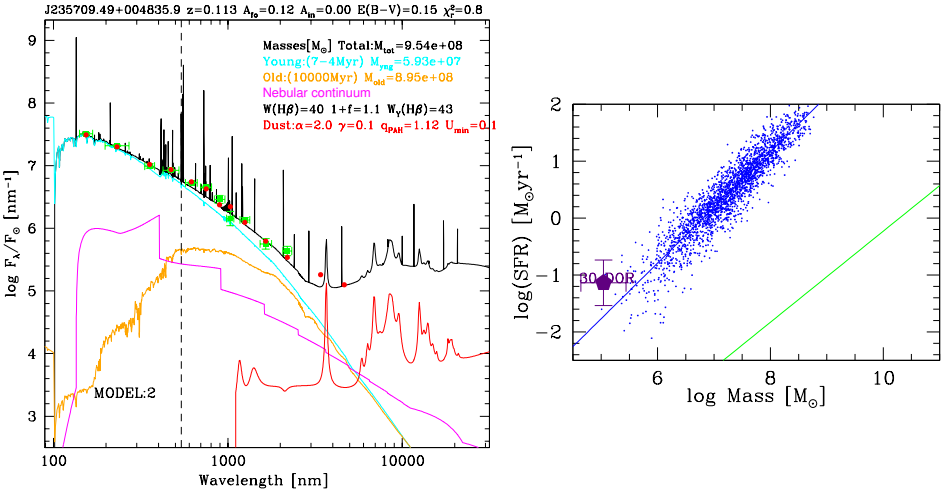

Figure 2. *Left:* An example of our SED fitting procedure. The green points are the input data. The red points are the model result from the best fit model with our three burst SFH stellar populations, with dust attenuation and emission, and nebular emission. *Right:* A starburst version of main sequence for star forming galaxies. The star formation rate (SFR) of the *current* episode of SF is plotted against the stellar mass of the *young* population only (blue points). The green line represents the usual main sequence for star forming galaxies (mean integrated SFR vs. total stellar mass) from Brinchmann et al. (2004)).

favors the younger bursts in low mass galaxies. For our final sample of ∼2700 HII galaxies for our multiwavelength photometric analysis from far-UV (FUV) to MIR, we cross-matched the resulting SDSS sample with GALEX, UKIDSS and WISE. We chose to use CIGALE (http://cigale.lam.fr/) for our SED modeling and fitting. Our choice of a star forming history is based on our previous work where we showed that the simplest bursty model to describe the optical spectra of HII galaxies requires an ionizing, an intermediate age, and an old stellar populations (Westera et al., 2004). Our extensive tests of model parameters, detailed analysis and results can be found in Telles & Melnick (2018), and the data are given in http://staff.on.br/etelles/SED.html.

Figure 2 shows an example of our SED fitting procedure (left panel), and a starburst (< 10Myr) version of the so-called main sequence of star forming galaxies (right panel).

It is fair to caution the readers that the plain existence of a correlation between SFR and stellar mass does not, by itself, have any meaning, simply because the total mass is derived by integrating the SFR ($M_\star = \int_0^{t_0} SFR(t)dt = t_0\langle SFR\rangle$.). There is always going to be a correlation! A misleading consequence is that, for a given SFH, if the integration is truncated, for instance for high redshift galaxies, where their lifetime is smaller than the Hubble time, their integrated SFR may naturally give a higher value for a given mass than the local galaxies. We may

test the SFH and galaxy evolution only if model-independent information can be added.

HII galaxies have SFR in the last 10 or 100 Myrs greater than the main sequence locus – again a natural consequence of the assumed SFH and integration over a much smaller dt. However, in our case we can compare the independent determination of the starburst SFR of our favorite laboratory of massive star formation 30 Dor as in Figure 2 (right panel). 30 Dor is known to be forming massive stars at very high efficiency. This empirical comparison means that HII galaxies are forming stars at rates close to the "speed limit" for star formation set by 30 Dor.

In conclusion, our stellar population analysis, again, has shown that the star formation histories of HII Galaxies are well parametrised by three bursts (i) the current ionizing burst; (ii) an intermediate-age burst; and (iii) an old stellar population. Although the current episode of star formation overwhelmingly dominate the star light, it contributes to only a few per cent of the total stellar mass. Most of the stellar mass in HII galaxies was produced in their past and early history.

Acknowledgments. I would like to acknowledge the contributions of my main collaborators Jorge Melnick and Patricio Lagos in the topics discussed here.

References

Brinchmann J., Charlot S., White S. D. M., Tremonti C., Kauffmann G., Heckman T., Brinkmann J., 2004, *MNRAS*, **351**, 1151

Cresci G., Vanzi L., Telles E., Lanzuisi G., Brusa M., Mingozzi M., Sauvage M., Johnson K., 2017, *A&A*, **604**, A101

Huchra J., Geller M., Hunter D., Gallagher J., 1982, Y. Kondo (ed.), *NASA Conference Publication*, Vol. 2238 of *NASA Conference Publication*

Lagos P., Demarco R., Papaderos P., Telles E., Nigoche-Netro A., Humphrey A., Roche N., Gomes J. M., 2016, *MNRAS*, **456**, 1549

Lagos P., Papaderos P., 2013, *Advances in Astronomy*, **2013**, 631943

Lagos P., Scott T. C., Nigoche-Netro A., Demarco R., Humphrey A., Papaderos P., 2018, *MNRAS*, **477**, 392

Lagos P., Telles E., Melnick J., 2007, *A&A*, **476**, 89

Lagos P., Telles E., Muñoz-Tuñón C., Carrasco E. R., Cuisinier F., Tenorio-Tagle G., 2009, *AJ*, **137**, 5068

Lagos P., Telles E., Nigoche-Netro A., Carrasco E. R., 2011, *AJ*, **142**, 162

Lagos P., Telles E., Nigoche Netro A., Carrasco E. R., 2012, *MNRAS*, **427**, 740

Telles E., 2002, D. P. Geisler, E. K. Grebel, and D. Minniti (eds.), *Extragalactic Star Clusters*, Vol. 207 of *IAU Symposium*, p. 357

Telles E., Melnick J., 2018, *A&A*, **615**, A55

Telles E., Melnick J., Terlevich R., 1997, *MNRAS*, **288**, 78

Telles E., Terlevich R., 1997, *MNRAS*, **286**, 183

Telles E., Thuan T. X., Izotov Y. I., Carrasco E. R., 2014, *A&A*, **561**, A64

Torres-Campos A., Terlevich E., Rosa-González D., Terlevich R., Telles E., Díaz A. I., 2017, *MNRAS*, **471**, 2829

Westera P., Cuisinier F., Telles E., Kehrig C., 2004, *A&A*, **423**, 133

Chemical Abundances in Gaseous Nebulae:
Open problems in Nebular astrophysics
AAA Workshop Series 11, 2019
M. Cardaci, G. Hägele & E. Pérez-Montero, eds.

Contributed Paper

Abundance estimations in the NLRs of Type 2 AGNs

M. V. Cardaci[1], O. L. Dors[2], G. F. Hägele[1] and A. Krabbe[2]

[1] *Instituto de Astrofísica de La Plata (CONICET–UNLP), Argentina*
[2] *Universidade do Vale do Paraíba, Av. Shishima Hifumi 2911, 12244-000, São José dos Campos - SP, Brasil*

Abstract. Chemical abundances of the Narrow Line Regions (NLRs) of Active Galactic Nuclei (AGNs) are still poorly estimated. It is not clear that the methods developed for the study of the gas phase in HII regions are valid and/or provide accurate/realistic estimations of the NLRs abundances. Here we present a brief summary of the work carried out by our group on the study of chemical abundances of the NLRs associated to type 2 AGNs. We used different grids of photoionization models built using the Cloudy code. We derived new indexes to estimate the oxygen abundances of the NLRs using ultra violet and optical emission lines combined with the grids of photoionization models. We also obtained new quantitative determinations of the nitrogen abundance and a consistent relation between the nitrogen and oxygen abundances for a sample of nearby Seyfert 2 galaxies, located at redshift $z < 0.1$. Our results for N/O vs. O/H abundance ratios derived for Seyfert 2 galaxies are in consonance with those derived for a sample of extragalactic disc HII regions with high metallicity.

Key words: galaxies: abundances — galaxies: ISM — galaxies: active — galaxies: Seyfert

1. Introduction

Active Galactic Nuclei (AGNs) show strong recombination and prohibited emission lines in their spectra such as Hα, Hβ, [OIII]]5007, and the auroral emission lines [OII]3727, [SII]4071, [OIII]4363, [OIII]4959,5007, [SII]6717,6731) between others. These lines are used to estimate densities and temperatures of the gas in wich the lines are originated.
Type-1 AGNs exhibit broad recombination lines that would be produced by the superposition of the contribution from the emission coming from a diffuse gas region, the Narrow Lines Region (NLR), and the emission originated in a denser region called Broad Lines Region. In this type of objects the continuum emission is another factor to take into account to estimate the line fluxes. Prohibited lines are expected to be originated in the NLR in which the gas density is expected to be in the order of $500\,\mathrm{cm}^{-3}$ (see e.g. Dors et al., 2014).
Type-2 AGNs do not show prominent continuum emission and present only narrow recombination emission lines that are assumed to be produced in the same

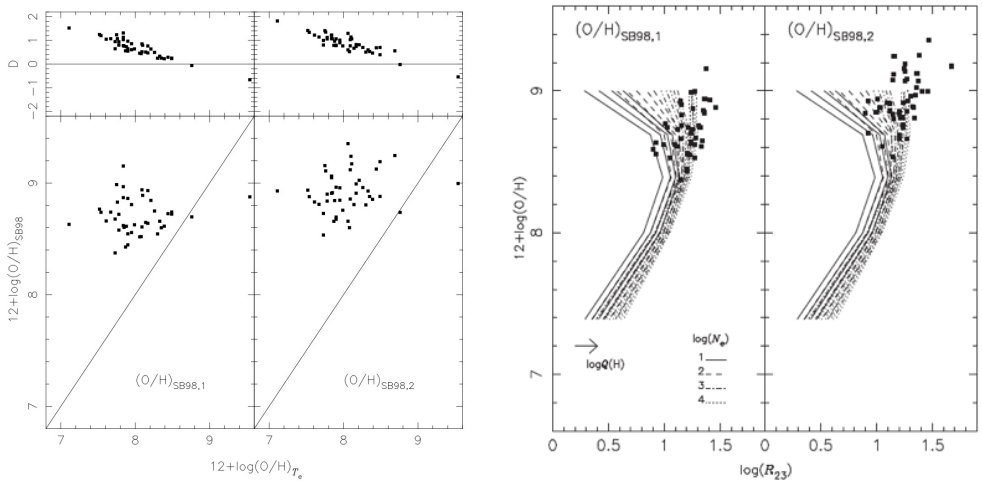

Figure 1. *Left:* Taken from Dors et al. (2015, Fig.1). *Right:* Taken from Dors et al. (2015, Fig.3)

gas than the prohibited lines. This type of AGNs are preferable to tackle the study of the physical parameteres of gas producing emission lines and associated to an Active Nuclei. Hence we restricted our sample to the Seyfert 2 objects.
Storchi-Bergmann et al. (1998, hereafter SB98) derived two theoretical calibrations based on strong emission-lines to estimate metallicities of NLRs associated to Seyfert 2 objects. They found these objects have solar or super-solar metallicities. Using the Te-method based on emission-line ratios and that is widely used for HII regions, other authors found NLRs metallicities to be solar or undersolar (e.g. Alloin et al., 1992; Zhang et al., 2013). The disagreement between the abundances obtained through these methods is the so-called temperature problem.
Comparing the O/H abundances obtained trough the Te-method and the SB98 relations, Dors et al. (2015) found that, for a sample of 47 objects, the Te-method provides lower O/H abundances by up to about 2 dex with an average value of about 0.8 dex (left panel of Fig.1). These authors argued that temperature problem in the NLRs could be (in part) caused by the presence of a secondary heating source, probably related to shocks, in addition to the radiation from the gas accretion onto the AGN. It is worth to take into account that the Te-method to estimate O/H abundances involves the use of Ionization Correction Factors (ICFs), that are, up to now, estimated for HII regions. The validity of this assumption could (probably) be also responsable of the temperature problem in the metallicity determination of NLRs associated to Seyfert 2 AGNs. Therefore the Te-method is still not providing accurate chemical abundances in this kind of objects.
Dors et al. (2015) also compared the metallicity estimations by the central intersect oxygen abundances of this kind of objects derived from the radial abundance gradients and by the central abundances determined from the spectra of the central regions Ho et al. (1997) through the Storchi-Bergmann et al. (1998) first

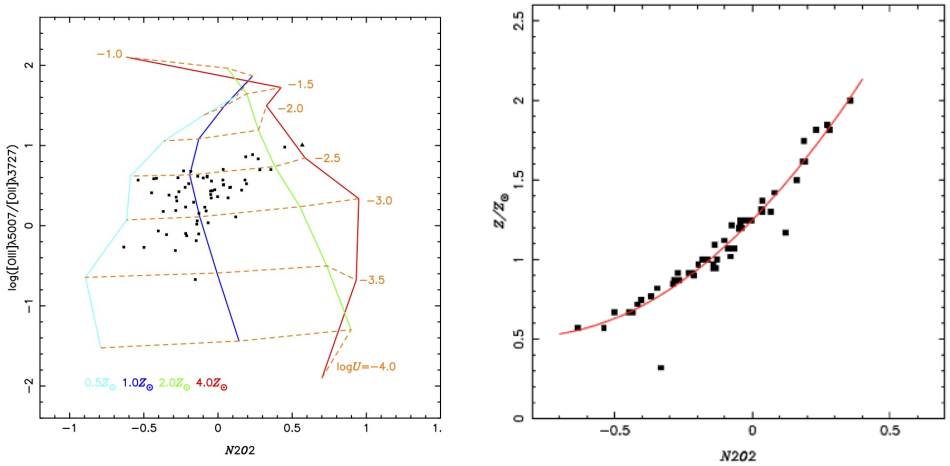

Figure 2. *Left:* Taken from Castro et al. (2017, Fig.3). *Right:* Castro et al. (2017, Fig.4).

calibration for AGNs and through the C_{NS} method (Pilyugin et al., 2006, 2007) for HII-like regions. Dors et al. (2015) found an almost one-to-one correlation between them (see Fig, 3 in Dors et al., 2015).

2. Strong-lines - Empirical calibrations

Empirical emission-line ratios such us R_{23}=([OII]3727+[OIII]4959,5007)/Hβ, are used as metallicity indicators in star-forming regions. It is interesting to explore the use of such emission-line ratios to estimate metallicities in Seyfert 2 NLRs. It has been done taking into account that the relation between this R_{23} parameter and the 12+log(O/H) metallicity indicator is actually calibrated for HII regions.

2.1. 12+log(O/H)–R_{23} calibration

Using photoionization models with an AGN-source model as SED, and comparing their results for the R_{23} parameter as a function of the oxygen abundances, with the estimations of the oxygen abundances of the objects in their sample obtained trough the Storchi-Bergmann et al. (1998) relations, Dors et al. (2015) concluded that a better agreement is obtained when the abundances are determined through the first relation of Storchi-Bergmann et al. (1998) (see the right panel of Fig. 1).

2.2. $Z/Z_{\odot}$–N2O2 calibration

Another parameter used as metallicity indicator in HII regions is the N2O2=log([NII]λ6584/[OII]λ3727) emission-line ratio. In the work by Castro et al. (2017) we derived a new relation between the metallicity of NLRs of type-2 AGNs and the N2O2 parameter for NLRs of type-2 AGNs. The calibration of the N2O2 parameter was performed trough the observational data of 58 objects (taken from the literature) and trough a diagram containing the observational

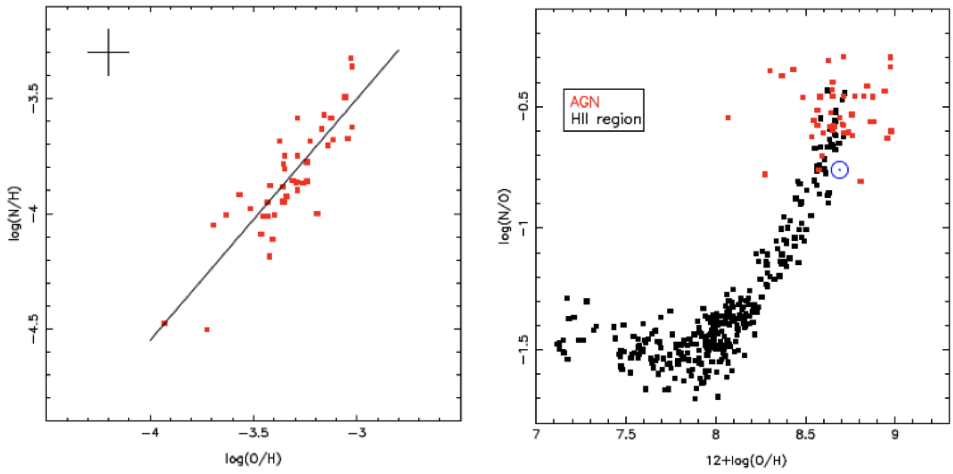

Figure 3. *Left:* Taken from Dors et al. (2017, Fig.3). *Right:* Dors et al. (2017, Fig.4).

data and the results of a grid of photoionization models (see the left panel of Fig. 2. The calibration found:

$$(Z/Z_{\odot}) = 1.08(\pm0.19) \times \mathrm{N2O2}^2 + 1.78(\pm0.07) \times \mathrm{N2O2} + 1.24(\pm0.01)$$

is shown in Fig.2 (right panel). In this work we also found that NLRs of Seyfert 2 AGNs show metallicities in the $0.3 \leq \mathrm{Z/Z_{\odot}} \leq 2.0$ range with a median value of $\mathrm{Z} \sim \mathrm{Z_{\odot}}$.

Thomas et al. (2019) investigated the relation between the NLRs metallicity and the host galaxy stellar mass. They performed detailed models including NLR excitation together with HII exitation. They found that their $\mathrm{M/M_{\odot}}$ vs. Z relation was very similar to the one found estimating metallicities with the N2O2 parameter calibrated by Castro et al. (2017), concluding that N2O2 is a very robust metallicity diagnostic for NLRs of Seyfert 2s.

2.3. N/H vs. O/H relation

We also derived new quantitative determinations of the nitrogen abundance and a consistent relation between nitrogen and oxygen abundances for NLRs of a sample of Seyfert 2 galaxies located at redshift z< 0.1 using the Cloudy code to build detailed photoionization models for 44 selected objects (Dors et al., 2017).

$$\log(N/H) = (1.5 \pm 0.09) \times \log(O/H) - (0.35 \pm 0.33)$$

We found that N/O abundance ratios in Seyfert 2 galaxies are similar to those derived by Pilyugin & Grebel (2016) for a sample of extragalactic HII regions with high metallicity.

2.4. Metallicities from UV lines: the C43 parameter

For the Seyfert 2 AGNs observed in the UV it is also possible to estimate their NLR metallicity using e.g. NV 1240, CIV 1549 and HeII1640, between others. The

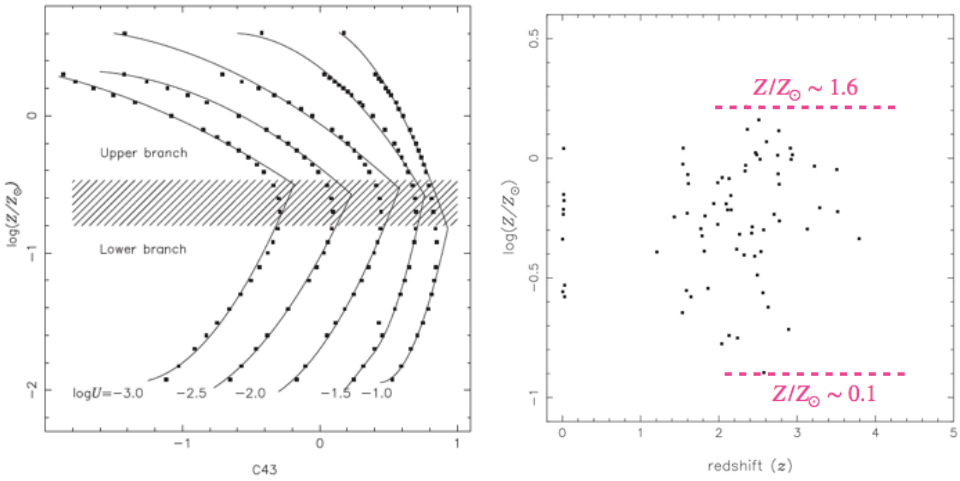

Figure 4. *Left:* Taken from Dors et al. (2014, Fig.4). *Right:* Taken from Dors et al. (2014, Fig.7).

NV 1240/CIV 1549 emission-lines ratio generally used as metallicity indicator for AGNs (Hamann & Ferland, 1992) can yield uncertain Z estimations since the NV emission-line could be enhanced by Lyα photons scattered from a broad absorption line wind (Hamann et al., 2002).
On the other hand, the CIV1549/HeII1640 ratio proposed by Nagao et al. (2006) as metallicity indicator is dependent on the ionization parameter U. In the work by Dors et al. (2014), we found that the introduction of a lower ionization stage in the CIV/HeII ratio weakens this dependence with U. Hence, in that work we proposed the new index: C43 = log[(CIV +CIII])/HeII] as a metallicity indicator. The relation between the C43 parameter with the metallicity $Z/Z_{\odot}$ is shown in Fig. 4 and it has the general form:

$$\log(Z/Z_{\odot}) = a \times C43^2 + b \times C43 + c$$

(see the a and b values in Dors et al., 2014).
In the same work, we used the C43 parameter to investigate the metallicity range of the NLRs of Type-2 AGNs and the existence of a metallicity evolution. We selected from the literature a sample of 81 objects with z between 0 and 4 and found that the metallicities of the objects in the sample are in a similar range than that found with the N2O2 parameter (see Fig. 4, right panel). We do not found a correlation between the metallicity and the redshift, even though we found the objects in our sample with redshifts between 1 and 3 show metallicities $Z/Z_{\odot}$ lower than 0.2.

References

Alloin D., Bica E., Bonatto C., Prugniel P., 1992, *A&A*, **266**, 117
Castro C. S., Dors O. L., Cardaci M. V., Hägele G. F., 2017, *MNRAS*, **467(2)**, 1507

Dors O. L. J., Arellano-Córdova K. Z., Cardaci M. V., Hägele G. F., 2017, *MNRAS*, **468(1)**, L113
Dors O. L., Cardaci M. V., Hägele G. F., Krabbe Â. C., 2014, *MNRAS*, **443(2)**, 1291
Dors O. L., Cardaci M. V., Hägele G. F., Rodrigues I., Grebel E. K., Pilyugin L. S., Freitas-Lemes P., Krabbe A. C., 2015, *MNRAS*, **453(4)**, 4102
Hamann F., Ferland G., 1992, *ApJ*, **391**, L53
Hamann F., Korista K. T., Ferland G. J., Warner C., Baldwin J., 2002, *ApJ*, **564(2)**, 592
Ho L. C., Filippenko A. V., Sargent W. L. W., 1997, *ApJS*, **112(2)**, 315
Nagao T., Maiolino R., Marconi A., 2006, *A&A*, **447(3)**, 863
Pilyugin L. S., Grebel E. K., 2016, *MNRAS*, **457(4)**, 3678
Pilyugin L. S., Thuan T. X., Vílchez J. M., 2006, *MNRAS*, **367(3)**, 1139
Pilyugin L. S., Thuan T. X., Vílchez J. M., 2007, *MNRAS*, **376(1)**, 353
Storchi-Bergmann T., Schmitt H. R., Calzetti D., Kinney A. L., 1998, *AJ*, **115(3)**, 909
Thomas A. D., Kewley L. J., Dopita M. A., Groves B. A., Hopkins A. M., Sutherland R. S., 2019, *ApJ*, **874(1)**, 100
Zhang Z. T., Liang Y. C., Hammer F., 2013, *MNRAS*, **430(4)**, 2605

Posters

Chemical Abundances in Gaseous Nebulae:
Open problems in Nebular astrophysics
AAA Workshop Series 11, 2019
M. Cardaci, G. Hägele & E. Pérez-Montero, eds.

Poster

Physical Conditions, Kinematics, and Morphology of the Planetary Nebula Tc 1 from VLT X-Shooter Observations

I. Aleman[1,2,3], M. L. Leal-Ferreira[3,4], J. Cami[5,6], S. Akras[7,8], B. Ochsendorf [9], R. Wesson[10], N. L. J. Cox[11], C. Morisset[12], J. Bernard-Salas[11], C. E. Paladini[2], E. Peeters[5,6], D. J. Stock[5], H. Monteiro[1], A. G. G. M. Tielens[3]

[1]*Instituto de Física e Química, Universidade Federal de Itajubá, Av. BPS 1303 Pinheirinho, 37500-903 Itajubá, MG, Brazil*
[2]*IAG-USP, Universidade de São Paulo, Rua do Matão 1226, Cidade Universitária, 05508-090, São Paulo, SP, Brazil*
[3]*Leiden Observatory, University of Leiden, PO Box 9513, 2300 RA, Leiden, The Netherlands*
[4]*Argelander-Institut für Astronomie, Universität Bonn, Auf dem Hügel 71, 53121 Bonn, Germany*
[5]*Department of Physics and Astronomy and Centre for Planetary Science and Exploration (CPSX), The University of Western Ontario, London, ON N6A 3K7, Canada*
[6]*SETI Institute, 189 Bernardo Ave, Suite 100, Mountain View, CA 94043, USA*
[7]*Observatório Nacional/MCTIC, Rua Gen. José Cristino, 77, 20921-400, Rio de Janeiro, RJ, Brazil*
[8]*Instituto de Matemática, Estatística e Física, Universidade Federal do Rio Grande, Rio Grande 96203-900, Brazil*
[9]*Space Telescope Science Institute, 3700 San Martin Drive, Baltimore, MD 21218, USA*
[10]*Department of Physics and Astronomy, University College London, Gower Street, London WC1E 6BT, UK*
[11]*ACRI-ST, 260 Route du Pin Montard, Sophia-Antipolis, France*
[12]*Instituto de Astronomia, Universidad Nacional Autonoma de Mexico, Apartado postal 106, C.P. 22800 Ensenada, Baja California, México.*

Abstract. We present preliminary results of the analysis of ESO/VLT/X-Shooter observations of the planetary nebula Tc 1. Physical conditions and abundances for several species were calculated from the analysis of the integrated and spatially resolved line fluxes. The latter provided the distribution of such quantities across the nebula. The spatially resolved analysis also revealed that several lines show a double peak spectral profile in some spatial positions, indicating that the instrument resolved the blue- and red-shifted components of the nebular expansion. Such information allowed us to construct a three-dimensional morphological model for Tc 1, which revealed that it is a slightly elongated spheroid with an equa-

torial density enhancement seen almost pole on. A few Tc 1 bright lines present extended wings (velocities up to a few hundred km s^{-1}), but the underlying mechanism is not known yet. Our preliminary photoionization model, obtained by modelling the line emission of the Tc 1 intermediate shell, indicate that the central star has a temperature of ∼32 000 K and a luminosity of ∼2 000 $L_{\odot}$, and that the nebula is located at a distance of 2 kpc.

Key words: planetary nebulae: general — planetary nebulae: individual: Tc 1 — ISM: abundances

1. Introduction

The bulk of the UV/optical Tc 1 emission originates from a fairly round nebula of 12 arcsec in diameter. Tc 1 also presents a faint, also spherical halo of approximately 50 arcsec in diameter. Previous spectroscopy studies of Tc 1 showed that it is a young, low-excitation object.

A remarkable characteristic of this otherwise regular C-rich PN is the recent detection of fullerenes (Cami et al., 2010). Fullerenes are a class of large carbonaceous molecules in the shape of an ellipsoidal or spheroidal cage (Kroto, 1987). Tc 1 was the first PN where the fullerene molecule C_{60} was detected, and to date the only object known to also show the corresponding emission features due to C_{70} (Cami et al., 2010). The fullerene formation route in PNe and the condition for its survival are not yet clear.

Here we present the preliminary results of the analysis of ESO/VLT/X-Shooter observations aimed at characterising the nebular physical conditions, abundances, and structure of the main 12 arcsec shell. The full description of this work is presented in Aleman et al. (2019, submitted). The study aims to expand the knowledge about this PN and to assist in future studies on the survival mechanisms of fullerenes in Tc 1.

2. Observations

Ultraviolet (UVB) to near infrared (NIR) observations of Tc 1 were obtained with the X-Shooter spectrograph (Vernet et al., 2011) mounted on the Very Large Telescope (VLT; Program 385.C-0720; P.I. N.L.J. Cox). In this work, we focused on the UVB and VIS X-Shooter arms data, which covers the spectral range from 3 200 to 10 100 Å. The observations were carried out in stare mode with the narrowest slit settings, i.e. 11×0.5 arcsec (UVB) and 11×0.4 arcsec (VIS). The resulting resolving powers are ∼9 100 and 17 000 for the UVB and VIS, respectively. The slit was positioned across the nebula, in a Position Angle of -56.0 degrees and slightly north of the central star position to avoid its emission. The data were reduced using the ESO X-Shooter pipeline (version 2.5.2). The standard LTT7987 was used for flux calibration. We use local standard measurements for the sky subtraction.

3. Results and Conclusions

VLT/X-Shooter spectra for the PN Tc 1 was obtained and analysed. The spectra show a large number of atomic emission lines, from which we derived physical conditions, ionization structure, elemental abundances, morphology and central star characteristics. A total of 230 emission lines from 14 elements (20 ions) were identified in the Tc 1 spectrum. The spectrum is characteristic of a low-ionization PN.

While the forbidden line diagnostics provide electron densities of $n_{\rm e} \sim 2\,000$ cm^{-3}, typical for ionized nebulae, the Balmer and Paschen decrements indicate that much higher densities are present ($n_{\rm e} > 10^5$ cm^{-3}). Zhang et al. (2004) suggested that such discrepancy could be explained by the presence of high-density clumps embedded in the ionized gas such as cometary knots. Such differences needs to be further investigated.

Elemental abundances were derived from colisionally excited lines (CELs) for N, O, Ne, Ar, and S, and from optical recombination lines (ORLs) for He, C, N, and O. The values are compatible to previous studies. The lines of [N II], [S II], and [Cl II] show a clear double peaked structure, which is consistent with a homologously expanding nebula.

A 3-D morpho-kinematical model that reproduces the [S II] line emission characteristics shows that Tc 1 is a slightly elongated spheroid with an equatorial density enhancement. The nebula is seen almost pole-on (5–7 degrees inclination with respect to the line-of-sight). The presence of broad wings in the bright lines is evidence of a fast "wind" with velocities up to several hundreds of km s^{-1}.

Preliminary photoionization models provide a nebular gas density of around 2 500 cm^{-3}, and central star temperature and luminosity close to, respectively, 32 kK and 2 000 $L_{\odot}$. The models also indicate that Tc 1 is located at approximately 2 kpc from Earth.

Acknowledgments. Studies of interstellar chemistry at Leiden Observatory are supported through the advanced-ERC grant 246976 from the European Research Council, through a grant by the Dutch Science Agency, NWO, as part of the Dutch Astrochemistry Network, and through the Spinoza prize from the Dutch Science Agency, NWO. I.A. acknowledges the partial support of CNPq/Brazil (Senior Postdoctoral Fellowship number 157806/2015-4) and CAPES/Brazil (PNPD fellowship). M.L.L.-F. and S.A. acknowledge the support of CNPq, Conselho Nacional de Desenvolvimento Científico e Tecnológico - Brazil, processes numbers 248503/2013-8 and 300336/2016-0 respectively. CM thanks the CONACyT project CB2015/254132 and the UNAM-PAPIIT project 107215. RW is supported by ERC Grant 694520 SNDUST. Work based on observations collected at the European Organisation for Astronomical Research in the Southern Hemisphere under ESO programme 385.C-0720. This work has made use of the computing facilities of the Laboratory of Astroinformatics (IAG/USP, NAT/Unicsul), whose purchase was made possible by the Brazilian agency FAPESP (grant 2009/54006-4) and the INCT-A. This research has made use of NASA's Astrophysics Data System.

References

Cami J., Bernard-Salas J., Peeters E., Malek S. E., 2010, *Science*, **329**, 1180
Kroto H. W., 1987, *Nature*, **329**, 529
Vernet J., Dekker H., D'Odorico S., Kaper L., Kjaergaard P., Hammer F., Randich S., Zerbi F., Groot P. J., Hjorth J., Guinouard I., Navarro R., Adolfse T., Albers P. W., Amans J.-P., Andersen J. J., Andersen M. I., Binetruy P., Bristow P., Castillo R., Chemla F., Christensen L., Conconi P., Conzelmann R., Dam J., de Caprio V., de Ugarte Postigo A., Delabre B., di Marcantonio P., Downing M., Elswijk E., Finger G., Fischer G., Flores H., François P., Goldoni P., Guglielmi L., Haigron R., Hanenburg H., Hendriks I., Horrobin M., Horville D., Jessen N. C., Kerber F., Kern L., Kiekebusch M., Kleszcz P., Klougart J., Kragt J., Larsen H. H., Lizon J.-L., Lucuix C., Mainieri V., Manuputy R., Martayan C., Mason E., Mazzoleni R., Michaelsen N., Modigliani A., Moehler S., Møller P., Norup Sørensen A., Nørregaard P., Péroux C., Patat F., Pena E., Pragt J., Reinero C., Rigal F., Riva M., Roelfsema R., Royer F., Sacco G., Santin P., Schoenmaker T., Spano P., Sweers E., Ter Horst R., Tintori M., Tromp N., van Dael P., van der Vliet H., Venema L., Vidali M., Vinther J., Vola P., Winters R., Wistisen D., Wulterkens G., Zacchei A., 2011, *A&A*, **536**, A105
Zhang Y., Liu X.-W., Wesson R., Storey P. J., Liu Y., Danziger I. J., 2004, *MNRAS*, **351**, 935

Chemical Abundances in Gaseous Nebulae:
Open problems in Nebular astrophysics
AAA Workshop Series 11, 2019
M. Cardaci, G. Hägele & E. Pérez-Montero, eds.

Poster

Chemical abundance determination of the Seyfert 2 nuclei of Mrk 1066

A. Mesquita[1] & O. L. Dors[1]

[1] *Universidade do Vale do Paraíba, Brazil*

Abstract. We derive the ionization structure, features of the ionizing source and the chemical abundance of heavy elements of the Narrow Line Region of the Seyfert 2 nuclei of Mrk 1066. For that, we used the CLOUDY code combined with observational Spectral Energy Distribution to construct detailed photoionization model in order to reproduce the optical emission-line intensities. The abundance of O, N, S, Ne in relation the hydrogen one was found be sub-solar. These abundance values were compared with those computed by using direct measurement of the electron temperature (T_e-method). From this comparison, we found that only the nitrogen abundance derived by our detailed photoionization model is in consonance with the one from the T_e-method.

Key words: galaxies: abundances — galaxies: spectroscopy

1. Introduction

Abundance determinations of heavy elements (e.g. O, N, S) are essential to study the nature of AGNs as well as to input constraints in chemical galaxy evolution models. In particular, due to the oxygen presents strong emission-lines of the most abundant ions in the optical spectra, it is relatively easy to derive its abundance. Dors et al. (2015) found that oxygen elemental abundances derived by using direct measurements of the electron temperature (hereafter T_e-method), considered as reliable for star-forming regions, are underestimated by about 0.8 dex of in comparison to the expected value derived from extrapolation of the gradient of metallicity (independent estimations). This discrepancy, called by "T_e-problem", is an indication of the presence of a secondary ionization source or electron temperature fluctuations in the gas phase of AGNs or that is need to revise the application of the T_e-method for AGNs.
One way to investigate the origin of the T_e-problem is to know the ionization structure of AGNs and obtaing informations about the ionizing source. About the ionization structure, this can be obtained by detailed photoionization model built with the goal to reproduce emission-line intensities in the wider range of wavelength. Although theoretical (e.g., Kraemer et al., 1994) and observational (e.g., Revalski et al., 2018) studies has been carried out in order to investigate the ionization structure of AGNs, these have been limited to narrow spectral range or have used photoionization models with large number of assumptions.

Regarding the secondary ionization source in AGNs, it is very known the existence of the ionizing photon deficit in these objects (Wilson et al., 1985, e.g.,). In general, for AGNs, the number of ionizing phothons computed directly from the observational flux of emission lines (e.g. Hβ) is higher (by a factor of ~ 6) in comparison to that calculated directly from the AGN continuum in a wide wavelength range. This discrepancy can be an indication that some physical process (e.g. gas shock) is increasing the ionization of the gas in AGNs and, consequently, producing the oxygen discrepancy found by Dors et al. (2015).
In this context, the nuclei of the galaxy Mrk 1066 (UGC 2456) can be used as prototype system for studying the "T_e-problem" in AGNs. This galaxy present a nuclei classified as Seyfert 2 and emission line fluxes in pratically all range of wavelength (e.g., Goodrich & Osterbrock, 1983; Knop et al., 2001; Levenson et al., 2001; Rhee & Larkin, 2005; Spinelli et al., 2006; Riffel et al., 2006; Muñoz Marín et al., 2007; Gorjian et al., 2007; Riffel & Storchi-Bergmann, 2011; Rodríguez-Ardila et al., 2011; Kraemer et al., 2011) are available in the literature. In this work, we present an analysis of the abundance determination of the oxygen, sulfur and neon in the narrow line regions (NLRs) of the Seyfet 2 nuclei of Mrk 1066, a SB0 galaxy (de Vaucouleurs, 1991) located at a distance of 48.6 Mpc.

1.1. Methodology and Results

We used the version C17.00 of the CLOUDY code to built detailed photoionization models in order to reproduce narrow optical emission-line intensities compiled in the literature of the nuclei of Mrk 1066. We used as input parameter the observational Spectral Energy Distribution (SED) extracted from Dors et al. (2012), electron density of 839 cm^{-3} calculated by using the observational line ratio [S II]λ6716/λ6731, and the internal radius of 3 pc. We used the PHYMIR optimize method to vary the nebular parameters (e.g. abundances, number of ionizing photons) in order to reproduce the observational emission lines considering an uncertainty of $\pm$20% in these. In Table 1 the observed and the model predicted emission-line intensities are listed. The elemental abundances in relation to the hydroden one predicted by the best solution model were 12+log(O/H)=8.34, 12+log(N/H)=7.82 and 12+log(Ne/H)=7.04. The ionization fraction structure for hydrogen, helium, nitrogen, oxygen and sulfur, derived by our model is shown in Fig. 1.

2. Discussion and Conclusions

Through the photoionization model using the CLOUDY code we reproduce narrow optical strong emission-line intensities Mrk 1066 observed by Goodrich & Osterbrock (1983) with a tolerance of 10 per cent difference. However, it was not possible to find agreement for the intensity of the emission line [O III] λ4363. This implied the difference between the abundances presented by the CLOUDY model and the T_e-method. The latter presents values higher than those predicted by the CLOUDY model: for oxygen the difference was 0.5 dex while for the neon it was 0.39 dex. The best agreement was for nitrogen, with only 0.02 dex difference.

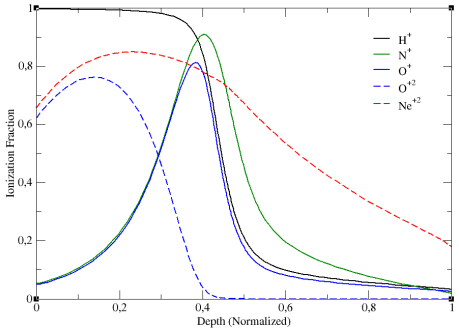

Figure 1.: Ionization fraction structure for hydrogen, helium, nitrogen, oxygen and sulfur derived by the best photoionization model solution. The radius is normalized in relation the outermost radius.

Table 1.: Dereddened fluxes (relative to Hβ=100) for Seyfert 2 nuclei of Mrk 1066. The observational values taken from Goodrich & Osterbrock (1983) are referred as "Obs." while the predicted values by the photoionization models as "Mod." The line [S II]λ6725 corresponds to sum of λ6716 and λ6731.

Ion	Line (Å)	Obs.	Pred.
[O II]	3727	335	364
[Ne III]	3869	71	10
[S II]	4071	24	6
[O III]	4363	8	3
Hβ	4861	100	100
He II	4685	13	5
[O III]	4959	123	120
[O III]	5007	385	358
[N II]	5755	4	4
[O I]	6363	7	10
[N II]	6548	81	75
Hα	6563	277	281
[N II]	6384	242	221
He I	6670	3	1
[S II]	6725	107	107

These differences in metallicity for oxygen suggest the presence of shock as a source of secondary ionization. This hypothesis is favored by Knop et al. (2001) who, through the analysis of near-infrared spectra the nuclei of Seyfert 2 circumnuclear regions, suggested that the presence of shocks due to the interaction of the radio jets with the rotating disk of the Mrk 1066 can create large partially ionized regions. Another suggestion favoring the existence of a second ionizing source is the presence of the signature of a prominent circumnuclear starbust activity presented by Riffel et al. (2006).

A second possibility may be associated with the existence of temperature fluctuations of the electrons. Although Revalski et al. (2018) has not found large differences in oxygen abundances as a function of the distance to the core of Mrk 573, it is not exactly true that this feature applies to all Seyfert 2 galaxies. Thus, it is possible that the average NLR temperature is not a true representation.
A preliminary analysis of the structure of the ionization fraction as a function of depth (Fig. 1) derived from the final model shows a drop in the ionization zone of the nitrogen occurring earlier than the hydrogen. This difference may also explain this disagreement.
Finally, a third possibility may be that the $T_{\rm e}$-method simply does not apply correctly to AGNs.

Acknowledgments. We would like to thank SOC and LOC members of the Workshop Chemical Abundance Determinations in Gaseous Nebulae

References

de Vaucouleurs G., 1991, *Science*, **254**, 1667
Dors O. L., Cardaci M. V., Hägele G. F., Rodrigues I., Grebel E. K., Pilyugin L. S., Freitas-Lemes P., Krabbe A. C., 2015, *MNRAS*, **453**, 4102
Dors Jr. O. L., Riffel R. A., Cardaci M. V., Hägele G. F., Krabbe Á. C., Pérez-Montero E., Rodrigues I., 2012, *MNRAS*, **422**, 252
Goodrich R. W., Osterbrock D. E., 1983, *ApJ*, **269**, 416
Gorjian V., Cleary K., Werner M. W., Lawrence C. R., 2007, *ApJL*, **655**, L73
Knop R. A., Armus L., Matthews K., Murphy T. W., Soifer B. T., 2001, *AJ*, **122**, 764
Kraemer S. B., Schmitt H. R., Crenshaw D. M., Meléndez M., Turner T. J., Guainazzi M., Mushotzky R. F., 2011, *ApJ*, **727**, 130
Kraemer S. B., Wu C.-C., Crenshaw D. M., Harrington J. P., 1994, *ApJ*, **435**, 171
Levenson N. A., Weaver K. A., Heckman T. M., 2001, *ApJS*, **133**, 269
Muñoz Marín V. M., González Delgado R. M., Schmitt H. R., Cid Fernandes R., Pérez E., Storchi-Bergmann T., Heckman T., Leitherer C., 2007, *AJ*, **134**, 648
Revalski M., Crenshaw D. M., Kraemer S. B., Fischer T. C., Schmitt H. R., Machuca C., 2018, *ApJ*, **856**, 46
Rhee J. H., Larkin J. E., 2005, *ApJ*, **620**, 151
Riffel R., Rodríguez-Ardila A., Pastoriza M. G., 2006, *A&A*, **457**, 61
Riffel R. A., Storchi-Bergmann T., 2011, *MNRAS*, **411**, 469
Rodríguez-Ardila A., Prieto M. A., Portilla J. G., Tejeiro J. M., 2011, *ApJ*, **743**, 100
Spinelli P. F., Storchi-Bergmann T., Brandt C. H., Calzetti D., 2006, *ApJS*, **166**, 498
Wilson A. S., Baldwin J. A., Ulvestad J. S., 1985, *ApJ*, **291**, 627

Chemical Abundances in Gaseous Nebulae:
Open problems in Nebular astrophysics
AAA Workshop Series 11, 2019
M. Cardaci, G. Hägele & E. Pérez-Montero, eds.

Poster

The radial abundance gradients of O, Ne, S and Cl of the Milky Way

K. Z. Arellano-Córdova[1,2,3], C. Esteban[1,2] and J. García-Rojas[1,2]

[1]*Instituto de Astrofísica de Canarias, E-38200 La Laguna, Tenerife, Spain*
[2]*Departamento de Astrofísica, Universidad de La Laguna, E-38206 La Laguna, Tenerife, Spain*
[3] *Instituto Nacional de Astrofísica, Óptica y Electrónica (INAOE), Apdo. Postal 51 y 216, Puebla, Mexico*

Abstract. We present preliminary results of the O, Ne, S and Cl abundance gradients of the Milky Way. We analyze in a homogenous way the physical conditions and chemical abundances of a sample of 35 HII regions with deep spectra observed mainly with the GTC and VLT telescopes. The sample covers a range in Galactocentric distances from 5 to 17 kpc. We reanalyze the O abundance gradient, obtaining a similar complex shape than previously reported in the literature. We calculate the Cl abundance gradient including a significantly larger number of objects than in previous works. Our results show a gradient for Cl/H of -0.034 dex kpc^{-1} and a dispersion around the gradient of 0.14 dex. We obtain values for the Ne/H and S/H abundance gradients with slopes of -0.038 dex kpc^{-1} and -0.046 dex kpc^{-1}, respectively, with dispersions around the gradient higher than 0.25 dex. We also report the values for the slopes of the Cl/O, Ne/O and S/O abundance ratio gradients, which show dispersions around the gradient up to 0.4 dex. Such high dispersion although may be interpreted as indications of chemical inhomogeneities in the Galactic ISM, it might be also an artifact produced by the selected ionization correction factor.

Key words: ISM: abundances — Galaxy: abundances — Galaxy: disc — Galaxy: evolution — HII regions.

1. Introduction

The Milky Way is an excellent laboratory to study chemical abundances of HII regions as a function of their Galactocentric distances since it helps to constrain chemical evolution models. Deep spectra from Galactic HII regions are necessary to have a better estimate of the electron temperature and to derive precise ionic and total abundances. Such high quality observations allow to study in detail the temperature structure of the nebula, the ionization corrector factors (ICF), which are used to account for the contribution of unseen ions in the calculation of the total abundance, and the abundance gradients of most of the observable

elements. It is important the use of ICF to calculate the total abundances of elements such as C, N, Ne, S, Cl and Ar. Several studies have proposed ICF based on the ionization potential of given ions, photoionization models or observational data (e.g. Peimbert & Costero 1969; Izotov et al. 2006; Delgado-Inglada et al. 2014; Esteban et al. 2015; Esteban & García-Rojas 2018).
On the other hand, the radial abundance gradients in the Milky Way of elements as Cl, O and N have been studied in detail by Esteban et al. (2015, 2017) and Esteban & García-Rojas (2018). In the case of Cl, Esteban et al. (2015) reported values for the gradients of Cl/H and Cl/O for a sample of nine objects without using ICF. These authors found similar slopes between Cl/H and O/H of -0.043 dex kpc^{-1} and a flat slope for the Cl/O abundance gradient. Recently, Esteban & García-Rojas (2018) reported a new determination for the N/H abundance gradient, where for objects with very low ionization degree they assume the approximation N/H $\approx$ N^+/H^+ (N^{++} contribution is expected to be negligible due to the low ionization degree). Esteban & García-Rojas (2018) compared three different schemes of ICF concluding that there are not large differences or trends between the objects where ICF was used and those ones without using ICF. Note that the ICF reported in the literature are based mainly on either photoionization models of extragalactic HII regions or planetary nebulae. Therefore, it is necessary to analyze the applicability of ICF in Galactic HII regions to have a better estimate of the total abundance in these objects. In this work, we present preliminary results on the Ne, S and Cl abundance gradients and a reanalysis of the O abundance gradient in the Milky Way by using a sample of deep spectra of HII regions.

2. Sample

We gathered a sample of 35 HII regions observed mainly with the Gran Telescopio Canarias (GTC) in La Palma, Spain and the Very Large Telescope (VLT) in Chile from García-Rojas et al. (2014); Esteban et al. (2015, 2017); Fernández-Martín et al. (2017); Esteban & García-Rojas (2018). The Galactocentric distances for our sample go from 5 to 17 kpc.

3. Physical conditions and chemical abundances

The physical conditions and chemical abundances were computed in a homogenous way using the same atomic data set than Esteban & García-Rojas (2018), and by using the Python package PyNeb (Luridiana et al. 2015). We adopt a two-zone ionization structure characterized by T_e[NII] for O^+, S^+ and Cl^+ and by T_e[OIII] for O^{++}, Ne^{++}, S^{++}, Cl^{++} and Cl^{3+} ionic abundances. We also use the temperature relation proposed by Esteban et al. (2009, in their equation 3) to estimate T_e[OIII] in those objects where this temperature was not available.
The total abundances of O, Cl, Ne, and S were calculated as follows: for O/H, we add the contribution of both ions, O/H = $O^+/H^+ + O^{++}/H^+$. For the other elements, it was necessary the use of ICF. For Cl, we use the ICF of Izotov et al. (2006), which depends on metallicity. Note that in the sample compiled by Esteban et al. (2015), the total Cl abundance was determined without the use of ICF. In the case of Ne, we use the ICF reported by Peimbert & Costero (1969),

which is based on the similar ionization potentials of Ne^{++} and O^{++}. For S, we use the ICF($S^+ + S^{++}$) reported by Izotov et al. (2006), which also depends on metallicity.

4. Preliminary results

We reanalize the O abundance gradient in the Milky Way as a function of its Galactocentric distance for the whole sample of HII regions. We obtain a similar O/H gradient than that previously reported by Esteban & García-Rojas (2018), with a dispersion of 0.08 dex at a given Galactocentric distance.
Figure 1 shows the Cl/H and Cl/O abundance gradients from the HII regions in the Milky Way as a function of their Galactocentric distances. The different symbols indicate the references in the literature where the samples were compiled. We used the least-squares method to fit all the objects in Figure 1. Our results show that the slope of the Cl/H gradient is slightly flattened in comparison to the one reported by Esteban et al. (2015) with a dispersion of 0.14 dex. We report a slope of −0.020 dex for the Cl/O gradient and a dispersion around the gradient of 0.10 dex. However, Esteban et al. (2015) found a flat Cl/O gradient for objects located between 5 and 12 kpc, the expected behaviour because the bulk of both elements – O and Cl – are thought to be produced by massive stars. We will explore the effect of the selected ICF onto this apparent odd behaviour. The Ne and S abundance gradients show a large dispersion around the gradient of 0.25 dex and 0.45 dex, respectively, which also might be due to the selected ICF. We plan to study in detail the different ICF proposed in the literature for these elements, and hence, to improve the chemical abundance determinations and have a better estimate of the gradient. We also calculated the Ne/O and S/O abundance gradients, which shows slopes of -0.008 dex kpc^{-1} and -0.016 dex kpc^{-1} and dispersions of 0.22 dex and 0.40 dex, respectively. It is curious that these elements also show somewhat negative slopes as that of the Cl/O ratio. The reasons of this fact will be further investigated.

5. Summary and work in progress

We present preliminary results of the Ne, S and Cl abundance gradients of the Milky Way. We recalculate the physical conditions and obtain new determinations of the chemical abundances of these elements for a sample of Galactic HII regions with available deep, high-quality spectra. We obtain similar values for the abundance gradients than those reported in the literature. Our determinations for the total abundance gradients show a large dispersion around the gradient up to 0.45 dex (ICF problems?). For upcoming research, we plan to analyze the argon and carbon abundances and explore in detail the ICF, mainly those proposed by Medina-Amayo (in prep) for HII regions based on photoionization models and the ICF for Cl based on observational data by Domínguez-Guzmán (in prep).

Acknowledgments. KZA-C acknowledges support from Mexican CONACYT grant 711183. CEL and JRG acknowledge support from the project

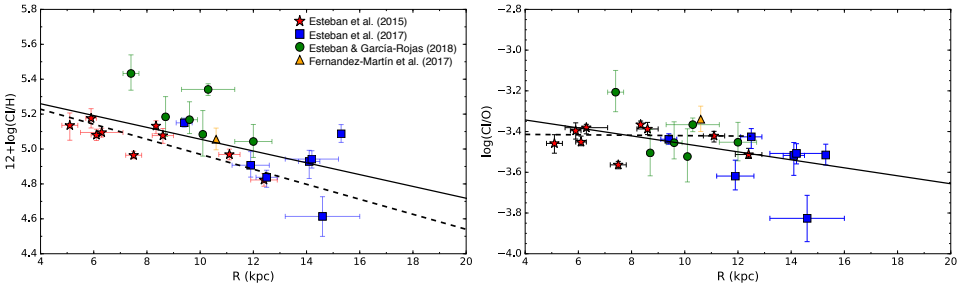

Figure 1. *Left:* Cl abundances in HII regions of the Milky Way as a function of their Galactocentric distances. *Right:* The Cl/O abundances as a function of their Galactocentric distances. Note that the Cl abundances for the sample of HII regions of Esteban et al. (2015) were computed without the use of ICF. The solid line represents our fit to all the objects and the dashed line the radial abundances of Cl/H and Cl/O reported by Esteban et al. (2015).

AYA2015-65205-P. JGR acknowledges support from an Advanced Fellowship from the Severo Ochoa excellence program (SEV-2015-0548).

References

Delgado-Inglada G., Morisset C., Stasińska G., 2014, *MNRAS*, **440**, 536
Esteban C., Bresolin F., Peimbert M., García-Rojas J., Peimbert A., Mesa-Delgado A., 2009, *ApJ*, **700**, 654
Esteban C., Fang X., García-Rojas J., Toribio San Cipriano L., 2017, *MNRAS*, **471**, 987
Esteban C., García-Rojas J., 2018, *MNRAS*, **478**, 2315
Esteban C., García-Rojas J., Pérez-Mesa V., 2015, *MNRAS*, **452**, 1553
Fernández-Martín A., Pérez-Montero E., Vílchez J. M., Mampaso A., 2017, *A&A*, **597**, A84
García-Rojas J., Simón-Díaz S., Esteban C., 2014, *A&A*, **571**, A93
Izotov Y. I., Stasińska G., Meynet G., Guseva N. G., Thuan T. X., 2006, *A&A*, **448**, 955
Luridiana V., Morisset C., Shaw R. A., 2015, *A&A*, **573**, A42
Peimbert M., Costero R., 1969, *Boletin de los Observatorios Tonantzintla y Tacubaya*, **5**, 3

Chemical Abundances in Gaseous Nebulae:
Open problems in Nebular astrophysics
AAA Workshop Series 11, 2019
M. Cardaci, G. Hägele & E. Pérez-Montero, eds.

Poster

Spatial and velocity resolved studies of NGC 6153 emission lines

A. Arrieta[1], L. Arias[1], A. Galindo[1], M.G. Richer[2] and S. Torres-Peimbert[3]

[1] *Universidad Iberoamericana, Mexico City, 01219, Mexico*
[2] *Universidad Nacional Autónoma de México, Ensenada, B.C., 22860, Mexico*
[3] *Universidad Nacional Autónoma de México, Mexico City, 04510, Mexico*

Abstract. We will study the kinematical behavior of the forbidden and permitted emission lines of NGC 6153 in order to ascertain whether these lines arise from the same volume elements or from different clumps of ejecta. In this preliminary study we obtain the physical conditions at different velocities along the slit.

Key words: planetary nebulae: individual: NGC 6153 — Techniques: spectroscopic — ISM: abundances

1. Introduction

Emission lines are used to infer the abundances of C, N, O, Ne, Cl, S, and Ar in ionized plasmas throughout the universe. There is a long-known result that the optical recombination lines (ORLs or permitted lines) indicate higher abundances than the collisionally excited lines (CELs or forbidden lines). This result gives rise to what is known as the *abundance discrepancy factor* (ADF). Several mechanisms have been suggested to explain the discrepancy, e.g., temperature fluctuations (Peimbert, 1967; Peimbert & Costero, 1969) or/and bi-abundance nebular clumps (Liu et al., 1995). The discrepancies have been traditionally analyzed using spectra with intermediate spectral resolution. In this case we will study the individual kinematical behavior of different emission lines following the analyses of NGC 7009 by Richer et al. (2013, 2019).
NGC 6153 was selected for its large ADF value ∼9 (Liu et al., 1995). From long slit high resolution spectroscopy of the planetary nebula NGC 6153 we derive the position-velocity, PV, diagram for each emission line. We aim to study whether the kinematical behavior of the forbidden lines and permitted lines of the same ion have the same pattern in order to ascertain whether the recombination and collisionally excited emission lines arise from the same or from different plasmas. We will derive the extinction and the physical conditions to compare the electronic temperature and density for each observed individual points of the P-V grid, (hereinafter, PV parcels) from both sets of lines. In this paper we present preliminary data from forbidden lines.

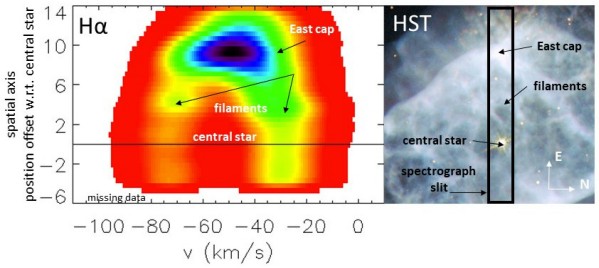

Figure 1. Hα PV diagram (left) and an image (right) of NGC 6153 with the same spatial scale where the observed slit is marked.

2. Temperature and density diagrams

The data were acquired from the ESO archive from spectra obtained on 2002 June 8th using the UV-Visual Echelle Spectrograph (UVES) at ESO. The standard star observed was CD-32-9927 with the same program ID. The blue spectrum covers from 3750 to 5000 Å, and the red spectra covers 5000-7020 Å in two different detectors. The data were reduced using IRAF. We have extracted individual spectra along the slit with extraction windows of 1 pixel wide. We calibrated all the slices in wave length and flux and constructed position-velocity (PV) maps from the echelle spectra.

Figure 2 shows position velocity diagrams for different emission lines. For each panel, the line and its maximum intensity are identified in the upper left corner. The colour scale spans the range of 0%-100% of the maximum intensity. Spatial scale is given in seconds of arc from the position of the central star, which is indicated by the horizontal line. Radial velocity scale spans from -110 to +10 km s^{-1}, where no heliocentric correction has been applied. It should be noted that the light contribution from the star has been removed assuming for each velocity pixel a gaussian profile derived from the external zones. A few pixels of the dark area of [NII] 6583 line are saturated.

For each PV parcel we applied the PyNeb rutines by Luridiana et al. (2015) to determine the extinction coefficient and physical conditions Figure 3 presents the reddening coefficient, c(β) for each PV parcel. This coefficient was derived from the observed HI ratios for the lines shortward of β which were compared with the theoretical Case B.

For each PV parcel we derived the physical conditions, and constructed the temperature and density diagnostics along the slit which are presented on Figure 4. The electron temperatures derived from [OIII] and [ArIII] are similar in NGC 6153. They are relatively uniform throughout the nebula, of about 13000 K; by contrast, the [NII] temperature distribution is very different; in this case the temperature close to the star is extremey high. The electron density derived from [ArIV] and [SII] is relatively uniform within the slit and is of approximately 3000 cm^{-3}; on the other hand, the [OII] density is considerably higher near the central star. The average integrated parameters are in agreement with McNabb et al. (2016) study of this nebula.

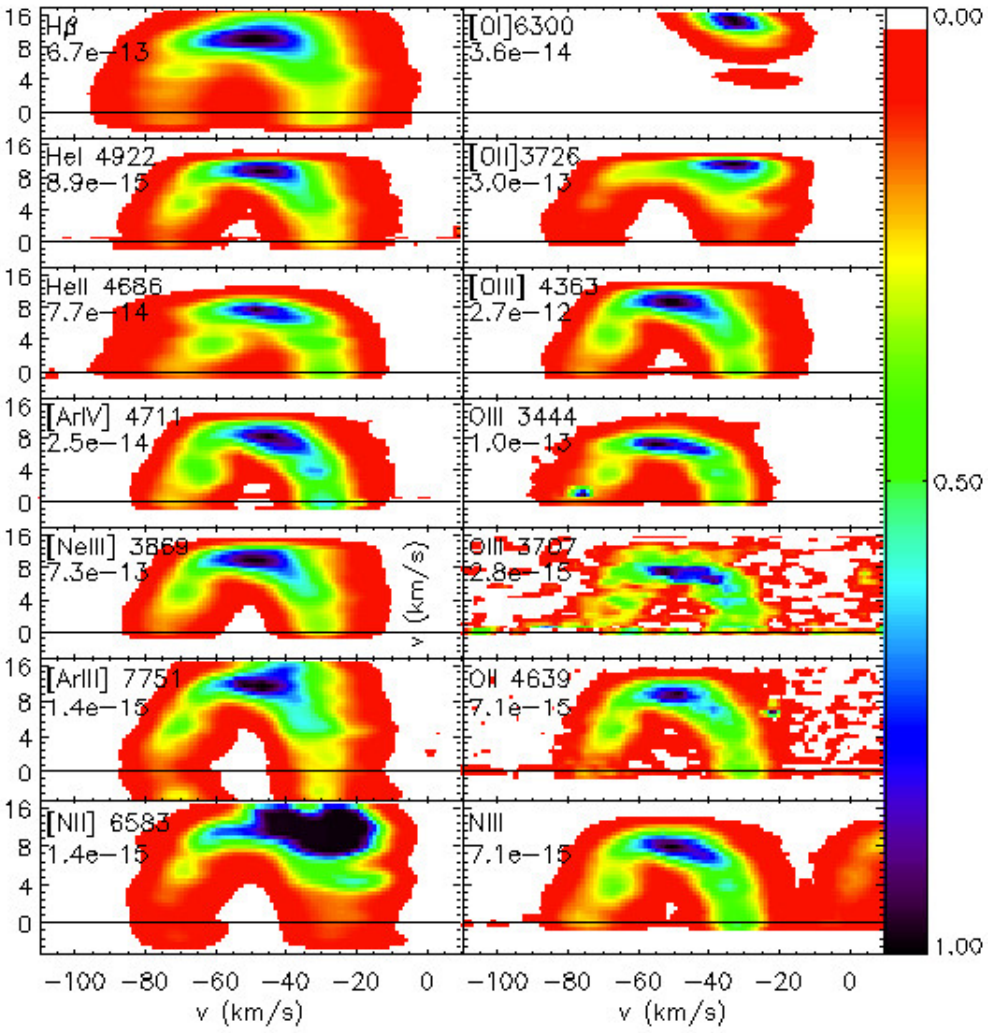

Figure 2. Position velocity diagrams for different emission lines, where the identification and its maximum intensity are given in the upper left corner. Also given are the intensity range, the angular distance (in arc sec) from the central star and the radial velocity (in km s^{-1}). The parcels where the [NII] 6583 line is saturated are marked.

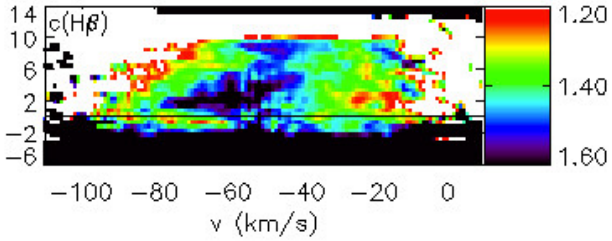

Figure 3. Reddening coefficient, c(β) for each PV parcel along the slit.

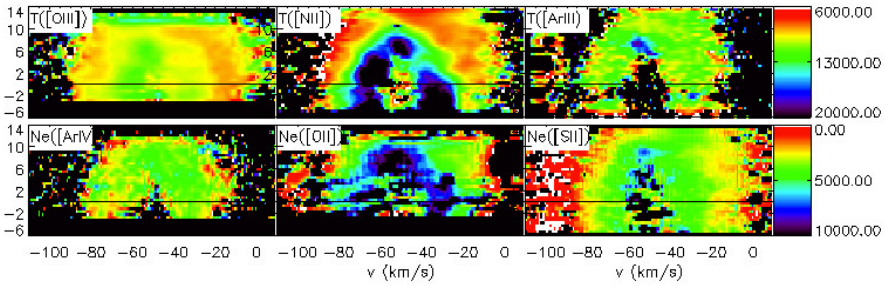

Figure 4. Electron temperatures and electron density

We will extend this study to the derivation of the physical parameters from the permitted emission lines to compare with the results from the forbidden lines.

Acknowledgments. We are grateful to Dirección de Investigación, Universidad Iberoamericana and to CONACYT Grant -241732 for the support received.

References

Liu X.-W., Storey P. J., Barlow M. J., Clegg R. E. S., 1995, *MNRAS*, **272**, 369
Luridiana V., Morisset C., Shaw R. A., 2015, *A&A*, **573**, A42
McNabb I. A., Fang X., Liu X.-W., 2016, *MNRAS*, **461**, 2818
Peimbert M., 1967, *ApJ*, **150**, 825
Peimbert M., Costero R., 1969, *Bulletin of the American Astronomical Society*, Vol. 1 of *BAAS*, p. 256
Richer M. G., Georgiev L., Arrieta A., Torres-Peimbert S., 2013, *ApJ*, **773**, 133
Richer M. G., Guillén Tavera J. E., Arrieta A., Torres-Peimbert S., 2019, *ApJ*, **870**, 42

Chemical Abundances in Gaseous Nebulae:
Open problems in Nebular astrophysics
AAA Workshop Series 11, 2019
M. Cardaci, G. Hägele & E. Pérez-Montero, eds.

Poster

The formation of the Galactic bulge in an inside-out scenario

O. Cavichia[1] and M. Mollá[2]

[1]*Instituto de Física e Química, Universidade Federal de Itajubá, Av. BPS, 1303, 37500-903, Itajubá-MG, Brazil*
[2]*Departamento de Investigación Básica, CIEMAT, Avda. Complutense 40, E-28040 Madrid, Spain*

Abstract. Chemical evolution models (CEM) are important tools to understand the formation and evolution of the components of the Milky Way Galaxy and other galaxies in the universe. The Galactic bulge is the only galaxy bulge that can be resolved and can be studied with exquisite details. In this way, the bulge metallicity distribution function (MDF) can be traced for different regions within the bulge and can give us clues about the bulge formation scenario. In this work we have assumed an inside-out formation for the Galactic bulge and using a CEM we were able to compute the chemical evolution in nine different radial regions, from 0 to 2 kpc, in steps of 0.25 kpc . The preliminary results show that in the inner regions of the bulge the MDF is skewed to higher metallicities, while at the outer regions there is a metal rich component but also a metal poor component much more extended than in the inner regions. These results may explain the metallicity gradient observed in the Galactic bulge.

Key words: galaxies: abundances — galaxies: ISM — techniques: imaging spectroscopy

1. Introduction

Chemical evolution models (CEM) have been extensively used to study the formation and evolution of the Milky Way Galaxy (MWG) and other galaxies in the universe. The outputs of a CEM depend on the physics adopted, e.g. the stellar yields, initial mass function, star formation rate and gas infall law. One of the most important constraints for CEM is the metallicity distribution function (MDF). In the results of the first studies, the Galactic bulge (GB) appeared as composed mostly by old stars and the MDF was well characterized by a broad single population. Nowadays this picture has changed and the observations (e.g. Rojas-Arriagada et al., 2014) have shown that the GB MDF is much more complex than previous thought, composed by at least two populations. Zoccali et al. (2017), hereafter Z17, have demonstrated that the two components present a different spatial distribution, with the metal poor population concentrated near the Galactic centre (GC).

In this regarding, the CEM can give important clues to understand the formation and evolution of the components of the MWG and other galaxies in the universe. Since the MDF in a CEM is sensible to the time-scale, in this work we use the GB MDF to constraint the time-scale of the GB formation in order to test a scenario where the it is formed inside-out.

2. Method

In the case of spiral galaxies, the central bulge brightness profile can be well described by a Sérsic function (Sérsic, 1968). By assuming that the mass distribution follows the light distribution, the GB total mass can be calculated by integrating this profile. Using the properties of the gamma function, we may show that the GB mass enclosed in a radius R_k of the k-th radial region can be calculated as:

$$M_B(< R_k) = M_B \left(1 - e^{-\xi} \sum_{i=0}^{2n-1} \frac{\xi^i}{i!}\right), \quad (1)$$

where $M_B = \pi I_0 h^2 (2n)!$ is the GB total mass and $\xi = (R_k/h)^{1/n}$. In these equations, I_0 is the central intensity, h is a scale radius and n the Sérsic index. Values used for these parameters are: $n = 4$, $k = 7.66925$, $h = 1.67944 \times 10^{-4}$ and $M_B = 1.7891 \times 10^8 \mathrm{M}_\odot$. We have assumed an inside-out formation for the GB and, using a CEM described in Mollá et al. (2015, 2016), we were able to compute the chemical evolution in nine different radial regions, from 0 to 2 kpc, in steps of 0.25 kpc . The time-scale to form each radial region of the GB is calculated with the initial mass available in the halo to form the region and the final mass in the respective k-th region: $\Delta M_{B_k} = M_B(< R_k) - M_B(< R_{k-1})$ (see Mollá et al., 2015, for details).

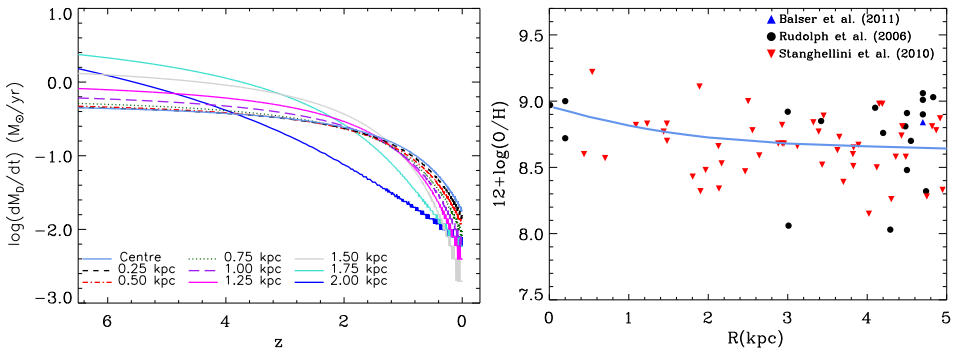

Figure 1. *Left:* The infall of gas in the GB as a function of the redshift for each k-th radial region, as labelled in the figure. *Right:* The radial O/H gradient in the GB and inner disc of the Galaxy. Data are from HII regions and planetary nebulae, as labelled.

3. Results

The results of the simulations for each GB k-th region are presented in Fig. 1 to 3. In Fig. 1 the infall of gas is more constant in the central regions than in the outer ones. For the lower redshifts, the infall is higher in the central parts of the GB. This results in the negative radial O/H gradient observed in the right panel of the same figure. The GB MDF is shown in Fig. 2 and is compared with the

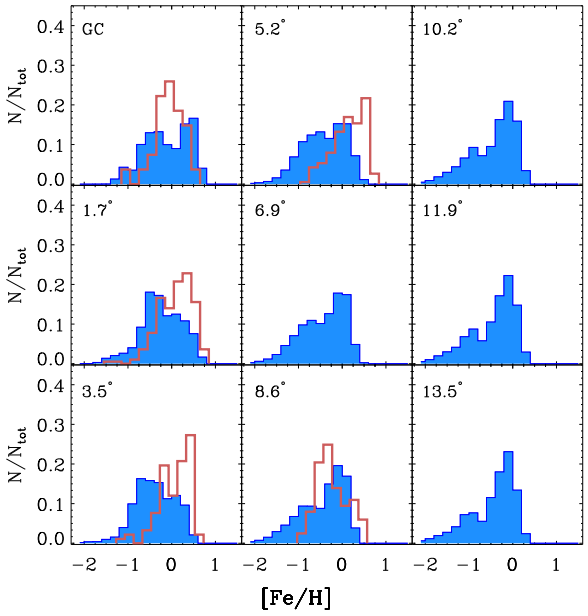

Figure 2. The GB MDF for each field from simulations (filled blue histograms) and observational data (unfilled red histograms) from Z17 and R16 (GC only). The histograms of the simulations in the same line of sight were convolved in order to compare with the observations.

observational data from Z17, except for the GC, where we plotted the data from Ryde et al. (2016), hereafter R16. Since the observational data is a projection of stars in the line of sight, and it is given in terms of the angular distance of the GC instead of radial distance in kpc, the predictions of the model in the same line of sight were convolved to simulate the observational results. Hence, the histograms for the MDF are given for each field of the GB in degrees. The shape of the MDF depends upon the selection effects of the survey, so that we do not intend to reproduce the shapes of the MDF, but more global aspects such as the metallicity range. The model predictions for [α/Fe]] ratio are displayed in Fig. 3 for different regions in the GB (left panel) and only for the central region (right panel). The models are compared with the observational data, as labelled. A higher [α/Fe] ratio is predicted for the central regions, which is in agreement with the observational data (right panel). The scenario adopted for the formation of the GB may explain the spread of observational data in these figures.

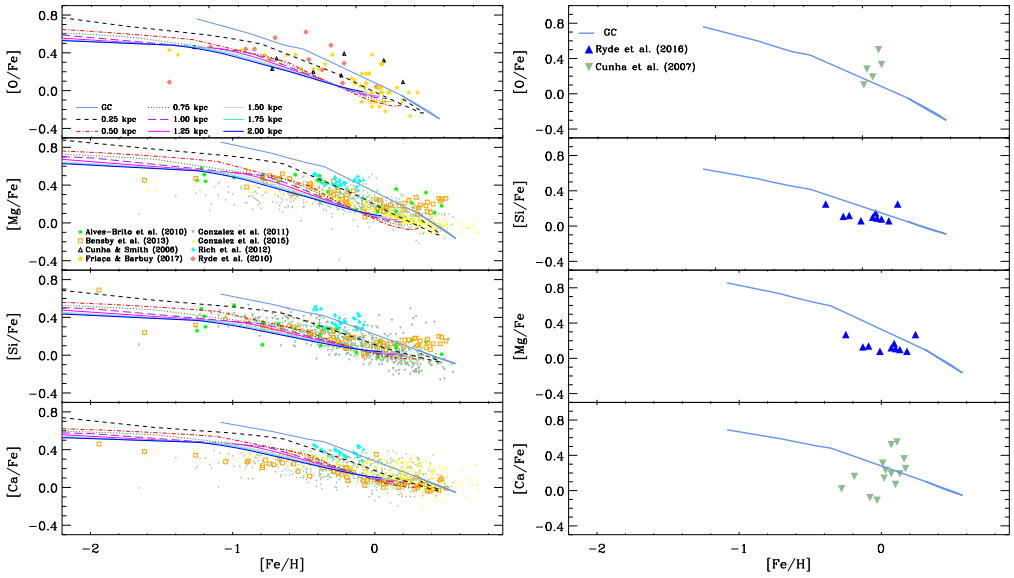

Figure 3. *Left:* The [α/Fe] ratio from models compared with stellar observational data, as labelled. *Right:* Predictions of the simulations only for the GC contrasted with observational data inferred from the GC stars, as labelled.

4. Conclusions

The formation of the GB in an inside-out scenario, where the collapse time-scale is calculated from the GB mass distribution, is a plausible one which is able to reproduce some observational data from the literature. Most important, the simulations show a difference in the MDF depending on the GB region, as found by the observations. The models also point to a higher [α/Fe] ratio in the inner regions of the GB, that reproduces the spread of stellar data.

Acknowledgments. CAPES and FAPEMIG (APQ-00915-18).

References

Mollá M., Cavichia O., Gavilán M., Gibson B. K., 2015, *MNRAS*, **451**, 3693
Mollá M., Díaz Á. I., Gibson B. K., Cavichia O., López-Sánchez Á.-R., 2016, *MNRAS*, **462**, 1329
Rojas-Arriagada A., Recio-Blanco A., Hill V., et al., 2014, *A&A*, **569**, A103
Ryde N., Schultheis M., Grieco V., Matteucci F., Rich R. M., Uttenthaler S., 2016, *AJ*, **151**, 1
Sérsic J. L., 1968, *Atlas de Galaxias Australes*, Observatorio Astronómico, Córdoba, Argentina
Zoccali M., Vasquez S., Gonzalez O. A., Valenti E., Rojas-Arriagada A., Minniti J., Rejkuba M., Minniti D., McWilliam A., Babusiaux C., Hill V., Renzini A., 2017, *A&A*, **599**, A12

Chemical Abundances in Gaseous Nebulae:
Open problems in Nebular astrophysics
AAA Workshop Series 11, 2019
M. Cardaci, G. Hägele & E. Pérez-Montero, eds.

Poster

Spectroscopic study of the HII regions in the galaxy NGC1232

F. Costa[1], L. Martins[1] and A. Rodríguez-Ardila[2]

[1] *Universidade Cruzeiro do Sul, Rua Galvão Bueno 868, São Paulo-SP, 01506-000. BR*
[2]*Laboratório Nacional de Astrofísica, Rua Estados Unidos 154, Itajubá-MG, 37530-000. BR*

Abstract.
NGC 1232 is a face-on spiral galaxy, and an excellent laboratory for the study of star formation due to its proximity. Recent studies reveal characteristics that make this galaxy extremely interesting: diffuse x-ray observations suggest that it has recently suffered a collision with a dwarf galaxy - of which there is no apparent remnant. High resolution imaging studies in Hα reinforce this hypothesis, suggesting an excess of star formation in the northeastern region of the galaxy, where the intensity of X-rays is minimal, and a suppression of the star formation in the region where the emission of X-rays is more intense.

Key words: HII regions – galaxies: star formation – galaxies: individual: NGC 1232

1. Introduction

Extragalactic HII regions trace the recent star formation of a galaxy, and through analysis of their chemical composition, reveal details of the history of star formation of their galaxies; characteristics of the gas can be determined through the spectrum, which can be used to calculate electronic density and temperature of the gas, measure the abundance of elements and construct BPT diagrams.

2. Methodology

We obtained spectra of NGC 1232 in the optical using a long slit and the Goodman spectrograph of the SOAR telescope. The slit was positioned in the north-south direction, and 17 HII regions were detected (plus background galaxy), of which 11 have intense emission lines besides Hα, with a spectral coverage of 3600 to 7500 Å. The emission lines of all regions were measured using the SMART (Spectroscopy Modeling Analysis and Reduction Tool) software. The lines were used to determine the physical characteristics of the gas and chemical abundances.

3. Results

As a first result we calculated the extinction through the Hα/Hβ ratio. Figure 1 shows the values obtained for each region as a function of the distance to the center. Black points represent HII to the north of the galaxy, red points to the south and blue points NGC 1232B (background galaxy). It seems that the north region has, in average, a higher extinction than the south, which again reinforces the excess of star-formation in the northern part of the galaxy.

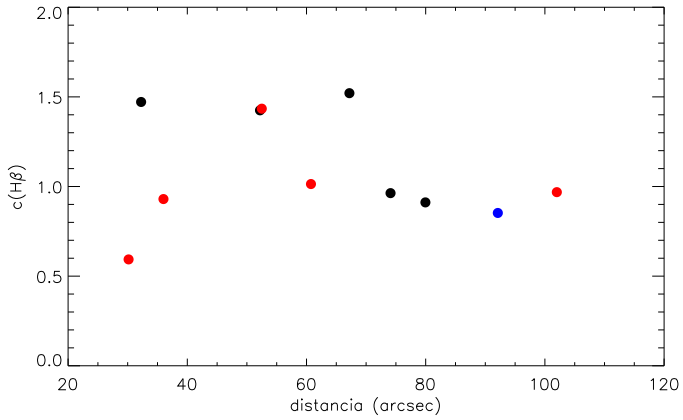

Figure 1.: Extinction variation as a function to the distance to the center of the galaxy.

We determined the values N_2 and O_3S_2 for all regions that had the required lines. Figures 2 and 3 show the values of N_2 and O_3S_2 respectively in the HII regions, as a function of the distance to the galaxy's nucleus. Dotted lines provide the corresponding values for solar abundance (12 + log(O/H)=8.69, Alloin et al., 1979), using the calibrations of the different indices of Pettini & Pagel (2004).The O_3S_2 index suggests a negative abundance gradient for the galaxy.
Emission line ratios [NII]6583/Hα, [SII]6716,6731/Hα and [OI]6300/Hα, can be used with the ratio [OIII]5007/Hβ, to place the galaxy NGC 1232B found in this work in the BPT diagrams (Figure 4). The black dot in this figure represents NGC 1232B. In the diagram (a) the red line represents the curve defined by (Kauffmann et al., 2003), the lower bound to classify regions and galaxies as star-forming.
The blue curve defined by (Kewley et al., 2001) suggests that galaxies with AGNs tend to occupy the upper area of this curve. The galaxies located between the two curves are composites, that is to say, they have contributions of regions of star formation and AGNs. Diagrams (b) and (c) further classify galaxies in Seyferts or LINERS. Through our measurements we classify NGC 1232B as a Starburst Galaxy.

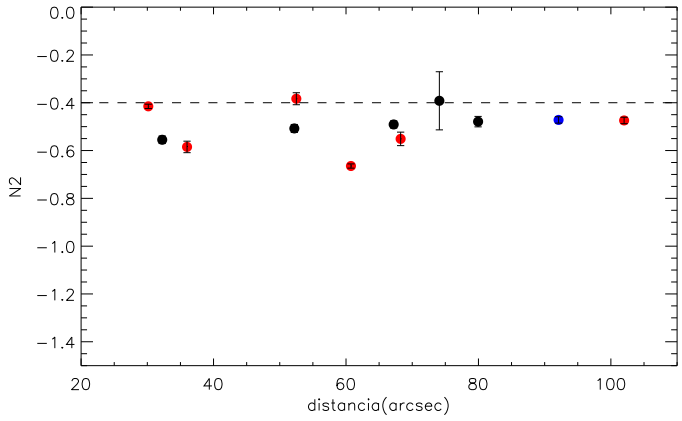

Figure 2.: Statistical inicators of abundance using the N2.

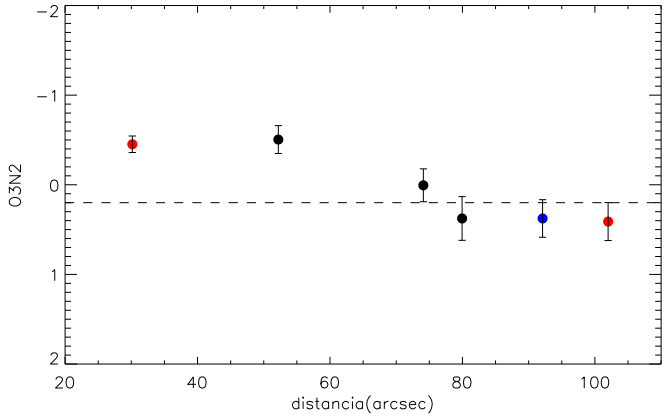

Figure 3.: Statistical inicators of abundance using the O3N2.

4. Conclusions

The emission lines were used to determine the physical characteristics of the gas and the abundance patterns in the spiral galaxy NGC 1232. The chemical abundances tracers using the indices N_2 and O_3S_2 were obtained by the method of the bright lines for both the HII regions and the background galaxy. By including the data of the galaxy NGC 1232B in the graphs of the HII regions of this work, it was possible to obtain information through its spectrum and make a preliminary analysis of its characteristics. Through BPT diagrams we characterized the galaxy NGC 1232B as a starburst galaxy.

Acknowledgments. F.L.C thanks CAPES for financial support.

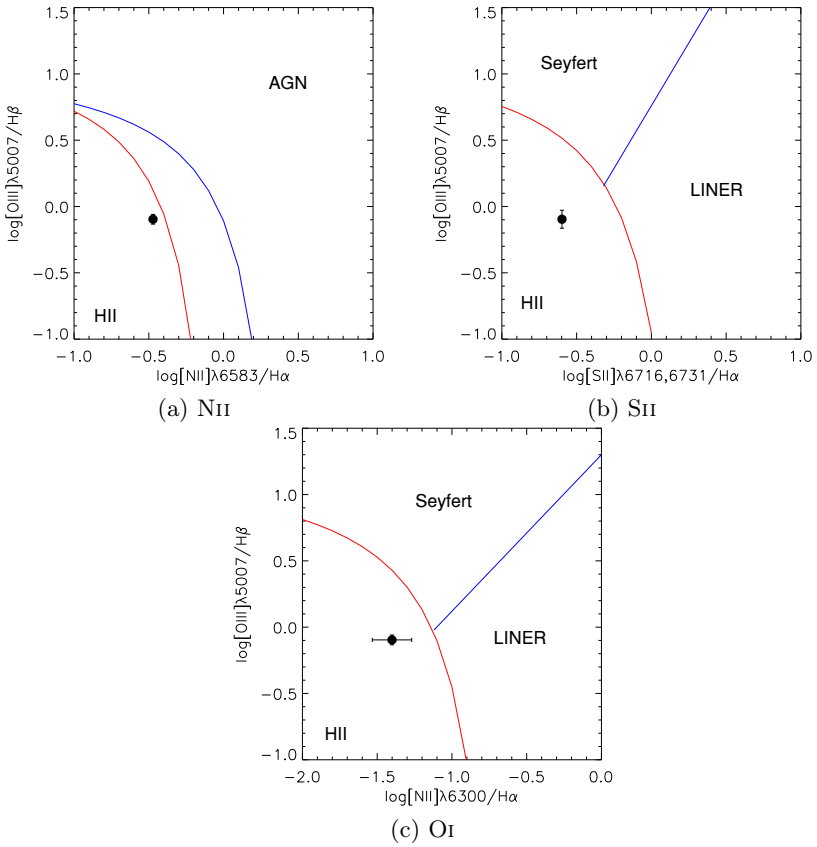

(a) NII (b) SII

(c) OI

Figure 4.: BPT diagrams

References

Alloin D., Collin-Souffrin S., Joly M., Vigroux L., 1979, *A&A*, **78**, 200

Kauffmann G., Heckman T. M., Tremonti C., Brinchmann J., Charlot S., White S. D. M., Ridgway S. E., Brinkmann J., Fukugita M., Hall P. B., Ivezić Ž., Richards G. T., Schneider D. P., 2003, *MNRAS*, **346**, 1055

Kewley L. J., Heisler C. A., Dopita M. A., Lumsden S., 2001, *ApJS*, **132**, 37

Pettini M., Pagel B. E. J., 2004, *MNRAS*, **348**, L59

Chemical Abundances in Gaseous Nebulae:
Open problems in Nebular astrophysics
AAA Workshop Series 11, 2019
M. Cardaci, G. Hägele & E. Pérez-Montero, eds.

Poster

A spectrophotometric study of planetary nebulae and HII regions in the M83 galaxy

Monique M. de Brito[1] and Oscar Cavichia[1]

[1]*Instituto de Física e Química, Universdidade Federal de Itajubá, Av. BPS, 1303, 37500-903, Itajubá-MG, Brazil.*

Abstract. Low and intermediate mass stars (0.8-8M⊙) in the end of their evolution pass through a series of events of mass loss, which contributes for the enrichment of the interstellar medium. The end of this evolutionary process is preceded by the planetary nebulae (PNe) phase, representing an important source of information for understanding the chemical enrichment of galaxies. The M83 barred galaxy is a relatively nearby galaxy, which allows the spectrophotometric study of its photoionized objects. In the literature, HII regions have been extensively explored in this galaxy, though its PNe population has not previously been addressed. In this work we report, for the first time, a spectrophotometric study of the PNe population in the M83 galaxy. The data was observed with the Gemini GMOS multi-object spectrograph in 2014 using two grating configurations (R400 and B600) and under an excellent seeing condition (< 0.8 arcsec). These data are curently being reduced with the Gemini Pyraf package. In the first phase of this project we wish to confirm spectroscopically the PNe candidates of the sample to further analyze, for the first time, the radial gradient of chemical abundances from the PNe population in this galaxy.

Key words: galaxies: chemical evolution – planetary nebulae and HII regions: ISM – techniques: multi-object spectroscopy

1. Introduction

The concept of stellar populations distinguishes objects belonging to a galaxy according to a series of parameters: age, chemical composition, spatial distribution and kinematic characteristics. The analysis of the different star populations gives us a much information about the evolution of galaxies. As for spiral galaxies, most information on chemical abundances comes from photoionized nebulae, such as PNe and HII regions.

PNe and HII regions represent important links to the understanding the enrichment and chemical composition of galaxies. Both are considered as the best tracers of the chemical evolution of galaxies (Gonçalves, 2018).

PNe are the result of the final stages of life of a star with mass in the range of 0.8-8M⊙, also called low mass and intermediate stars. The gas layers ejected from these stars represent a source of information to understanding the influence

of PNe in the chemical enrichment of galaxies. The HII regions, so called by the amount of atomic and ionized hydrogen present in these clouds of gas, are regions of star formation. In spiral galaxies, HII regions are concentrated in the spiral arms and are very important in determining the chemical composition of galaxies.

The galaxy M83 (or NGC 5236), known as Southern Pinwheel Galaxy, is a barred spiral [SAB (s)]. M83 is located approximately 4.59 Mpc away from us in the direction of the Hydra constellation. In the literature there is a vast content regarding the HII regions in this galaxy on different subjects, including the determination of the radial gradient of oxygen abundance for M83 (Bresolin et al., 2009). However the population of PNe to date has not been studied in detail in this galaxy.

Herrmann et al. (2008) performed a photometric survey of PNe candidates in M83, where they obtained precise astrometric positions of these objects. However, a PNe can be confused with HII regions and/or remnants of supernovae at these distances in photometric studies. The M83 galaxy, to date in the literature, does not have a spectroscopic survey regarding its PNe population. In view of this, it is necessary and interesting to confirm spectrophometrically whether these objects are actually PNe.

Our work aims a the spectrophotometric characterization of this sample of PNe in M83. In section 2 we present the procedures adopted, such as information regarding observation and data processing. In section 3 we discuss what the expected results are, since this is an undergoing project. And finally in section 4, our final considerations and perspectives.

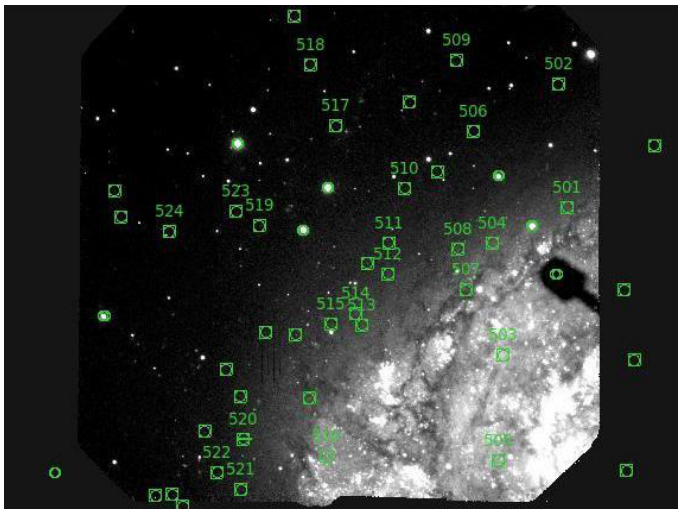

Figure 1. Field of galaxy M83 that was observed. The positions of the candidates for PNe are represented by the green squares, and the circles represent stars that were used for aligning the mask.

2. Procedure

The observations were made with the 8m Gemini South telescope, located in Chile in 2014. The multi-object spectrograph (GMOS) was used for these observations. This mode of spectroscopy was chosen because it was advantageous to simultaneously collect several spectra of objects located in the field of the telescope.
Only one field of M83 was observed. The Figure 1 shows the M83 field in which MOS spectroscopy was made and the observed PNe sample are indicated by green squares. Pre-images of the analyzed field of M83 were used to produce the spectroscopic masks (Figure 2), with the purpose of selecting only our objects of interest, the candidates for PNe. We employed the R400 and B600 gratings, in which differ only in the adopted central wavelengths and spectral coverage. Our data were obtained under an excellent seeing condition (< 0.8 arcsec).

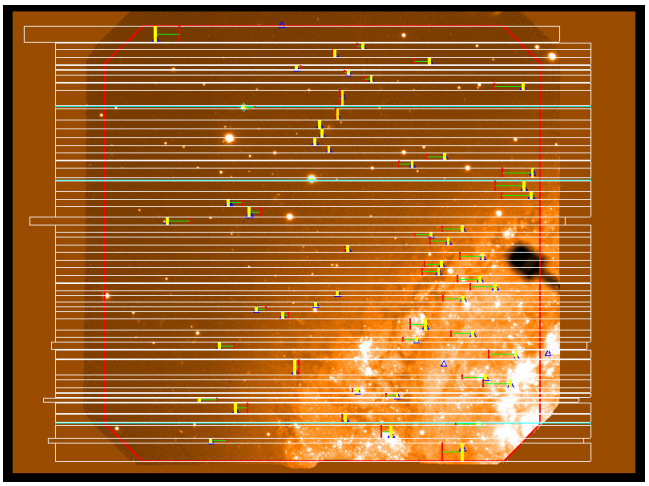

Figure 2. One of the spectroscopic masks made, in this example for the B600 grating. The positions of the slitlets in the masks exactly match the positions of the PNe in which we wish to obtain their spectra.

The data is currently being reduced with the Gemini PyRAF package, which allows scripts and execution of Image Reduction and Analysis Facility (IRAF) tasks from the Python environment. The reduction of data from this project is based on the tutorial available on the Gemini Observatory platform for multi-object spectra reductions. This tutorial is based on the work of Stanghellini et al. (2014).
The reduction process included bias and flat correction, twilight flats, mosaic the CCDs, wavelength calibration and flux calibration.

3. Results

This work is still under development, and in this first moment we intend to carry out the spectroscopic confirmation of the PNe sample of the M83 galaxy. Once

the process of data reduction is finished, we will have the spectra of these objects and in this way we can characterize them.
The objects of our sample are all PNe candidates, which do not have spectroscopic observations available in the literature, but with enough quality and distance to derive physical parameters and possibly chemical abundances.
At the conclusion of this work we hope to characterize the population of PNe as well as cataloging and discovery of new HII regions and/or supernovae remnants in this galaxy.

4. Conclusions

In this work we present a study about the PNe population in the galaxy M83, observed with the Gemini multi-object spectrograph (GMOS). We intend to carry out the spectrophotometric characterization of these objects, as they do not have, up to the present moment in the literature, a detailed spectroscopic study of the PNe population in this galaxy.
The spectroscopic confirmation of the sample of PNe in the galaxy M83 will later enable us to study of the chemical enrichment of the galaxy's interstellar medium. In this way, the radial gradient of chemical abundances of the PNe population in M83 may be obtained for the first time.
These data will be fundamental to study the chemical evolution of the M83 galaxy, and may contribute to the study of the influence of bars on the radial gradient of chemical abundances of barred spiral galaxies (Cavichia et al., 2014).

Acknowledgments. We would like to thank FAPEMIG for the financial support.

References

Bresolin F., Ryan-Weber E., Kennicutt R. C., Goddard Q., 2009, *ApJ*, **695**, 580
Cavichia O., Mollá M., Costa R. D. D., Maciel W. J., 2014, *MNRAS*, **437**, 3688
Gonçalves D. R., 2018, *Proceedings IAU Symposium No. 344*
Herrmann K. A., Ciardullo R., Feldmeier J. J., Vinciguerra M., 2008, *ApJ*, **683**, 630
Stanghellini L., Magrini L., Casasola V., Villaver E., 2014, *A&A*, **567**, A88

Chemical Abundances in Gaseous Nebulae:
Open problems in Nebular astrophysics
AAA Workshop Series 11, 2019
M. Cardaci, G. Hägele & E. Pérez-Montero, eds.

Poster

Physical conditions and chemical abundances in Planetary Nebula M 2–36. Results from UVES.

J. Espíritu,[1], A. Peimbert[1] and G. Delgado-Inglada[1]

[1]*Instituto de Astronomía, Universidad Nacional Autónoma de México, Apartado Postal 70-264, Ciudad de México-04510, Mexico.*
email: jespiritu@astro.unam.mx

Abstract. An analysis of the chemical composition of planetary nebula M 2-36 is presented using the direct method. Spectra of this object were obtained with the Ultra Violet and Visual Echelle Spectrograph (UVES) at the Very Large Telescope (VLT), providing very high spectral resolution. 491 emission lines were detected. Electron temperature and density were computed using a variety of methods, including forbidden line ratios, balmer jump, and O^{++} recombination lines. We present ionic abundances for He^{+}, He^{++}, O^{+}, and O^{++} with small error bars. From collisionally excited lines and recombination lines of O^{++} we have obtained a new value for the Abundance Discrepancy Factor (ADF) of this nebula, being $\mathrm{ADF}(O^{++}) = 7.93 \pm 0.44$. Finally, we discuss the contribution of physical mechanisms that may contribute to originate said ADF.

Key words: galaxies: abundances — galaxies: ISM — techniques: imaging spectroscopy

1. Introduction

Chemical abundances in Planetary Nebulae (PNe) and HII regions can be derived from the analysis of their emission spectra. Collisionally excited lines (CELs) of heavy elements are used typically to derive the chemical composition of these objects; deep spectra also provide the opportunity to obtain chemical abundances from optical recombination lines (ORLs) of heavy elements (Liu et al., 2001). For more than seventy years, it has been found that ORLs yield systematically higher abundances than CELs for a given ion; this discrepancy is quantified by the Abundance Discrepancy Factor (ADF), defined as the ratio of ORL to CEL ionic abundances. Most PNe studied thus far present ADFs in the range of 1.4 to 10 (McNabb et al., 2013); but an important number of them exhibit large ADFs, exceeding 100 in some cases (see Corradi et al., 2015).
Recent works have shown the necessity of deep optical spectra to provide insight into the origin of CEL and ORL and the physical conditions in PNe.
We present an analysis of one such spectrum obtained from the Very Large Telescope UVES spectrograph for PN M 2-36, a planetary nebula from the galactic bulge with known chemistry (Liu et al., 2001).

2. Observations and data reduction

Observations were carried out during the night of march 30, 2003, using the Ultraviolet and Visual Echelle Spectrograph (UVES) installed at the Very Large Telescope in Cerro Paranal, Chile. We observed simultaneously with the red and blue arms in two settings, covering the region from 3100 to 10360 Å, except for small gaps resulting from the separation between the two CCDs used in the red arm. The slit width was set to 2″, with a North-South orientation (0° position angle); effectively covering M 2–36 (Fig. 1) while avoiding the central star.
The spectra were reduced using IRAF[1] following the standard procedure of bias subtraction, aperture extraction, flat fielding, wavelength calibration and flux calibration. For the latter, standard stars EG 274 and CD–329927 were observed.

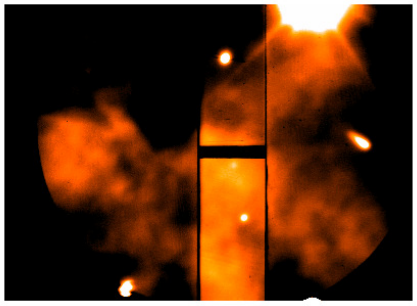

Figure 1. Slit position across M 2–36. Its dimensions are 2 × 10 arcsec^2.

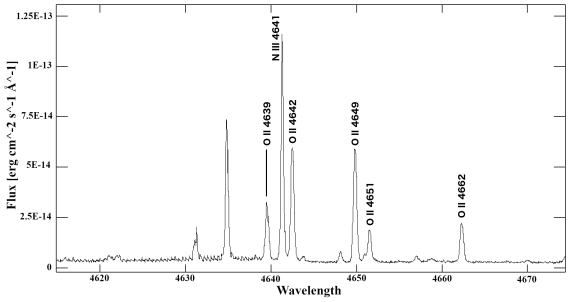

Figure 2. Portion of the echelle spectrum showing multiplet V1 of OII.

3. Results

From the integrated spectra, 491 emission lines were identified. Using the methodology described in section 2, we were able to fully resolve multiplet V1 of OII (Fig.2). Line intensities were measured integrating the flux in the line between two given limits over a local continuum estimated by eye. The reddening coefficient $C(\mathrm{H}\beta)$ was determined by comparing the observed intensity of the Balmer and Paschen hydrogen lines with the theoretical values computed using INTRAT (Storey & Hummer, 1995), considering $T_e = 8000$ K and $n_e = 4000$ cm^{-3}. We used the reddening law of Cardelli et al. (1989), obtaining the best fit with $R_v = 2.75$, resuling in $C(\mathrm{H}\beta) = 0.331$.
Electron temperature and density were computed from classical diagnostics using PyNeb (Luridiana et al., 2015). We distinguished between high ionization and low ionization zones. The electron temperature of the high-ionization zone is represented by the classical diagnostics of [OIII], [ArIII], and [SIII]; meanwhile, the low-ionization zone is represented by [NII], [OII], [SII]. For electron density,

[1]IRAF is distributed by NOAO, which is operated by AURA, Inc., under cooperative agreement with NSF.

the high-ionization zone is represented by the [ArIV] nd [ClIII] diagnostics; for the low-ionization zone, we refer to the [OII] and [SII] diagnostics. Tables 1 and 2 show the adopted values for T_e and N_e used to compute ionic abundances. We also determined T_e from the HI Balmer jump, and from the ratio of the intensity of multiplet V1 of OII to the intensity of [OIII] λ4959.

Table 1. Adopted electron temperatures [K].

T_e (High I)	T_e(Low I)	T_e (BJ)	T_e (VI/4959)
8380 ±100	14100 ±300	6100 ±900	5420 ±430

Table 2. Adopted electron densities [cm^{-3}].

n_e (High I)	n_e(Low I)	n_e (VI/4959)
6530 ±1800	4570 ±600	1100 $\pm^{1000}_{600}$

Ionic abundances are presented in Table 3. O^{++} abundance was computed in two ways: from CELs and RLs, the latter based on the work by Storey et al. (2017). He^{+} abundance was computed using HELIO 14 (Peimbert et al., 2000).

Table 3. Ionic abundances with $t^2 = 0.00$.

Ion (X)	12+log(n(X)/n(H$^+$))
He^{+}	11.101 ± 0.004
He^{++}	9.52 ± 0.02
O^{+}	7.04 ± 0.04
O^{++}_{CEL}	8.72 ± 0.02
O^{++}_{RL}	9.63 ± 0.03

Table 4. t^2 computed from different sources.

$t^2(O^{++})$	$t^2(He^{+})$	t^2(BJ)
0.088 ± 0.003	0.017 ± 0.003	0.048 ± 0.010

From O^{++}_{CEL} and O^{++}_{RL} we have obtained ADF(O^{++}) = 7.93 ± 0.44 which exceeds the value of 6.86 obtained by Liu et al. (2001). Considering the presence of temperature variations and the formalism developed by Peimbert (1967) and Peimbert & Costero (1969) we can obtain t^2 from O^{++}, He^{+} and the Balmer jump temperature; the corresponding values are presented in Table 4.
Using the values from Table 4 we computed new ionic abundances for O^{++}_{CEL} with $t^2 \neq 0.00$, presented in Table 5.

Table 5. O^{++}/H^{+} corrected for temperature variations ($t^2 \neq 0.00$).

Abundance	$t^2(O^{++})$	$t^2(He^{+})$	t^2 (BJ)
$12+\log(O^{++}/H^{+})$	9.64 ± 0.04	8.85 ± 0.05	9.13 ± 0.13

4. Conclusions

We have computed T_e and n_e for PN M 2-36 using a wide range of diagnostics. Chemical abundances are reported for a sample of ions with reduced error bars. The different values obtained for t^2 reveal a complicated structure within the nebula. While the observed value for ADF(O^{++}) cannot be attributed solely to the presence of temperature variations, we can argue that they contribute a significant amount to the t^2 value. The low T_e(V1/4959) implies that the bulk of OII emission lines originate from a cold, hydrogen-poor, metal rich phase.

Acknowledgments. We would like to thank M. T. Ruiz and M. Peimbert for their collaboration in acquiring the observations. This project was supported by CONACyT grant 464709 and PAPIIT IG 100319.

References

Cardelli J. A., Clayton G. C., Mathis J. S., 1989, *ApJ*, **345**, 245
Corradi R. L. M., Kwitter K. B., Balick B., Henry R. B. C., Hensley K., 2015, *ApJ*, **807**, 181
Liu X.-W., Luo S.-G., Barlow M. J., Danziger I. J., Storey P. J., 2001, *MNRAS*, **327**, 141
Luridiana V., Morisset C., Shaw R. A., 2015, *A&A*, **573**, A42
McNabb I. A., Fang X., Liu X.-W., Bastin R. J., Storey P. J., 2013, *MNRAS*, **428**, 3443
Peimbert M., 1967, *ApJ*, **150**, 825
Peimbert M., Costero R., 1969, *Boletin de los Observatorios Tonantzintla y Tacubaya*, **5**, 3
Peimbert M., Peimbert A., Ruiz M. T., 2000, *ApJ*, **541**, 688
Storey P. J., Hummer D. G., 1995, *MNRAS*, **272**, 41
Storey P. J., Sochi T., Bastin R., 2017, *MNRAS*, **470**, 379

Chemical Abundances in Gaseous Nebulae:
Open problems in Nebular astrophysics
AAA Workshop Series 11, 2019
M. Cardaci, G. Hägele & E. Pérez-Montero, eds.

Poster

ESO 287-IG50: a possible Polar-Ring Galaxy

P. Freitas-Lemes[1], M. Faúndez-Abans[2], P. Rocha-Poppe[3,4], M. de Oliveira-Abans[2], I. Rodrigues[1], V. P. Reshetnikov[5], J. Tello[7] and V. A. Fernandes-Martin[3]

[1] *UNIVAP - Universidade do Vale do Paraíba. Av. Shishima Hifumi, 2911, CEP:12244-000, São José dos Campos, SP, Brazil*
[2] *MCTIC/ Laboratório Nacional de Astrofísica, CEP:37.504-364, Itajubá, MG, Brazil mfaundez@lna.br mabans@lna.br*
[3] *UEFS, Departamento de Física, Av. Transnordenstina, S/N, Novo Horizonte, CEP 44036-900 Feira de Santana, BA, Brazil*
[4] *UEFS, Observatório Astronômico Antares, Rua da Barra, 925, Jardim Cruzeiro, CEP 44015-430 Feira de Santana, BA, Brazil*
[5] *St. Petersburg State University, 7/9 Universitetskaya nab., St. Petersburg, 199034, Russia*
[7] *UNI: Universidad Nacional de Ingeniería, Facultad de Ciencias, Grupo Astronomía, Av. Túpac Amaru s/n, Rimac, Lima 25, Perú.*

Abstract. This observational study is about the effects of interaction on the kinematics and chemical abundance of the galaxies of the ESO 287-IG50. This system could be a polar ring galaxy. Our study was based on the V broad band imagery as well as longslit spectroscopy in the wavelength range 4240-8700Å. Image analysis through a Gaussian filtering revealed what appears to be a bar, with perpendicular structures at both ends, which could be the inner part of a bissimetric spiral structure. We estimated heliocentric radial velocities of 17 689±58 km/s. The velocity profile shows a clear rotational behavior, with peak velocities of 110 km/s to the SW and 80 km/s to the other side.
We used the stellar population synthesis code `STARLIGHT`. Standard diagnostic diagrams will be used to classify the main ionizing source of selected emission-line regions. Using empirical methods, we intend to investigate the metallicity of the HII regions in ESO 287-IG50. With all this information, we are going to study the implications on the formation history of this galaxy.

Key words: galaxies: abundances — galaxies: ISM — techniques: imaging spectroscopy

1. Introduction

Interacting galaxies exhibit typical tidal structures like tails, plumes, bridges, twisted arms, and some other structures which are the result of a variety of galaxy encounters. One result of such galaxy interactions are the Collisional Ring

Galaxies (RGs), a class of galaxies that encompasses a large number of different ring and ring-like structures: with or without clumps, spokes and warped shapes, to name a few. RGs have given rise to signicant interest since Lynds & Toomre's numerical simulations, showing that the ring phenomenon can be the result of a small (compact) galaxy passing through a larger one (Lynds & Toomre, 1976; Appleton & Struck-Marcell, 1987; Appleton & James, 1990; Struck-Marcell & Lotan, 1990; Struck-Marcell, 1990; Struck-Marcell & Higdon, 1993; Tutukov & Fedorova, 2016).

Our study was based on a dedicated V broad band imagery as well as longslit spectroscopy in the wavelength range 4240-8700Å. We used the stellar population synthesis code `STARLIGHT`. Standard diagnostic diagrams will be used to classify the main ionizing source of selected emission-line regions. Using empirical methods, we intend to investigate the metallicity of the HII regions in ESO 287-IG50. With all this information, we are going to study the implications on the formation history of this galaxy.

The galaxy ESO 287-IG50 (AM 2138-461; PRC C-65), is a near Universe object with z = 0.0589 without dedicated observations. There are nine quoted references on this object in NED, most catalogues/surveys. The 5 arcmin field around ESO 287-IG50 is shown in Fig. 1a. The image shows leftover extended material around the galaxy, as well as some fainter close field galaxies. One, at the SW direction, is APMUKS(BJ) B213841.61-461509.1 a galaxy of 17.2r mag (NED), without redshift data in the literature.

2. Observations and data reduction

The observations were performed with the 1.6-m telescope at the Observatório do Pico dos Dias - OPD, Brazil. For a dedicated image, three 900 sec direct V broad-band images were obtained out with the Camera-1, detector Ikon-L936-EX, a back-illuminated sensor (2 048x2 048 array and pixel size 13.5x13.5 μm^2, scale of $0\farcs56$ pix^{-1}). The 3 images were processed using standard procedures employing IRAF[1]. The spectroscopic observations were performed with a Cassegrain spectrograph, the same telescope and detector. A 300-lines mm^{-1} grating was centred at λ6400 Å. The galaxy was observed with a slit of $3''$ wide, while the spectrophotometric standards stars were observed with $5''$, both in the spectral range 3 790-9 000 Å. Two slit position and two spectra of 1800 sec for each were obtained under conditions better than $1\farcs1$ FWHM seeing. The stars used for extinction and flux calibrations are tertiary standards from Baldwin & Stone (1984), as revised by Hamuy et al. (1992), see also Hamuy et al. (1994). The slit positions are over-plotted in image of AM 2229-735, presented in Figure 1b.

[1]Image Reduction and Analysis Facility, distributed by the National Optical Astronomy Observatory, which is operated by the Association of Universities for Research in Astronomy, Inc., under a cooperative agreement with the National Science Foundation

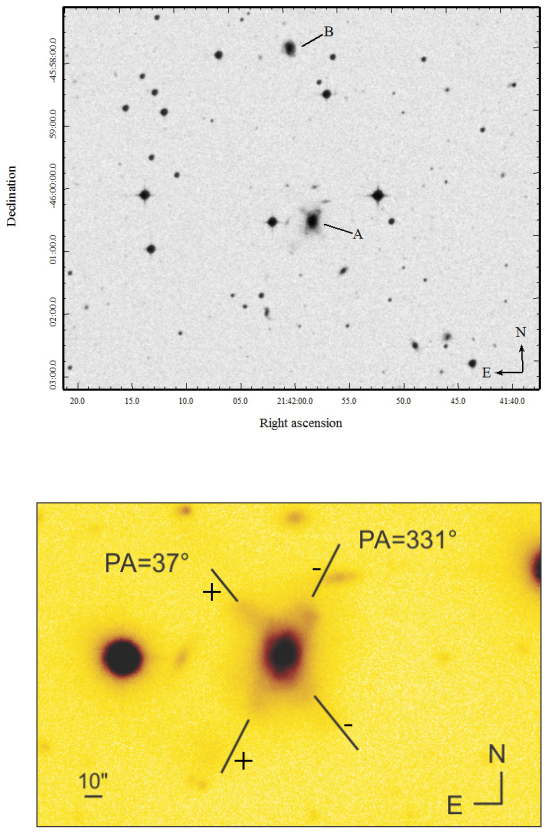

Figure 1. *Top:* Objects near the PRG candidate ESO 287-IG50. Image obtained from the Digitized Sky Survey. *Botom:* Direct V-filter combined image. Both, the PA = 37° and PA = 331° slit position are displayed.

3. Preliminary Results

- **Structures**: The original image (Fig. 1b) show a galaxy with a round central shape up to $r = 10$ arcsec, surrounded by a a structure thar seems to be a highly inclined ring (75°) in the direction of PA = 331°, with a clear hook like apearence to the NW direction.

- **The Spectra and kinematics**: The spectral apertures were extracted using the APALL/IRAF package. The heliocentric radial velocity was calculated using the RVSAO/EMSAO package, where each spectral aperture was cross-correlated with the composite emission-line template "femtemp97" distributed by RVSAO/IRAF external package (Mink & Wyatt, 1995). We measured a redshift of z=0.058897 corresponding to a radial velocity of $V_r = 17\,689 \pm 45$ km/s, which is in good agreement with the values obtained by Keel (1985), Jones et al. (2009) and Lavaux & Hudson (2011). Adopting $H_0 = 70$ km s^{-1}Mpc^{-1}, a distance of 93 Mpc was calculated. In order

to investigate the velocity profile behavior we used the Hα emission-line, which is the stronger line, detected with $4 < S/N < 55$. The rotational behavior and orientations of both slits suggests that the Position Angle of the kinematic major axis (PA = 37°) is somewhere between these slit directions, something around the East–West direction.

- **Stellar population synthesis**:the star formation history of the ESO 287-IG50 was investigated through stellar population synthesis. We found that the bulge of this galaxy is dominated by old and intermediate stellar populations.

- **Activity in ESO 287 IG-50**: the emission line spectrum suggests the presence of a AGN nucleus in the host object.

References

Appleton P. N., James R. A., 1990, *Self-consistent simulations of ring galaxies.*, pp 200–204
Appleton P. N., Struck-Marcell C., 1987, *ApJ*, **318**, 103
Baldwin J. A., Stone R. P. S., 1984, *MNRAS*, **206**, 241
Hamuy M., Suntzeff N. B., Heathcote S. R., Walker A. R., Gigoux P., Phillips M. M., 1994, *PASP*, **106**, 566
Hamuy M., Walker A. R., Suntzeff N. B., Gigoux P., Heathcote S. R., Phillips M. M., 1992, *PASP*, **104**, 533
Jones D. H., Read M. A., Saunders W., Colless M., Jarrett T., Parker Q. A., Fairall, 2009, *MNRAS*, **399**, 683
Keel W. C., 1985, *AJ*, **90**, 2207
Lavaux G., Hudson M. J., 2011, *MNRAS*, **416**, 2840
Lynds R., Toomre A., 1976, *ApJ*, **209**, 382
Mink D. J., Wyatt W. F., 1995, R. A. Shaw, H. E. Payne, and J. J. E. Hayes (eds.), *Astronomical Data Analysis Software and Systems IV*, Vol. 77 of *Astronomical Society of the Pacific Conference Series*, p. 496
Struck-Marcell C., 1990, *AJ*, **99**, 71
Struck-Marcell C., Higdon J. L., 1993, *ApJ*, **411**, 108
Struck-Marcell C., Lotan P., 1990, *ApJ*, **358**, 99
Tutukov A. V., Fedorova A. V., 2016, *Astronomy Reports*, **60**, 116

Chemical Abundances in Gaseous Nebulae:
Open problems in Nebular astrophysics
AAA Workshop Series 11, 2019
M. Cardaci, G. Hägele & E. Pérez-Montero, eds.

Poster

The Influence of Shocks in Abundances Calculation

Lago, P.J.A.[1], Costa, R.D.D.[2] and Faúndez-Abans, M.[1]

[1]*LNA-Laboratório Nacional de Astrofísica, R. dos Estados Unidos, 154 - Nações, Itajubá-MG, Brazil*
[2]*Departamento de Astronomia, IAG, Universidade de São Paulo, Rua do Matão, 1226 - Cidade Universitária São Paulo-SP, Brazil*

Abstract. Planetary Nebulae (PNe) have a large morphological diversity, such characteristics reflect the complexity of formation scenarios; these scenarios have a close relationship with the parent star and its environment, where the binarity of the central star (CS) seems to play an important role. The determination of PNe abundances can be a hard task, and two ways are common in the literature: (a) Using empirical ionization correction factors (ICF's) and spectral data, (b) or using photoionization codes. "Secondary" ionization effects could be important and these two approaches do not consider them, and these effects could be linked with morphological types. Shocks are a way of energy input in gas, and recently new diagrams were introduced for shocks diagnostics. Using these diagrams we present results for a sample of PNe and check the impact of shocks in the abundances calculation. Our preliminary results are shown for a sample and a new interpretation of the mechanism is introduced, being considered as a general effect instead of a local one.

Key words: ISM: kinematics and dynamics — ISM: abundances — radiation mechanisms: non-thermal

1. Introduction

PNe are the result of stellar evolution processes, their parent stars have masses between 0.8 to 8 solar masses. The final stages of these stars consist of mass ejection episodes, the exposed core will be the source of the radiation field, that will interact with previously ejected mass. The remaining star will get colder turning itself into a white dwarf, at this time the PN will be already dispersed. The stellar evolution sequence could be different in case of a multiple system.
The theory about PNe formation dates from 70's being generalized some years later (Kwok et al., 1978; Balick, 1987), these descriptions of the phenomenon are still acceptable, being a robust approach in a general way. Nowadays, the state of art of this field is related to the particular features of each PN. Why so many different PNe shapes can be observed?
Some works advocate that we are overestimating the morphology diversity (Chong et al., 2012), the way that we observe (the line of sight) could also be responsible

for it (García-Díaz et al., 2012). But still considering this: some shapes are really intriguing and seem to be related to a particular feature of parent star(s).
The photoionization process in PNe is well understood, consisting of common sense in the area. A large number of works related to computational tools (Ercolano et al., 2003; Ferland et al., 2017) reinforce the status of theory; however, inadequate descriptions for some scenarios still exist. The high flux of some lines from low ionization ions, especially related to substructures, makes the authors invoke other excitation/ionization mechanisms.
Here we present some preliminary results. The aim is to explore a recurrent "deus ex machina" used by astronomers to justify deviations from purely photoionized nebulae: the shocks. We have used observational markers to characterize this mechanism in a sample of PNe.

2. Procedure

Computational models for shocks as well as the observational techniques are still difficult to apply in PNe context. The kinematics of PNe put them in a distinct energy regime, outside of approaches applied to other kinds of target. The lack of organized and multiband efforts to characterize the phenomenon makes harder to predict its effects in the derivation of parameters. It is still unclear how to separate photoionization effects from shocks, and due to this we choose the diagnostics diagrams by Akras & Gonçalves (2016) as tools to characterize this phenomenon in our sample; these diagrams use observational data practically without theoretical/model constraints. To acquire the markers some parameters are necessary; the ratio f_{shock}/f_* is derived based on the equation:

$$f_{shock}/f_* = 9.12 \times 10^{-3} (\frac{Vs}{100 kms^{-1}})^3 \times (n_e/cm^{-3}) \times \frac{\pi d^2}{L} \quad (1)$$

Where Vs is the shock velocity, n_e is the electronic density, and d is the distance to the CS.
Some restrictions should be considered. Equation 1 represents the flux ratio instead of the photon ratios, as suggested originally in Akras & Gonçalves (2016); seems unlikely that shocks emit as a blackbody as the assumptions of the original approach could suggest. Another important aspect is that is inappropriate to use this equation outside of the diagrams context. This ratio should be seen as a shock marker.
We combined data from different sources: our morpho kinematical models, physical parameters from literature and line flux ratios when available. We made this preliminary study for three PNe, our targets were NGC 6818, NGC 6153 and NGC 6445.

3. Results

We summarize our results in Tables 1 and 2.

Table 1.

NGC 6445	V(km/s)	Distance (kpc)	n_e (cm^{-3})	$\log(f_{shock}/f_*)$
Ring	48	1.37	1100	-0.71
Rim	145	1.37	250	1.28

Table 1 displays our results for NGC 6445. This PN presents a low luminosity star 933 L_{sun} and using the velocities fields from our SHAPE models [1] and the parameters in Table 1 [2], it could be seen that the ring and rim markers suggest the presence of shocks, and the rim have the strongest marker of our sample. It should be emphasized that NGC 6445 is a type 1 PN, and we will present an enlarged discussion about this class in Lago et al (2019, in preparation).
The marker was acquired in the same way for the other two PNe. Both objects present weaker markers in their borders (Table 2 [3]), pointing to a possible link between this marker and morphology.
It was not possible to derive the line flux ratios for our sample. In the near future, after another observational campaign, dedicated especially to these targets, the diagrams will be explored in more detail; for now, we are making a discussion on the ratio of fluxes.

Table 2.

Nebula	Luminosity (L_{Sun})	Distance (kpc)	n_e (cm^{-3})	$\log(f_{shock}/f_*)$
NGC 6818	1260	1.7	1500	-1.57
NGC 6153	2034	1.5	3000	-1.53

4. Conclusions

Considering this preliminary study, we advocate for the need of a large survey and development of better tools to evaluate shocks in PNe environment. Assuming that the shocks increase the energy of gas, they alterate the line fluxes. Since is common to use these lines and line ratios in derivation of abundances, is natural to suppose that, depending on the strength of shock, this could compromise the abundance derivations.
The kinematics of PNe is a particular feature, some objects have similarities due to the morphology; but particularities should be remarkable. Due to this aspect,

[1] the modelling toll is described in Steffen & López (2006) and the used P-V diagrams are from López et al. (2012)

[2] The data are from Cahn et al. (1992); Cuesta & Phillips (1999)

[3] The data are from Benetti et al. (2003); Yuan et al. (2011), and the used P-V diagrams were from Observatório do Pico dos Dias, observed by us.

the calculation of abundances should consider particularities of each object if shocks are relevant.

Acknowledgments. P.J.A. Lago would like to thank CNPq for his post-doctoral fellowship (PCI Program - Process 300106/2019-0).

References

Akras S., Gonçalves D. R., 2016, *MNRAS*, **455**, 930
Balick B., 1987, *AJ*, **94**, 671
Benetti S., Cappellaro E., Ragazzoni R., Sabbadin F., Turatto M., 2003, *A&A*, **400**, 161
Cahn J. H., Kaler J. B., Stanghellini L., 1992, *A&AS*, **94**, 399
Chong S.-N., Kwok S., Imai H., Tafoya D., Chibueze J., 2012, *ApJ*, **760**, 115
Cuesta L., Phillips J. P., 1999, *AJ*, **117**, 974
Ercolano B., Barlow M. J., Storey P. J., Liu X.-W., 2003, *MNRAS*, **340**, 1136
Ferland G. J., Chatzikos M., Guzmán F., Lykins M. L., van Hoof P. A. M., Williams R. J. R., Abel N. P., Badnell N. R., Keenan F. P., Porter R. L., Stancil P. C., 2017, *RevMexAA*, **53**, 385
García-Díaz M. T., López J. A., Steffen W., Richer M. G., 2012, *ApJ*, **761**, 172
Kwok S., Purton C. R., Fitzgerald P. M., 1978, *ApJL*, **219**, L125
López J. A., Richer M. G., García-Díaz M. T., Clark D. M., Meaburn J., Riesgo H., Steffen W., Lloyd M., 2012, *RevMexAA*, **48**, 3
Steffen W., López J. A., 2006, *RevMexAA*, **42**, 99
Yuan H.-B., Liu X.-W., Péquignot D., Rubin R. H., Ercolano B., Zhang Y., 2011, *MNRAS*, **411**, 1035

Chemical Abundances in Gaseous Nebulae:
Open problems in Nebular astrophysics
AAA Workshop Series 11, 2019
M. Cardaci, G. Hägele & E. Pérez-Montero, eds.

Poster

Study of planetary nebulae observed with integral field spectroscopy

B. Marques[1], H. Monteiro[1] and I. Aleman[1]

[1] *Universidade Federal de Itajubá, Av. BPS 1303, Itajubá - MG, Brazil*

Abstract.
We are conducting the analysis of integral field spectroscopic data obtained with VIMOS at the VLT-ESO telescope of four planetary nebulae (PNe). In this paper, we describe the methodology, preliminary results and the perspectives of this work. From an original sample of 16 PNe observed, we select 4 objects based on the quality and completeness of the data needed to calculate physical conditions and abundances. From the reduced data cubes, we determined intensity maps for typical diagnostic lines for the selected the objects. Temperature and density maps were derived from such maps. Preliminary results are shown for He 2-434 and IC 4191, PNe not previously studied with 3D spectroscopy.

Key words: planetary nebula: abundances – nebulae: flux maps – techniques: integral field spectroscopy

1. Introduction

Planetary nebulae (PNe) are produced by the mass ejection of low- and intermediate-mass stars in the final phases of their evolution. The study of PNe contributes to the investigation of stellar evolution theories and also the origin, abundances, and evolution of the chemical elements in galaxies. An important part of such contribution is obtained from the physical and chemical study of gas.
Spectroscopy gives not only flux measurements, but by using emission line intensities it also provides information on the chemical elements present and their abundances. With 3D spectroscopy, as obtained with Integral Field Units (IFUs), we additionally have the 2D spatial information (image projected on the sky for each wavelength bin). The data cubes obtained from the IFUs consist of several individual spectra collected from a group of optical fibers, covering a contiguous region of the sky.
In this paper, we describe the integral field spectroscopy data analysis of four planetary nebulae observed with VLT-ESO telescope. Section 2 describes the data analysis procedure, while Section 3 shows our preliminary results. In Section 4 we present our conclusions and perspectives.

2. Procedure

A sample of 16 PNe was observed with the VIsible Multi-Object Spectrograph (VIMOS) in the Very Large Telescope (VLT), in Chile, using its Integral Field Unit Mode. In this configuration, each fiber captures the spectrum in a given position of the nebula. The data collected forms a 3D table (two spatial and one spectral dimension) forming what we call a data cube.
From the original sample, four PNe were selected, namely He 2-108, He 2-117, He 2-434, and IC 4191, based on the quality of the data and the availability of the information we need to derive physical conditions and abundances. We only use data obtained during clear nights and observations of PNe that fit entirely inside the instrumental field-of-view. We further excluded objects with poor-quality data or with spectrum that do not cover the lines needed for the standard empirical analysis. The four selected objects have interesting morphology and are still poorly studied.
We obtained emission line flux maps for the selected planetary nebulae. The analysis of these maps provides their 2D morphology and velocity structure, which allow us to deduce some information on their 3D structures. From the maps we can also derive their density and electronic temperature distributions, as well as chemical abundances of some elements. Examples of the several emission line flux maps we obtain are shown in Fig. 1 (smoothing filters have been applied).
We obtained flux maps for the [SII] and [NII] spectral lines. From the line ratios taken pixel-by-pixel, we estimated the density from [NII] and temperature from the [SII] line ratio. We present the maps for He 2-434 in Fig. 2. No smoothing filters were applied. We exclude pixels with line fluxes below 3σ from the noise level.

3. Results

The He 2-434 Hα map (Fig. 1) shows an elliptical morphology, while the [SII] emission reveals a pair of ansae. The morphology of this nebula in the SDSS and WISE filter is spherical. Corradi et al. (1996) found low-ionization structures in 23 PNe, that are small-scale knot- or jet-like structures with lower ionization compared to the surrounding gas. They observed two ansae in He 2-434 and they classified it as two radially symmetrical knots. They suggested that those structures could be the result of collimation process or FLIERs (Balick et al., 1993).
On the other hand, the morphology of IC 4191 in Hα and [SII] is very similar. There is indication of radially symmetric structures, but differently from the He 2-434 case, they are composed of fully ionized material (Hα emitting gas). We suspect that the structure of IC 4191 is an outcome of the interstellar medium interaction.
From the [SII] and [NII] spectral line maps it was possible to calculate the temperature and density maps for the He 2-434 nebula. These maps are shown in Fig. 2. The results are still preliminary as we still need to apply the correction for differential refraction. We, however, do not expect that this will cause great differences in the results.

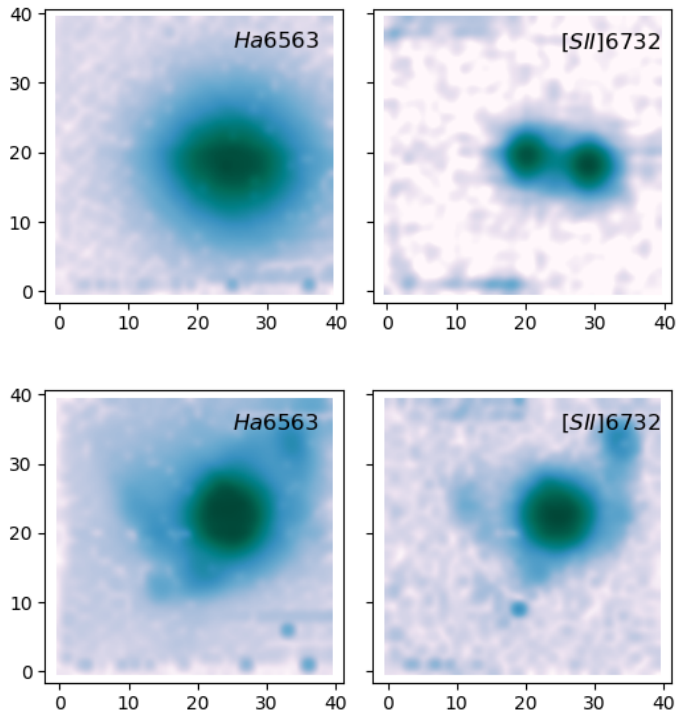

Figure 1. Flux maps of two of the selected PNe, He 2-434 (top) and IC 4191 (bottom). Maps of Hα λ6563 (left) and [SII] λ6732 (right) are shown.

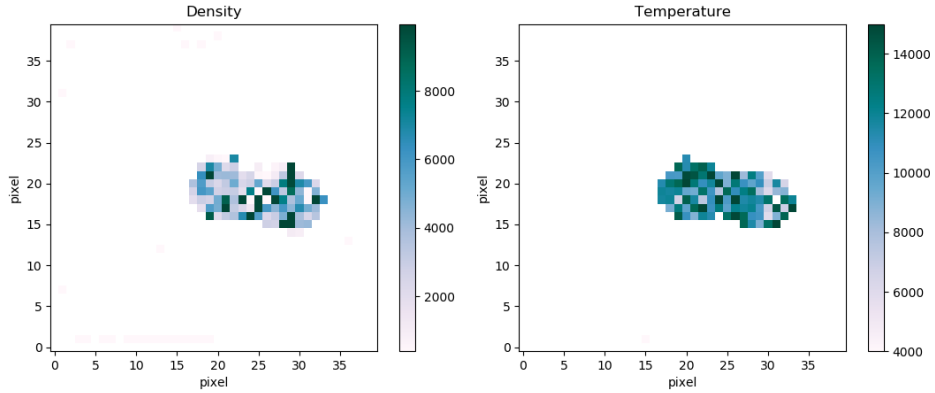

Figure 2. He 2-434 electronic density (left) and temperature (right) maps. The spatial scale is pixels.

The electronic density was calculated from the [SII] line ratios. As we only use pixels where the emission was significantly higher than the noise level, the density map is limited to the region close to the ansae. The density varies between ∼2000-8000 cm^{-1}, with no clear structure. As the density map, the temperature map do no show any particular temperature distribution. The electronic temperature calculated varies between ∼5000 and 14000 K.

4. Conclusions

In this paper, we present preliminary results from our study of four PNe observed with the VIMOS spectrograph mounted on VLT/ESO. We study He 2-434 and IC 4191, still poorly-known PNe, which have never been studied with 3D spectroscopy.
Line emission maps of He 2-434 and IC 4191 show interesting non-spherical emission structures. The He 2-434 shows two symmetrical structures, not seen in the Hα map. Such structures have been previously observed by Corradi et al. (1996), who classify them as low ionization structures.
The electronic temperature and density maps were obtained for the region surrounding the ansae structures in He 2-434. No clear structure was seen in the maps.

Acknowledgments. BM and IA would like to thank CAPES for the financial support.

References

Balick B., Rugers M., Terzian Y., Chengalur J. N., 1993, *ApJ*, **411**, 778
Corradi R. L. M., Manso R., Mampaso A., Schwarz H. E., 1996, *A&A*, **313**, 913

Chemical Abundances in Gaseous Nebulae:
Open problems in Nebular astrophysics
AAA Workshop Series 11, 2019
M. Cardaci, G. Hägele & E. Pérez-Montero, eds.

Poster

Radial distribution of helium in the Milky Way

J.E. Méndez-Delgado[1,2], C. Esteban[1,2] and J. García-Rojas[1,2]

[1]*Instituto de Astrofísica de Canarias, E-38200 La Laguna, Spain.*
[2]*Departamento de Astrofísica, Universidad de La Laguna, E-38206, La Laguna, Spain.*

Abstract.
We present preliminary results of the study of the radial distribution of helium in the Milky Way. We use 37 spectra from 23 Galactic HII regions observed with VLT, GTC and Magellan Telescope. Using PyNeb, we calculate the abundance of He^+ with all the HeI detected lines. In most cases, both the average abundance of He^+ and its associated dispersion are higher when triplet lines are used. Although corrections for collisional processes are considered in the calculations, the differences in the He^+ abundance are not negligible between both spin configurations. This suggests that self-absorption processes are important in most triplet lines. Four ICFs were used to estimate the contribution of He^0 in the total abundance. The resulting radial distribution of helium has a negative slope when singlet lines are used, regardless of the ICF used.

Key words: ISM: abundances — Galaxy: abundances — Galaxy: disc — Galaxy: evolution — HII regions.

1. Introduction

The star formation history and the gas flows determine the distribution of chemical abundances in galaxies. The existence of radial gradients of chemical abundances in spiral galaxies is a well known fact, and is thought to be caused by 'inside-out' galaxy formation scenario, where the number of generations of stars that have existed is smaller as the galactocentric distance increases.
Almost no metals were created in the beginning of the Universe. Thus, the difference in metallic content between two stellar generations is noticeable and a radial gradient can be traced. On the other hand, the biggest fraction of helium was created during the Primordial Nucleosynthesis and the determination of its radial gradient is highly sensitive to errors and uncertainties in the calculation of He/H ratio.
To determine a radial gradient in the Galactic distribution of helium requires a sample of objects with good quality spectra that covers a wide range of Galactocentric distances. HII regions are suitable for this purpose since they trace the present-day chemical composition of the Galaxy.

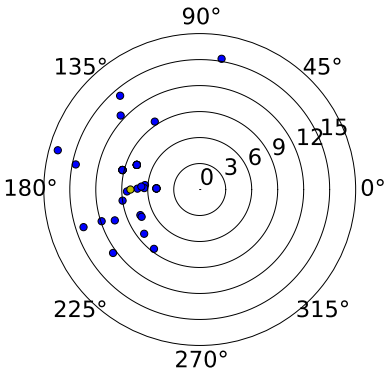

Figure 1. Distribution of HII regions of the sample. The Galactocentric distance is presented in kpc. The yellow dot indicates the position of the Sun (8 kpc).

2. Procedure

Our sample consists on 37 deep spectra of 23 Galactic HII regions, covering a range of radial distance between 5 and 17 kpc. In Figure 1 the distribution of the HII regions in the Galaxy disk is shown.
The data have been obtained with the high-resolution spectrograph UVES at VLT, OSIRIS at GTC and MagE at Magellan Telescope (García-Rojas et al., 2004; Esteban et al., 2004; García-Rojas et al., 2005, 2006, 2007; Esteban et al., 2013, 2016, 2017). The spectral resolution and wavelength coverage allowed us to detect several HeI recombination lines in each spectrum in both spin configurations: triplet and singlet.
We calculated the abundance of He^+ using PyNeb (Luridiana et al., 2015) with all the detected HeI lines in the sample. Some lines as λ3889, λ7065, λ7281 and λ9464 were discarded from the analysis for being deeply affected by line blending, self-absorption, collisions or blending with sky lines. Some other lines were also discarded in particular cases, as λ5016 in the Orion Nebula (Esteban et al., 2004). The effective recombination coefficients used were those calculated by Porter et al. (2013), which include corrections for collisional effects.
To calculate the total helium abundance, the He^0/H^+ ratio was estimated using four Ionization Correction Factors (ICF) based on similarities between ionisation potentials of sulfur and/or oxygen and helium (Peimbert & Torres-Peimbert, 1977; Kunth & Sargent, 1983; Peimbert et al., 1992; Zhang & Liu, 2003). Using Galactocentric distance estimates from the literature for each region of the sample, we derived the radial distribution of helium, analysing separately the results based on singlet and triplet lines.

3. Results and conclusions

Estimates of He^+/H^+ and their associated dispersions were comparatively higher using triplet lines. As an example, Figure 2 shows calculations of He^+/H^+ ob-

tained with every detected HeI line in the Orion Nebula. Figure 3 shows the overestimate of He^+/H^+ in calculations based on the triplet HeI λ5876 line compared to the average value from singlets.

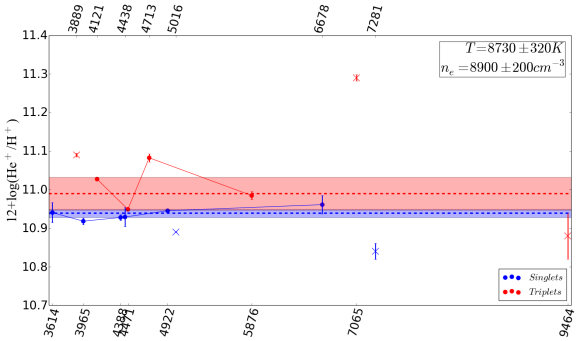

Figure 2. Abundance of He^+ obtained with several recombination lines. Horizontal lines represent the average value for the singlets and triplets. The coloured band indicates the associated uncertainty. The red symbols represent triplets while blue ones represent singlets. Crosses indicate discarded lines.

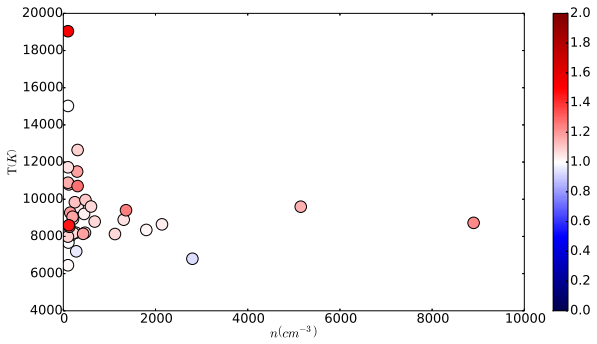

Figure 3. Representation of the He^+/H^+ ratio determined for HeI 5876Å with respect to the mean He^+/H^+ ratio determined from singlets (indicated by the color of the circles) as a function of T_e and n_e.

The resulting radial distribution of helium has negative slope when singlet lines were used regardless of the ICF used. In the case of triplet lines, the slope depends on the ICF used. Calculations based on triplet lines are affected by self-absorption mechanisms that are not easy to correct. Figure 4 shows the radial distribution of helium based on singlet lines and the average value if all the ICF are considered.
Our preliminar results are summarised as follows:

1. Almost all triplet lines comparatively provide overabundances in the He^+/H^+ ratio. The dispersion is also larger. Corrections for collisional processes

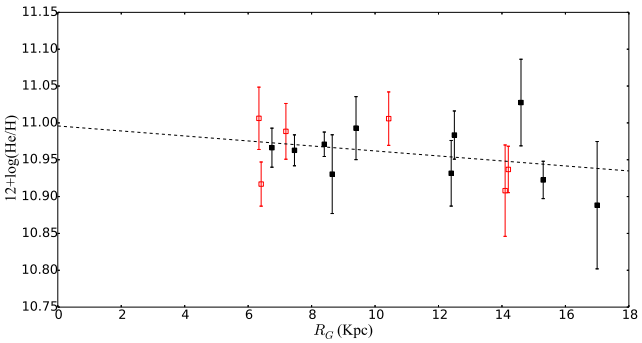

Figure 4. Radial distribution of He/H calculated with singlet lines and the average value of all ICF used. Red symbols have ICF≥1.2 and were not used for the linear fit.

are considered in the He abundance determinations. This suggests that the effects of self-absorption are not negligible in most triplet lines.

2. Discarding triplet lines, the radial distribution of helium has a negative slope regardless of the ICF used. Nevertheless, due to the uncertainty introduced by the ICFs, errors in the slope are still consistent with a flat distribution.

3. HII regions associated with Wolf-Rayet or evolved O stars present helium overabundances.

Acknowledgments. CEL and JRG acknowledge support from the project AYA2015-65205-P. JGR acknowledges support from an Advanced Fellowship from the Severo Ochoa excellence program (SEV-2015-0548).

References

Esteban C., Carigi L., Copetti M. V. F., et al., 2013, *MNRAS*, **433**, 382
Esteban C., Fang X., García-Rojas J., et al., 2017, *MNRAS*, **471**, 987
Esteban C., Mesa-Delgado A., Morisset C., et al., 2016, *MNRAS*, **460**, 4038
Esteban C., Peimbert M., García-Rojas J., et al., 2004, *MNRAS*, **355**, 229
García-Rojas J., Esteban C., Peimbert A., et al., 2005, *MNRAS*, **362**, 301
García-Rojas J., Esteban C., Peimbert A., et al., 2007, *RevMexAA*, **43**, 3
García-Rojas J., Esteban C., Peimbert M., et al., 2004, *ApJS*, **153**, 501
García-Rojas J., Esteban C., Peimbert M., et al., 2006, *MNRAS*, **368**, 253
Kunth D., Sargent W. L. W., 1983, *ApJ*, **273**, 81
Luridiana V., Morisset C., Shaw R. A., 2015, *A&A*, **573**, A42
Peimbert M., Torres-Peimbert S., 1977, *MNRAS*, **179**, 217
Peimbert M., Torres-Peimbert S., Ruiz M. T., 1992, *RevMexAA*, **24**, 155
Porter R. L., Ferland G. J., Storey P. J., et al., 2013, *MNRAS*, **433**, L89
Zhang Y., Liu X.-W., 2003, *A&A*, **404**, 545

Chemical Abundances in Gaseous Nebulae:
Open problems in Nebular astrophysics
AAA Workshop Series 11, 2019
M. Cardaci, G. Hägele & E. Pérez-Montero, eds.

Poster

Metallicity Determination in Seyfert 2 AGNs

Monteiro, A. F.[1,2], Dors, O. L.[1], Cardaci, M. V.[3,4], Hägele, G. F.[3,4]

[1] *Universidade do Vale do Paraíba, Av. Shishima Hifumi 2911, 12244-000, São José dos Campos - SP, Brasil*
[2] *Instituto Federal do Maranhão - Campus Imperatriz, Av. Newton Bello s/n, Vila Maria, 65906-335, Imperatriz - MA, Brasil*
[3] *Instituto de Astrofísica de La Plata (CONICET-UNLP), Argentina*
[4] *Facultad de Ciencias Astronómicas y Geofísicas, Universidad Nacional de La Plata, Paseo del Bosque s/n, 1900 La Plata, Argentina*

Abstract. Aims: To study calibrations of line ratios that can estimates metallicities of galaxies even in large redshift where the measurement of faint emission lines is not easy to obtain. Methods: We use the Cloudy Code to build a grid of photoionization models with lines ratios from the UV and, we compare with a sample of 77 object AGNs Seyfert 2. Results: We build semi-empirical calibrations between the metallicity of studied objects and the rest-frame intensity of the line ratios Nv λ1240 / Heii λ1640, C43=log[(Civ λ1549 + Ciii] λ1909) / Heii λ1640] and Ciii] λ1909 / Civ λ1549.

Key words: galaxies: abundances — galaxies: Seyfert — galaxies: active — galaxies: ISM

1. Introduction

Metalicity determination in Active Galactic Nuclei (AGN) is essential to understand the evolution of galaxies. In general, the method that is considered more reliable for estimations of metallicity (Z) of emission-line objects (e.g. AGNs, Hii regions, and Planetary Nebulae) is the Te-method, which consists of using fluxes of collisionally-excited emission-lines from different ionic levels of a given element to estimate the electron temperature and the abundance in relation to the hydrogen abundance, usually O/H (e.g. Pérez-Montero, 2017; Peimbert et al., 2017). Unfortunately, some auroral line fluxes cannot be easily measured in distant objects or objects with low excitation (e.g. Bresolin et al., 1999) and estimates using the strong-line method can be used as an alternative. The main idea of this method is to calibrate the relationship between the abundance of an element in an ionized region and relatively strong emission lines in its spectrum (Maiolino & Mannucci, 2019). Most of the calibrations between AGN narrow-line ratio and the metallicity is purely theoretical. One that was proposed by Dors et al. (2014) is between the metallicity of the gas in the Narrow Line Regions (NLR) of AGN and the intensity of a ultraviolet (UV) emission-lines through the use of the C43=log[(Civ λ1549 + Ciii] λ1909)/Heii λ1640] emission-lines

ratio. This calibration is strongly dependent on the gas ionization degree which can be estimated from the CIII] λ1909/CIV λ1549 emission-lines ratio. To add observational constraints to produce better reliable metallicity calibrations and also to investigate the use of other strong UV line ratio as a metallicity indicator, in this case, the NV λ1240/HeII λ1640 ratio suggested by Ferland et al. (1996), have motivated this work. The objective is to form a computational method that we can apply to hundreds or thousands of spectra.

2. AGN Sample

To investigate the metallicity in NLR of AGN, we compiled from the literature AGN type 2 line ratios in the range $1000 < \lambda(\text{Å}) < 2000$. It was composed of 77 spectra (redshift, $z < 4.0$), that we took most part from Matsuoka et al. (2018) and we included some objects at low redshifts ($z < 0.04$). The criteria used for selection is the presence of fluxes of CIII] λ1909, CIV λ1549 and HeII λ1640. The flux of NV λ1240 is only available for 22 of the objects of our sample. We did not correct emission-lines reddening due to the small effect of dust extinction on determinations of metallicity and ionization degree obtained from the considered emission-line ratios (Nagao et al., 2006b).

3. Photoionization models

We use the Cloudy code version 17.01 (Ferland et al., 2017) to build a grid of photoionization models representing AGN for comparing the predicted UV emission-line intensity ratios with those measured for the type-2 AGNs. All models have the Spectral Energy Distribution (SED) composed by two parts: one representing the Big Blue Bump peaking at 1 Ryd, and the other a power law with spectral index alpha parameter of -1.4 representing the non-thermal X-ray radiation (Miller et al., 2011). The electronic density is set to be 500cm^{-3} as well for all models, an average value calculated for a sample of Seyfert 2 AGN by Dors et al. (2014). For the ionization parameter (U), we use values in the range $-4.0 \leq \log U \leq -1.0$, with a step of 0.5 dex, and the following values for the metallicity in relation to the solar one ($Z/Z_{\odot}$): 0.2, 0.5, 0.75, 1.0, 1.5, 2.0, 3.0 and 4.0. We adopt that all elements abundance, except nitrogen, scales linearly with the oxygen abundance, for that, we use the relation found by Hamann & Ferland (1993), $(\text{N/H}) = (Z/Z_{\odot})^2 \times (\text{N/H})_{\odot}$, where the value of $\log(\text{N/H})_{\odot} = -4.07$ was taken from Holweger (2001).
In Figure 1, on the left panel, the grid composed by log(CIII] λ1909/CIV λ1549) and C43 line ratios, and, on the right panel, other one composed by log(CIII] λ1909/CIV λ1549) and log(NV λ1240/HeII λ1640) line ratios. An important caveat is that a strong line metallicity diagnostics can degenerate when employing some indirect correlations, such as the correlation between metallicity and ionization parameter (Maiolino & Mannucci, 2019; Nagao et al., 2006a). In the grids, we do not found degenerescence in metallicity for the values considered for the C43 index, but one is present for the diagnostic with NV/HeII line ratio, and we do not consider values in range $0.2 < Z/Z_{\odot} < 0.5$ because values above 0.5 seems to be more realistic to AGN.

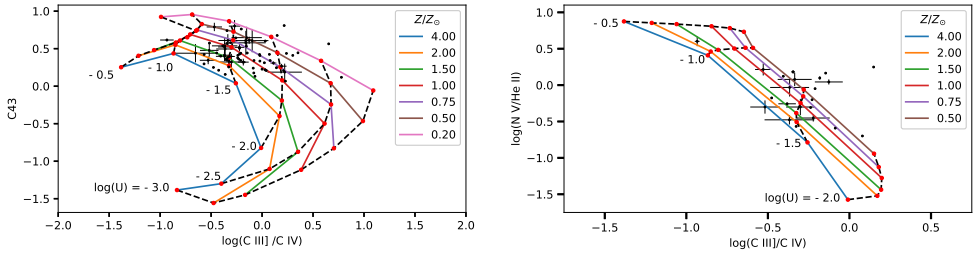

Figure 1. On the left panel, the grid composed by log(CIII] λ1909/CIV λ1549) and C43 line ratios, and, on the right panel, it shows one with log(CIII] λ1909/CIV λ1549) and log(NV λ1240/HeII λ1640) line ratios.

4. Method

We used the same methodology of Castro et al. (2017) to obtain semi-empirical calibrations between metallicities and the indexes. For each point inside the grid shown in Figure 1, we found the value of Z by linear interpolation with line segments, which contain a point we are interested in estimating, bounded by the two nearest solid lines, the assumption is that a point over these line has the same metallicity indicated by the legend. We made an analogous process with the dashed lines for the values of the $\log U$. With the interpolated parameters and the observational line ratios of the sample, we have adjusted semi-empirical calibrations using the method of least squares.

5. Results

In Figure 2, the values of metallicity obtained with the grids shown in Figure 1. On the left panel, we plot the calibration found using the C43 line ratio, and, on the right panel, the calibration using the log(NV/HeII) line ratio.

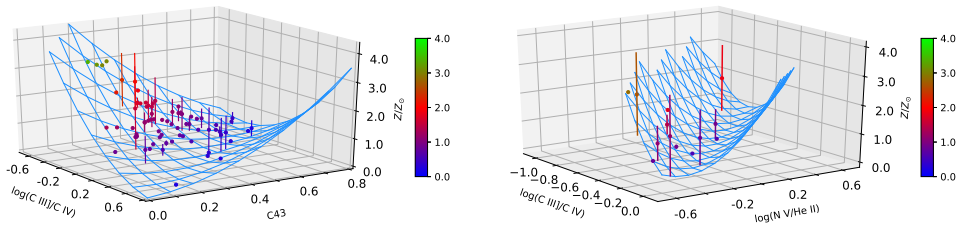

Figure 2. On the left panel, the calibration found using the C43 line ratio, and, on the right panel, the calibration using the log(NV/HeII) line ratio.

We compared our results with the calibration between Z and $N2O2$ = log([NII] λ6584 / [OII] λ3727) index on optical range proposed by Castro et al. (2017). We found only three objects in common in both samples, they are presented in Table 1, and it shows that the closest values were calculated by the calibration of the C43 line ratio.

Table 1. Metallicities ($Z/Z_\odot$) comparison of NV/HeII and C43 line ratios obtained in this work and $N2O2$ line ratio obtained by Castro et al. (2017).

	$Z/Z_\odot$		
	NV/HeII	C43	$N2O2$
NGC 5506	—	0.47	1.15
Mrk 3	2.47	1.00	1.16
Mrk 573	1.09	1.67	1.12

6. Conclusions

We compared the observational intensities of UV emission lines with results of photoionization models to obtain two semi-empirical calibrations between the metallicity of the Narrow Line Region of Seyfert type-2 Active Galactic Nuclei. The calibrations found seems to be more reliable than the results of Dors et al. (2014) once we use observational constraints.

Acknowledgments. A. F. Monteiro would like to thank Coordenação de Aperfeiçoamento de Pessoal de Nível Superior (CAPES).

References

Bresolin F., Kennicutt, Jr. R. C., Garnett D. R., 1999, *Astrophys. J.*, **510(1)**, 104

Castro C. S., Dors O. L., Cardaci M. V., Hägele G. F., 2017, *Mon. Not. R. Astron. Soc.*, **467(2)**, 1507

Dors O. L., Cardaci M. V., Hägele G. F., Krabbe Â. C., 2014, *Mon. Not. R. Astron. Soc.*, **443(2)**, 1291

Ferland G. J., Baldwin J. A., Korista K. T., Hamann F., Carswell R. F., Phillips M., Wilkes B., Williams R. E., 1996, *Astrophys. J.*, **461**, 683

Ferland G. J., Chatzikos M., Guzmán F., Lykins M. L., van Hoof P. A. M., Williams R. J. R., Abel N. P., Badnell N. R., Keenan F. P., Porter R. L., Stancil P. C., 2017, *Rev. Mex. Astron. y Astrofísica*, **53**, 385

Hamann F., Ferland G., 1993, *Astrophys. J.*, **418**, 11

Maiolino R., Mannucci F., 2019, *Astron. Astrophys. Rev.*, **27(1)**, 3

Matsuoka K., Nagao T., Marconi A., Maiolino R., Mannucci F., Cresci G., Terao K., Ikeda H., 2018, *Astron. Astrophys.*, **616**, L4

Miller B. P., Brandt W. N., Schneider D. P., Gibson R. R., Steffen A. T., Wu J., 2011, *Astrophys. J.*, **726(1)**, 20

Nagao T., Maiolino R., Marconi A., 2006a, *Astron. Astrophys.*, **459(1)**, 85

Nagao T., Maiolino R., Marconi A., 2006b, *Astron. Astrophys.*, **447(3)**, 863

Peimbert M., Peimbert A., Delgado-Inglada G., 2017, *Publ. Astron. Soc. Pacific*, **129(978)**, 082001

Pérez-Montero E., 2017, *Publ. Astron. Soc. Pacific*, **129(974)**, 043001

Chemical Abundances in Gaseous Nebulae:
Open problems in Nebular astrophysics
AAA Workshop Series 11, 2019
M. Cardaci, G. Hägele & E. Pérez-Montero, eds.

Poster

Extragalactic Star-forming Regions: a Study of the Physical Properties and Chemical Abundances

Dania Muñoz-Vergara[1,2], Verónica Firpo[2,1], Guillermo Hägele[3,4], Guillermo Bosch[3,4], Mónica Cardaci[3,4], David Sanmartim[2] and Germán Gimeno[2]

[1] *Universidad de La Serena, La Serena, Chile*
[2] *Gemini Observatory, Southern Operations Centre,La Serena, Chile*
[3] *Instituto de Astrofísica de La Plata, CONICET–UNLP, Argentina*
[4] *Facultad de Ciencias Astronómicas y Geofísicas, Universidad Nacional de La Plata, Argentina*

Abstract. Extragalactic star-forming regions are characterized by the large number of young and massive stars that ionize the surrounding gas. These regions can be observed as very luminous spots in the disk of spiral galaxies and as large areas in Blue Compact Dwarf galaxies. We present preliminary results of the study of a sample of star-forming regions in two spiral and one Blue Compact Dwarf galaxies observed with the GMOS/Long-slit configuration on the Gemini-South Telescope. We are presenting a preliminary study of two regions of each galaxy for which we estimated: reddening, electron densities, and electron temperatures by using direct method, temperature relations based on photoionization models, and empirical relations. From the electron temperatures we derived ionic and total chemical abundances of, O, S, N, Ne, Ar and He. In addition we computed star formation rates and the ionization state for all regions.

galaxies: abundances — galaxies: ISM

1. Observation and Data Reduction

We have observed the two spiral galaxies: NGC 5861 and NGC 6070, and the Blue Compact Galaxy: Tol 1924-416A. Data were acquired with the Gemini-South Multi-Object Spectrograph (GMOS) in longslit configuration on April 27, 2007 (program ID: GS-2007A-Q-30, PI: V. Firpo), using the B600 (blue) and R400 (red) gratings to cover a wavelength range ∼3350-9600 Å. Data reduction was performed using the Gemini GMOS IRAF tasks including bias and overscan subtraction, flat fielding, wavelength calibration, and flux calibration. Observing conditions were good, with an average seeing of $0\farcs7$. The R400 grating centered at 7700 Å gives a dispersion of ∼1.3 Å pix^{-1}. The B600 grating centered at 4800 Å gives a dispersion of ∼0.9 Å pix^{-1}. From these observations we have extracted spectroscopic data of 10 star-forming regions, 5 of them located in NGC 5861, 3 in NGC 6070 and the last 2 in Tol 1924-416A. Here we are presenting

preliminary results obtained for two star-forming regions on each galaxy. The whole sample analysis will be presented in Muñoz-Vergara et al. (in prep.).

2. Results

Following the method described by Hägele et al. (2006), we have measured the line and continuum fluxes and estimated the equivalent width (EW) for a good number of emission-lines. Tables 1-3 present the list of emission-lines measured for the two studied regions of the three galaxies (NGC 5861, Tol 1924-416A and NGC 6070, respectively) together with the estimated reddening corrected emission-line intensities, I(λ), in terms of Hβ (assuming F(Hβ)=I(Hβ)=10000), their estimated Equivalent Width (EW), the line intensities percentage error and the Correction Factor f(λ). The reddening constant estimated for each region and its error are also listed in these tables.
The physical conditions of the ionized gas in the star-forming regions were derived following the same methodology as Hägele et al. (2012) and are presented in Table 4. As the [SIII] λ9532 Å could not be measured, its flux was estimated assuming the theoretical value of 2.44× [SIII] λ9069 Å. The electronic density, N_e, was determined from the ratio R_{S2} of the lines [SII] λ6717,6731 Å. The electron temperatures for each ion were derived using the strategy described by Hägele et al. (2012, section 3.2).

Table 1. NGC 5861

		I			II$_{1stComp}$		
λ(Å)	f(λ)	-EW(Å)	I(λ)	Error(%)	-EW(Å)	I(λ)	Error(%)
3727 [OII]dob	0.271	29.11	16112±589	3.7	36.48	21091±592	2.8
4102 Hδ	0.188	8.87	2917±917	31.4	20.00	4730±1575	33.3
4340 Hγ	0.142	32.30	3884±880	22.7	18.00	3829±1504	39.3
4861 Hβ	0.000	50.28	10004±153	1.5	51.00	10006±158	1.6
4959 [OIII]	-0.024	9.02	1917±66	3.4	7.00	1061±188	17.7
5007 [OIII]	-0.035	25.99	5215±32	0.6	16.00	2499±264	10.5
5876 HeI	-0.209	16.73	1622±752	46.4	9.00	844±36	4.3
6300 [OI]	-0.276	2.64	363±18	4.9	2.00	266±57	21.5
6548 [NII]	-0.311	21.05	2474±214	8.7	28.00	3182±310	9.8
6563 Hα	-0.313	251.78	28760±532	1.8	235.00	28899±779	2.7
6584 [NII]	-0.316	61.91	7455±214	2.9	80.00	8828±341	3.9
6678 HeI	-0.329	3.67	365±213	58.4	4.00	301±55	18.2
6717 [SII]	-0.334	34.34	3687±123	3.3	42.00	3936±221	5.6
6731 [SII]	-0.336	22.92	2489±101	4.0	3200	2962±179	6.0
7136 [ArIII]	-0.385	4.46	350±39	11.0	3.00	188±66	35.2
9069 [SIII]	-0.561	18.03	884±41	4.6	17.00	697±64	9.1
c(Hβ)			0.74 ± 0.03			0.94 ± 0.04	
I(Hβ)(erg seg^{-1} cm^{-2})			0.24×10^{-14}			0.17×10^{-14}	

Total chemical abundances derived for the regions considered here are listed in the botom part of Table 4. The total chemical abundances from forbidden lines O, S, Ne and Ar were derived from the measured forbidden emission-lines and using the estimated line temperatures as described by Hägele et al. (2008, 2012). This table includes the adopted value for He^+/H^+ as the average value, weighted by the errors, of the He ionic abundances derived from each He emission-line. In general, all regions are in a low density regime. In both regions of Tol 1924-416 was possible to derive the oxygen abundances with values of ∼0.18 and ∼0.15 times the solar value ($12+\log(O/H)_\odot = 8.69$, Allende Prieto et al., 2001) for region I and II, respectively. These results, as well as the derived sulfur abundance, are in good agreement with the obtained by Kehrig et al. (2006), 0.16 times the solar value for the oxygen abundances and 6.08±0.12 for the

Table 2. Tol1924-416A

		I			II		
λ(Å)	f(λ)	-EW(Å)	I(λ)	Error(%)	-EW(Å)	I(λ)	Error(%)
3727 [OII]dob	0.271	87.82	13631±325	2.4	89.45	14065±421	3.0
3868 [NeIII]	0.238	36.64	4208±88	2.1	48.39	4957±169	3.4
3889 HeI+H8	0.233	13.58	1646±72	4.4	23.21	2027±92	4.5
3970 [NeIII]+He	0.215	47.78	3292±168	5.1	30.59	2673±133	5.0
4102 Hδ	0.188	34.26	2700±176	6.5	27.98	2664±437	16.4
4340 Hγ	0.142	74.78	4842±334	6.9	91.75	5263±149	2.8
4363 [OIII]	0.138	11.30	815±50	6.1	14.40	901±90	10.0
4471 HeI	0.106	7.32	471±30	6.4	. . .	. . .	. . .
4861 Hβ	0.000	179.99	10003±228	2.3	178.10	10001±200	2.0
4959 [OIII]	-0.024	281.76	17729±65	0.4	299.76	17691±26	0.1
5007 [OIII]	-0.035	786.43	53184±120	0.2	782.22	52661±106	0.2
5876 HeI	-0.209	25.48	971±19	1.9	34.18	1228±50	4.1
6300 [OI]	-0.276	11.33	363±18	5.1	13.57	548±19	3.5
6312 [SIII]	-0.278	4.43	141±9	6.1	6.04	245±27	11.1
6364 [OI]	. . .	. . .	. . .	. . .	5.80	234±19	8.3
6548 [NII]	-0.311	10.52	319±21	6.5	6.85	272±19	7.1
6563 Hα	-0.313	663.25	28366±186	0.7	767.78	29504±385	1.3
6584 [NII]	-0.316	28.02	854±30	3.5	18.01	727±30	4.1
6678 HeI	-0.329	11.86	311±13	4.3	8.87	302±53	17.7
6717 [SII]	-0.334	46.62	1283±32	2.5	43.76	1666±43	2.6
6731 [SII]	-0.336	32.97	928±29	3.1	30.51	1171±33	2.8
7065 HeI	-0.377	7.60	189±14	7.3	. . .	. . .	. . .
7136 [ArIII]	-0.385	20.23	476±18	3.7	18.48	544±22	4.1
7319 [OII]dob	-0.406	7.47	174±14	8.3	8.13	239±20	8.3
7330 [OII]dob	-0.407	7.69	179±22	12.3	5.89	174±17	9.8
7751 [ArIII]	-0.451	6.31	138±9	6.2	71.00	205±14	7.0
9069 [SIII]	-0.561	41.43	617±26	4.2	38.41	801±34	4.2
c(Hβ)			0.43 ± 0.03			0.25 ± 0.02	
I(Hβ)(erg seg^{-1} cm^{-2})			2.76×10^{-14}			1.60×10^{-14}	

sulfur abundances. The derived oxygen abundance values for NGC 5861 are 0.1 and 0.15 times the solar value in regions I and II$_{1stComp}$, respectively. The value derived for NGC 6070-I is 0.19 times the solar values. These oxygen abundances are consistent with the values estimated for both regions on Tol 1924-416.

Table 3. NGC 6070

			NGC6070				
			I			II	
λ(Å)	f(λ)	-EW(Å)	I(λ)	Error(%)	-EW(Å)	I(λ)	Error(%)
3727 [OII]dob	0.271	53.19	15976±686	4.3	. . .	. . .	. . .
3970 [NeIII]+He	0.215	6.42	1417±153	10.8	. . .	. . .	. . .
4102 Hδ	0.188	30.07	2785±353	12.7	. . .	. . .	. . .
4340 Hγ	0.142	146.72	3672±729	19.8	. . .	. . .	. . .
4861 Hβ	0.000	106.78	10004±145	1.4	57.00	10006±352	3.5
4959 [OIII]	-0.024	68.16	6417±79	1.2	22.00	4592±407	8.9
5007 [OIII]	-0.035	176.47	18617±122	0.7	61.00	12961±591	4.6
5876 HeI	-0.209	17.94	1043±21	2.0	. . .	. . .	. . .
6300 [OI]	-0.276	2.28	169±25	14.7	. . .	. . .	. . .
6548 [NII]	-0.311	30.18	1710±54	3.1	15.00	2022±221	10.9
6563 Hα	-0.313	488.98	28775±586	2.0	261.00	28500±621	2.2
6584 [NII]	-0.316	85.91	4860±128	2.6	45.00	6132±414	6.8
6678 HeI	-0.329	6.40	309±9	2.9	. . .	. . .	. . .
6717 [SII]	-0.334	50.76	2496±68	2.7	34.00	3814±265	7.0
6731 [SII]	-0.336	34.36	1712±50	2.9	22.00	2477±190	7.7
7136 [ArIII]	-0.385	17.77	676±23	3.3	. . .	. . .	. . .
9069 [SIII]	-0.561	63.61	1324±60	4.5	14.00	606±129	21.3
c(Hβ)			0.68 ± 0.03			1.00 ± 0.08	
I(Hβ)(erg seg^{-1} cm^{-2})			0.45×10^{-14}			0.04×10^{-14}	

Table 5 presents the values of Star Formation Rates (SFRs), Hα luminosity (logarithmic scale) for the presented star forming region. For spiral galaxies, SFR and Hα luminosity values are in agreement with values found by Skillman et al. (2003) in 11 spiral galaxies. On the other hand, Tol 1924-416 presents very high values, and they are similar to the values of other BCD galaxies studied by Hopkins et al. (2002); Ramya et al. (2009).

Acknowledgments. DM gratefully acknowledges support from the Gemini Observatory, SoutherOperations Centre, Internship Program and CONICYT-

Table 4. Densities in cm^{-3} and temperatures in 10^4K.

	NGC5861		NGC6070		Tol1924-416	
	I	II$_{1stComp}$	I	II	I	II
n([SII])	10:	80:	10:	20:	25:	10:
T([OIII])	1.0[e]	1.0[e]	1.0[e]	1.0[e]	1.35±0.03	1.42±0.06
T([SIII])	0.87± 0.13[c]	0.87 ± 0.13[c]	0.87[c]	0.87[c]	1.29±0.12	1.47±0.12
T([OII])	1.21±0.04[f]	1.05[f]	1.21[f]	1.15[f]	1.286[d]	1.37[d]
T([SII]	0.98[f]	0.98[f]	0.98[f]	0.94±0.01[f]	1.296[e]	1.208[e]
T([NII])	1.21±0.04[a]	1.05[a]	1.21±0.04[g]	1.15[g]	1.04[b]	1.16[b]
Total and Relative Abundances						
12+log(O/H)	7.67±0.01	7.87±0.03	7.96±0.01	. . .	7.85±0.03	7.79±0.05
12+log(S/H)	6.39±0.11	6.40±0.10	6.53±0.13	. . .	5.87±0.08	5.91±0.07
12+log(Ne/H)	. . .	. . .	. . .	. . .	7.23±0.04	7.24±0.07
12+log(Ar/H)	5.73±0.21	5.50±0.30	5.99±0.18	. . .	5.10±0.05	5.04±0.07
He^+/H^+(adopted)	0.107±0.012	0.062±0.011	0.078±0.002	. . .	0.078±0.011	0.097±0.009

[a]Derived using temperatures predicted by photoinizaton models [b]Derived using temperatures estimated from photoionization models and/or empirical methods. [c]Derived using Hägele et al. (2006) empirical method. [d]Derived using Díaz et al. (2007) empirical method. [e]Assumed temperature=10^4K. [f]Derived using Pérez-Montero & Díaz (2003) method.

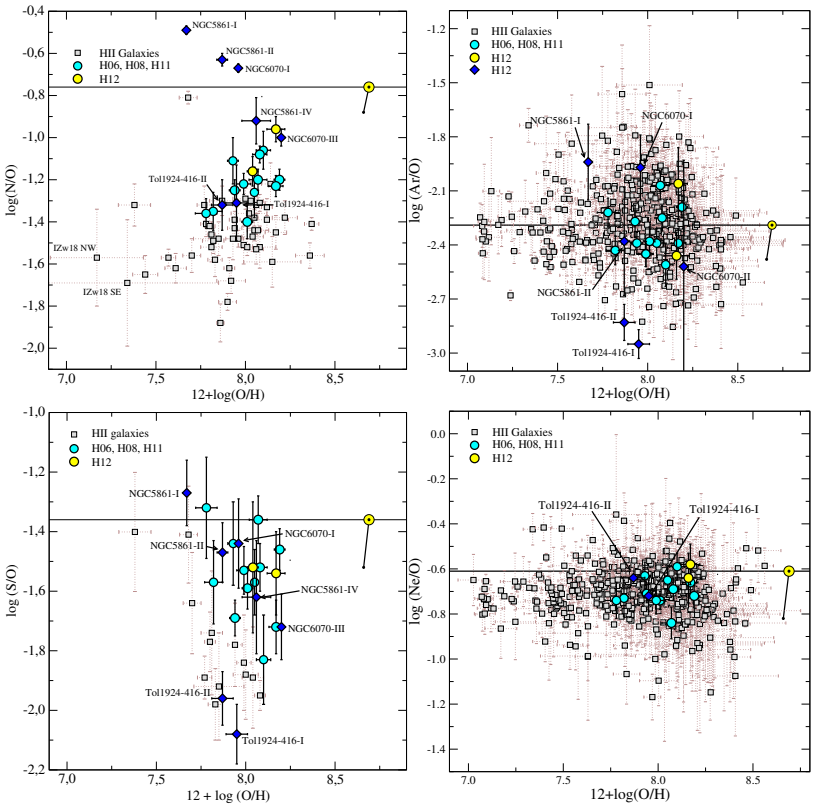

Figure 1. From left to right: N, Ar, S, and Ne relative abundances. The yellow filled sun symbol indicates the solar value. Yellow filled circles are values from Hägele et al. (2012) and cyan filled circles are results from Hägele et al. (2006, 2008, 2011)

PFCHA/Doctorado Nacional/2019-21191543. VF acknowledges support from CONICYT Astronomy Program-2015 Research Fellow GEMINI-CONICYT

Table 5.

Regions	SFR ($\times 10^{-3}$ $M_\odot$ yr^{-1})	log(L(Hα))	err%[L(Hα)]
NGC 5861_I	5.19±0.92	38.82	18
NGC 5861_II$_{1stComp}$	3.69±0.69	38.66	19
NGC 6070_I	10.3±1.93	39.11	19
NGC 6070_II	0.91±0.21	38.06	23
Tol 1924-416_I	103±20.3	40.12	20
Tol 1924-416_II	62.4±12.3	39.90	20

(32RF0002). Based on observations obtained at the Gemini Observatory, which is operated by the Association of Universities for Research in Astronomy, Inc., under a cooperative agreement with the NSF on behalf of the Gemini partnership: the National Science Foundation (United States), the National Research Council (Canada), CONICYT (Chile), Ministerio de Ciencia, Tecnología e Innovación Productiva (Argentina), and Ministério da Ciência, Tecnologia e Inovação (Brazil) and the Korea Astronomy & Space Science Institute (Korea).

References

Allende Prieto C., Lambert D. L., Asplund M., 2001, *ApJL*, **556**, L63
Díaz Á. I., Terlevich E., Castellanos M., Hägele G. F., 2007, *MNRAS*, **382**, 251
Hägele G. F., Díaz Á. I., Terlevich E., Terlevich R., Pérez-Montero E., Cardaci M. V., 2008, *MNRAS*, **383**, 209
Hägele G. F., Firpo V., Bosch G., Díaz Á. I., Morrell N., 2012, *MNRAS*, **422**, 3475
Hägele G. F., García-Benito R., Pérez-Montero E., Díaz Á. I., Cardaci M. V., Firpo V., Terlevich E., Terlevich R., 2011, *MNRAS*, **414**, 272
Hägele G. F., Pérez-Montero E., Díaz Á. I., Terlevich E., Terlevich R., 2006, *MNRAS*, **372**, 293
Hopkins A. M., Schulte-Ladbeck R. E., Drozdovsky I. O., 2002, *AJ*, **124**, 862
Kehrig C., Vílchez J. M., Telles E., Cuisinier F., Pérez-Montero E., 2006, *A&A*, **457**, 477
Pérez-Montero E., Díaz A. I., 2003, *MNRAS*, **346**, 105
Ramya S., Sahu D. K., Prabhu T. P., 2009, *MNRAS*, **396**, 97
Skillman E. D., Côté S., Miller B. W., 2003, *AJ*, **125**, 593

Chemical Abundances in Gaseous Nebulae:
Open problems in Nebular astrophysics
AAA Workshop Series 11, 2019
M. Cardaci, G. Hägele & E. Pérez-Montero, eds.

Poster

Spatially Resolved Abundances: The Case of the Planetary Nebula Menzel 1

P. Santos[1] and H. Monteiro[1]

[1]*Instituto de Física e Química, Universidade Federal de Itajubá, Av. BPS 1303, Itajubá - MG, Brazil*

Abstract. In this work we present a study of spattially resolved abundances using a three dimensional photoionization model for the planetary nebula Menzel 1. The code used is MOCASSIN, and the three dimensional structure used takes into account the bipolar structure of the nebula. We first validate the model of Monteiro et al. (2005) which used a different code and compare results. We then fit a final model witht the updated structure and Mocassin to the data observed. Finally we present a comparison of the fitted model with results obtained through the usual empirical method.

Key words: planetary nebula: abundances — nebula: flux maps — techniques: three-dimensional photoionization model

1. Introduction

Planetary Nebulae (PNe) are objects that can show very complex morphologies and the details of the formation of their spatial structures is still under investigation. Some works take into account the three-dimensional structure of objects but many still consider the symmetrically spherical approximation. In addition to the spherical structure, most older models also assume that the abundance of the elements is uniform throughout the PNe extension. However, some recent studies suggest that there may be variations in these abundances, and few studies explore this hypothesis in detail.
Walsh et al. (2018) made the first detailed study of a PN using the MUSE spectograph. They have obtained images for mapping the emission lines, and from them physical and chemical condition maps were made. Only the total abundance for the He and the O were obtained. The map of the He/H is not homegeneous, presenting a variation corresponding to the ionization structure. They compared total abundance of O using three different ICF's and show a deficit in the central region where the He^{++} is more intense.
The PN Menzel 1 is a bright object, and yet it is still not very well studied. As can be seen in the Figure 1 of the Monteiro et al. (2005), this PN has a bipolar morphology with a evident ring. Monteiro et al. (2005) did a detailed study using spectophotometric mapping and a tridimensional model. In their work the distance, luminosity and ionizing star temperature were obtained with

reasonable accuracy with values of 1050 ± 150 pc, 164 ± 25 $L_{\odot}$ and 120 ± 16 kK respectively.
In this work we present a three dimensional photoionization model for the planetary nebula Menzel 1 using the MOCASSIN code, taking into account its bipolar structure. The main objective in this work was to verify if the empirical method is able to reproduce the results obtained in the model. The proceedure and results obtained are discussed in the following sections.

2. Procedure

First, we remade the Monteiro et al. (2005) model with the MOCASSIN code using the same structure. The objective was to evaluate the influence of the diffuse radiation and updated atomic data present in Moccasin code which were not included in the old code used. After validation, to obtain the final fit, we made some changes in the structure to obtain a model that best fit the observational data. Finally, we analyzed the generated maps of abundances and temperature obtained from the model using the empirical method.

3. Results

Our results show that the model obtained with the updated code and atomic data lead to significantly different values when compared to previous models for the same object under the same conditions (Table 1). The code used to generate the previous model, different from MOCASSIN, did not take into account the effect of the diffuse radiation. The lack of diffuse radiation in the old code is the likely cause for the discrepancies found. The temperature map obtained from the model through the empirical proceedure, shown in Figure 1 is qualitatively similar to the cut through the temperature cube obtained from the model. However there are differences seen. In particular these maps do not agree with the observed ones.
The determined abundances (Figure 2 and Table 1) show important discrepancies both in relation to empirical determination and the determination using three-dimensional photoionization models. In particular it is evident that there are variation that are not real since the input abundancers were constant.

4. Conclusions

In this work we present a comparison of the model generated using the MOCASSIN code with the model made by Monteiro et al. (2005) and with results obtained through the empirical method. The new model shows significantly different values when compared to previous models for the same object under the same conditions and the main cause for the discrepancies is the diffuse radiation. Comparing the model with the results obtained from the empirical method it is evident that the empirical method can not recover the input values of the model, in particular it shows variations in abundances when the input ones were constant. The preliminary results indicate that the structure complexity plays an important role in the results of the empirical abundance method determinations.

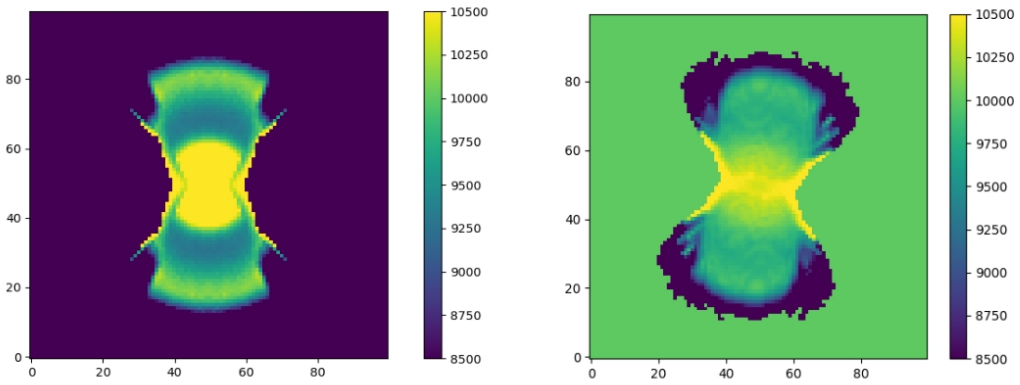

Figure 1. *Left:* Section of the temperature structrure from model. *Right:* Temperature map obtained from de flux maps of the model using de empirical method.

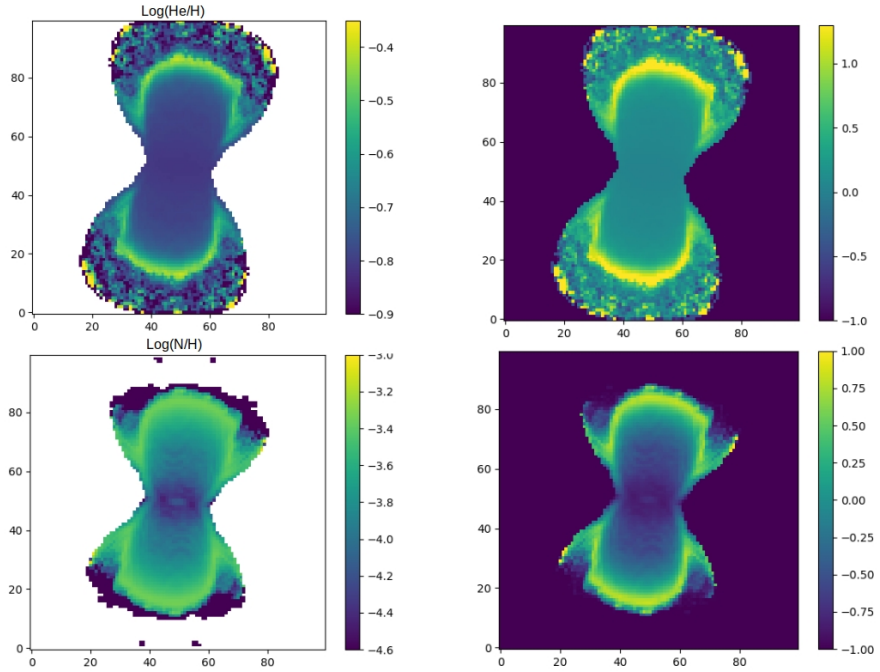

Figure 2. *Left:* Abundances maps obtained from de flux maps of the model using de empirical method. *Right:* Residuals maps of the abundances maps from de model compared with the abundance value in the last column of the Table 1.

Table 1. Table to compare the physical and chemical parameters of the models and from observational data.

	Empirical	Model		
	Perinotto & Corradi (1998)	Monteiro et al. (2005)	Remade	New
Teff	–	120 kK	120 kK	100 kK
L	–	123	123	113
Te	–	–	9,8 kK	10 kK
Ne	–	100-1400	200-1400	200-1100
$[OIII]$5007	–	6,68	6,36	7,38
HeI 5875	–	0,26	0,17	0,21
$[NII]$6584	–	5,30	7,82	5,99
$[SII]$6717	–	0,49	0,87	0,48
$[SII]$6731	–	0,45	0,91	0,42
He/H	1,46E-01	1,14E-01	1,14E-01	1,5E-01
N/H	3,00E-04	2,20E-04	2,20E-04	2,50E-04
O/H	4,80E-04	4,70E-04	4,70E-04	3,80E-04
Ne/H	2,10E-04	3,50E-04	3,50E-04	3,80E-04
S/H	8,30E-06	1,10E-05	1,10E-05	1,20E-05

Acknowledgments. We would like to thank CAPES for the financial support.

References

Monteiro H., Schwarz H. E., Gruenwald R., Guenthner K., Heathcote S. R., 2005, *The Astrophysical Journal*, **620(1)**, 321

Perinotto M., Corradi R. L., 1998, *Astronomy and Astrophysics*, **332**, 721

Walsh J., Monreal-Ibero A., Barlow M., Ueta T., Wesson R., Zijlstra A., Kimeswenger S., Leal-Ferreira M., Otsuka M., 2018, *Astronomy & Astrophysics*, **620**, A169

General Bibliography

This bibliography is a compilation of all bibliographic references from each paper. Page numbers that appear at the end of each entry link to the bibliography sections that include it. Please click on the URL or on the page number to access the linked item.

List of Authors

The purpose of this second worshop was to address crucial questions related to the open problems in nebular astrophysics related with the estimation of the chemical abundances and the temperature discrepancy problem. The discussions included studies on HII regions and Planetary Nebulae as well as in Active Galactic Nuclei. The workshop gathered scientist and students and covered all major theoretical and observational aspects of the specific issues promoting interesting discusions.

ISBN 978-987-24948-6-5

9 789872 494865

AAA Workshop Series Vol. 11